Self-Consistent Field Theory for Inhomogeneous Homopolymers and Grafted Polymers

Apostolos T. Lakkas

ii

ΕΘΝΙΚΟ ΜΕΤΣΟΒΙΟ ΠΟΛΥΤΕΧΝΕΙΟ
ΣΧΟΛΗ ΧΗΜΙΚΩΝ ΜΗΧΑΝΙΚΩΝ

Η Θεωρία του Αυτοσυνεπούς Πεδίου

σε Ανομοιογενή Ομοπολυμερή και Εμφυτευμένα Πολυμερή

Self-Consistent Field Theory for

Inhomogeneous Homopolymers and Grafted Polymers

Απόστολος Θ. Λάκκας
Apostolos T. Lakkas

Διδακτορική Διατριβή υποβληθείσα στην Σχολή Χημικών Μηχανικών του Εθνικού Μετρόβιου Πολυτεχνείου για την απόκτηση του τίτλου του Διδάκτορος του Εθνικού Μετσόβιου Πολυτεχνείου

Αθήνα, Ιούνιος 2021

Thesis examination committee:

- **Professor Doros Theodorou** (supervisor)
  School of Chemical Engineering
  National Technical University of Athens

- **Professor Andreas Boudouvis** (member of the advisory committee)
  School of Chemical Engineering
  National Technical University of Athens

- **Professor Vissarion Papadopoulos** (member of the advisory committee)
  School of Civil Engineering
  National Technical University of Athens

- **Professor Costas Charitidis**
  School of Chemical Engineering
  National Technical University of Athens

- **Professor Vlasis Mavrantzas**
  Department of Chemical Engineering
  University of Patras

- **Associate Professor Antonis Karantonis**
  School of Chemical Engineering
  National Technical University of Athens

- **Dr. Konstas Daoulas**
  Project Leader
  Department of Polymer Theory
  Max Planck Institute for Polymer Research

The Dissertation is dedicated to my beloved son,

Odysseus.

Contents

Contents

Contents

Acknowledgements

I would like to start by expressing my deep appreciation and gratitude to my advisor *Prof. Doros N. Theodorou* for motivating, teaching and guiding me throughout this exciting trip in polymer science. His aptitude for perfection and rigor coupled with his persistence in attacking serious problems with no straightforward solutions pushed me to my limits and made me appreciate the virtues of patience and determination. He has been a tremendous mentor and role model for me, providing support at *all* levels, encouraging me into becoming an independent researcher.

Secondly, I would like to thank *Prof. Andreas Boudouvis* and *Prof. Vissarion Papadopoulos* for being members of my thesis advisory committee and for their generous help and support at all levels. I would like to specially acknowedge them for giving the opportunity to visit their groups and develop an active collaboration with them.

I could not proceed without thanking the other members of my examination committee *Professor Costas Charitidis*, *Professor Vlasis Mavrantzas, Associate Professor Antonis Karantonis* and *Dr. Kostas Daoulas* for their thoughtful questions and remarks, generating a very fruitful discussion around my thesis. I would like to thank *Professor Dimitrios Karonis* for our continuous fruitful collaboration over the years, for the scientific support received as well as for transferring to me crucial knowledge that guided my initial footsteps as a researcher.

Many past and present colleagues have been extremely helpful to me during my PhD and I am thankful for that. First of all I would like to thank the senior members of the Computational Materials Science and Engineering Group, *Dr. George Vogiatzis* and *Dr. Stefanos Anogiannakis*, for their help during the first steps of my thesis and our active collaboration throughout its course. Furthermore, I would like to offer my special thanks to *Dr. Aristotelis Sgouros* and *Mr. Constantinos Revelas* for the very active and fruitful collaboration we had. Without their contribution the completion of this thesis would be impossible. Since a long time I have considered all of them not just as colleagues, but also as good friends.

I would like to thank my office-mates *Dr. Orestis Ziogos, Dr. Panagiotis Tzounis*, *Dr. Georgios Kritikos, Dr Christos Tzoumanekas* and *Dr. Spyros Kallivokas and Mr Vasilis Georgilas* with whom I shared my office for about four years. I really had a great time working with them. At this point I should mention the interesting discussions I had with *Dr. Eleni Koronaki*, *Dr. George Paschos,* and *Dr Nikos Chamakos* who kindly shared with me their experience on the Finite Element Method .

Many thanks are due to *Mr. George Kissas* and *Mr Konstantinos Zinelis*. I had the pleasure to work with them in the framework of their Diploma and Master's theses and very much enjoyed it.

Very special thanks to my parents, *Thomas* and *Theodora* for their love, support and encouragement. They stood by me in difficult times and they always had a way of guiding me to make the right decisions. I would like to extend my special thanks to my sister *Eftychia,* my grandparents *Lazaros* and *Paraskevi*, my sister in law *Stella*, my brother in law *Costas*, my cousin *Lazos* and my best friends *Bill*, *Tasos*, *Leonidas*, *Stratos* and *Costas* for their unconditional love. I would never have finished this work without their love and support.

Last but not least, a special thanks to my beloved wife *Myrto* for being by my side and supporting me at all levels all these years. Words cannot express how grateful I am towards *Myrto* with whom we spent sleepless nights discussing when there was no one to answer my queries. I would like to thank my wonderful kids *Thomais*, *Odysseas* and *Iasonas* for all the love, comfort, and strength they have given me during those years. Especially my son *Odysseas* is an inspiration for me and I take courage from his strength.

Summary

The exponential growth of computational resources over the past decades, combined with the advent of models and advanced computational tools, have assisted significantly in guiding the design of improved polymer materials of high technological importance in a broad range of industrially relevant applications. Atomistic simulations have assisted a great deal in understanding elusive microscopic phenomena manifesting themselves at polymer interfaces and of their mechanisms and in establishing structure-property relations; they have a drawback, however, namely their high computational cost. Mesoscopic simulations, on the other hand, employ a higher level of description and are quite useful in studying a variety of important systems and phenomena at mesoscopic time- and length-scales, albeit the task of parameterizing the effective interactions between coarse-grained segments is rather complicated.

There is an alternative strategy, however, which is the primary focus of the present thesis: field-theoretic methods. To carry out a field-theoretic computer calculation, we require a statistical field theory model of a fluid. A statistical field theory is a description of a system in which the fundamental degrees of freedom are not particle coordinates, but rather one or more continuous fields that vary with position. More specifically, we focus on one of the most successful theoretical frameworks for inhomogeneous polymeric systems, the so-called self-consistent field theory (SCFT). Our primary goal is to formulate, validate and develop SCFT approaches, and then apply them in the description of interfacial systems involving high molar mass polymer melts under equilibrium conditions.

The SCFT models of this research will comprise three main stages:

1. *Validation*. The aim of this procedure is to allow for a comparison of the field theoretic model with previous atomistic simulations and experimental works in a rigorous and predictable manner. This is a key step to ensure that the theoretical models can successfully describe realistic systems.

2.   *Structural properties.* This will be the phase where the SCFT will be used to compute structural properties of *bulk* and *inhomogeneous* melts under equilibrium conditions.

3.   *Thermodynamic calculations.* This is the highest goal of the theoretical strategy presented in this thesis. Through these calculations we will be able to determine measurable thermodynamic properties and behavior of high molar mass polymer/gas and polymer/solid interfaces.

A self-consistent field (SCF) theoretic approach, using a general excess Helmholtz energy density functional that includes a square gradient term, is derived for polymer melt surfaces and implemented for linear polyethylene films over a variety of temperatures and chain lengths. The formulation of the SCF plus square gradient approximation (SGA) developed is generic and can be applied with any equation of state (EoS) suitable for the estimation of the excess Helmholtz energy. As a case study, the approach is combined with the Sanchez-Lacombe (SL) EoS to predict reduced density profiles, chain conformational properties, and interfacial free energies, yielding very favorable agreement with atomistic simulation results and noticeable improvement relative to simpler SCF and SGA approaches. The new SCF_SL+SGA approach is used to quantify the dominance of chain end segments compared to middle segments at free polyethylene surfaces. Schemes are developed to distinguish surface-adsorbed from free chains and to decompose the surface density profiles into contributions from trains, loops, and tails; the results for molten polyethylene are compared with the observables of atomistic simulations. Reduced chain shape profiles indicate flattening of the chains in the surface region as compared to the bulk chains. The range of this transitional region is approximately 1.6 times the radius of gyration (R_g). The inclusion of chain conformational entropy effects, as described by the modified Edwards diffusion equation of the SCF, in addition to the square gradient term in density, provides more accurate predictions of the surface tension, in good match with experimental measurements on a variety of polymer melts and with atomistic simulation findings.

A model for the prediction of key structural and thermodynamic properties of Polymer matrix nanocomposites (PNC) is described. Our approach is applied to single spherical silica (SiO_2) nanoparticles or planar surfaces grafted with polystyrene chains and embedded at low concentration in a matrix phase of the same chemical constitution. Our model is based on self-consistent field theory, formulated in terms of the Edwards diffusion equation. The properties of the PNC are explored across a broad parameter space, spanning the mushroom regime (low

grafting densities, small NPs and chain lengths), the dense brush regime, and the crowding regime (large grafting densities, NP diameters, and chain lengths). We extract several key quantities regarding the distributions and the configurations of the polymer chains, such as the radial density profiles and their decomposition onto contributions of adsorbed and free chains, the chains/area profiles, and the tendency of end segments to segregate at the interfaces. Based on our predictions concerning the brush thickness, we revisit the scaling behaviors proposed in the literature and we compare our findings with experiment, relevant simulations, and analytic models, such as Alexander's model for incompressible brushes.

Finally, a method is formulated, based on combining self-consistent field theory with the finite element method (SCFFEM), for studying structural and thermodynamic features of three-dimensional polymeric systems. Initially, this approach is tested on a planar polyethylene/vacuum and a polyethylene/graphite system, hand in hand with atomistically detailed molecular simulations as well as with one dimensional SCF approaches. This new approach is employed to predict reduced density profiles and interfacial free energies, yielding very favorable agreement with previous SCF studies, thus validating the SCFFEM methodology. An *h-*, *r-*, *p-* refinement process is developed to optimize the finite element mesh. Furthermore, two new criteria and an innovative successive substitution scheme are introduced for accurate convergence. The methodology is employed on a more complicated system consisting of polystyrene brushes grafted on silica walls immersed in polystyrene melt. In most implementations, the grafted chains are dealt with by smearing them across shells parallel to the surface of the modeled nanoparticle. The SCFFEM approach allows to distinguish the positions where the grafted chains are tethered, since it does not employ any smearing. The reduced density profiles are compared against the end-segment distributions along specific lines in the system. The structural properties and grand potential contributions are obtained for a broad range of grafting densities, molar masses and swelling ratios (i.e., ratio of the matrix to the grafted chains), and are compared to experimental data, theoretical models, and earlier simulation studies.

Περίληψη

Η εκθετική αύξηση των υπολογιστικών πόρων τις τελευταίες δεκαετίες, σε συνδυασμό με την ανάπτυξη μοντέλων και προηγμένων υπολογιστικών εργαλείων, έχουν αποβεί πολύ χρήσιμες στο σχεδιασμό πολυμερών υλικών με βελτιωμένες ιδιότητες, τα οποία παρουσιάζουν μια πληθώρα εφαρμογών κορυφαίας τεχνολογικής σημασίας για την βιομηχανία. Οι ατομικές προσομοιώσεις έχουν βοηθήσει σε μεγάλο βαθμό στην κατανόηση των ποικίλων μικροσκοπικών φαινομένων που απαντώνται στις διεπιφάνειες πολυμερών, καθώς και στην εδραίωση σχέσεων μεταξύ μικροσκοπικής δομής και ιδιοτήτων. Έχουν όμως ένα μειονέκτημα, και αυτό είναι το υψηλό υπολογιστικό κόστος. Οι μεσοσκοπικές προσομοιώσεις, από την άλλη μεριά, λαμβάνουν χώρα σε ένα υψηλότερο (αδροποιημένο) επίπεδο περιγραφής και ειναι αρκετά χρήσιμες στη μελέτη ποικίλων σημαντικών διεπιφανειακών συστημάτων και φαινομένων, στη μεσοκλίμακα. Ωστόσο η παραμετροποίηση των αλληλεπιδράσεων μεταξύ των τμημάτων αδροποιημένων μοντέλων αποτελεί μια ιδιαιτέρως περίπλοκη διαδικασία.

Μια εναλλακτική στρατηγική, η οποία αποτελεί και το επίκεντρο της παρούσας διατριβής, είναι οι υπολογιστικές μέθοδοι βασισμένες στη θεωρία πεδίου. Για να εδραιώσουμε ένα τέτοιο υπολογιστικό μοντέλο, ειναι άκρως απαραίτητη η χρήση μιας στατιστικής θεωρίας πεδίου ενός ρευστού. Η στατιστική θεωρία πεδίου αποτελεί μια περιγραφή ενός συστήματος στο οποίο οι θεμελιώδεις βαθμοί ελευθερίας δεν είναι οι συντεταγμένες σωματιδίων, αλλά μάλλον ένα ή περισσότερα συνεχή πεδία και η αλληλεπίδραση εξαρτάται απο τη θέση μέσα στα πεδία αυτά. Πιο συγκεκριμένα, εστιάζουμε σε ένα από τα πιο επιτυχημένα θεωρητικά πλαίσια για ανομοιογενή πολυμερή συστήματα, τη θεωρία του αυτο-συνεπούς πεδίου (SCFT). Αποδίδουμε ιδιαίτερη προσοχή κυρίως στη διαμόρφωση, την επικύρωση και την ανάπτυξη διαφορετικών προσεγγίσεων της θεωρίας του αυτοσυνεπούς πεδίου, και στη συνέχεια την εφαρμόζουμε στην περιγραφή διεπιφανειακών συστημάτων που περιλαμβάνουν τήγματα πολυμερών υψηλής μοριακής μάζας σε συνθήκες ισορροπίας.

Περίληψη

Τα μοντέλα θεωρίας του αυτοσυνεπούς πεδίου αυτής της μελέτης περιλαμβάνουν τρία κύρια στάδια:

1. Επικύρωση. Ο στόχος αυτής της διαδικασίας είναι να επιτρέψει τη σύγκριση του θεωρητικού μοντέλου με προηγούμενες ατομικές προσομοιώσεις και πειραματικά δεδομένα με σχολαστική και μεθοδική προσέγγιση. Αυτό είναι ένα βασικό βήμα για να διασφαλιστεί ότι τα θεωρητικά μοντέλα μπορούν να περιγράψουν με επιτυχία ρεαλιστικά συστήματα.

2. Εξέταση δομικών ιδιοτήτων. Η θεωρία του αυτοσυνεπούς πεδίου χρησιμοποιείται για την περιγραφή των δομικών ιδιοτήτων ομοιογενών και ανομοιογενών φάσεων πολυμερικών τηγμάτων υπό συνθήκες ισορροπίας.

3. Θερμοδυναμικοί υπολογισμοί. Αυτός είναι ο βασικότερος σκοπός της θεωρητικής στρατηγικής που παρουσιάζεται σε αυτή τη Διατριβή. Μέσω των υπολογισμών μετρήσιμων θερμοδυναμικών ιδιοτήτων είναι εφικτός ο προσδιορισμός και η πρόβλεψη της συμπεριφοράς συστημάτων που αποτελούνται από ελεύθερες επιφάνειες πολυμερών ή/και διεπιφάνειες μεταξύ πολυμερών και στερεών με τη χρήση ή όχι εμφυτευμένων πολυμερικών αλυσίδων .

Η θεωρία του αυτοσυνεπούς πεδίου, με μια γενικευμένη έκφραση ενεργειακής πυκνότητας Helmholtz, που περιλαμβάνει έναν όρο τετραγωνικής βαθμίδας (SGA), χρησιμοποιείται για επιφάνειες τήγματος πολυμερούς και εφαρμόζεται σε υμένια γραμμικού πολυαιθυλενίου για ενα πλήθος θερμοκρασιών και μοριακών βάρων. Η αναπτυξη της θεωρητικής μεθοδολογίας του SCF σε συνδιασμό με την θεωρία SGA είναι γενικευμένη και μπορεί να εφαρμοστεί με οποιαδήποτε καταστατική εξίσωση (EoS). Χρησιμοποιείται η Sanchez-Lacombe (SL) EoS (SCF_SL+SGA) για εφαρμογή της θεωρητικής μεθοδολογίας με σκοπό την πρόβλεψη των προφίλ ανηγμένης πυκνότητας (σε σχέση με την πυκνότητα στον κυρίως όγκο του υλικού) και δομικών ιδιοτήτων των αλυσίδων των ελεύθερων επιφανειών. Τα αποτελέσματα βρίσκονται σε συμφωνία με εκείνα των ατομικών προσομοιώσεων και επιδεικνύουν αξιοσημείωτη βελτίωση σε σχέση με τις απλούστερες επί μέρους θεωρητικές προσεγγίσεις SCF και SGA. Η SCF_SL+SGA χρησιμοποιήθηκε επίσης και για τον ποσοτικό προσδιορισμό των κατανομών των ακραίων τμημάτων των αλυσίδων σε αντιδιαστολή με τα μεσαία τμήματα σε ελεύθερες επιφάνειες πολυαιθυλενίου. Αναπτύχθηκαν διαδικασίες διακρισης των προσροφημένων στην επιφάνεια αλυσίδων και των ελεύθερων αλυσίδων. Τα προφίλ ανηγμένου σχήματος αλυσίδων δείχνουν μια πιο επίπεδη κατανομή των νεφών μονομερικών τμημάτων των αλυσίδων στην περιοχή της επιφάνειας σε σύγκριση με τις αλυσίδες στον κύριο όγκο του υλικού. Το εύρος αυτής της μεταβατικής περιοχής είναι περίπου 1,6 γυροσκοπικές

ακτίνες (R_g). Η επιφανειακή τάση που υπολογίζεται με τη θεωρητική μεθοδολογία SCF_SL + SGA για ενα πλήθος πολυμερών τηγμάτων βρίσκεται σε πλήρη αντιστοιχία με πειραματικές μετρήσεις και με ευρήματα ατομικών προσομοιώσεων.

Στην συνέχεια αναπτύσσεται ένα μοντέλο για την πρόβλεψη των βασικών δομικών και θερμοδυναμικών ιδιοτήτων των πολυμερικών νανοσύνθετων (PNC). Η προσέγγισή μας εφαρμόστηκε σε σφαιρικά νανοσωματιδία ή επίπεδες επιφάνειες πυριτίας (SiO_2) οι οποίες φέρουν εμφυτευμένες αλυσίδες πολυστυρενίου (PS) και είναι διεσπαρμένες σε μήτρα πολυστυρενίου.Το μοντέλο μας βασίζεται θεωρία του αυτοσυνεπούς πεδίου, που διατυπώνεται με βάση την εξίσωση διάχυσης Edwards. Οι ιδιότητες των PNC εξετάταζονται σε ένα φασμα παραμέτρων, που εκτείνεται απο χαμηλές πυκνότητες εμφύτευσης, μικρά NP και μήκη αλυσίδας, προς πιο πυκνές (σχηματισμός πολυμερικης ψήκτρας) έως και πολύ υψηλές πυκνότητες εμφύτευσης. Μελετώνται βασικά χαρακτηριστικά σχετικά με τις κατανομές και τις διαμορφώσεις των πολυμερών αλυσίδων, όπως τα προφίλ ακτινικής πυκνότητας, η διάκριση μεταξύ προσροφημένων και ελεύθερων αλυσίδων και η τάση των τελικών τμημάτων να συγκεντρώνονται στις διεπιφάνειες. Πραγματοποιείται εκτίμηση του πάχους της πολυμερικής ψήκτρας των εμφυτευμένων αλυσίδων η οποία περιβάλλει το νανοσωματίδιο και επανεξετάζονται οι προβλέψεις κλιμάκωσης που προτείνονται απο την βιβλιογραφία. Τα αποτελέσματά μας συγκρίνονται με ευρήματα από διαθέσιμες πειραματικές μετρήσεις, σχετικές προσομοιώσεις και αναλυτικά μοντέλα, όπως το μοντέλο Alexander για ασυμπίεστα ρευστά.

Ως τελευταίο μοντέλο προτυποποίησης διαμορφώνεται μια μέθοδος που βασίζεται στο συνδυασμό της SCFT με τη μέθοδο πεπερασμένων στοιχείων (FEM), για τη μελέτη δομικών και θερμοδυναμικών χαρακτηριστικών τριδιάστατων πολυμερών συστημάτων. Η προσέγγιση αυτή (SCFFEM) δοκιμάστηκε αρχικά σε διεπιφάνειες πολυαιθυλενίου με κενό και πολυαιθυλενίου με γραφίτη, όπου η μεθοδολογία παραμετροποίησης στηρίζεται σε μοριακές προσομοιώσεις και μελετήθηκε προηγουμένως με μονοδιάστατες μεθόδους SCF. Αυτή η νέα προσέγγιση χρησιμοποιείται για την πρόβλεψη προφίλ ανηγμένης πυκνότητας και τον υπολογισμό της ελεύθερης ενέργειας διεπιφανειών, με τα αποτελέσματα να βρίσκονται σε καλή συμφωνία με προηγούμενα αποτελέσματα SCF, επικυρώνοντας τη μεθοδολογία SCFFEM. Στόχος αυτής της εργασίας είναι και η διερεύνηση της συμπεριφορά του συστήματος των εξισώσεων όταν εφαρμόζεται η μέθοδο πεπερασμένων στοιχείων. Στην συνέχεια αναπτύχθηκε μια τεχνική *h*-, *r*-, *p*- βελτιστοποίησης, μέσω της οποίας είναι δυνατόν να βελιστοποιηθούν οι παράμετροι του πλέγματος πεπερασμένων στοιχείων. Επιπλέον, εισάχθηκαν δύο νέα κριτήρια για την ακρίβεια

Περίληψη

της σύγκλισης και ένα καινοτόμο σχήμα διαδοχικών επαναλήψεων. Τα ευρήματά μας χρησιμοποιήθηκαν σε ένα πιο περίπλοκο σύστημα αποτελούμενο άπο επιφάνειες πυριτίας οι οποίες φέρουν εμφυτευμένες αλυσίδες πολυστυρενίου (PS) και είναι διεσπαρμένες σε μήτρα πολυστυρενίου. Μεχρι τώρα, η ακριβής αναπαράσταση των σημείων πρόσδεσης των εμφυτευμένων αλυσίδων ήταν ανέφικτη. Με την μέθοδο SCFFEM ειναι δυνατό να διακριθούν στον τριδιάστατο χώρο οι θέσεις όπου οι εμφυτευμένες αλυσίδες είναι συνδεδεμένες με την επιφάνεια της πυριτίας, από τις θέσεις που δεν φέρουν εμφυτευμένες αλυσίδες. Συγκρίνουμε τα προφίλ ανηγμένης πυκνότητας και τις κατανομές ακραίων τμημάτων των αλυσίδων κατά μήκος συγκεκριμένων γραμμών μέσα στο σύστημα. Τέλος προσδιορίζονατι οι δομικές ιδιότητες και οι συνεισφορές στο δυναμικό του μεγάλου κανονικού στατιστικού συνόλου για ένα ευρύ φάσμα πυκνοτήτων εμφύτευσης, μοριακών μαζών και λόγων διόγκωσης και συγκρίνονται με πειραματικά δεδομένα, θεωρητικά μοντέλα και προηγούμενες μελέτες προσομοίωσης.

.

List of Figures

List of Tables

Nomenclature

Symbols and Notation

Latin symbols

A	Helmholtz free energy
A^{IG}	Helmholtz free energy of an ideal gas
A^{SL}	Helmholtz free energy calculated by Sanchez Lacombe equation of State
A_0	Helmholtz free energy of a chain with constrained end-to-end $\mathbf{R}_e$ vector of ideal chain
A_{PS}, A_{SiO_2}	Hamaker constant for PS and SiO_2
A_{chain}	Helmholtz energy contribution, of a Gaussian chain grafted at $\mathbf{r}_{i_g}$
A^g_{conf}	Free energy associated with the conformations of the grafted chains
$A^g_{stretch}$	Stretching free energy obtained by the density profiles of the grafted chain ends
a_{ch}	Average surface area occupied in plane by a chain passing through that plane
a_{mix}	Relaxation parameter
b	Effective bond length
$\mathbf{b}_i$	Bond vector
b_K	Kuhn length
C_N	Flory's characteristic ratio

Nomenclature

C_∞	Flory's characteristic ratio at infinite chain length
c	$c=$m matrix and $c=$g for grafted chains
d	Thickness of the adsorption regions
d_{th}	Hyperbolic tangent
E	Enthalpy
F	Helmholtz free energy is approximated by a functional
f	Excess Helmholtz energy density relative to an ideal gas of chains
f_{EoS}^{HFD}	Excess Helmholtz energy density relative to an ideal gas of chains based Helfand approximation
f_{EoS}^{SL}	Excess Helmholtz energy density relative to an ideal gas of chains based on Sanchez-Lacombe EoS
f_{star}	Number of branches
G	Gibbs free energy
$G(\mathbf{r},\mathbf{r}_0;s)$	Green function for the Gaussian thread in the presence of the field
$G_0(\mathbf{r},\mathbf{r}_0;s)$	Green function for the Gaussian thread without the presence of the field
G^{IG}	Gibbs free energy of an ideal gas
$\mathcal{H}$	Hamiltonian of the system
$\mathcal{H}_C$	Hamiltonian of the canonical ensemble
$\mathcal{H}_G$	Hamiltonian of the grand canonical ensemble
h	Film thickness in planar geometry/ segment-surface distance in spherical geometry
h	spring potential
$\hbar$	Planck constant

$h_{99\%}$	Distance between the center of the nanoparticle and a surface, and encloses 99% of grafted chain segments
h_{avg}	average element size
h_{edge}	Edge of the brush length
h_{HS}	Segment-surface distance
h_{g}	Grafting point-surface distance
$\left\langle h_{\text{g}}{}^{2} \right\rangle^{1/2}$	Mean brush thickness
$\mathbf{J}^{e}$	Jacobian matrix of the transformation from natural to real coordinates of an element
$\mathbf{J}^{e,-1}$	Inverse Jacobian matrix
k	Diffusion coefficient
K_{IJ}^{e}	Stiffness matrix of FEM
k_{B}	Boltzmann's constant, $k_{\text{B}}=1.3806488 \times 10^{-23}$ m^{2}kgs^{-2}K^{-1}
$l_{\text{C-C}}$	Length of the carbon-carbon bond
L_x, L_y, L_z	Domain dimensions
l_{g}	Quantity with dimensions $\left(\text{kg/mol}\right)^{-n}$ nm^{2m+1} of scaling law for polymer brushes
M	Molar mass
M_{IJ}^{e}	Mass matrix of FEM
M_{g}	molar mass of the grafted chains
m	Mass
N	Number of segments
$\tilde{N}$	Normalizing prefactor which includes the contribution from integration over momentum space
N_{el}	Number of elements

Nomenclature

N_i	Shape functions
N_K	Number of Kuhn steps
N_m	Length of the matrix chains
N_{nod}	Number of nodal points of the whole domain
$N_{nod,e}$	Number of nodal points of an element
N_g	Length of and grafted chains
N_{gp}	Number of integration points in Gauss Quadrature
N_{star}	Number of segments constituting a branch of star polymer
n	Total number of atoms/particles/chains of the system
$\bar{n}$	The mean number of chains in the system
n_g	Number of grafted chains of the system
n_m	Number of matrix chains of the system
n_{ch}	Number of chains that intersect a plane
n_s	Chain shape (Intersections per chain going through a plane)
$n_{s,bulk}$	Chain shape in the bulk
P	Pressure
P^*	characteristic Sanchez-Lacombe pressure
$P(\mathbf{R}_e; N)$	Probability density function for end-to-end vector $\mathbf{R}_e$
$\mathscr{P}\left[\mathbf{r}_\alpha(\bullet)\right]$	A statistical weight for path $\mathbf{r}_\alpha(s)$ of chain α in the absence of any field in the Gaussian string model
$\tilde{P}$	reduced pressure
P_s	Phase coexistence pressure
P^{IG}	Pressure of an ideal gas

$\mathbf{p}^n$	Generalized momenta $\left(\mathbf{p}^1, ...,\mathbf{p}^n\right)$
p_{int}	Probability of a chain, that started anywhere in the system, to intersect a plane
p_{SL}^*	Sanchez-Lacombe pressure parameter
Q	Single chain partition function
Q_{nVT}	Canonical partition function
q	Restricted partition function for the Gaussian thread model /chain propagator
$\dot{q}$	Propagator derivative
q_{ads}	Propagator of segments belonging to adsorbed chains
q_c	Propagator of segments $c = $ m matrix, and $c = $ g grafted chains
q_{free}	Propagator of segments belonging to free chains
q_{shape,z_0}	Propagator for chains that do not intersect a plane z_0
$\mathbf{R}_{\text{e}}$	The end to end vector
$\mathscr{R}$	Three-dimensional region
R_{g}	Radius of gyration
R_{NP}	Radius of nanopatricle
R_{star}	Radius of a star polymer
$\mathbf{r}$	Contour position $\mathbf{r}$
$\mathbf{r}^e$	Global coordinates of element
$\mathbf{r}^n$	Generalized coordinates $\left(\mathbf{r}^1, ...,\mathbf{r}^n\right)$
$\mathbf{r}^{N+1}$	$N+1$ particle positions
$\mathbf{r}_\alpha$	Contour position $\mathbf{r}$ of a chain α
$\mathbf{r}_{\text{cm}}$	Center of mass position

Nomenclature

r_{ads}	Distance from NP center to the region where the segments of matrix chains are considered to be "adsorbed"
r_g	Grafting points
$\mathbf{r}_{g i_g}$	Grafting point of the $i_g{}^{th}$ grafted chain
r_{SL}	Number of Sanchez-Lacombe segments constituting a molecule
S	Entropy
S_{h_g}	Surface area over which grafting points are smeared
S, S_{solid}	Total interfacial area
s	Contour length along a chain
T	Temperature
T^*	Characteristic Sanchez-Lacombe temperature
$\tilde{T}$	Reduced temperature
$t_{iteration}$	Time of a single iteration
U	Potential energy of the system
U_0	Potential energy associated with a particular conformation of the polymer of ideal chain model
U_s	Interaction energy between the polymer chain segments and the solid surfaces
υ^*	Hard core volume of a Sanchez-Lacombe segment
$\tilde{u}$	Reduced volume
u	Pair potential function
V	Volume of the system
V^*	Close packed volume of the n r-mers
V_{el}	Volume of an element

W	Weight Function
W_{IJ}^e	Field matrix of FEM
w	Purely imaginary position-dependent field
$\mathbf{w}_j$	Independent weight functions
$\bar{w}$	Chemical potential field after imposing saddle point approximation
w'	Real position-dependent field
$\tilde{w}'$	Field evaluated after substituting the calculated reduced densities in iteration scheme
$w'^{\text{ new}}$	New field for next iteration
w'_{bulk}	Chemical potential field of the bulk
w'_{ifc}	Chemical potential field of the interface
w_m	Weight factor of the integration point
w_{th}	the measure of the thickness of the sigmoidal curve
$\mathcal{Z}$	Configurational partition function
$\mathcal{Z}_0$	Configurational partition function of ideal chain model
$\mathcal{Z}_{\text{free}}$	Configurational partition function of a free chain
$\mathcal{Z}_{\text{intra}}$	The configurational integral of a single, atomistically represented, molecule over all but three translational degrees of freedom
$\mathcal{Z}_{nVT}$	Configurational partition function of canonical ensemble
z	Activity of grand canonical ensemble

Greek Symbols

β	Inverse of the thermal energy $(k_{\text{B}}T)^{-1}$
γ	Surface tension

Nomenclature

γ	Geometric factor depending on bond-angles along the chain backbone
γ_{sp}	Interfacial tension of a solid/polymer interface
γ_s	Surface tension of a solid
γ_{calc}	Surface tension calculated by SCFFEM method with mesh with low accuracy
γ_{conv}	Surface tension calculated by SCFFD or by SCFFEM method with mesh with high accuracy
ΔA_g	Conformational entropy of n_g grafted chains subject to the field w'
ΔA_{field}^g	Contribution to the Free Energy of the field experienced by the grafted chains
$\Delta w_{ifc}'^{max}$	Maximum difference between the fields of two iterations
$\Delta w_{ifc}'^{tol}$	A tolerance value of $\Delta w_{ifc}'^{max}$
$\Delta\Omega_{coh}$	Cohesive interaction component (relative to the bulk melt chains) arising due to segment-segment interactions in the polymer
$\Delta\Omega_{field}$	Interaction energy between the density field and the chemical potential field
$\Delta\Omega_m$	Translational and conformational entropy (relative to the bulk melt entropy) of noninteracting matrix chains subject to a chemical potential, $N_m\mu_m$,
$\Delta\Omega_{solid}$	Contribution of the potential energy exerted from the solid
$\delta(...)$	Dirac delta-function.
ε^*	Attractive energy between Sanchez-Lacombe segments in adjacent sites
Θ	Heaviside step function
κ	Influence parameter
$\tilde{\kappa}$	Dimensionless influence parameter
κ_{SL}	Influence parameter from Sanchez-Lacombe EOS
κ_T	Isothermal compressibility

Λ_i	Thermal wavelength of atom i of a molecule
λ	Symmetry measure of hyperbolic tangent curve
λ_m	location of the integration point m in Gauss Quadrature
μ	Chemical potential
μ_0	Chemical potential of bulk phase
μ^{IG}	Chemical potential of an ideal gas
$\Xi_{\mu VT}, \Xi(\mu, V, T)$	Grand canonical partition function
ρ	Segment density
ρ^*	Characteristic Sanchez-Lacombe density
$\tilde{\rho}$	Reduced density
$\hat{\rho}$	Microscopic particle density
$\tilde{\rho}_{bulk}$	Reduced bulk density
ρ_{end}	Density of the end segments of a chain
ρ_g	Gas density
ρ_l	Liquid density
ρ_m	Molecular density
ρ_{mass}	Mass density
$\rho_{seg,bulk}$	Bulk segment density
ρ_{SL}^*	SL density parameter
σ_g	Grafting density
$\sigma_{PS}, \sigma_{SiO_2}$	Hamaker effective radii for PS and SiO_2
φ	Reduced segment density
φ_{ads}	Reduced volume fraction of segments belonging to adsorbed molecules

Nomenclature

φ_c	Reduced segment density of c = m matrix, and c = g grafted chains
φ_{end}	End segment reduced density
φ_{free}	Reduced volume fraction of segments belonging to free molecules
φ_i	Trial function
φ_{loop}	Reduced volume fraction of adsorbed loop segments
φ_{middle}	Middle segment reduced density
φ_{tails}	Reduced volume fraction of adsorbed tail segments
φ_s	Segment reduced density of chain segments lying at reduced contour length s
χ	Flory-Huggins parameter
Ψ	Probability density function
ψ	Probability density function probability distribution
Ω	Number of configurations available to a system of n molecules
Ω	Finite element domain
Ω_{bulk}	Grand potential of bulk phase
Ω_e	Domain occupied by a single element
Ω_h	Finite element domain approximation
$\Omega_{\mu VT}, \Omega(\mu, V, T)$	Grand potential
ω	Absorption coefficient of diffusion equation

Abbreviations

DFT Density functional theory

DPD Dissipative particle dynamics

EoS Equation of state

FOMC Fast Off-lattice Monte Carlo

FEM Finite element method

FF Free film

kMC Kinetic Monte Carlo

LAMMPS Large-scale Atomic/ Molecular Massively Parallel Simulator

MC Monte Carlo

MD Molecular Dynamics

MUMPS MUltifrontal Massively Parallel Solver

NC Nanocomposites

NP Nanoparticle

μVT Grand canonical ensemble

NVT Canonical ensemble

PDE Partial differential equation

PDMS Poly(dimethylsiloxane)

PE Polyethylene

PEO poly(ethylene oxide)

PGNP Polymer grafted nanoparticles

PIB Polyisobutylene

PMMA Poly(methyl methacrylate)

PMF Potential of mean force

PNC Polymeric nanocomposites

PnBMA Poly (n-butyl methacrylate)

PS Polystyrene

PVAc Poly(vinyl acetate)

SANS Small angle neutron scattering

SCFFEM Self-consistent field combined with finite element method

SCFFD Self-consistent field combined with finite differences method

SCFT Self-consistent field theory

SCF_Helfand Self-consistent field Helfand model

SCF_SL+SGA SCFT with SGA model, based on the Sanchez- Lacombe EoS

SGA-PS SGA model developed by Poser and Sanchez

SL Sanchez-Lacombe Equation of state

SGA Square gradient approximation

SGT Square Gradient Theory

TraPPE Transferable Potentials for Phase Equilibria Force Field

WRM Method of Weighted Residuals

1 Introduction

In this short introductory chapter, the framework of the thesis is established. We will try to introduce the reader to the world of nanoscale macromolecules by presenting and discussing the main definitions utilized later in this thesis. Moreover, we will explain the important role of polymers in our life, why interfaces are of major technological importance, how polymer matrix nanocomposites have been established as a state-of-the-art field in research and industry, and the value of Self Consistent Field Theory in describing the complex structure of these polymeric materials.

1.1 Polymers

In the literature, polymers refer to materials whose shared structural feature is the presence of long covalently bonded chains of atoms.[1] According to the International Union of Pure and Applied Chemistry (IUPAC) definition of a polymer:[2] "a *polymer* is a substance composed of molecules characterized by the multiple repetition of one or more species of atoms or groups of atoms (constitutional repeating units) linked to each other in amounts sufficient to provide a set of properties that do not vary markedly with the addition of one or a few of the constitutional repeating units". A *monomer* is the substance that the polymer is made of (usually coinciding with the structural unit), and the process that converts a monomer to a polymer is called *polymerization*. When a structural unit is connected to precisely two other structural units, the resulting chain structure is called a *linear* macromolecule, whilst when existing structural units are connected to three or more units in the same chain we talk of *branched* macromolecules. If there is only one type of chemical unit the corresponding polymer is referred to as a *homopolymer*;[3] if there are more than one types, it is referred to as a *copolymer*. Special units called *end groups* are found where the polymeric chains terminate.

Polymers are chain-like macromolecules, which are composed of sequences of various types of repeating units. Therefore, there can be infinitely many types of polymers depending on the combinations and sequences of these units along the chain. The term *configuration* refers to the "permanent" stereo-structure of a polymer. The configuration is defined by the polymerization method, and a polymeric chain preserves its configuration until it reacts chemically. Due to its flexibility, a polymer chain with a certain configuration can exhibit a very large number of possible 3-dimensional folding shapes. This degree of freedom is called the *conformation*.

Most commercial synthetic polymers are considered to be flexible, because the natural conformation of such a polymer, either in the molten state or dissolved in a solvent, is not a rigid rod but rather a *random coil*. The flexibility necessary for polymer coiling is derived in many polymers from relatively unhindered rotations around carbon–carbon single bonds along the polymer backbone.[4] The "random" character of a coiled polymer reflects the fact that an extremely large number of conformational states of the backbone bonds are available. A direct result of this character is that the equilibrium behavior of polymers resists situations, such as strong extension or compression, where the number of conformational states is reduced relative to that in the random coil.[5] Such a reduction in available states is described macroscopically as a decrease in "*conformational entropy*."

Even though many people probably do not realize it, everyone is familiar with polymers. They are one of the most popular category of materials encountered in everyday use, since they are the main components of plastics, rubber, resins, biomaterials, foods and adhesives. Polymers are remarkably involved in comfort and facilitation of human life and it is difficult to imagine modern human society without polymers. Over the last decades, an explosive scientific and technological revolution is underway and polymers play an essential role in it.. This is because polymers constitute an amazingly versatile class of materials, with properties of a given type (e.g., thermodynamic, rheological, mechanical) often having enormously different values, sometimes even for the same polymer in different physical states.[1,3] Although a large number of material scientists, chemists and chemical engineers, physicists, textile technologists, mechanical engineers, pharmacists and other scientific groups are involved in the development of projects related to polymers,[6] there is still immerse room for development and improvement.

Since most chemists and chemical engineers are now involved in certain aspects of polymer science or technology, some have called this the polymer age.[7] Actually, humans have used naturally occurring polymers for centuries without realizing that they were dealing with macromolecules. Synthetic polymers appeared in the middle of the nineteenth century when chemists started using polymerization reactions without realizing that they were creating very large molecules.[8] The realization that polymers are molecules made of covalently bonded elementary units, called monomers (macromolecular hypothesis) was proposed by Staudinger in 1920.[9] From 1930 to 1960 polymers entered a golden age, during which new types were discovered and quickly emerged in commercial applications replacing naturally-sourced materials. At the same time, polymer synthesis tools were developed and refined. These include seminal works such as that of Flory on the swelling of a single chain in a good solvent,[4] that of Kuhn on macromolecular sizes,[10] that of Huggins and Flory on thermodynamics of polymer solutions,[11,12] that of Flory and Stockmayer on gelation[13,14] and that of Kuhn, James, and Guth on rubber elasticity.[15] The single-molecule models of polymer dynamics were also developed during this period by Rouse[16] and Zimm.[17] In the subsequent 20 years, the main principles of modern polymer physics were developed. These include the Edwards model of the polymer chain and its confining tube,[18] the modern view of semidilute solutions established by des Cloizeaux and de Gennes,[19] and the reptation theory for chain diffusion developed by de Gennes,[20] which led to the Doi-Edwards theory for the flow properties of polymer melts.[21]

During the following years, the attention of many scientists focused on the development of exotic plastic materials with advanced properties based on novel monomer units. This tendency in polymer development has been overcome by the realization that polymers built from readily available, low-priced, environmentally friendly monomers[22–31] will continue to lead the science innovation.[32] The combination of modern polymer synthesis strategies with theoretical and empirical designing tools results in polymers with new or better-defined molecular architectures.[33–36] Current research activity is largely focused on the class of self-assembled[37–40] and nanostructured composites[41–45] created by simultaneous control over macrophase and microphase separation.[40,46–51] In this effort, the use of theoretical and computational tools is imperative. Investigation and optimization of appropriate numerical simulations will allow the exploration of the self-assembly behavior and physical properties of new materials by reducing the cost and the time of experimental processes.

1.2 Polymers at Surfaces and Interfaces

The generally accepted use of term *interface* refers to an intermediate three dimensional boundary region separating two phases of matter with different physicochemical properties, in thermodynamic equilibrium.[52] The phases separated by the interface can be of the same (e.g., solid/liquid, liquid/gas and gas/solid interfaces for a pure substance) or of different (e.g., immiscible fluids) chemical constitution. For many scientists, the word *surface* implies the boundary separating a solid or a liquid in contact with air or vapor phase, whereas the word *interface* conjures up the notion of a solid/solid, liquid/liquid, or liquid/solid contact. The use of words surfaces and interfaces is probably redundant according to the above definitions. Although the word interface would suffice, we use the words surface and interface because they correspond to different images in peoples' minds. [53]

It is worthwhile to look at a few examples, so as to get a feeling of the technological importance of understanding the behavior of polymers at interfaces. The quality of products obtained through polymer-processing operations, such as extrusion and film blowing, is profoundly affected by surface-related dynamic phenomena.[54] Colloidal suspensions encompass commercial products such as paints and inks.[55] Adhesives constitute a category of materials where molecular-level design involving polymers at interfaces is of crucial importance. The design of polymeric resins, encapsulants, and dielectrics used in the microelectronics industry requires understanding of the behavior of polymers at interfaces. The thermodynamics at interfaces is governed by delicate microscopic phenomena; understanding these phenomena and the microscopic mechanisms that are associated with them is of major technological importance in a broad range of industrially relevant applications.

Each of the theoretical methods that are used to study polymer interfaces can be categorized as being either an analytical or a simulation technique. Simulation methods for studying polymer interfaces are nearly always based on microscopic models, which can vary extensively in the level of detail of the simulated particles and the accuracy of the intra- and inter-molecular potentials that describe the interactions among them. The techniques most frequently used for polymer simulations are Monte Carlo,[25,45,56–59] Molecular Dynamics,[30,56,58,60,61] and Brownian dynamics.[62–64] The analytical techniques can be further classified into microscopic or phenomenological. A phenomenological theory is one whose starting point is a statistical mechanics description with the fundamental variables being

collective variables (i.e., many-molecule), such as concentration fields. These theories generally involve one or more phenomenological coefficients, such as interaction energy parameters, viscosities, and elastic constants, whose microscopic origins are not addressed by the theory. Landau[65,66] theories of phase transitions and Cahn-Hilliard theory[67] are familiar examples of such an approach. In contrast, a microscopic theory is defined as one whose starting point is a statistical mechanics description using the generalized monomer coordinates and conjugate momenta as the fundamental variables. Such microscopic approaches include lattice mean-field theories[68], self-consistent field theories,[3,32,69,70] and certain scaling and renormalization group theories.[71]

1.3   Polymer Nanocomposites

Nanocomposites (NC) are multiphase solid materials where one of the phases has one, two or three dimensions of less than 100 nanometers (nm) or structures having nano-scaled repeated distances between the different phases that make up the material. The composite consists of two main parts: the *matrix* and the reinforcing phase (*filler*). The main classification in NCs is based on the different types of matrix phases: ceramic-matrix NCs, metal-matrix NCs and polymer-matrix NCs. Depending on the reinforcing phase, nanoparticle (NP) additives are divided into classes such as glass, carbon, and aramid. The present thesis investigates polymer-matrix NCs consisting of polymer-grafted nanoparticle additives ("fillers") embedded in a polymer matrix. Polymer-grafted nanoparticles comprise two primary components: the nanoparticle *core* and the polymer *brush*. The core can be either organic or inorganic and in many cases has a unique functionality itself. While many different core geometries have been successfully synthesized, such as nanocubes, nanorods, or nanoplatelets, spherical cores are perhaps the simplest to understand from a theoretical standpoint. In addition to the core geometry, there are numerous varieties of materials that constitute the core of Polymer grafted nanoparticles PGNP ranging from the simple (silica), to functional (magnetite), optically active (gold), or even more complex materials such as viruses and protein capsids.[72] The matrix chain-brush interfacial interactions may be "tuned" by controlling the *grafting density* (polymer chains per area tethered to NP surface), the degree of polymerization of the grafted chains (usually measured in number of monomer units) and of the polymer host, the nanoparticle size (core size and polymer brush height), and its shape.

Polymeric nanocomposites (PNCs) have been an area of intense industrial and academic research for the past thirty years. No matter the measure - articles, patents, or research and development funding - efforts in PNCs have been exponentially growing worldwide over the last twenty years. PNCs represent a radical alternative to conventional filled polymers or polymer blends - a staple of the modern plastics industry. In contrast to conventional composites, where the reinforcement is on the order of microns, PNCs are exemplified by discrete constituents on the order of a few nanometers.[73] In light of the diversity of PNCs, their potential is nearly immeasurable. Among PNCs, PGNPs is a topic of broad research interest. It has been demonstrated that dispersed spherical nanoparticles can yield a range of multifunctional behavior, including a viscosity decrease, reduction of thermal degradation, increased mechanical damping, enriched electrical and/or magnetic performance, and control of thermo-mechanical properties [51,74–83]

The practice of adding nanoscale particles to reinforce polymeric materials can be traced back to the early years of the composite industry in the second half of the 19th century. In 1856, Charles Goodyear attempted to formulate nanoparticle-toughened automobile tires by blending carbon black, zinc oxide, and magnesium sulfate particles with vulcanized rubber.[84] In 1909, another example was the clay-reinforced resin known as Bakelite, which was introduced as one of the first mass-produced polymer-nanoparticle composites and fundamentally transformed the nature of practical household materials.[72] Then, a long period of time passed till PNCs development was stimulated by research at Toyota where polyamide-6 nanocomposites with improved toughness, stiffness and heat distortion temperature balance became available in 1993.[8586] During the next decades, an explosion of experimental research occurred in the areas of nanocomposites based on inorganic materials, polymer based nanoparticle filled composites and naturally occurring systems of nanocomposites.[87,88]As part of this renewed interest in NPs, theoretical researchers also started seeking designing rules that would help them engineer materials with tailor-mode properties. For ceramic NPs, one can argue that the interface width is still small relative to the filler size or the filler-to-filler distance; thus, extension or modification of standard composite theory or modeling approaches may be sufficient. For polymer NPs, the modification of the matrix may extend over several radii of gyration from the particle surface. In turn, this situation results in novel macroscopic properties, which are dictated qualitatively and quantitatively, by the behavior of the confined polymer that forms the modified matrix. The development of rigorous models that describe these new materials, and particularly an in-depth

understanding of their properties, are still in their infancy. The greatest stumbling block to the large-scale production and commercialization of NPs is the dearth of cost-effective methods for controlling the dispersion of the nanoparticles in their polymeric hosts. The nanoscale particles typically aggregate, and this usually negates any benefits associated with their nanoscale dimension. The second challenge is associated with understanding and predicting the properties of these upgraded materials, which are intimately connected to their internal structure and morphology.

1.4   Self-Consistent Field Theory of Inhomogeneous Polymeric Systems

Understanding the formation and structure of these rich morphologies demands predictive theoretical frameworks that can be used to describe phase behavior and structural properties of polymeric systems. Ideally, the theory should take the molecular properties of the polymers as input and be able to predict the thermodynamically stable phases, the phase transition boundaries among them, as well as the physical properties of the phases, with low computational cost. Towards this goal, a variety of theoretical methods have been developed to study the phases and phase behavior of inhomogeneous polymeric systems.

One of the most successful theoretical frameworks for inhomogeneous polymeric systems, including polymer blends, polymer solutions and block copolymers, is the self-consistent field theory (SCFT). The polymeric SCFT has its origin in the work by Edwards in the 1960.[89] This theoretical framework was explicitly adapted to treat block copolymers by Helfand in 1975[90] and later important contributions to the theory were made by Hong and Noolandi among others.[91] The most fruitful application of SCFT to polymeric systems is the study of phases and phase transitions of block copolymers. In particular, powerful methods have been developed over the last decades to obtain highly accurate solutions of the SCFT equations using numerical techniques. The earliest attempts to obtain numerical solutions of SCFT for block copolymers were made by Helfand and coworkers.[90] Later, Shull[92] and Whitmore and coworkers[93] have computed phase diagrams of block copolymer melts and solutions using approximate numerical techniques. SCFT has been employed to investigate numerous polymeric systems with advanced properties in recent years. The first three-dimensional numerical solutions of block copolymer phases were obtained by Matsen and Schick[94] who utilized the crystalline symmetry of the ordered phases and provided exact numerical solutions to the SCFT equations. This technique has been applied to a variety of block copolymer systems. Further

development of the SCFT included the theory for Gaussian fluctuations in ordered phases,[95] numerical techniques for solving the mean field theory in real space[96] and fully fluctuating field-theoretical simulations.[97] There is a large body of literature on the SCFT of polymeric systems, including a number of valuable review articles,[34,98,99] book chapters and books.[3,32,69,70] Based on these numerous studies, it can be stated that SCFT forms a powerful basis for the study of inhomogeneous polymeric systems.

The self-consistent field theory can be outlined in terms of three fundamental steps. Firstly, the shape of the polymeric fluid can be designated by an ideal chain model describing the statistical mechanics associated with the conformational states of a single polymer chain. Secondly, a particle-based statistical-mechanical system is mathematically transformed into a field-based description. Within this field-based description, the many-body interactions are replaced by the interaction of each particle with certain fluctuating fields and the Hamiltonian of the system has a functional dependence on these fields. Lastly, further appoximations can be implemented based on the previous steps. In particular, a saddle-point approximation of the functional integral leads to the mean-field approximation of the system. The resulting mean-field equations, or SCFT equations, can then be solved analytically or numerically, providing information about the structure and property of the inhomogeneous polymeric phases. This theoretical framework is flexible in that it applies to any statistical-mechanical system.

1.5   Motivation

1.5.1   Molten Polymer Free Surfaces at Equilibrium

The thermodynamics of simple fluids and polymer melts in contact with a gas phase have been explored in great detail in previous works via theoretical approaches and atomistic simulations.[92,94,100–112] Thin liquid films exposed to gas phases on both sides, the so-called freely standing liquid films (FF), have attracted considerable research interest and attention.[92,94,100–102,107,109–113] It has been shown that film thickness has a considerable effect on thermodynamics: thick polymer films exhibit bulk properties in their central region,[107] whilst thin films display altered thermodynamics affecting their stability (emergence of disjoining pressure).[102,110,112] Moreover, the properties of thin films and the phase behavior of block copolymers have been studied extensively by means of self-consistent field theory (SCFT).[92,94,100,101,111] The importance of including nonlocal terms in polymer density and the

Helmholtz free-energy functional to deal with the inhomogeneous environment of surfaces and interfaces has generally been recognized by numerous authors.[5,67,114–130] Besides surface tension, the knowledge of the macroscopic properties of polymer interfaces is quite important, since they dictate the stable configurations of the system (contact angles, film wettability, phase separation, etc.). Even though SCFT has been used extensively to predict and explain the structure and phase diagrams of block copolymers and polymer blend systems, few authors have applied it to investigate the properties of homopolymeric interfaces.[24,131–133] To be more specific, several of the following issues have not yet been addressed in literature:

i)   *Investigation of the structure and thermodynamics of linear polyethylene films over a variety of temperatures and chain lengths, using the SCFT in conjunction with the Square Gradient approximation.*

ii) *Bottom-up comparative studies regarding the structural features (reduced density profiles, chain conformational properties) and thermodynamics (e.g., interfacial free energies) of thin films among SCFT combined with Square Gradient Approximation approaches with particle-based methods such as molecular dynamics.*

iii) *Hardly any studies report schemes to distinguish surface-adsorbed from free chains and to decompose the surface density profiles into contributions from trains, loops, and tails. Side-by-side comparisons with atomistic particle-based simulations are rarely addressed in the literature.*

iv) *There are also limited studies that provide accurate predictions of the surface tension, in good match with experimental measurements and atomistic simulation findings over a broad variety of polymer melts.*

1.5.2 Nanoparticles in Polymer Matrix

Polymer chains anchored on the surface of solid particles are widely used to stabilize inorganic nanoparticles (NPs) inside a host polymer matrix.[134,135 136] In most cases, the embedded NPs tend to stick to each other due to attractive forces between them.[137] Under certain conditions, the entropic cost related to the configurational restriction of grafted chains when the particles get closer to each other is able to keep the particles separated. The key factors influencing NP separation are their size, the molecular weight of grafted and matrix chains, and the surface grafting density.

When the matrix chains wet the grafted polymer brush, they are able to interpenetrate with grafted chains and therefore diffuse inside the space occupied by the polymer brush, leading to the eventual dispersion of NPs across the polymer matrix. It has been shown that in

most cases, when matrix chains are longer than the grafted chains, it is harder for them to penetrate into the interfacial region due to the higher entropy loss they experience.[136] This phenomenon is known as "autophobic dewetting"; in practice one aims to suppress such phenomena in order to enhance the dispersion of NPs across the polymer matrix.[42] When grafting density is lower than a threshold value, the particle cores are no longer screened by the grafted chains surrounding them, so they attract each other, leading to aggregation. This is known as "allophobic dewetting". Sunday et al.[136] derived experimentally a phase diagram demonstrating the regions where autophobic, allophobic dewetting, and complete wetting occurs.

Major experimental work has been conducted to understand the behavior of polymer grafted NPs and their influence on the properties of the composite material.[51,74–83] Atomistic molecular dynamics simulations have been performed by Ndoro et al.[138], while Meng et al.[139] and Kalb et al.[140] have performed coarse-grained molecular dynamics simulations representing the polymer chains by the Kremer-Grest bead-spring model. Dissipative particle dynamics (DPD)[141] and density functional theory (DFT)[142] simulations addressing systems of polymer brushes are also reported. Vogiatzis et al.[143] devised a hybrid particle-field approach called *FOMC* (Fast Off-lattice Monte Carlo) which is a coarse-grained class of Monte-Carlo simulations, where the nonbonded interactions are described by a mean-field inspired Hamiltonian. A useful approach for investigating the structure and thermodynamics of polymer grafted NPs and brushes is SCFT.[43,144–153] However, the literature lacks results from SCFT simulating realistic NP-polymer systems such as silica in contact with polysrtyrene (PS), with industrial relevance over a broad parameter space:

v) *Even though radial segment density profile distributions of matrix and grafted chains have been studied excessively, there are hardly studies focused on comparison of SCFT results with other experimental and simulation works.*

vi) *Reports extracting the density profiles of the grafted and matrix chains, which provide a direct picture of their conformations across the parameter space and the density profiles of the matrix chains decomposed into contributions from "adsorbed" and "free" chains, are scarce.*

vii) *A considerable number of the aforementioned studies do not take into account the contributions to the grand potential or contributions of the chain stretching energy .*

viii) *There is a limited number of SCFT works in the literature reporting the profiles of chains/area, the chain end segregation at the interface and the brush thickness over an*

extensive parameter space involving the molecular weight of the chains, grafting density and the size of the nanoparticles.

1.5.3 Self Consistent Field Finite Element Method

Spectral and quasi-spectral methods are predominant tools for solving three dimensional SCFT problems, but they are inflexible in handling geometrically complex domains, since they can be applied on problems exhibiting some kind of symmetry. Their main limitation in the frequency-domain approaches encourages consideration of alternate real space approaches, such as the finite element method (FEM).

FEM is a widely used analysis and design technique and enjoys plenty of advantages and privileges. First among these advantages is the ease of handing complex geometries. Compared to purely spectral methods, the FEM does not require masking techniques in order to address complex geometries. Another benefit when using the FEM is that is not limited to periodic systems and naturally allows the use of heterogeneous and mixed boundary conditions. Additionally, real space methods allow local mesh adaptation to selectively increase the resolution in a targeted region without requiring increased computational effort over the entire geometry of the investigated system. The FEM, in particular, can incorporate rigorous a posteriori error estimates (due to its inherent variational character) for mesh adaptivity, which enable substantial computational profits. Furthermore, there is a push to design solvers and frameworks (like MUMPS[154]) for real space approaches that are suitable for deployment on next generation computational clusters. Motivated by these factors, some researchers developed real space formulations of the SCFT problem using the finite element method.[155–157] Even so, there are several aspects in which state-of-the-art SCFT combined with FEM (SCFFEM) literature is lacking:

ix) *The majority of the aforementioned studies are applied to ideal model systems, offering good qualitative information regarding the structural properties of copolymers. There is a scarcity of studies where SCFT approaches are applied to realistic model systems, comparing the observables of mesoscopic simulations to detailed atomistic simulations and experiments.*

x) *There are no SCFFEM works in the literature reporting structural properties of polymeric melts at interfaces.*

xi) *There are no SCFT studies applied in grafted polymeric interfaces with explicit representation of long polymer chains grafted on solid surfaces.*

xii) *There are no SCFFEM studies assessing the interfacial free energy of polymer/solid interfaces with attractive segment/wall interactions.*

1.6   Aim of the Thesis

Based on the aforementioned realizations, the aim of the present PhD thesis is to formulate, validate and develop a SCFT approach, and then apply it in the description of homogeneous and inhomogeneous systems involving high molar mass polymer melts in equilibrium conditions.
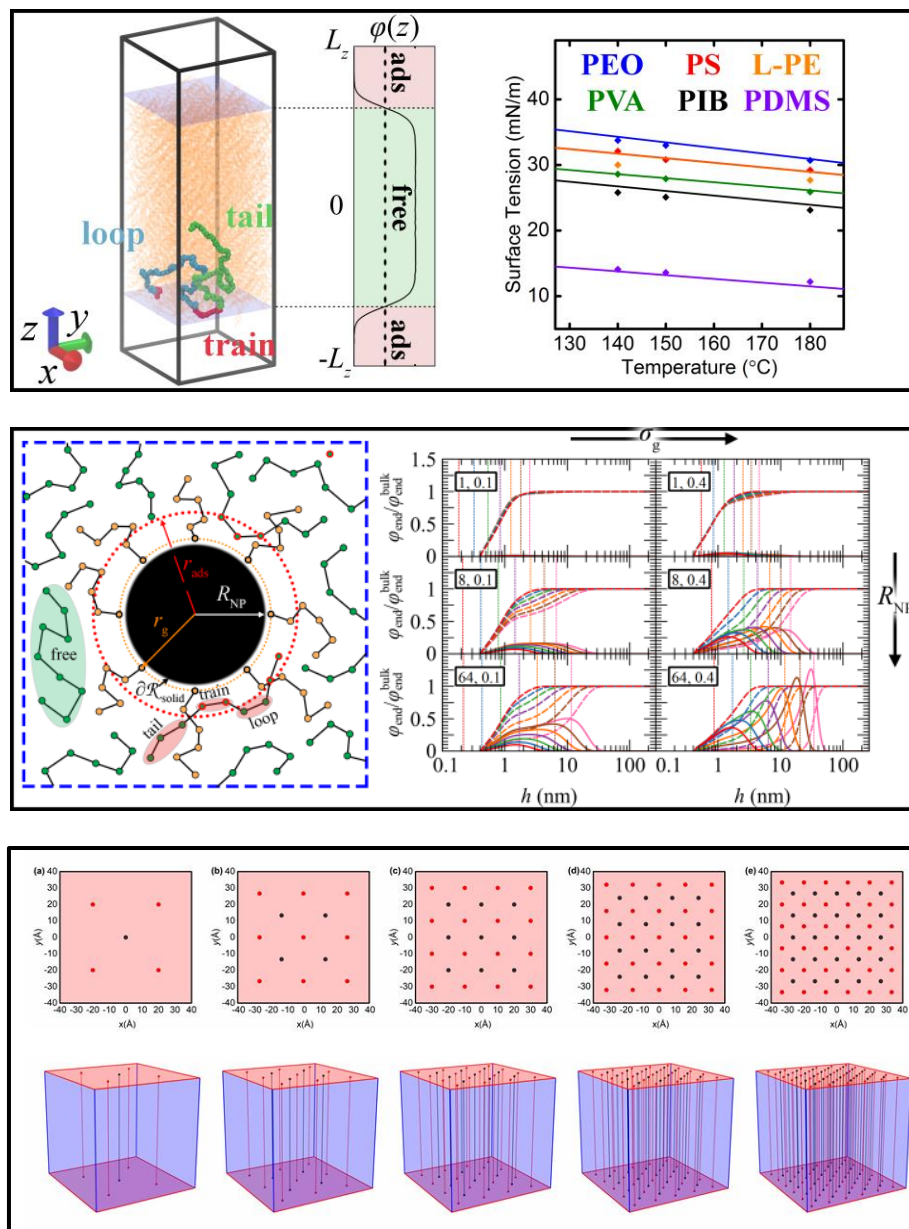
Figure 1.1. Graphical Abstracts.

The SCFT models of this research will comprise three main stages:

1. *Validation*. The aim of this procedure is to allow for a comparison of the theoretical model with previous atomistic simulations and experimental works in a rigorous and predictable manner. This is a key step to ensure that the theoretical models can successfully describe realistic systems.

2. *Structural properties.* This will be the phase where the SCFT will be used to compute structural properties of *bulk* and *inhomogeneous* melts under equilibrium conditions.

3. *Thermodynamic calculations*. This is the highest goal of the theoretical strategy presented in this thesis. Through these calculations we will be able to determine the thermodynamic properties and behavior of high molar mass polymer/gas and polymer/solid interfaces.

1.7   Outline of the Thesis

In the following Chapter, a brief self-contained summary of a generic SCFT formulation compared to other molecular simulation concepts is provided. We limit ourselves to the absolute minimum of definitions and methods to be presented, trying not to sacrifice consistency and rigor. Chapter 3 of the thesis deals with the development of a formulation of SCFT coupled with square gradient theory for predicting properties of free surfaces of molten polymers indirect comparison with atomistic simulations and experimental data. The scope of this chapter is to compare the local density profiles and several structural properties of theoretic models, with those obtained from atomistic simulations, as well as the prediction of the surface tension of various polymers in a broad range of temperatures. Chapter 4 of the thesis implements the strategy developed in Chapter 3 to address systems of grafted polymeric NPs. This allows for the description of structural properties of polymer grafted NPs with various size, grafting density and chain length related to previous simulations and the contribution of entropic and cohesive energy terms. In Chapter 5, the Edwards diffusion equation is solved with the finite element method. Each Chapter is self-contained, incorporating its own introduction (summarizing previous work and experimental findings) and the main conclusions reached. However, a separate list of the innovations at three levels (methodology, physical insight and computational tools) is provided in Chapter 6. Finally, in Chapter 7 an outlook of the closely related future work is presented.

2 Theoretical Background

In this chapter, we present definitions and background knowledge that will outline the framework of the new concepts and methods to be developed in the subsequent chapters. As a starting point of our discussion, we outline the perspectives that are adopted in building a physical model and how that model can be translated into mathematics. Then, the statistical properties of coarse-grained particle-based models of single polymers are described, and these models of single-chain statistical mechanics are extended to include the presence of an external field. The description of this external field completes the particle-to-field transformation. We describe how field theoretic models can be constructed for a variety of many chain inhomogeneous polymer systems. The important case of self-consistent field theory (SCFT) is illustrated, which is obtained by imposing a mean-field approximation. As a final point, square gradient theory and the Sanchez Lacombe Equation of State (EoS) are briefly described.

2.1 Modeling Perspective and Scales

An important challenge faced by researchers of complex materials is that the structure and dynamics of these materials are characterized by extremely broad spectra of length and time scales. One of the first decisions to be made is the approach to be adopted in modeling. Approaches for modeling materials consist of many levels, each level addressing phenomena over a specific window of length and time scales. The approach of primary interest here starts with *ab-initio* and *atomistic* methods, continues with *mesoscopic* methods, and extends to *field theoretic* methods.

2.1.1 Atomistic Methods

2.1.1/a First Principles (ab-initio) Simulation Methods

At a reasonably fundamental level, one could describe a polymeric fluid using ab-initio quantum mechanics and retain the nuclear coordinates and electronic degrees of freedom of the atoms composing the polymer and solvent molecules[158]. In quantum mechanics, a complete description of the microscopic state or "microstate" of the system is provided by the wave function Ψ, which is a function of the position coordinates of all nuclei and electrons. [159–162] Electronic structure calculations in the Born-Oppenheimer approximation attempt to solve the electronic Schrödinger quantum mechanical equation given the positions of the nuclei and the number of electrons in order to yield useful information such as electron densities, energies and other properties of the system. The solution of these equations comes with high computational cost.

First principles approaches require essentially no empirical or experimental knowledge to characterize the interactions among the fundamental particles composing a fluid. Their application to real materials, though, is still limited. Even if we employ the fastest supercomputer with the largest memory, we can treat at most a few thousand atoms, so pure ab initio simulation is inappropriate for modeling polymeric fluids, where each polymer molecule typically contains more than this number of atoms.

2.1.1/b Atomistic Simulation Methods

The next higher level of description, which we shall refer to as the atomistic level, is based on eliminating the electronic degrees of freedom and treating the nuclear coordinates classically or quantum mechanically. [163–167]The elimination of the electronic degrees of freedom leads to classical potentials expressing the potential energy as a function of the nuclear coordinates[168] These can in principle be obtained by carrying out ab initio quantum chemical calculations on small sets of atoms, or more typically by applying empirical potentials that contain parameters characterizing the range and strength of the inter-nuclear interactions. In this classical perspective, each nucleus becomes an "atom" and carries an effective mass that is approximately the nuclear mass. The Hamiltonian of the system, $\mathcal{H}$, is equal to the sum of the kinetic and potential energies of the atoms,

$$\mathcal{H}\left(\mathbf{r}^n, \mathbf{p}^n\right) = \sum_{i=1}^{n} \frac{\mathbf{p}_i^2}{2m_i} + U(\mathbf{r}^n) \tag{2.1}$$

where n is the total number of atoms in the system, m_i is the effective mass of the ith atom, and $\mathbf{r}^n = \left(\mathbf{r}^1, ..., \mathbf{r}^n \right)$ and $\mathbf{p}^n = \left(\mathbf{p}^1, ..., \mathbf{p}^n \right)$ denote the Cartesian coordinates and momenta, respectively. The $3n$-dimensional space from which the coordinates of the system $\mathbf{r}^n = \left(\mathbf{r}^1, ..., \mathbf{r}^n \right)$ take on values is referred to as *configuration space*. The $3n$-dimensional space from which the momenta $\mathbf{p}^n = \left(\mathbf{p}^1, ..., \mathbf{p}^n \right)$ take on values is referred to as *momentum space*. In many applications it is convenient to use generalized, rather than Cartesian coordinates. The two sets of coordinates are related through a well-defined transformation.

When referring to polymer simulations, each molecule contains thousands of atoms. A strategy for handling the apparent difficulties associated with fully atomistic simulations of inhomogeneous polymers is to "coarse-grain" the fluid model. In this case, groups of atoms are lumped into larger entities referred to as "particles." These particles interact by new effective interaction potentials that must be re-parameterized. The coarse-graining procedure requires a re-parameterization of the system which can be regarded as being more of an art than a science. At the lowest level, one can group adjacent atoms to form a particle, for example lumping each CH_2 unit into a particle along a polyethylene chain, and then using empirical knowledge or quantum chemical calculations to fit parameters in potential functions describing bonded and nonbonded interactions among particles. Such a "*united atom*" approach has been used quite successfully to simulate oligomeric fluids and single-phase polymeric fluids of low molecular weight, but does not go very far in alleviating the serious spatial and temporal limitations of fully atomistic simulations of inhomogeneous polymers.

2.1.1/c The Monte Carlo (MC) Method

Monte Carlo methods achieved a considerable improvement in the field of materials simulations in terms of simulation time. Monte Carlo is a numerical method of solving stochastic models without determination of the analytical representations of the system.[45,56,58,169,170] The Monte Carlo (MC) method is more of a statistical technique, which involves discrete random walks for sampling the phase space according to a certain probability distribution (e.g., Boltzmann) to solve problems involving materials or other systems. The Monte Carlo technique can be applied in the ab initio representation, too.

In their simplest version, MC simulations of simple fluids are carried out by attempting trial moves for the molecules from a uniform distribution and subsequently accepting or

rejecting these moves, such that the long sequence (Markov chain) of configurations generated asymptotically samples the probability distribution of interest (typically dictated by an equilibrium ensemble). MC algorithms can also involve sampling from other distributions, which do not have to be analytical. Metropolis MC normally simulates an equilibrium ensemble of statistical mechanics and is used for calculation of structural and thermodynamic properties of the system as ensemble averages. The Kinetic Monte Carlo (KMC) method, on the other hand, tracks the temporal evolution of a system as a sequence of thermally activated infrequent transitions. Atomic migration, occurring as a sequence of atomic jumps, is an example of such an evolutionary process. Rate constants for the individual transitions can be computed from the atomistic potential energy hypersurface and the atomic masses through the theory of infrequent (rare) events. MC techniques have the advantage of being able to explore probable (i.e., relevant) regions of configuration space rapidly, by permitting substantial configurational rearrangements. They can equilibrate some complex systems, such as polymer melts, orders of magnitude more rapidly than molecular dynamics techniques, by devising and implementing moves that do not mimic the actual physical dynamics, but ensure rigorous and vigorous sampling of the equilibrium probability distribution among microstates.

2.1.2 Mesoscopic Methods

Higher levels of coarse-graining than the "united atom" approach are more sophisticated. Sgouros et al.[22] lumped 52 monomers within a polymer backbone into a single bead. In linear polymers, two main approaches have been developed for the mapping of atomistic polymer segments into beads. A bead can be assigned either at the center of mass of a segment or at the coordinates of the central atom(s) of a segment. The task of parameterizing the effective interactions between those beads is rather complicated. Harmonic or anharmonic spring models can be employed to describe the connectivity, space-filling characteristics and architecture of beads belonging to the same chain and/or adjacent chains (slip springs). Potentials describing interactions between non-bonded beads on the same or different polymer chains are determined by empirical forms. A common choice is the Lennard-Jones potential[171], or excess free energy potentials (relative to an ideal gas of chains), calculated from an equation of state (EoS).[172] A disadvantage of this approach is that experimental input is needed, so simulation results are predictive only to the extent that a model system has already been parameterized. Another drawback of a coarse-grained description is that phenomena which depend on atomic-scale

packing effects in the fluid cannot be captured with this approach. Nevertheless, computer simulations of mesoscopic particle-based models of polymeric fluids have been quite useful in studying a variety of important systems and phenomena such as polymer brushes, block copolymers, and cohesive failure of polymer adhesives and glasses.[173–175]

2.1.3 Field-Theoretic Methods

In the mesoscopic approach of modeling polymer fluids described above, the fundamental degrees of freedom are particle positions and momenta. It is the phase space spanned by these coordinates that is explored in a particle-based computer simulation. There is an alternative strategy, however, which is the primary focus of the present thesis: field-theoretic methods. To carry out a field-theoretic computer simulation, we require a statistical field theory model of a fluid. A statistical field theory is a description of a system in which the fundamental degrees of freedom are not particle coordinates, but rather one or more continuous fields $w(\mathbf{r})$ that vary with position $\mathbf{r}$.[176] We can associate the relevant w fields of a polymeric fluid with spatially varying chemical potentials. From the perspective of a particle-based model, the fundamental problem of equilibrium statistical mechanics[168] is to evaluate a configurational partition function (configurational integral) of the form

$$Z = \int d\mathbf{r}^n \exp\left[-\beta U(\mathbf{r}^n)\right] \tag{2.2}$$

where $\beta \equiv 1/(k_B T)$ is the inverse of the thermal energy and $U(\mathbf{r}^n)$ is the potential energy of an n-particle system. The corresponding equilibrium problem for a field theory model is to evaluate an analogous expression, involving a functional integral over the field(s):

$$Z = \int \mathcal{D}w \exp\left[-\beta \bar{U}[w]\right] \tag{2.3}$$

The advantages of field-theoretic methods for studying inhomogeneous polymers can be easily understood. First of all, there is the flexibility of working with a field theory that originated from either an atomistic or a mesoscopic perspective. In addition, the spatial resolution of the field theory can be adjusted by giving the relevant fields a finer or coarser representation. There is also flexibility in the way the fields are represented and discretized (e.g. finite differences, finite elements, or spectral representations), which leverages the large body of knowledge surrounding the numerical solution of partial differential equations. With such an approach, it is possible to model, for example, polymer alloys exhibiting both macrophase and

microphase separation.[177] Such morphologies would be more difficult to be obtained with an atomistic, or even a coarse-grained, particle-based simulation. Another important advantage of using field-theoretic models is that they serve as a basis for most analytical theories of inhomogeneous polymers.[178,179] A large body of experimental data has been interpreted using this theoretical framework, and a common language involving parameters in mesoscopic field theories, such as Flory "chi" parameters and statistical segment lengths, has emerged. By providing access to the behavior of these same field theory models across a broader range of parameter space, field-theoretic models can couple very effectively with existing theory and experiment.

2.2   Single Chain Models

In order to investigate the theoretical description of a polymeric fluid, we have to introduce the notion of the ideal chain models. An ideal chain model describes the statistical mechanics associated with the conformational states of a single unperturbed polymer chain. We will try to analyze the differences of most prominent ideal chains models. The present discussion of the topic will be brief, with references to the literature that is relevant to this subject.[4,32,180]

2.2.1   From Flexible Polymers to Ideal Chains Models

The chains of common synthetic polymers exhibit elasticity, as a result of relatively unrestricted rotations about carbon–carbon single bonds along their backbones, and are considered to be *flexible*. Nevertheless, a large number of synthetic polymers and biopolymers are rigid and bend over large distances as a result of accumulated bond strains. These are termed *semi-flexible* or *rigid-rod* polymers, depending on their length and degree of flexibility. In the present work we address flexible macromolecules.

The effective interactions between segments along a flexible polymer chain are manifested with two types of contributions as shown in Figure 2.1: *local*, (short-ranged interferences) which are exerted between neighboring segments along the backbone and are strongly dependent on the bond geometry and energetics of the chain; and *nonlocal*, (long-ranged interferences) which are exerted between topologically distant segments, when the conformation of the chain brings them spatially close. "Excluded volume" interactions, preventing two segments from occupying the same position in space, belong to the nonlocal category.
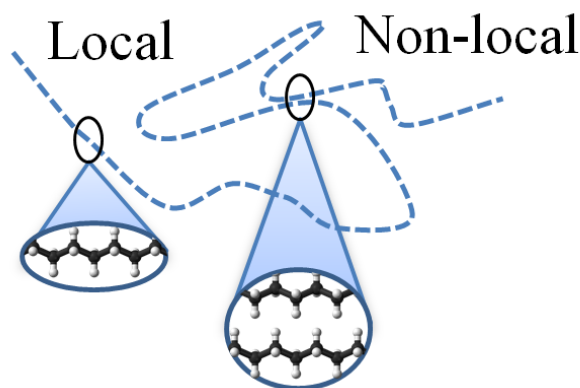
Figure 2.1. Local and non-local interactions along a polymer chain

In principle, long-ranged interferences are never completely absent. However, two situations are commonly encountered in which long-ranged interferences are essentially negligible.[4,32,180]The first one is observed in a dilute solution of a homopolymer of high molecular weight at the θ- temperature, while the second one concerns a homopolymer chain embedded in a melt of chemically identical homopolymers. The latter was described theoretically by P.J. Flory with the famous "random coil hypothesis" and has been confirmed by experimental and simulation evidence.

When the above solvent and/or temperature conditions occur, a single chain may behave as if it does not "feel" nonlocal interactions and is called *unperturbed*. The models that take into account only short-ranged interferences in the statistical mechanics of a polymer chain are referred in literature as *ideal chain models*. Ideal chain models are important in the theoretical description of polymeric chains, since they render feasible the theoretical calculation of the statistical probability distribution of the equilibrium chain conformations, one of the most fundamental problems in the statistical mechanics of polymers.

2.2.2   Freely Jointed Chain Model

A usually applied model with very similar behavior to a polymeric chain is the freely jointed chain model. In the freely jointed chain model, all interactions, except for the connectivity between structural units, are neglected. The chain conformations adopted by a linear flexible polymer chain can be described with the path of a random flight of constant step b. The terms random flight model and three-dimensional random walk are used interchangeably in the literature.

In the freely jointed model, the chain is represented as a sequence of "segments", which lie at positions $\mathbf{r}_0$, $\mathbf{r}_1$ ..., $\mathbf{r}_N$, and are connected by bond vectors $\mathbf{b}_1$, $\mathbf{b}_2$, ..., $\mathbf{b}_N$, where $\mathbf{b}_i = \mathbf{r}_i - \mathbf{r}_{i-1}$, as depicted in Figure 2.2. This sequence consists of $N+1$segments, and N bonds. All bonds are of the same length b and the direction of each bond is random. In a coarse-grained representation each "segment" stands for a larger section of the chain and each "bond" is a virtual bond between such sections.
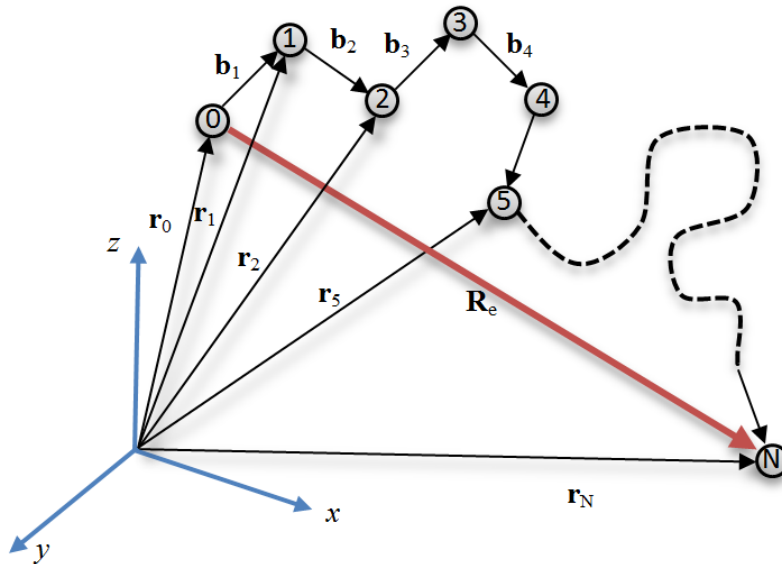
Figure 2.2. A freely jointed chain model with $N+1$ particles (indicated by the spheres) and N equally sized steps (indicated by the arrows connecting the spheres). The particle positions with respect to a Cartesian coordinate system are denoted by $\mathbf{r}_0$, $\mathbf{r}_1$ ..., $\mathbf{r}_N$, bond vectors by $\mathbf{b}_1$, $\mathbf{b}_2$, ..., $\mathbf{b}_N$, and the chain end-to-end vector by $\mathbf{R}_e$.

The configurational partition function of a single chain can be expressed by an equation similar to eq 2.2:

$$Z_0 = \int d\mathbf{r}^{N+1} \exp\left[-\beta U_0(\mathbf{r}^{N+1})\right] = V \int d\mathbf{b}^N \exp\left[-\beta U_0(\mathbf{b}^N)\right] \tag{2.4}$$

where $\mathbf{r}^{N+1}$ stands for the set of $N+1$ particle positions and U_0 is the potential energy associated with a particular conformation of the polymer. The notation $\int d\mathbf{r}^{N+1}$, $\int d\mathbf{b}^N$ is shorthand for a $3(N+1)$ and $3N$-dimensional integral over the $N+1$ particle positions and N bond vectors, respectively, within a three-dimensional domain of volume V. For an ideal chain model, U_0 contains only interaction potential terms reflecting short-ranged interactions. The subscript 0 is used to indicate that we are discussing the properties of a single, ideal chain.

A full description of the conformational statistics of the simple model of Figure 2.2 is provided by the probability density function $\Psi(\mathbf{b}_1, \mathbf{b}_2..., \mathbf{b}_N) \equiv \Psi(\mathbf{b}^N)$. This is defined so that $\Psi(\mathbf{b}_1, \mathbf{b}_2..., \mathbf{b}_N) d^3b_1 d^3b_2...d^3b_N \equiv \Psi(\mathbf{b}^N) d\mathbf{b}^N$ equals the probability of finding the chain in a conformation where the bond vector for bond 1 is between $\mathbf{b}_1$ and $d\mathbf{b}_1$, the bond 2 is between $\mathbf{b}_2$ and $d\mathbf{b}_2$, • • •, and the bond N is between $\mathbf{b}_N$ and $d\mathbf{b}_N$. In the ideal chain case, there are no constraints on the arrangements of the segments due to excluded volume effects, therefore the orientations of adjacent bond vectors are statistically independent. The probability density function for the partition function of chain conformations is of the form

$$\Psi(\mathbf{b}^N) = \prod_{n=1}^{N} \psi(\mathbf{b}_N) \tag{2.5}$$

Where

$$\psi(\mathbf{b}_n) = \frac{1}{4\pi b^2} \delta(|\mathbf{b}| - b) \tag{2.6}$$

with $\delta(\mathbf{r})$ being the Dirac delta-function.

To continue the mathematical treatment of conformation, it is necessary to introduce measures for the size of a polymer chain. One such measure is the distance between the two end segments of the chain. As shown in Figure 2.2 and in Figure 2.3, the end-to-end vector is defined as $\mathbf{R}_e = \mathbf{r}_N - \mathbf{r}_0$ and the length $R_e = |\mathbf{R}_e|$ as the end-to-end distance. The end-to-end vector can be conveniently expressed as $\mathbf{R}_e = \sum_{i=1}^{N} \mathbf{b}_i$. The isotropic distribution of the $\mathbf{b}_i$ implies that $\langle \mathbf{b}_i \rangle_0 = 0$ and, hence, a vanishing first moment for $\mathbf{R}_e$.
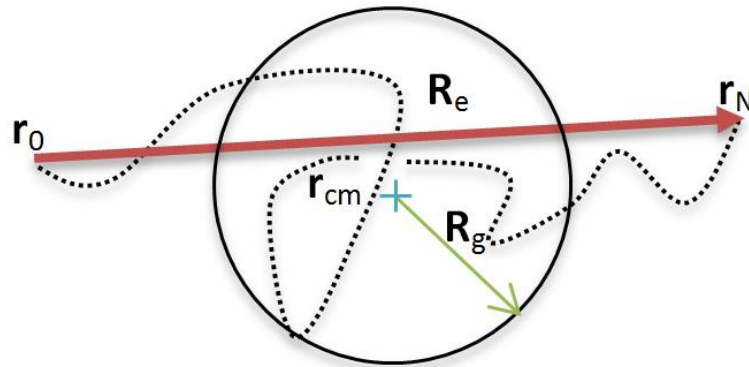
Figure 2.3. Definition of the end-to-end vector $\mathbf{R}_e$ and of the radius of gyration $\mathbf{R}_g$.

A measure of the polymer coil of high importance is the mean-square end-to-end distance, defined as either an ensemble or a time average of the squared norm of the end-to-end vector. The second moment of the end to end vector can be written as:

$$\left\langle \mathbf{R}_e^2 \right\rangle = \left\langle \left(\sum_{n=1}^N \mathbf{b}_n \right) \cdot \left(\sum_{m=1}^N \mathbf{b}_m \right) \right\rangle =$$
$$= \left\langle \sum_{n=1}^N \sum_{m=1}^N \mathbf{b}_n \mathbf{b}_m \right\rangle = \sum_{n=1}^N \mathbf{b}_n^2 + \sum_{n=1}^N \sum_{m=n+1}^N \left\langle \mathbf{b}_n \mathbf{b}_m \right\rangle \tag{2.7}$$

The absence of directional correlation between different bonds makes the second term of the above equation equal to zero, leading to the characteristic of random flight model result:

$$\left\langle \mathbf{R}_e^2 \right\rangle = Nb^2 \tag{2.8}$$

and the root-mean-squared end-to-end vector of the freely jointed chain model

$$\sqrt{\left\langle \mathbf{R}_e^2 \right\rangle} = N^{1/2} b \tag{2.9}$$

The important point in eq 2.9 is that the end-to-end distance is multiplied by a factor of λ when the chain length is multiplied by a factor of λ^ν. Such a property is called a scaling property. The exponent $\nu=1/2$ appearing in eq 2.9 is called the *scaling exponent* of an ideal chain and the scaling property is related to the fractal nature of the chain conformation.

The mean-squared end-to-end distance of a linear polymer chain is not an experimentally observable quantity. Of higher experimental relevance is the so-called *radius of gyration* of the chain around its center of mass. We define the center of mass by

$$\mathbf{r}_{cm} = \frac{\sum_{i=0}^N m_i \mathbf{r}_i}{\sum_{i=0}^N m_i} = \frac{1}{N+1} \sum_{i=0}^N \mathbf{r}_i \tag{2.10}$$

and the radius of gyration $\mathbf{R}_g$ is defined by

$$\mathbf{R}_g^2 = \frac{1}{N+1} \sum_{i=0}^N (\mathbf{r}_i - \mathbf{r}_{cm})^2 \tag{2.11}$$

According to the Lagrange Theorem, [181] for any collection of particles, the squared radius of gyration can be alternatively expressed in terms of the interparticle distances as

$$\mathbf{R}_{g}{}^{2} = \frac{1}{\left(N+1\right)^{2}} \sum_{i=0}^{N} \sum_{j=i+1}^{N} (\mathbf{r}_{i} - \mathbf{r}_{j})^{2} \tag{2.12}$$

Using this theorem, Debye proved[181] that in the context of the freely jointed model and in the limit of $N \gg 1$, the following equation connects the radius of gyration of the chain with its end-to-end distance:

$$\left\langle \mathbf{R}_{g}{}^{2} \right\rangle = \frac{1}{6} \left\langle \mathbf{R}_{e}{}^{2} \right\rangle \tag{2.13}$$

Eqs 2.8, 2.9 and 2.13 reveal some remarkable features of the freely jointed chain model. Of interest, though, are not only the moments of the above measures, but also the entire distribution of the end-to-end vector $\mathbf{R}_e$. In general, the probability density function $P(\mathbf{R}_e; N)$ of the end-to-end vector $\mathbf{R}_e$ is defined as

$$P(\mathbf{R}_{e}; N) = \int d\mathbf{b}^{N} \, \delta\left(\mathbf{R}_{e} - \sum_{n=1}^{N} b_{n} \right) \Psi\left(\mathbf{b}^{N} \right) \tag{2.14}$$

Although it is not easy to treat the Dirac delta-function appearing in eq 2.14, it can be rewritten in a convenient form using the Fourier transform of the delta function, defined by $\delta(\mathbf{r}) = \frac{1}{(2\pi)^{3}} \int d\mathbf{k} \, e^{i\mathbf{k}\cdot\mathbf{r}}$. Using this form we can rewrite eq 2.14 as:

$$P(\mathbf{R}_{e}; N) = \frac{1}{(2\pi)^{3}} \int d\mathbf{k} \int d\mathbf{b}^{N} \, \Psi\left(\mathbf{b}^{N} \right) \exp\left[i\mathbf{k} \left(\mathbf{R}_{e} - \sum_{n=1}^{N} b_{n} \right) \right] \tag{2.15}$$

$P(\mathbf{R}_e; N)$ is thus expressed as the inverse Fourier transform of a product of N identical integrals:

$$P(\mathbf{R}_{e}; N) = \frac{1}{(2\pi)^{3}} \int d\mathbf{k} \exp(-i\mathbf{k}\mathbf{R}_{e}) \left[\int d\mathbf{b}_{1} \exp(-i\mathbf{k}\mathbf{b}_{1}) \varphi\left(\mathbf{b}_{1} \right) \right]^{N} \tag{2.16}$$

The integral over $\mathbf{b}_1$ can be evaluated using spherical coordinates, with $\mathbf{k}$ as the reference axis:

$$\int d\mathbf{b}_{1} \exp\left(-i\mathbf{k}\cdot\mathbf{b}_{1}\right) \varphi\left(\mathbf{b}_{1} \right)$$

$$= \frac{1}{4\pi b^{2}} \int_{0}^{\infty} b_{1} db_{1} \int_{0}^{2\pi} d\varphi \int_{0}^{\pi} \sin\theta \, d\theta \exp\left(-ikb_{1}\cos\theta\right) \delta(b_{1} - b) \tag{2.17}$$

$$= \frac{1}{4\pi b^{2}} 2\pi b^{2} \int_{0}^{\pi} \sin\theta \, d\theta \cos(kb\cos\theta) = \frac{1}{2} \left[\frac{-\sin\left(kb\cos\theta\right)}{kb} \right]_{\theta=0}^{\theta=\pi} = \frac{\sin\left(kb\right)}{kb}$$

And therefore

$$P(\mathbf{R}_e;N) = \frac{1}{(2\pi)^3} \int d\mathbf{k} \exp(i\mathbf{k} \cdot \mathbf{R}_e) \left[\frac{\sin(kb)}{kb} \right]^N \tag{2.18}$$

The latter equation was first derived by Lord Rayleigh for random flight of N steps, who also evaluated analytically the integral for values of N up to $N = 6$. By far the most interesting case is for $N \gg 1$, where the quantity $\left[\frac{\sin(kb)}{kb} \right]^N$ becomes very small, unless kb is close to zero. Under these conditions:

$$\left[\frac{\sin(kb)}{kb} \right]^N \simeq \left(1 - \frac{k^2 b^2}{6} \right) \simeq \exp\left(-N \frac{k^2 b^2}{6} \right) \tag{2.19}$$

Then

$$P(\mathbf{R}_e;N) = \left(\frac{3}{2\pi N b^2} \right)^{3/2} \exp\left(-\frac{3\mathbf{R}_e^2}{2N b^2} \right) \tag{2.20}$$

Thus, the end-to-end vector of a freely jointed chain follows a Gaussian distribution in three dimensions, with zero mean and variance $\langle \mathbf{R}_e^2 \rangle$. This is a general result for long unperturbed chains. It provides a good approximation of the exact distribution of long enough ($N > 40$) freely jointed chains at not too high extensions.

The important notion of conformational entropy is manifested in eq 2.20. In making the transition from the full phase space distribution function of the freely jointed chain $\Psi(\mathbf{b}^N)$ to the reduced probability distribution function of the end-to-end vector, $P(\mathbf{R}_e;N)$, we have integrated over all sets of fixed-length bond vectors $\mathbf{b}$ consistent with the constraint of a fixed end-to-end vector $\mathbf{R}_e$. This integration amounts to an enumeration of the available conformational states. Because all states occur with uniform probability in the freely jointed model, the result is a purely entropic contribution to the free energy of a chain with constrained end-to-end vector $\mathbf{R}_e$:

$$A_0 = -k_B T \ln P(\mathbf{R}_e;N) \approx \frac{3k_B T}{2N b^2} |\mathbf{R}_e|^2 \tag{2.21}$$

The quadratic dependence on chain extension $|\mathbf{R}_e|$ in this expression can be viewed as an "entropic spring" potential. Fewer conformational states are available for chains with large

extensions, so the free energy increases with $|\mathbf{R}_e|$. Moreover, the "spring constant" $\dfrac{3k_B T}{Nb^2}$ softens in inverse proportion to the square of the polymer coil size.

2.2.3 Bead Spring Model

Another important category of ideal chain models is designated as bead-spring models. These models are easier to handle mathematically than the freely jointed models. The bead-spring model can be represented as a collection of beads connected by elastic springs. The bonds are now of variable length and each bond vector $\mathbf{b}_i$ is distributed independently with a statistical weight proportional to $\exp\left[-\beta h\left(|\mathbf{b}|\right)\right]$ with $\langle\mathbf{b}_n\rangle=\mathbf{0}$ and the probability density function is given by

$$\Psi\left(\{\mathbf{b}_1,\mathbf{b}_2,....,\mathbf{b}_N,\}\right)\equiv\Psi\left(\{\mathbf{b}\}\right)=\varphi\left(\mathbf{b}_1\right)\varphi\left(\mathbf{b}_2\right)....\varphi\left(\mathbf{b}_N\right)\tag{2.22}$$

Where $\varphi\left(\mathbf{b}_i\right)$ is the probability distribution that individual bond vectors follow and $h(x)$ is the spring potential between adjacent particles along the polymer backbone. If all of the *N* bonds of such a chain are equivalent, the potential energy can be expressed as

$$U_0(\mathbf{b}^N)=\sum_{i=1}^{N}h(|\mathbf{b}_i|)\tag{2.23}$$

The configurational partition function then becomes

$$Z_0=V\int d\mathbf{b}^N\exp\left[-\beta U_0(\mathbf{b}^N)\right]=V\left(\int d\mathbf{b}\exp\left[-\beta h(|\mathbf{b}|)\right]\right)^N\tag{2.24}$$

As we can see from the above equations, a central role is played by the bond potential of these elastic springs. In order to associate the freely jointed with the bead spring model, we have to specify a functional form for the spring potential $h(x)$. The harmonic bond potential given by

$$h(x)=\frac{3k_B T}{2b^2}x^2\tag{2.25}$$

is the most popular and convenient choice, making the bead spring to follow the same reduced probability distribution function of the end-to-end vector with the freely jointed model for long chains. This choice defines the so-called *discrete Gaussian chain model*. The remarkable point about the bond potential given in 2.25 is the fact that the spring constant depends on the

temperature. This is because the spring of the bead- spring model originates from the change in the conformation entropy. Using such a spring potential, it is easy to show that the average of the square of the bond length is given by b^2. The parameter b in this potential (often called the *effective bond length*) can be interpreted as the root-mean-squared length of a bond, since for any bond i

$$\langle \mathbf{b}_i \cdot \mathbf{b}_i \rangle = \frac{\int d\mathbf{b}_i \left(\mathbf{b}_i \cdot \mathbf{b}_i \right) \exp\left[-\beta h\left(|\mathbf{b}_i| \right) \right]}{\int d\mathbf{b}_i \exp\left[-\beta h\left(|\mathbf{b}_i| \right) \right]} = b^2 \tag{2.26}$$

The mean-squared end-to-end vector of the discrete Gaussian chain can be calculated. In particular,

$$\langle \mathbf{R}_e \cdot \mathbf{R}_e \rangle_0 = \sum_{i=1}^{N} \sum_{j=1}^{N} \langle \mathbf{b}_i \cdot \mathbf{b}_j \rangle_0 = N \langle \mathbf{b}_i \cdot \mathbf{b}_j \rangle_0 = Nb^2 \tag{2.27}$$

The terms with $i \neq j$ in this expression vanish because of the independent distribution of the bond vectors, which implies that $\langle \mathbf{b}_i \cdot \mathbf{b}_j \rangle_0 = \langle \mathbf{b}_i \rangle_0 \cdot \langle \mathbf{b}_j \rangle_0 = 0$ for $i \neq j$. Thus, the ideal chain scaling of eq 2.8 is recovered, $\langle \mathbf{R}_e^2 \rangle = Nb^2$. Apart from the interpretation of b as the fixed bond length in the freely jointed model versus the root-mean-squared bond length in the discrete Gaussian model, we see that the expressions for the mean-squared end-to-end vector in the two ideal chain models are identical. It is easy to show that the same equivalence holds for the radius of gyration $\mathbf{R}_g$, so that eq 2.13 also applies to the discrete Gaussian chain.

In order explore the relationship between the freely jointed and discrete Gaussian chain model in more detail, it is again useful to exploit the connection with stochastic processes. Since any pair of non-overlapping sub-chains of an ideal chain is statistically independent, the end-to-end vector of any sub-chain of an ideal chain obeys the Gaussian distribution. Assuming that any individual bond follows a Gaussian distribution:

$$\psi\left(\mathbf{b}_m \right) = \left(\frac{3}{2\pi b^2} \right)^{3/2} \exp\left(-\frac{3b_m^{\,2}}{2b^2} \right), \quad 1 < m < N \tag{2.28}$$

which is equivalent to

$$\Psi\left(\mathbf{b}^N \right) = \left(\frac{3}{2\pi b^2} \right)^{3N/2} \exp\left(-\sum_{m=1}^{N} \frac{3\left(\mathbf{r}_m - \mathbf{r}_{m-1} \right)^2}{2b^2} \right) \tag{2.29}$$
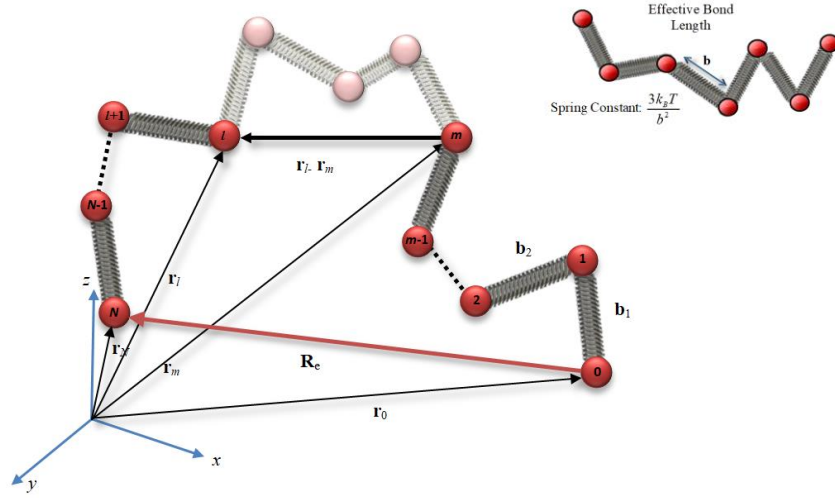
Figure 2.4. Schematic representation of the discrete Gaussian chain model. Each spring connecting successive beads has spring constant equal to $3k_{\mathrm{B}}T/b^2$

The distribution of the vector $\mathbf{r}_l - \mathbf{r}_m$, of a sub-chain connecting any two beads m and n along the Gaussian chain is given by

$$\Phi\left(\{\mathbf{r}_l - \mathbf{r}_m; l-m\}\right) = \left(\frac{3}{2\pi|l-m|b^2}\right)^{3/2} \exp\left(-\frac{3(\mathbf{r}_l - \mathbf{r}_m)^2}{2|l-m|b^2}\right) \tag{2.30}$$

With $\left\langle(\mathbf{r}_l - \mathbf{r}_m)^2\right\rangle_0 = |l-m|b^2$. As a special case, one recovers the Gaussian distribution for the end –to- end vector with $\left\langle \mathbf{R}_{\mathrm{e}}^2\right\rangle = Nb^2$. The probability density can be written as a function of the bead positions,

$$\Phi\left(\{\mathbf{r}_1, \mathbf{r}_2, \dots, \mathbf{r}_N; \mathbf{r}_0\}\right) = \left(\frac{3}{2\pi b^2}\right)^{3N/2} \exp\left(-\sum_{m=1}^{N} \frac{3(\mathbf{r}_m - \mathbf{r}_{m-1})^2}{2b^2}\right) \tag{2.31}$$

It leads to a free energy of the form

$$A\left(\{\mathbf{r}_1, \mathbf{r}_2, \dots, \mathbf{r}_N; \mathbf{r}_0\}\right) = \frac{3k_{\mathrm{B}}T}{2b^2} \sum_{m=1}^{N} (\mathbf{r}_m - \mathbf{r}_{m-1})^2 + const. \tag{2.32}$$

It is of interest to compare these results for the free energy of the discrete Gaussian chain with those obtained previously for the freely jointed chain model. At first glance, the

Hamiltonians for the freely jointed and the bead spring model appear to be very different, since on the one hand in the bead spring model, the bond which connects the segments is the harmonic one given by 2.25, while on the other hand in the freely jointed model, there is no apparent spring potential between the segments. Instead, there is a constraint on the arrangements of the segments, i.e., a pair of segments which are connected by a chemical bond should be located at a fixed distance. The chemical bonds are therefore introduced into the bead spring model as a spring potential (enthalpic contribution), in contrast to the freely jointed model where they are treated as an entropic term associated with the constraint on the arrangement of the segments (entropic contribution).[3,32] Because the final equilibrium is dictated by the free energy of the system, composed by the enthalpic contribution E and the entropic contribution S according to

$$A = E - TS \qquad (2.33)$$

we can understand that the two apparently different treatments of the chemical bonds will play essentially the same role in the canonical ensemble governed by the free energy A. Consequently, the free energy for these models given by 2.32 and 2.21 is thermodynamically equivalent in the case of very long chains.

2.2.4   Continuous Gaussian Chain Model

We can go one step further towards the model that we implemented in this thesis. Is is an elegant and particularly convenient ideal chain model for both analytical and numerical calculations, known as the continuous Gaussian chain model.[182] This model can be described as the continuous curve limit of the discrete Gaussian chain model, often called the "Gaussian thread" model. As shown in Fig. 2.5, in this model the polymer is viewed as a continuous, linearly elastic filament, whereas the segment index s becomes a continuous variable spanning the contour of the chain $(0 \leq s \leq N)$. The set of segment positions along the backbone of the chain, which describes the chain conformations, becomes a space curve $\mathbf{r}(s)$, where the contour position $\mathbf{r}$ is a vector function of the continuous variable s, and the end-to-end vector $\mathbf{R}_e$ can be expressed as $\mathbf{R}_e = \mathbf{r}(N) - \mathbf{r}(0)$. The probability density can be written as:

$$\Psi\left[\mathbf{r}(s)\right] = const.\exp\left[-\frac{3}{2b^2}\int_0^N ds\left(\frac{d\mathbf{r}}{ds}\right)^2\right] \qquad (2.34)$$

corresponding to a "potential" energy (more correctly, free energy or potential of mean force) of the Gaussian chain

$$U_0\big[\mathbf{r}(s)\big] = \frac{3k_{\mathrm{B}}T}{2b^2}\int_0^N \mathrm{d}s\left(\frac{\mathrm{d}\mathbf{r}}{\mathrm{d}s}\right)^2 \tag{2.35}$$

where the square bracket notation in $U_0\big[\mathbf{r}(s)\big]$ and $\Psi\big[\mathbf{r}(s)\big]$ is used to indicate that U_0 and Ψ are functionals of the space curve $\mathbf{r}(s)$ (Ψ is sometimes called a Wiener distribution[183]) defining the conformation of the polymer. A functional is a mapping between a continuous function and a number;[184] in this case the mapping is between $\mathbf{r}(s)$ and the value of U_0 and Ψ. The form of the potential energy is closely related to eq 2.32 for the discrete Gaussian chain. If we view $\mathrm{d}\mathbf{r}/\mathrm{d}s$ as the local "stretch" in a segment of length $\mathrm{d}s$ located at contour position s, then eq 2.35 sums a harmonic potential contribution from each such differential segment over the entire contour of the chain. It is important to note that s does not indicate arc length in the continuous Gaussian chain model, but it is simply a parameter indexing the segments along the chain. Thus, the stretch $\mathrm{d}\mathbf{r}/\mathrm{d}s$ is not constrained to be a unit vector, but is free to fluctuate in magnitude. Eq 2.35 for the potential energy is commonly referred to as the "Edwards Hamiltonian".

The configurational partition function of the continuous Gaussian chain can be written as

$$Z_0 = \int_{\mathbf{r}(0)=\mathbf{r}_0}^{\mathbf{r}(N)=\mathbf{r}} \mathcal{D}\big[\mathbf{r}(s)\big]\exp\big[-\beta U_0\big[\mathbf{r}(s)\big]\big] \tag{2.36}$$

where the notation $\int_{\mathbf{r}(0)=\mathbf{r}_0}^{\mathbf{r}(N)=\mathbf{r}} \mathcal{D}\big[\mathbf{r}(s)\big]$ indicates a functional integral over all possible space curves $\mathbf{r}(s)$ describing the conformation of the polymer. Such functional integrals, also termed path integrals, are familiar from the fields of quantum mechanics and probability theory, where $\mathbf{r}(s)$ corresponds to the position of a quantum particle or Brownian particle at time s.

Integrating over all possible spatial curves of length N with given starting and ending positions, we form a configurational partition function for the Gaussian thread, tethered at its two ends, given by:

$$Z_0 = \int_{\mathbf{r}(0)=\mathbf{r}_0}^{\mathbf{r}(N)=\mathbf{r}} \mathcal{D}\big[\mathbf{r}(s)\big]\exp\left[-\frac{3}{2b^2}\int_0^N \mathrm{d}s\left(\frac{\partial\mathbf{r}}{\partial s}\right)^2\right] \tag{2.37}$$

where $\beta = 1/(k_B T)$. The partition function is a path integral. From the above discussion of Gaussian chains, it is clear that the value of this partition function depends only on $|\mathbf{r}_0 - \mathbf{r}|$, N, and b.
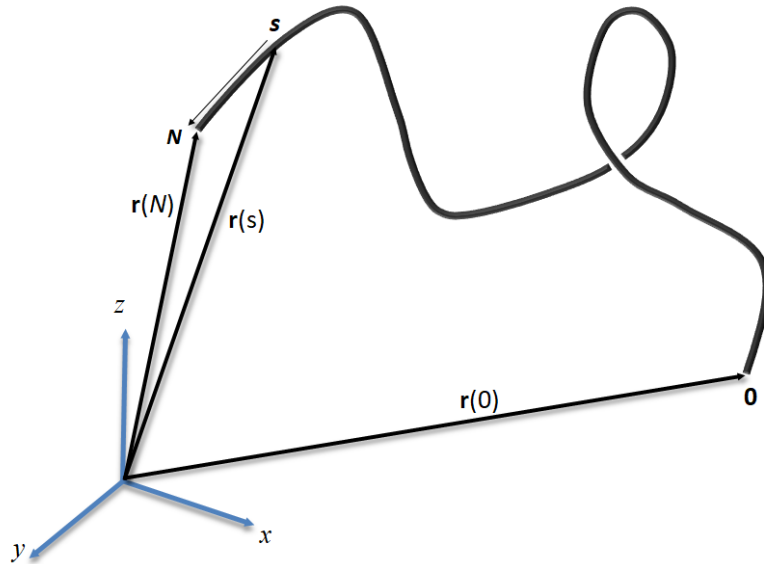
Figure 2.5. Schematic representation of the continuous Gaussian chain model (Gaussian Thread). The continuous Gaussian chain model describes the conformation of a polymer as a space curve $\mathbf{r}(s)$, where $s \in$ [0,N] is a variable spanning the contour of the chain. The chain end positions correspond to $\mathbf{r}(0)$ and $\mathbf{r}(N)$.

The inconvenience arising from the necessity to evaluate path integrals turns out to have no consequence in equilibrium statistical mechanics, because we are generally interested in ensemble averaged quantities, which can be expressed as ratios of two path integrals. For example, the mean-squared end-to-end vector of the continuous Gaussian chain can be expressed as:

$$R_e^2 = \langle \mathbf{R}_e \cdot \mathbf{R}_e \rangle = \frac{\int_{\mathbf{r}(0)=\mathbf{r}_0}^{\mathbf{r}(N)=\mathbf{r}} \mathcal{D}[\mathbf{r}(s)] |\mathbf{r}(N) - \mathbf{r}(0)|^2 \exp\left[-\beta U_0[\mathbf{r}(s)]\right]}{\int_{\mathbf{r}(0)=\mathbf{r}_0}^{\mathbf{r}(N)=\mathbf{r}} \mathcal{D}[\mathbf{r}(s)] \exp\left[-\beta U_0[\mathbf{r}(s)]\right]} \tag{2.38}$$

where the denominator is simply the configurational partition function. It is easy to prove that the continuous Gaussian chain shares the property of the discrete Gaussian chain in that its root-mean-squared end-to-end vector is given by $\langle R_e^2 \rangle^{1/2} = bN^{1/2}$ and the radius of gyration is given by the expected formula (eq 2.13).

A useful feature of path integrals in continuous chain models is that they can be viewed as Chapman-Kolmogorov integral equations, which in turn can be reduced to partial differential equations. These equations are referred to in probability theory as Fokker-Planck equations [185] and in quantum theory as Feynman-Kac formulas, [186] introduced into the polymer science by Doi and Edwards.[187] The advantage of working with partial differential equations will become more apparent in the next subsection, where we consider chains in external fields.

2.2.5 The Presence of External Field

In the current section we designate how the statistical mechanics of ideal chain models can be generalized to include one or more "external" potential fields that act on individual segments of a polymer chain. These potential fields are of primary importance and they are generated self-consistently by the force fields of the interacting polymer segments. Accurate evaluation of the statistical mechanics of a single polymer in a prescribed potential field proves to be the most computationally demanding component of a field-theoretic method.

The external field of primary interest is a spatially varying chemical potential field $w(\mathbf{r})$ that acts indiscriminately on contour length s of a continuous Gaussian chain. The conformation of a Gaussian thread will be now dictated by the following "energy" function:

$$U\big[\mathbf{r}(s)\big] = U_0\big[\mathbf{r}(s)\big] + \int_0^N \mathrm{d}s\, w\big(\mathbf{r}(s)\big) = \frac{3k_\mathrm{B}T}{2b^2}\int_0^N \mathrm{d}s\left(\frac{\mathrm{d}\mathbf{r}}{\mathrm{d}s}\right)^2 + \int_0^N \mathrm{d}s\, w\big(\mathbf{r}(s)\big) \tag{2.39}$$

Consequently, the configurational partition function of the continuous Gaussian chain becomes

$$\mathcal{Z} = \int_{\mathbf{r}(0)=\mathbf{r}_0}^{\mathbf{r}(N)=\mathbf{r}} \mathcal{D}\big[\mathbf{r}(s)\big]\exp\left[-\frac{3}{2b^2}\int_0^N \mathrm{d}s\left(\frac{\mathrm{d}\mathbf{r}}{\mathrm{d}s}\right)^2 - \frac{1}{k_\mathrm{B}T}\int_0^N \mathrm{d}s\, w\big(\mathbf{r}(s)\big)\right] \tag{2.40}$$

We define the Green function for the Gaussian thread as:

$$G(\mathbf{r},\mathbf{r}_0;s) = \frac{\int_{\mathbf{r}(0)=\mathbf{r}_0}^{\mathbf{r}(N)=\mathbf{r}} \mathcal{D}\big[\mathbf{r}(s)\big]\exp\left[-\beta U_0\big[\mathbf{r}(s)\big] - \beta\int_0^N \mathrm{d}s\, w\big(\mathbf{r}(s)\big)\right]}{\int \mathrm{d}\mathbf{r}\int_{\mathbf{r}(0)=\mathbf{r}_0}^{\mathbf{r}(N)=\mathbf{r}} \mathcal{D}\big[\mathbf{r}(s)\big]\exp\left[-\beta U_0\big[\mathbf{r}(s)\big]\right]} \tag{2.41}$$

Physically, $G(\mathbf{r},\mathbf{r}_0;s)$ is an un-normalized probability density that, in the presence of the field $w(\mathbf{r})$, a chain which started at position $\mathbf{r}_0$ will be at position $\mathbf{r}$, at contour length s. It has dimensions of inverse volume, i.e., spatial density. Note that the denominator in the definition of

$G(\mathbf{r},\mathbf{r}_0;s)$ is the partition function of an unrestricted, field-free Gaussian thread of length s; it is independent of $\mathbf{r}$ and $\mathbf{r}_0$ and depends only on s and b. Though the Green function has a physical meaning only for $s>0$, we extend the definition of $G(\mathbf{r},\mathbf{r}_0;s)$ to negative s, by requiring that $G(\mathbf{r},\mathbf{r}_0;s) = 0$ for $s < 0$. The probability density of the $\mathbf{r}-\mathbf{r}_0$ vector becomes

$$G_0(\mathbf{r},\mathbf{r}_0;s) = G_0(\mathbf{r}-\mathbf{r}_0;s) = \left(\frac{3}{2\pi sb^2}\right)^{3/2} \exp\left[-\frac{3(\mathbf{r}-\mathbf{r}_0)^2}{2sb^2}\right]\Theta(s) \tag{2.42}$$

with $\Theta(s)=1$ for $s>0$ and $\Theta(s)=0$ for $s<0$ (Heaviside step function). If we set $s=N$ and $\mathbf{r} = \mathbf{R}(N)$ in eq 2.42, the familiar Gaussian distribution function is recovered for the end-to-end vector of eq 2.29. On scales larger than a single bond, the discrete Gaussian chain and the continuous Gaussian chain evidently share the same chain end distribution function.

Recasting the latter expression as a Fourier transform of the Green function, the "diffusion" equation is derived:

$$\left[\frac{\partial}{\partial s} - \frac{b^2}{6}\nabla^2 + w(\mathbf{r})\right]G(\mathbf{r},\mathbf{r}_0;s) = \delta(\mathbf{r}-\mathbf{r}_0)\delta(s) \tag{2.43}$$

A detailed derivation of the above equation can be found in ref 187. The product of the Delta functions $\delta(\mathbf{r}-\mathbf{r}_0)\delta(s)$ on the right hand site takes into account the boundary conditions

$$G(\mathbf{r},\mathbf{r}_0;s) = 0, \text{ for } s<0 \text{ and } G(\mathbf{r},\mathbf{r}_0;s) = \delta(\mathbf{r}-\mathbf{r}_0) \tag{2.44}$$

$$q(\mathbf{r},s) = \int d\mathbf{r}_0 G(\mathbf{r},\mathbf{r}_0;s) = \frac{\int d\mathbf{r}_0 \int_{\mathbf{r}(0)=\mathbf{r}_0}^{\mathbf{r}(N)=\mathbf{r}} \mathcal{D}[\mathbf{r}(s)]\exp\left[-\beta U_0[\mathbf{r}(s)] - \beta\int_0^N ds w(\mathbf{r}(s))\right]}{\int d\mathbf{r} \int_{\mathbf{r}(0)=\mathbf{r}_0}^{\mathbf{r}(N)=\mathbf{r}} \mathcal{D}[\mathbf{r}(s)]\exp\left[-\beta U_0[\mathbf{r}(s)]\right]} \tag{2.45}$$

By definition $q(\mathbf{r},s)$ represents the statistical weight of a chain, which may have started anywhere in the system and finds itself at position $\mathbf{r}$ at contour length s (Figure 2.6). This object is commonly referred to as the chain propagator and is a functional of the external potential field. Again, note that the denominator in eq 2.45 is independent of $\mathbf{r}$ and $\mathbf{r}_0$. For $s>0$, integrating the diffusion eq 2.43 followed by the Green function $G(\mathbf{r},\mathbf{r}_0;s)$ with respect to $\mathbf{r}_0$ leads to

$$\frac{\partial}{\partial s}q(\mathbf{r},s)-\frac{b^2}{6}\nabla^2 q(\mathbf{r},s)+w(\mathbf{r})q(\mathbf{r},s)=0 \tag{2.46}$$

It is evident from eq. 2.45 that by construction, $q(\mathbf{r},s)$ is a dimensionless quantity and for $s=0$, the effect of the field disappears and the numerator and denominator become identical. The propagator $q(\mathbf{r},s)$ obeys the "initial" condition

$$q(\mathbf{r},0)=1 \tag{2.47}$$

(a)

(b)
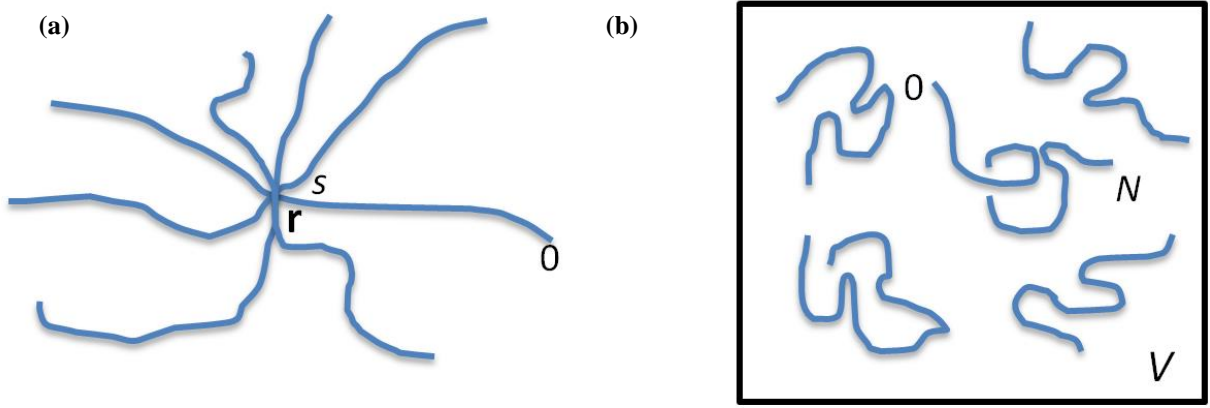
Figure 2.6. (a) Definition of the restricted partition function $q(\mathbf{r},s)$. **(b)** Definition of the partition function Q[w].

Of particular interest is the partition function $Q[w]$ for a chain subjected to an external potential $w(\mathbf{r})$ defined by the equation presented below:

$$Q[w]=\frac{\int \mathrm{d}\mathbf{r}_0 \int \mathrm{d}\mathbf{r} \int_{\mathbf{r}(0)=\mathbf{r}_0}^{\mathbf{r}(N)=\mathbf{r}} \mathcal{D}[\mathbf{r}(s)]\exp\left[-\beta U_0[\mathbf{r}(s)]-\beta \int_0^N \mathrm{d}s w(\mathbf{r}(s))\right]}{\int \mathrm{d}\mathbf{r}_0 \int \mathrm{d}\mathbf{r} \int_{\mathbf{r}(0)=\mathbf{r}_0}^{\mathbf{r}(N)=\mathbf{r}} \mathcal{D}[\mathbf{r}(s)]\exp\left[-\beta U_0[\mathbf{r}(s)]\right]} \tag{2.48}$$

Clearly, $Q[w]$ is a partition function for an *N*-long chain in a region of space of volume *V* subject to the field $w(\mathbf{r})$ reduced by the corresponding partition function of a field-free chain (Figure 2.6). As defined, $Q[w]$ is a dimensionless quantity. It is related to the restricted partition function $q(\mathbf{r},s)$, defined in eq. 2.45, as follows:

$$Q[w]=\frac{1}{V}\int \mathrm{d}\mathbf{r}q(\mathbf{r},N) \tag{2.49}$$

We now consider the problem of calculating the ensemble averaged segment number density for a single flexible polymer subjected to a chemical potential $w(\mathbf{r})$. This quantity is defined by

$$\rho(\mathbf{r}) \equiv \langle \hat{\rho}(\mathbf{r}) \rangle \tag{2.50}$$

The microscopic segment density generated by the chain is given by

$$\hat{\rho}(\mathbf{r}) = \int_0^N \delta(\mathbf{r} - \mathbf{r}(s)) \, \mathrm{d}s \tag{2.51}$$

The equation connecting the microscopic segment density and the restricted partition function is:

$$\rho(\mathbf{r}) = \frac{1}{VQ[w]} \int_0^N q(\mathbf{r}, N-s) q(\mathbf{r}, s) \, \mathrm{d}s \tag{2.52}$$
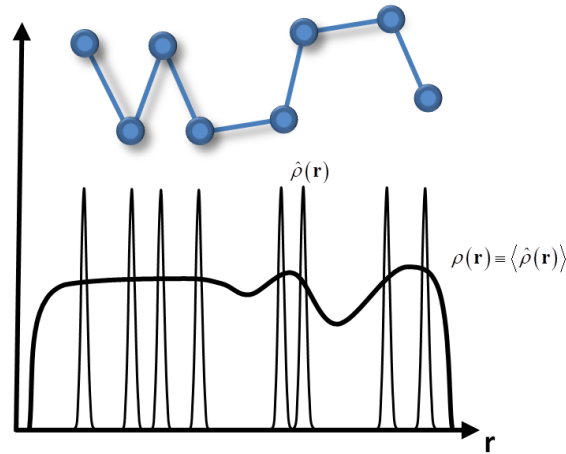
Figure 2.7. Illustration of a microscopic description of the density distribution $\rho(\mathbf{r})$ and its coarse-grained description $\hat{\rho}(\mathbf{r})$

which is known as *convolution integral equation* central to the theory of inhomogeneous polymers.[18,123,188] Eq 2.52 is an important formula in the theory of inhomogeneous polymers because it provides a recipe for calculating the average segment density of a continuous Gaussian chain experiencing an arbitrary potential $w(\mathbf{r})$. A proof of equation 2.52 is provided in Appendix B. The density operator $\rho(\mathbf{r})$ describes the average density of segments, regardless of their location along the polymer chain. Another useful density operator for the continuous Gaussian chain is the quantity

$$\rho(\mathbf{r},s) = \langle \hat{\rho}(\mathbf{r},s) \rangle \tag{2.53}$$

which represents the average density of segments located at contour position s. The microscopic density of segments at location s is derived from $\hat{\rho}(\mathbf{r},s) = \delta(\mathbf{r} - \mathbf{r}(s))$ as

$$\rho(\mathbf{r},s) = \frac{1}{VQ[w]} q(\mathbf{r}, N-s) q(\mathbf{r},s) \tag{2.54}$$
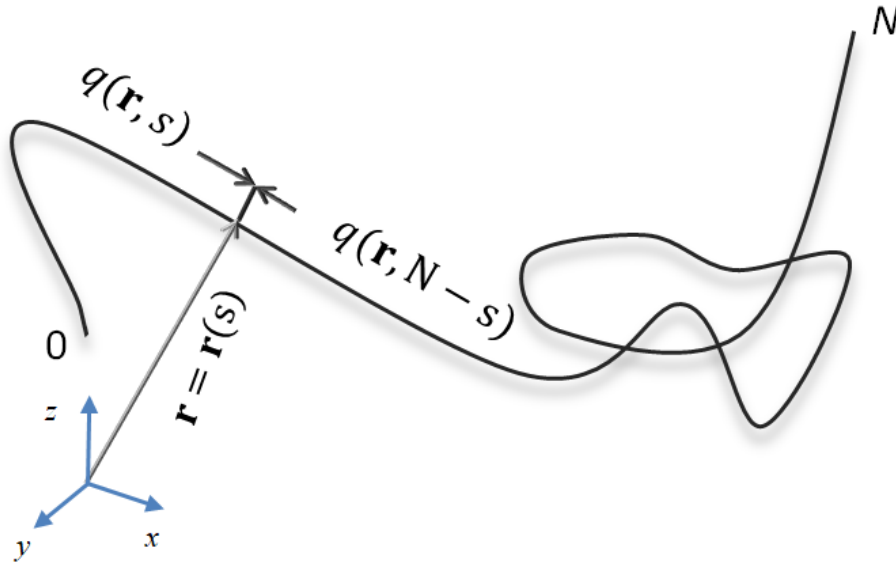
Figure 2.8. Illustration of the composition formula for the average density of segments (eq 2.54)located at position s along a continuous Gaussian chain. The statistical weight $q(\mathbf{r}, s)$ of a chain section of contour length s is joined at point $\mathbf{r} = \mathbf{r}(s)$ with the statistical weight $q(\mathbf{r}, N - s)$ of the "complementary" chain section having contour length $N - s$.

The physical content of eq 2.54 is explained in Figure 2.8. By comparing this expression with eq 2.53, we see that the average total segment density $\rho(\mathbf{r},s)$ is simply the integral of the average segment s density $\rho(\mathbf{r}, s)$ at all contour locations $0 \le s \le N$:

$$\rho(\mathbf{r}) = \int_0^N ds \rho(\mathbf{r},s) \tag{2.55}$$

This formula is clearly consistent with the relationship between the corresponding microscopic densities $\hat{\rho}(\mathbf{r})$ and $\hat{\rho}(\mathbf{r},s)$.

A special case of eq 2.54 is of particular interest. By setting $s = 0$ or $s = N$, one obtains the average density of a chain end segment. In the present case of a homopolymer obeying the

aforementioned continuous Gaussian chain model, the two chain ends are indistinguishable, so a total chain end density can be defined by

$$\rho_{\text{end}}(\mathbf{r}) = \rho(\mathbf{r},0) + \rho(\mathbf{r},N) = \frac{2}{VQ[w]}q(\mathbf{r},N) \tag{2.56}$$

where in the second line of this expression we have used $q(\mathbf{r},0)=1$. Thus, after applying the normalization $2/\{VQ[w]\}$, the propagator $q(\mathbf{r},N;[w])$ can be interpreted as the average density of chain ends at position $\mathbf{r}$.

2.3   From Particles to Fields

An additional, essential element for the construction of the field-theoretic method is the conversion of a particle-based model to a statistical field theory. The previous section dealt exclusively with the statistical properties of a single ideal polymer chain both in isolation and in the presence of an external potential field. Here, we shall focus on how the external potential field(s) can be determined. The intramolecular long-ranged interferences, also mentioned in the literature as the nonbonded interactions between the polymer segments, that have been neglected up to this point, will now be included in the formalism. An important objective of the present section is to illustrate how this particle-to-field transformation takes place for pure fluids. We set up the basic technique, since more rigorous and exact formulations for more complex polymer chain models and fluid systems will be fully explored next.

2.3.1   Canonical (*nVT*) Ensemble

In statistical mechanics, an ensemble (also statistical ensemble) is an idealization consisting of a large number of virtual copies (sometimes infinitely many) of a system, considered all at once, each of which represents a possible state that the real system might be in. In other words, a statistical ensemble is a probability distribution for the state of the system. The concept of an ensemble was introduced by J. Willard Gibbs in 1902.[189]

The canonical ensemble provides a powerful framework for deriving the thermodynamic properties of liquids and gases from molecular-level information. In the canonical ensemble, a system is considered to be closed to mass transfer, but it is open to energy transfer through the exchange of heat with a reservoir held at a fixed temperature *T*. Under these conditions, the partition function can be derived from the Hamiltonian (eq 2.1). The kinetic energy term in eq

2.1 depends exclusively on the center-of-mass momenta. The potential energy term depends exclusively on the center-of-mass positions (configurational degrees of freedom). The canonical partition function Q_{nVT} of a pure fluid with n indistinguishable particles confined in a volume V can be expressed as two separable contributions:

$$Q_{nVT} = \frac{1}{n!\hbar^{3n}} \int d\mathbf{p}^n \exp\left[-\beta \sum_{i=1}^{n} \mathbf{p}_i^2 \right] \int d\mathbf{r}^n \exp\left[\beta U\left(\mathbf{r}^n\right) \right] \tag{2.57}$$

Both integrals appearing in eq 2.57 are definite. The first integral is taken over the whole momentum space and the second integral is taken over the whole configuration space. The integral over momentum space is really a product of $3N$ independent Gaussian integrals which can be easily evaluated and then we obtain the so-called "semiclassical" partition function:

$$Q_{nVT} = \frac{1}{n!\Lambda^{3n}} \int d\mathbf{r}^n \exp\left[\beta U\left(\mathbf{r}^n\right) \right] \tag{2.58}$$

or

$$Q_{nVT} = \frac{Z_{nVT}}{n!\Lambda^{3n}} \tag{2.59}$$

where $\Lambda = \hbar/\sqrt{2\pi m k_B T}$ is the thermal wavelength, m is the mass of an atom, and $\hbar$ is the Planck constant. Z_{nVT} is the *configurational integral* of the canonical ensemble. The potential energy $U\left(\mathbf{r}^n\right)$ depends on the relative positions of the n particles, and by specifying its mathematical form, one defines a particular atomistic model of a fluid. It is often the case that the pair approximation described by eq 2.1 is sufficient for the description of the potential energy. For the purpose of illustration, we shall adopt this perspective and write

$$U\left(\mathbf{r}^n\right) = \frac{1}{2} \sum_{j=1}^{n} \sum_{k=1(\neq j)}^{n} u\left(\left|\mathbf{r}_j - \mathbf{r}_k\right|\right) \tag{2.60}$$

where $u(r)$ is the familiar pair potential function (Hansen and McDonald, 1986). The factor of (1/2) in this expression corrects for the counting of each pair of particles twice in the double sum. The external field is assumed to couple to the microscopic particle density $\hat{\rho}(\mathbf{r})$ defined as a sum of δ functions in the form already introduced implicitly in 2.51

$$\hat{\rho}(\mathbf{r}) = \sum_{j=1}^{n} \delta(\mathbf{r} - \mathbf{r}_j) \tag{2.61}$$

It follows that

$$U(\mathbf{r}^{n+1}) = \frac{1}{2} \int d\mathbf{r} \int d\mathbf{r}' \hat{\rho}(\mathbf{r}) u(|\mathbf{r}' - \mathbf{r}|) \hat{\rho}(\mathbf{r}') - \frac{1}{2} n u(0) \tag{2.62}$$

where the last term subtracts the self-interactions of the n particles that are included in the first term. Eq 2.58 can thus be written

$$Q_{nVT} = \frac{z_0^n}{n!} \int d\mathbf{r}^n \exp\left(-\frac{\beta}{2} \int d\mathbf{r} \int d\mathbf{r}' \hat{\rho}(\mathbf{r}) u(|\mathbf{r}' - \mathbf{r}|) \hat{\rho}(\mathbf{r}')\right) \tag{2.63}$$

where $z_0 \equiv \exp(\beta u(0)/2)\Lambda^3$. It can be seen from this result that the value of the potential at contact, $u(0)$, only affects the reference chemical potential of the fluid and has no thermodynamic consequences. The next step in the particle-to-field transformation is to invoke the definition of a delta functional, i.e.

$$\int \mathcal{D}\rho \, \delta[\rho - \hat{\rho}] F[\rho] = F[\hat{\rho}] \tag{2.64}$$

for any functional $F[\rho]$. The delta functional $\delta[\rho - \hat{\rho}]$ can be viewed as an infinite-dimensional version of the Dirac delta function that vanishes unless the fields $\rho(\mathbf{r})$ and $\hat{\rho}(\mathbf{r})$ are equal at all points $\mathbf{r}$ in the domain of interest. The delta functional can also be viewed as a formal definition of the functional integral $\int \mathcal{D}w$ over the auxiliary field $w(\mathbf{r})$ according to the following inverse Fourier transform

$$\delta[\rho - \hat{\rho}] = \int \mathcal{D}w \, e^{i \int d\mathbf{r} w(\mathbf{r})[\rho(\mathbf{r}) - \hat{\rho}(\mathbf{r})]} \tag{2.65}$$

It is important to note that $w(\mathbf{r})$ is a real scalar field and that the functional integral in eq 2.65 is taken along the whole real axis at each $\mathbf{r}$. The next step in transforming the canonical partition function into a statistical field theory is to insert eq 2.64 with $F[\rho] = 1$ into the integrand of eq 2.63. This leads to

$$Q_{nVT} = \frac{z_0^n}{n!} \int \mathcal{D}\rho \int d\mathbf{r}^n \delta[\rho - \hat{\rho}] \exp\left(-\frac{\beta}{2} \int d\mathbf{r} \int d\mathbf{r}' \hat{\rho}(\mathbf{r}) u(|\mathbf{r}' - \mathbf{r}|) \hat{\rho}(\mathbf{r}')\right) \tag{2.66}$$

Next, combining eqs 2.65 and 2.66, the following expression occurs for the canonical partition function of the system:

$$Q_{nVT} = \frac{z_0^n}{n!} \int \mathcal{D}\rho \int d\mathbf{r}^n \int \mathcal{D}w \, e^{i \int d\mathbf{r} w(\mathbf{r})[\rho(\mathbf{r}) - \hat{\rho}(\mathbf{r})] - \beta/2 \int d\mathbf{r} \int d\mathbf{r}' \rho(\mathbf{r}) u(|\mathbf{r}' - \mathbf{r}|) \rho(\mathbf{r}')} \tag{2.67}$$

It is important to note that as a result of these transformations, the only factor in the integrand that depends on the atomic coordinates $\mathbf{r}^n = \mathbf{r}_0, \mathbf{r}_1 ..., \mathbf{r}_n$ is $\exp\left[-i \int d\mathbf{r} w(\mathbf{r}) \hat{\rho}(\mathbf{r})\right]$. The integrals over the n particle positions thus factor out according to

$$\exp\left[-i \int d\mathbf{r} w(\mathbf{r}) \hat{\rho}(\mathbf{r})\right] = \left(VQ[iw]\right)^n \tag{2.68}$$

The functional $Q[iw]$ can be interpreted as a single-particle partition function, i.e., the contribution to the partition function from an atom which does not interact with the other atoms, but rather with the purely imaginary field $iw(\mathbf{r})$.

Upon combining eqs 2.68 and 2.67, the particle-to-field transformation is completed. The partition function can be expressed as the following statistical field theory:

$$Q_{nVT} = \frac{(z_o V)^n}{n!} \int \mathcal{D}\rho \int \mathcal{D}w \exp\left(-\mathcal{H}_c[\rho, w]\right) \tag{2.69}$$

where the functional

$$\mathcal{H}_c[\rho, w] = i \int d\mathbf{r} w(\mathbf{r}) \rho(\mathbf{r}) - \beta/2 \int d\mathbf{r} \int d\mathbf{r}' \rho(\mathbf{r}) u(|\mathbf{r}' - \mathbf{r}|) \rho(\mathbf{r}') - n \ln Q[iw] \tag{2.70}$$

is referred to as an "effective Hamiltonian" or "action".[176] . The prefactor in eq 2.69, $(z_o V)^n / n!$, is proportional to the partition function of an ideal gas.

The evaluation of the Helmholtz free energy requires the use of the familiar thermodynamic formula

$$A(n, V, T) = -k_B T \ln Q_{nVT} \tag{2.71}$$

where Q_{nVT} is obtained by performing functional integrals over the ρ and w fields according to eq 2.69.

2.3.2 Grand Canonical ($\mu V\,T$) Ensemble

The grand canonical ensemble provides a statistical microscopic description of an open equilibrium system of given volume or spatial extent, capable of exchanging energy and particles with its surroundings. This ensemble is particularly useful in the study of sorption equilibria and surface thermodynamic properties of fluids.[168]

In statistical mechanics, a grand canonical ensemble (also known as the macrocanonical ensemble) is the statistical ensemble that is used to represent the possible states of a mechanical system of particles that are in thermodynamic equilibrium (thermal and chemical) with a reservoir. The system can exchange energy and particles with a reservoir, so that various possible states of the system can differ in both their total energy and total number of particles. The system's volume, shape, and other external coordinates are kept the same in all possible states of the system. The relevant grand canonical partition function is given by

$$\Xi_{\mu VT} = \sum_{n=0}^{\infty} \exp(\beta \mu n) Q_{nVT} \tag{2.72}$$

where μ is the chemical potential and the sum is over all possible numbers of atoms. Insertion of eq 2.67 into the right-hand side of this expression leads immediately to

$$\Xi_{\mu VT} = \int \mathcal{D}\rho \int \mathcal{D}w\, e^{i\int d\mathbf{r}w(\mathbf{r})\rho(\mathbf{r}) - \frac{\beta}{2}\int d\mathbf{r}\int d\mathbf{r}'\rho(\mathbf{r})u(|\mathbf{r}'-\mathbf{r}|)\rho(\mathbf{r}')} \sum_{n}^{\infty} \frac{\left(zVQ[iw]\right)^n}{n!} \tag{2.73}$$

where $z = z_0 \exp(\beta\mu)$ is the activity. Evaluation of the sum over the number of particles results in the desired field theory for the grand canonical ensemble:

$$\Xi_{\mu VT} = \int \mathcal{D}\rho \int \mathcal{D}w \exp\left(-\mathcal{H}_{G}[w,\rho]\right) \tag{2.74}$$

with

$$\mathcal{H}_{G}[w,\rho] = i\int d\mathbf{r}w(\mathbf{r})\rho(\mathbf{r}) - \frac{\beta}{2}\int d\mathbf{r}\int d\mathbf{r}'\rho(\mathbf{r})u\left(|\mathbf{r}'-\mathbf{r}|\right)\rho(\mathbf{r}') - zVQ[iw] \tag{2.75}$$

Comparing eqs 2.70 and 2.75 and therefore the effective Hamiltonians of the canonical and grand canonical ensembles respectively, we see that they differ only in the form of the last translational entropy term. Thus, it is fairly straightforward to switch ensembles in the field-theoretic framework.

Equation 2.75 shows that the effective Hamiltonian has three principal contributions. The first term, $i\int d\mathbf{r}w(\mathbf{r})\rho(\mathbf{r})$, can be interpreted as the energy of interaction between the density field $\rho(\mathbf{r})$ and the purely imaginary "chemical potential" field $iw(\mathbf{r})$. The second term is proportional to $\int d\mathbf{r}\int d\mathbf{r}'\rho(\mathbf{r})u(|\mathbf{r}'-\mathbf{r}|)\rho(\mathbf{r}')$ and represents the energy associated with the nonbonded particle-particle interactions. This term can be replaced by the Helmholtz energy density (Helmholtz energy per unit volume), obtainable from an equation of state. In this thesis, we replace this term by identifying the Helmholtz energy with an excess Helmholtz energy, i.e., with the Helmholtz energy of a real polymer fluid consisting of a certain number of chains in a given volume minus the Helmholtz energy density of an equal number of noninteracting (ideal gas) unperturbed chains in the same volume. Finally, the term $-zVQ[iw]$ describes the translational entropy (relative to the ideal gas entropy) of a fluid of n noninteracting atoms experiencing the potential $iw(\mathbf{r})$.[32]

The grand canonical ensemble allows us to calculate thermodynamics potentials. At the outset, the quantity $\Omega_{\mu VT}$ is called *grand potential*. In a homogeneous system, the connection between the grand potential and macroscopic thermodynamics is

$$\Omega_{\mu VT} = -k_{\mathrm{B}}T\ln\Xi_{\mu VT} = -PV \tag{2.76}$$

where P is the pressure, and the ensemble averaged number of particles in the system is controlled by adjusting the chemical potential μ or activity z according to

$$\langle n\rangle = \left(\frac{\partial\ln\Xi_{\mu VT}}{\partial\ln z}\right)_{V,T} \tag{2.77}$$

The Gibbs Energy is found as

$$G = \langle N\rangle\mu = \langle N\rangle k_B T\ln z = k_B T\left(\frac{\partial\ln\Xi_{\mu VT}}{\partial\ln\mu}\right)_{T,V} \tag{2.78}$$

And the Helmholtz energy as

$$A = G - PV = \langle N\rangle\mu - k_{\mathrm{B}}T\ln\Xi_{\mu VT} = k_B T\left[\left(\frac{\partial\ln\Xi_{\mu VT}}{\partial\ln\mu}\right)_{T,V} - \ln\Xi_{\mu VT}\right] \tag{2.79}$$

For interfacial systems, the Grand canonical ensemble is the most suitable choice in calculating the interfacial tension, since it allows the mass transfer between phases. For the special case of a liquid bounded by an undeformable solid surface,

$$\Omega(V,T,\mu) - \Omega_{\text{bulk}}(V,T,\mu) = S_{\text{solid}}\left(\gamma_{\text{sp}} - \gamma_{\text{s}}\right) \tag{2.80}$$

where S_{solid} is the total interfacial area of contact, γ_{sp} is the solid-polymer interfacial tension, γ_{s} is the solid surface tension, and $\gamma_{\text{s}} - \gamma_{\text{sp}}$ is the *adhesion tension* between the polymer and the solid.

2.4   Self-Consistent Field Theory

The previous section demonstrated how statistical field theories can be constructed from particle-based models of simple fluids. It is now appropriate to discuss how to analyze such field theories and extract useful information about the structure and thermodynamic properties of polymeric fluids at equilibrium.

The field-theoretic models of section 2.3 generically express the relevant partition function as a functional integral over one or more chemical potential fields $w(\mathbf{r})$, i.e.,

$$Z = \int \mathcal{D}\rho \int \mathcal{D}w \exp\left(-\mathcal{H}\left[w,\rho\right]\right) \tag{2.81}$$

where $\mathcal{H}\left[w,\rho\right]$ is an effective Hamiltonian which is a non-local functional of the field variables and is generally complex (not strictly real). The form of $\mathcal{H}\left[w,\rho\right]$ depends on the particular interaction and chain model used to construct the field theory and is thus sensitive to polymer architecture, molecular weight, polydispersity, composition, etc. To compute the ensemble average of some observable G, one applies the equation

$$\left\langle G[w,\rho]\right\rangle = Z^{-1}\int \mathcal{D}\rho \int \mathcal{D}w\, G[w,\rho]\exp\left(-\mathcal{H}\left[w,\rho\right]\right) \tag{2.82}$$

The evaluation of free energies and derivative quantities through a thermodynamic formula connecting it to Z involves the computation of the functional integral given by eq 2.81. Similarly, by application of eq 2.82, with $G[w,\rho]$ corresponding to an appropriate density operator, the fluid structure is computed as a ratio of two functional integrals.

This expression of the partition function is exact. However, the evaluation of this partition function is in general a formidable task. A variety of approximate methods have been developed
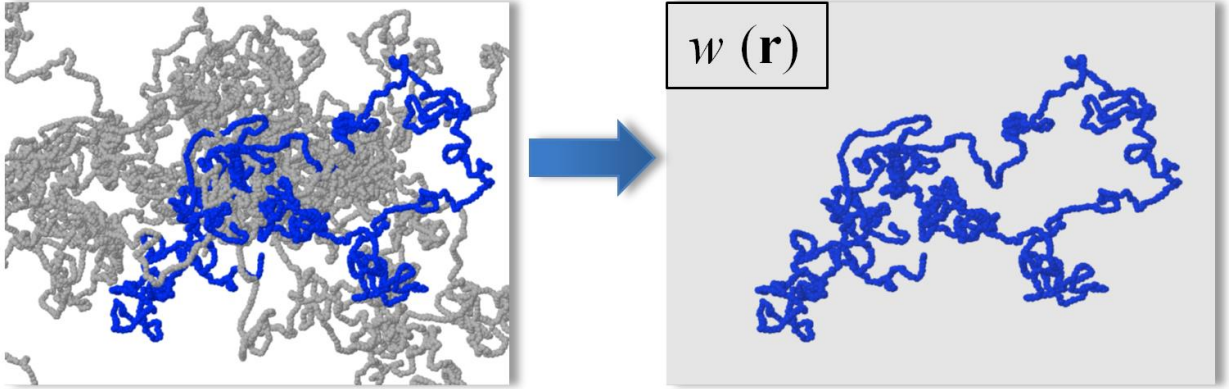
Figure 2.9. An illustrative explanation of the mean field approximation. An interacting many-chain system is approximated by a single ideal chain in an averaged potential field $w(\mathbf{r})$.

to evaluate this partition function. The most fruitful method is the mean-field approximation, which amounts to evaluating the functional integral using a saddle-point technique. Technically the saddle-point approximation is obtained by demanding that the functional derivative of the integrand is zero. This is the most important analytical approximation technique, which is widely known in the polymer physics literature as self-consistent field theory (SCFT). [89,190] This technique is widely used in many physical contexts, perhaps most notably in the theory of phase transformations. [176] In the present case, the mean-field approximation amounts to the assumption that a single field and density configuration $\bar{w}(\mathbf{r})$ and $\bar{\rho}(\mathbf{r})$ dominate the functional integrals in eqs 2.83 and 2.84. This field configuration is obtained by demanding that $\mathcal{H}_{\mathrm{G}}[w,\rho]$ be stationary with respect to variations in $w(\mathbf{r})$ and $\rho(\mathbf{r})$, i.e.,

$$\left.\frac{\delta\mathcal{H}_{\mathrm{G}}[w,\rho]}{\delta w}\right|_{w=\bar{w}} = 0, \quad \left.\frac{\delta\mathcal{H}_{\mathrm{G}}[w,\rho]}{\delta\rho}\right|_{\rho=\bar{\rho}} = 0 \tag{2.83}$$

Having obtained the "mean-field" potential and segment density fields $\bar{w}(\mathbf{r})$ and $\bar{\rho}(\mathbf{r})$ from this equation, one completes the approximation by imposing the following:

$$\bar{\mathcal{H}}[\bar{w},\bar{\rho}] = -\ln Z, \quad \langle G[w,\rho]\rangle = G[\bar{w},\bar{\rho}] \tag{2.84}$$

If Z represents either a canonical partition function or the grand canonical partition function, then the Helmholtz free energy and the grand canonical potential are derived immediately as $\beta A = -\ln Z = \mathcal{H}[\bar{w},\bar{\rho}]$ or $\beta\Omega = -\ln Z = \bar{\mathcal{H}}_{\mathrm{G}}[\bar{w},\bar{\rho}]$, respectively.

In the mean-field approximation, all configurations of the spatially varying fields are neglected, except for the most probable configurations $\bar{w}(\mathbf{r})$ and $\bar{\rho}(\mathbf{r})$. For atomic or small molecule fluids, this approximation of neglecting all "field fluctuations" is usually quite poor. This is because the typical coordination number of an atom or small molecule at liquid densities is quite low, so large fluctuations occur in the potential experienced by a particle as neighboring particles change positions. Indeed, these strong local field fluctuations are responsible for producing the density correlations that characterize the atomic-scale structure of liquids.[32] The mean-field approximation is also inaccurate in polymer solutions or melts at the atomic scale because the coordination number remains small. However, at mesoscopic scales, the situation changes qualitatively due to the ability of polymer coils to interpenetrate one another. For mesoscopic scales, the fluctuations in the environment of each polymer diminish with increasing molecular weight, since the potential field variations are averaged out by contact with increasingly large numbers of surrounding chains. This constitutes the standard argument that the mean-field approximation is accurate for concentrated solutions or melts of high-molecular-weight polymers. [191]

2.5   Real Polymer Chain Conformation

A major weakness of previous works employing SCFT is that they are primarily aimed at producing qualitative and not quantitative results. Another weakness of the SCFT formulation is that single chain models (especially the discrete and the continuous Gaussian chain model) refer to Kuhn segments, while statistical ensembles used to describe a fluid system mostly refer to particle or monomer segments. Some researchers interchangeably treat the Kuhn length, the statistical segment length, and the monomer length as being the same. Their claims seem to be somewhat inaccurate. The purpose of this section is to make clear to the reader the difference between a Kuhn segment and a monomer segment.

In a typical polymer chain, there are correlations between bond vectors (especially between neighboring ones). The physical origins of these local correlations between bond vectors are restricted bond angles, torsional potentials, and steric hindrance. If we assume that the length of every skeletal bond of the real chain is $l_{C\text{-}C}$, we can ask this chain to follow the scaling law of a freely jointed chain, $N_b l_{C\text{-}C}{}^2$, with N_b being the count of skeletal bonds along the chain. In order to achieve quantitative agreement, we should introduce a coefficient, C_N, in order to account for the stiffness of the chain:

$$\left\langle R_e^{\;2} \right\rangle = N_b C_N l_{c\text{-}c}^{\;2} \tag{2.85}$$

with C_N being Flory's characteristic ratio. The characteristic ratio is larger than unity for all polymers. All models of ideal polymers ignore nonlocal interactions between monomers separated by many bonds and result in characteristic ratios saturating at a finite value C_∞ for large number of backbone bonds ($N_b \to \infty$). Thus, the mean-squared end-to-end distance can be approximated for long chains as:

$$\left\langle R_e^{\;2} \right\rangle = N_b C_\infty l_{c\text{-}c}^{\;2} \tag{2.86}$$

The numerical value of Flory's characteristic ratio depends on the local stiffness of the polymer chain. The contour length L of the chain at full extension, on the other hand, is given by

$$L = \gamma N_b l_{c\text{-}c} \tag{2.87}$$

where γ is a geometric factor that depends on the bonding along the real chain. For a symmetric homopolymer chain such as polyethylene, where the equilibrium bending angle θ is the same between all pairs of successive skeletal bonds, $\gamma = \sin\dfrac{\theta}{2}$.

Flexible polymers exhibit universal properties that are independent of the local chemical structure. A simple unified description of all ideal polymers was needed. The first attempts to use random flight concepts to describe the linear polymers in solution are usually attributed to Kuhn, who argued that the Rayleigh random flight model might be used. It soon became evident that such a model was not appropriate to address very short chains (less than a few hundred chemical bonds), or relatively stiff chains which cannot adopt tortuous configurations. Moreover, it is not appropriate to use as "steps" in the random flight the individual bond lengths, or even the monomeric units the chain consists of. Thus, the length of an individual step, b_K, became an adjustable parameter of the model, namely the Kuhn length. The equivalent freely jointed chain should have the same mean-squared end-to-end distance $\left\langle R_e^{\;2} \right\rangle$ and the same end-to-end distance at full extension L as the actual polymer, but N_K freely-jointed effective bonds of length b_K. The end to end distance $\left\langle R_e^{\;2} \right\rangle$ of this equivalent freely jointed chain is:

$$\left\langle R_e^{\;2} \right\rangle = N_K b_K^{\;2} = N_b C_\infty l_{c\text{-}c}^{\;2}, \qquad L = \gamma N_b l_{c\text{-}c} = N_K b_K \tag{2.88}$$

From the above equations we can easily extract the equation which connects the Kuhn length with the monomer length:

$$\frac{b_K}{l} = \frac{C_\infty}{\gamma} \tag{2.89}$$

A typical value for $\gamma = \sin(\theta/2) \sim 0.83$, with $\theta \sim 112°$ being the bond angle between successive skeletal carbon-carbon bonds. The numerical value of Flory's characteristic ratio depends on the local stiffness of the polymer chain with typical values ranging from 7 to 9 for many flexible polymers. From eq 2.89 we can easily came to the conclusion that usually the Kuhn length is approximately 10 times larger than a typical bond length.

2.6   Phenomenological Theoretical Methods

As mentioned in the previous chapter, the theoretical methods that are used to study polymer interfaces can be categorized as being either an analytical or a simulation technique, while the analytical techniques can be further classified into microscopic or phenomenological. One of the most dominant phenomenological techniques is related to Cahn-Hilliard theory[67], widely known as Square Gradient Theory (SGT).

For systems with a nearly uniform one-body density profile, the Helmholtz energy may be approximated by a functional Taylor expansion with reference to the Helmholtz energy of a uniform system with an average density ρ_0:

$$F\left[\rho(\mathbf{r})\right] = F\left[\rho_0\right] + \mu \int \Delta\rho(\mathbf{r})d\mathbf{r} + \frac{1}{2}\int d\mathbf{r}_1 \int d\mathbf{r}_2 \Delta\rho(\mathbf{r}_1)\Delta\rho(\mathbf{r}_2)K(\mathbf{r}_1,\mathbf{r}_2) \tag{2.90}$$

where $\Delta\rho(\mathbf{r}) \equiv \rho(\mathbf{r}) - \rho_0$. In the density expansion above, the reference system has the same temperature and particle chemical potential as the real system. $K(\mathbf{r}_1,\mathbf{r}_2)$ has units of energy and is referred to as the vertex function.

For systems with a slow varying one-particle density $\rho(\mathbf{r})$, $\Delta\rho(\mathbf{r})$ is small and the functional Taylor expansion for the intrinsic Helmholtz energy may be truncated after the quadratic term. Similarly, the local density may be expressed as a truncated Taylor series

$$\rho(\mathbf{r}) = \rho(\mathbf{r}_0) + (\mathbf{r}-\mathbf{r}_0)\nabla\rho(\mathbf{r}) + \frac{1}{2}(\mathbf{r}-\mathbf{r}_0)(\mathbf{r}-\mathbf{r}_0):\nabla\nabla\rho(\mathbf{r}) + O\left(\nabla^3\rho\right) \tag{2.91}$$

where $\nabla\rho(\mathbf{r})$ denotes the density gradient and the symbol ":" denotes the scalar product of two tensors. The gradient expansions lead to a simple expression for the Helmholtz energy of inhomogeneous systems:

$$F\big[\rho(\mathbf{r})\big] = \int d\mathbf{r}\left\{f_0\big[\rho(\mathbf{r})\big] + \frac{\kappa}{2}\big|\nabla\rho(\mathbf{r})\big|^2\right\} \tag{2.92}$$

where f_0 represents the Helmholtz energy density of the uniform system at system temperature T and local density $\rho(\mathbf{r})$, and κ is called the influence parameter.

2.6.1 Interfacial Tension

The most important application of the eq 2.92 is the calculation of interfacial tension. The interfacial tension between two coexisting fluid phases, say α and β, is defined as the change in free energy in response to variation of the interfacial area. For two bulk phases at equilibrium, the interfacial area refers to an imaginary surface S dividing the total mass of a particular component in the system into those corresponding to two bulk phases. The imaginary surface is called the Gibbs dividing surface.

For an inhomogeneous system containing two coexisting bulk phases coming together at a planar interface, SGT predicts that the grand potential per unit area is given by

$$\Omega/S = \int_{-\infty}^{+\infty} dz\left\{f_0\big[\rho(z)\big] + \frac{\kappa}{2}\left(\frac{d\rho(z)}{dz}\right)^2 - \mu\rho(z)\right\} \tag{2.93}$$

For bulk systems, the grand potential reduces to $\Omega = -pV$ where pressure p is the same for the coexisting phases. The interfacial tension is defined as the grand potential per unit area relative to those corresponding to the bulk phases

$$\gamma = \frac{\left(\Omega - \Omega_{bulk}\right)}{S} = \int_{-\infty}^{+\infty} dz\left\{f_0\big[\rho(z)\big] + \frac{\kappa}{2}\left(\frac{d\rho(z)}{dz}\right)^2 - \mu\rho(z) + p\right\} \tag{2.94}$$
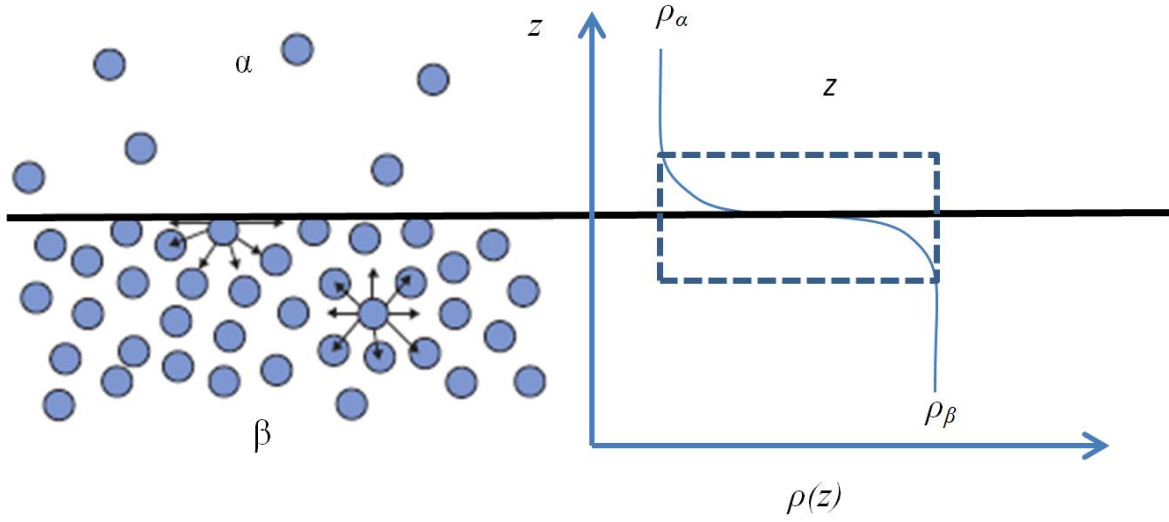
Figure 2.10. The Gibbs dividing surface between two bulk phases (*a* and *β*) and a schematic representation of the density profile in the interfacial region.

To use eq 2.94, we need an equation of state for the bulk phase and the density profile. By minimization of the grand potential with respect to $\rho(\mathbf{r})$ (Euler-Lagrange condition on the functional on the right-hand side of eq 2.94 under constant μ and p) we obtain:

$$\left(\frac{\partial f_0(\rho)}{\partial \rho}\right)_{\rho=\rho(z)} - \kappa\left(\frac{\mathrm{d}^2\rho(z)}{\mathrm{d}z^2}\right) - \mu = 0 \tag{2.95}$$

If we consider a vapor- liquid phase separation and combine eqs 2.94 and 2.95, we reach a simple expression for the surface tension:

$$\gamma = k\int_{-\infty}^{+\infty} \mathrm{d}z\left(\frac{\mathrm{d}\rho}{\mathrm{d}z}\right)^2 \equiv \kappa\int_{-\infty}^{+\infty} \mathrm{d}z\left|\rho'(z)\right|^2 \tag{2.96}$$

More specifically, to obtain eq 2.96 from eqs 2.94 and 2.95 it is helpful to remember that, for the two coexisting bulk fluid phases α and β (say, liquid and gas) at equilibrium, the chemical potential is the same, equal to μ:

$$\left(\frac{\partial f_0(\rho)}{\partial \rho}\right)_{\rho=\rho_\alpha} = \left(\frac{\partial f_0(\rho)}{\partial \rho}\right)_{\rho=\rho_\alpha} = \mu \tag{2.97}$$

and also the pressure is the same, equal to the saturation pressure p:

$$\left(\rho\frac{\partial f_0(\rho)}{\partial \rho}\right)_{\rho=\rho_\alpha} - f_0(\rho_\alpha) = \left(\rho\frac{\partial f_0(\rho)}{\partial \rho}\right)_{\rho=\rho_\beta} - f_0(\rho_\beta) = p \tag{2.98}$$

Eq 2.95 can be written as

$$\left(\frac{\partial}{\partial \rho}\left[f_0(\rho)-\mu\rho\right]\right)_{\rho=\rho(z)} = \kappa\left(\frac{d^2\rho(z)}{dz^2}\right) \tag{2.99}$$

Multiplying both sides of the equation by $d\rho/dz$ and integrating from $z=-\infty$, where bulk phase α conditions prevail, up to an arbitrary point z, where the local density is $\rho(z)$, we obtain

$$\int_{-\infty}^{z}\left(\frac{\partial}{\partial \rho}\left[f_0(\rho)-\mu\rho\right]\right)_{\rho=\rho(z)}\frac{d\rho(z)}{dz}dz = \kappa\int_{-\infty}^{z}\left(\frac{d^2\rho(z)}{dz^2}\right)\frac{d\rho(z)}{dz}dz \tag{2.100}$$

or

$$\int_{\rho_\alpha}^{\rho(z)}\frac{\partial}{\partial \rho}\left[f_0(\rho)-\mu\rho\right]d\rho = k\int_{-\infty}^{z}\frac{d\rho(z)}{dz}\frac{d}{dz}\left(\frac{d\rho(z)}{dz}\right)dz = \frac{1}{2}\kappa\int_{-\infty}^{z}\frac{d}{dz}\left[\left(\frac{d\rho(z)}{dz}\right)^2\right]dz =$$

$$= \frac{k}{2}\left[\left(\frac{d\rho(z)}{dz}\right)^2 - \lim_{z\to-\infty}\left(\frac{d\rho(z)}{dz}\right)^2\right] = \frac{\kappa}{2}\left(\frac{d\rho(z)}{dz}\right)^2 \tag{2.101}$$

or

$$f_0\left[\rho(z)\right]-\mu\rho(z)-f_0(\rho_\alpha)+\mu\rho_\alpha = \frac{k}{2}\left(\frac{d\rho(z)}{dz}\right)^2 \tag{2.102}$$

On the other hand, substituting p in terms of $f_0(\rho_\alpha)$, μ, and ρ_α as shown above and invoking the differential equation we just derived, we can rewrite the right-hand side of eq 2.94 as

$$\gamma = \int_{-\infty}^{+\infty}dz\left\{f_0\left[\rho(z)\right]-\mu\rho(z)+\mu\rho_\alpha-f_0(\rho_\alpha)+\frac{\kappa}{2}\left(\frac{d\rho(z)}{dz}\right)^2\right\} =$$

$$= \int_{-\infty}^{+\infty}dz\left\{\frac{\kappa}{2}\left(\frac{d\rho(z)}{dz}\right)^2+\frac{\kappa}{2}\left(\frac{d\rho(z)}{dz}\right)^2\right\} = \kappa\int_{-\infty}^{+\infty}dz\left(\frac{d\rho(z)}{dz}\right)^2 \tag{2.103}$$

which is eq 2.96. The penultimate equation in this development is an ordinary differential equation that can readily be integrated to find $z(\rho)$ given an equation of state for the fluid, which dictates the Helmholtz energy density function $f_0\left[\rho(z)\right]$ and the chemical potential at coexistence, μ. Thus, in the framework of SGT, the density profile and the interfacial tension can be calculated from the equation of state of the bulk fluid and the influence parameter κ. The

51

main advantage of SGT is simplicity, while a quantitative representation of the surface tension can be accomplished by using an accurate equation of state that can describe the bulk phases α and β and an optimized influence parameter.

2.6.2 Equation of State

An *equation of state* (EoS) is a thermodynamic relation between the state variables, which describe the state of matter under a given set of physical conditions of a homogeneous system. It takes the form of an equation relating the density to temperature, pressure, and composition, the latter playing a role in multicomponent systems. In statistical mechanics and the context of the isothermal-isobaric ensemble (*nPT*), the Gibbs free energy, *G*, is related to the configurational integral $\mathcal{Z}_{nPT}$ by the following equation:

$$G = -\frac{1}{\beta}\ln \mathcal{Z}_{nPT} \tag{2.104}$$

where the configurational integral $\mathcal{Z}_{nPT}$ is:

$$\mathcal{Z}_{nPT} = \sum_{V}\sum_{E}\Omega(E,V,n)\exp\left[-\beta(E+pV)\right] \tag{2.105}$$

with $\Omega(E,V,n)$ being the number of configurations available to a system of *n* molecules whose potential (configurational) energy and volume are *E* and *V*, respectively. The reader should take care not to confuse $\Omega(E,V,n)$ with the grand potential, for which the symbol Ω is also used. The summations in eq 2.98 extend over all feasible values of *E* and *V*. The isothermal-isobaric ensemble and the associated Gibbs potential are the most convenient of the potential ensembles to invoke in the study of fluid phase equilibria.

The fundamental problem in deriving the equation of state for a system is to determine Ω. One of the most widely used equations of state for polymer fluids is the one derived by Sanchez and Lacombe.[192] Inspired by Flory's model for binary mixtures, these authors have employed an Ising or lattice formulation, wherein the polymer segments are occupying discrete lattice sites, while there also exist empty lattice sites (holes). The Gibbs free energy, *G*, based on the Sanchez-Lacombe equation of state, can be expressed in terms of dimensionless variables as:

$$\frac{G}{nr_{SL}\varepsilon^{*}} \equiv \tilde{G} = -\tilde{\rho} + \tilde{P}\tilde{u} + \tilde{T}\left[(\tilde{u}-1)\ln(1-\tilde{\rho}) + \frac{1}{r_{SL}}\ln\frac{\tilde{\rho}}{\omega}\right] \tag{2.106}$$

Table 2.1. Sanchez-Lacombe notation

Symbol	Explanation
υ^{*}	hard core volume of a Sanchez-Lacombe segment
r_{SL}	number of Sanchez-Lacombe segments constituting a molecule
$r_{SL}\rho_{m}$	segmental density (Sanchez-Lacombe segments per unit volume)
ε^{*}	attractive energy between Sanchez-Lacombe segments in adjacent sites
$T^{*} = \varepsilon^{*} / k_{B}$	characteristic Sanchez-Lacombe temperature
$P^{*} = \varepsilon^{*} / \upsilon^{*}$	characteristic Sanchez-Lacombe pressure
$V^{*} = n\left(r_{SL}\upsilon^{*}\right)$	close packed volume of the n r_{SL}-mers
$\tilde{\rho} = \rho_{m}r_{SL}\upsilon^{*} = \rho_{mass}r_{SL}RT^{*} / \left(MP^{*}\right)$	reduced segmental density
ρ_{mass}	mass density (kg m^{-3})
M	molar mass of a chain (kg mol^{-1})
$\tilde{T} = T/T^{*}$	reduced temperature
$\tilde{P} = P/P^{*}$	reduced pressure
$\tilde{u} = 1/\tilde{\rho} = V/V^{*}$	reduced volume

where $\tilde{T}, \tilde{\rho}, \tilde{u}$ and $\tilde{p}$ are the reduced temperature, density, volume and pressure respectively. The parameter ω is connected to the number of different configurations available to a system of n r_{SL}-mers. The Sanchez-Lacombe parameters are presented in Table 2.1. The corresponding equation of state can be extracted by minimizing G *with respect to* $\tilde{\rho}$ ρ, yielding

$$\tilde{\rho}^{2} + \tilde{P} + \tilde{T}\left[\ln(1-\tilde{\rho}) + \left(1 - \frac{1}{r_{SL}}\right)\tilde{\rho}\right] = 0 \tag{2.107}$$

According to the discussion in the above subsection in SGT, we are interested in the Helmholtz energy density of a homogeneous phase. The Helmholtz energy under the Sanchez Lacombe formalism can be obtained from eq 2.106:

$$A^{SL}(\rho,T) = G - PV = G - \tilde{P}\frac{nr_{SL}\varepsilon^*}{\tilde{\rho}}$$

$$= -\tilde{\rho}nr_{SL}\varepsilon^* + \tilde{P}\tilde{u}nr_{SL}\varepsilon^* + \tilde{T}nr_{SL}\varepsilon^*\left[(\tilde{u}-1)\ln(1-\tilde{\rho}) + \frac{1}{r_{SL}}\ln\frac{\tilde{\rho}}{\omega}\right] - \tilde{P}\frac{nr_{SL}\varepsilon^*}{\tilde{\rho}} \quad (2.108)$$

$$= -\tilde{\rho}nr_{SL}\varepsilon^* + \tilde{T}nr_{SL}\varepsilon^*\left[(\tilde{u}-1)\ln(1-\tilde{\rho}) + \frac{1}{r_{SL}}\ln\frac{\tilde{\rho}}{\omega}\right]$$

In order to avoid double counting in SCFT (taking into account eq 2.69), we have to subtract the Helmholtz energy of an ideal gas of chains. This quantity is given by:

$$A^{IG}(\rho,T) = G^{IG}(\rho,T) - P^{IG}V = -n\mu^{IG}(\rho,T) - nk_BT = nk_BT\left[\ln\left(\frac{\rho_m\prod_i\Lambda_i^3}{Z_{intra}}\right) - 1\right] \quad (2.109)$$

3 SCFT Combined with SGA of Free Polymer Surfaces /Films

The current chapter presents a self-consistent field (SCF) theoretic approach, using a general excess Helmholtz energy density functional that includes a square gradient term, for polymer melt surfaces.[26] The approach is implemented for linear polyethylene films over a variety of temperatures and chain lengths. The formulation of the SCF plus square gradient approximation (SGA) developed is generic and can be applied with any equation of state (EoS) suitable for the estimation of the excess Helmholtz energy. As a case study, the approach is combined with the Sanchez-Lacombe (SL) EoS to predict reduced density profiles, chain conformational properties, and interfacial free energies, yielding very favorable agreement with atomistic simulation results and noticeable improvement relative to simpler SCF and SGA approaches. The reduced influence parameter invoked in the SGA to achieve accurate density profiles and interfacial free energies is consistent with the definition of Poser and Sanchez.[121] The new SCF_SL+SGA approach is used to quantify the dominance of chain end segments compared to middle segments at free polyethylene surfaces. Schemes are developed to distinguish surface-adsorbed from free chains and to decompose the surface density profiles into contributions from trains, loops, and tails; the results for molten polyethylene are compared with the observables of atomistic simulations. Reduced chain shape profiles indicate flattening of the chains in the surface region as compared to the bulk chains. The range of this transitional region is approximately 1.6 radii of gyration (R_g). The inclusion of chain conformational entropy effects, as described by the modified Edwards diffusion equation of the SCF, in addition to the square gradient term in density, provides more accurate predictions of the surface tension, in good match with experimental measurements on a variety of polymer melts and with atomistic simulation findings.

3.1   Background

Many significant properties of soft condensed matter are determined by the structure, thermodynamics, and dynamics of surfaces and interfaces. Such properties play a dominant role in the manufacturing of materials by controlling adhesion, capillary and wetting phenomena, which influence, for example, the characteristics of protective films and membranes, bioactivity and biocompatibility of biomaterials, formation of microemulsions, and rheological behavior of lubricants.[32,193] It is fascinating and tempting to fully explore the complex mechanisms of these phenomena and establish relations between macroscopically observable surface properties and molecular-level chemical constitution and structure. Toward this goal, various theoretical methods have been developed to elucidate inhomogeneous polymeric systems.

3.1.1   Freely Standing Liquid Polymer Films

The topological characteristics, structure, and thermodynamics of phases of simple fluids and polymer melts coexisting with gas have been explored to great length in previous works via theoretical approaches and atomistic simulations.[92,94,100–112] Thin liquid films exposed to gas phases on both sides, the so-called freely standing liquid films (FF), attract great interest and attention among liquid/gas systems.[92,94,100–103,107,109–112] The thickness of these films is a significant characteristic with deep implications concerning their stability. On one side, films of thickness on the order of 10 nm have been shown to display an apparent bulk behavior in their central region.[107] On the other side, ultrathin films of molten polymers, with a thickness of a few radii of gyration of the constituent polymer chains, exhibit reduced densities and an altered structure in their central region[194,195] as compared to their equivalent bulk sample. Moreover, with decreasing film thickness the two interfacial regions begin to overlap and as a result disjoining pressure effects emerge, affecting the stability of the films, as has been showed in Lennard-Jones fluids.[102,110,112] In case the film thickness is reduced further, below the range of van der Waals forces, the disjoining pressure exceeds a critical absolute value, rupture occurs, and the film collapses into energetically more favorable structures.[109,196]

Thin films and the phase behavior of block copolymers have been studied extensively with self-consistent field theory (SCFT).[92,94,100,101,111] SCFT has its origin in the work by Edwards.[89] Helfand and Tagami in 1972 adapted the theoretical framework to predict properties at the interface between immiscible polymers.[197] Subsequently, Hong and Noolandi, among

others, made important contributions to the theory.[198] Since then, SCFT has supported a huge number of applications in the literature and has been applied to a large count of polymeric systems with outstanding results, which have been summarized in review articles,[34,98,199] book chapters, and books.[3,32,69] Even though SCFT has been used extensively to predict and explain the structure and phase diagrams of block copolymers and polymer blend systems, few authors have applied it to homopolymeric systems.[24,131–133]

3.1.2 Previous Works

As outlined in Chapter 2, in polymer field theory, the configurational partition function of a system of chains interacting with each other, as well as with solvent, ions, and solid surfaces that may be present, is reexpressed in terms of the configurational partition function of a set of noninteracting chains subject to a fluctuating field. The way the conformations of each chain species develop in the field is described by an Edwards diffusion equation. Based on a saddle point approximation, SCFT replaces the field by an optimal function of space which depends on the mean segment densities, and therefore on the conformations. The resulting system of equations, expressing self-consistency of the field that shapes chain conformations but is in turn shaped by them, is solved to convergence. The model that defines the statistical mechanics of a noninteracting polymer chain can be more or less detailed. Two models that have been invoked are the semi-flexible worm-like model and the fully flexible Gaussian model. The semi-flexible wormlike chain model is unnecessarily complicated[199] when applied to high molecular weight polymers, but has the advantage of being more realistic in the case of short chains, because it can deal better with orientational tendencies associated with conformational stiffness.[98] Even in the case of the simple Gaussian model, the statistical mechanical formulation of SCFT is not trivial. A particle-to-field transformation has to be carried out in the canonical or in the grand canonical ensemble. The effective Hamiltonian is required to be stationary with respect to the field and/or density variations and the equations must be solved in a self-consistent way.

SCFT, as originally formulated for polymeric systems, requires the system to be incompressible. Incompressibility, however, is but a poor approximation when dealing with the free surfaces of polymer systems. Hong and Noolandi overcame this inconsistency by introducing vacancies and treating them as small molecules.[91] This formulation increases the number of equations to be solved and is only compatible with Flory- Huggins type equations of state (EoS). Thompson[200] used the vacancy treatment to distinguish the two regimes of molar

mass dependence of surface tension, at lower and higher molar masses. A compressible model with no explicit consideration of voids was initially introduced by Helfand and Tagami for binary polymer mixture interfaces by assuming that the excess chemical potential is known for one polymer; in their calculations the total density was found to decrease at the interface.[197] Schmid in 1996 first attempted to investigate compressible polymer blends at surfaces by using SCFT.[132] Daoulas et al. in 2005 used the compressible model with a semi-flexible –flexible continuum description to address conformational properties of a polyethylene melt under confinement and compared the results with atomistic simulations.[24] In 2013 by using a three-dimensional compressible SCFT scheme, Daoulas and Müller explored the thermodynamic stability of the stalk fusion-intermediate in amphiphilic membranes.[201]

The importance of including nonlocal terms in density in the Helmholtz free-energy functional to deal with the inhomogeneous environment of surfaces and interfaces has generally been recognized by numerous authors.[5,67,114–130] The nonlocal gradient density expansion term was initially introduced by van der Waals for the vapor liquid interface for a one component system. Nowadays, it is widely known as the square gradient approximation (SGA). SGA is known alternatively as Ginzburg-Landau theory or Landau expansion.[69] Cahn and Hilliard theory, developed in 1958, included gradient terms in the mole fraction, in the same spirit as SGA, to describe binary mixtures.[67] SCFT incorporated the square gradient approximations from early on. Helfand et al. first conceived the importance of nonlocal terms in calculating the chemical potential of copolymer and polymer blend systems in a SCF.[123,197] de Gennes combined the Flory-Huggins theory with the square gradient contribution.[5] A number of works [91,124,202,203] since then have used the gradient expansion in the free-energy functional with several variations in the coefficient of the gradient term; much of this work has focused on the difference between the weak and strong segregation limits of polymer blends and copolymers. The coefficient(s) of the gradient term(s) is (are) mostly referred to as the influence parameter(s).

In the most general case, square gradient theory requires the contribution of a local Helmholtz energy density that can be retrieved from an EoS and the contribution of the square gradient density multiplied by the influence parameter. Theoretically, the influence parameter is related to a two body direct correlation function and can be computed either from integral equation theories or from analytical functions and mean field approximations.[204–207]The theoretical results, however, rely on approximations and rough estimations, resulting in

relatively poor performance when compared against experimental or atomistic simulations results. Semi-empirical approaches[130,208–211] have thus been used to correlate influence parameters to EoS parameters.

3.1.3 Current Research Approach

The present work aims at combining two of the most widely used theoretical frameworks for the estimation of the interfacial properties of freestanding polymer surfaces, namely SCFT and square gradient theory, in a manner that enables prediction with a minimum of adjustable parameters. As a case study, the theoretical framework is applied to free polymer films comprising polymer chains modeled as Gaussian threads, whilst the thermodynamics of the polymer in the bulk is described by the Sanchez-Lacombe EoS.[192] The influence parameter of the SGA term is calculated through correlations arising from the atomistic density profiles of polyethylene melts. Furthermore, there is a direct connection between the reduced influence parameter estimated by Poser and Sanchez[121] and our estimation; hence, allowing us to extend the model to a variety of polymers for the purpose of calculating surface tension. It should be noted, however, that the developed framework is generic, because the excess Helmholtz energy density functional can be derived from any EoS. The SL EoS was chosen in this study because it has been shown to provide accurate results for such systems and it allows for comparisons with past works.[91,121] Our primary aim is to calculate various thermodynamic and structural characteristics of thin films such as the surface tension, the reduced density profile and its decomposition into contributions from "adsorbed" and "free" segments, the long-range conformational properties of the chains quantified by the chain shape, and the segregation of chain ends at the free surface. The SCF calculations are vigorously compared against atomistic simulation results and experimental data.

3.2 Model System and Theoretical Formulation

3.2.1 SCF Formulation of Grand Partition Function

The SCF approach has been employed to describe polymer melt interfaces in several earlier works.[24,31,131,132,212,213] Here we keep the presentation of our theoretical formulation as brief as possible, focusing mainly on novel points introduced in the present work. We consider a polymer melt whose surfaces are allowed free contact with a vapor phase. In our treatment, each one of the polymer chains is envisioned as a Gaussian thread consisting of N chemical

segments.[31] We focus on a region of total volume V occupied by polymer at temperature T, which is delimited by the free surface(s). The polymer near the surfaces is at equilibrium with a bulk polymer phase, with which it can exchange chains without restrictions. Because of this phase equilibrium, it is more convenient to work in the grand canonical ensemble. The polymer thermodynamic properties in the interfacial region of volume V at temperature T and chemical potential μN, can be fully described by the grand canonical partition function. We define μ as a chemical potential per segment, therefore the chemical potential of a chain everywhere is μN. We follow the statistical mechanical formulation developed by Daoulas et al.[24] and generalize it, following Schmid et al.[98] The interaction between polymers, which was described by a Helfand-type effective Hamiltonian,[197] is now replaced by a coarse-grained excess Helmholtz energy functional. The grand partition function described by eq 2 of Daoulas et al.[24] is rewritten as

$$\Xi = \sum_{n=0}^{\infty} \frac{1}{n!} \exp(\beta\mu N n) \tilde{N}^n \int \prod_{\alpha=1}^{n} \mathcal{D}\mathbf{r}_\alpha(\bullet) \mathcal{P}\big[\mathbf{r}_\alpha(\bullet)\big] \ \exp\big(-\beta F[\hat{\rho}(\mathbf{r})]\big) \tag{2.1}$$

where $\beta = 1/k_{\mathrm{B}}T$, k_{B} is the Boltzmann constant, and n is the number of chains in the system. $\tilde{N}$ is a normalizing prefactor which includes the contribution from integration over momentum space, and $\int \mathcal{D}\mathbf{r}_\alpha(\bullet)\mathcal{P}\big[\mathbf{r}_\alpha(\bullet)\big]$ represents the weighted sum over all chain conformations, which is a path integral in the case of continuous curves. For a given configuration, one can define the local monomer density operator

$$\hat{\rho}(\mathbf{r}) = N \sum_{\alpha=1}^{n} \int_0^1 \delta\big(\mathbf{r} - \mathbf{r}_\alpha(\tilde{s})\big)\mathrm{d}\tilde{s} \tag{2.2}$$

where $\mathbf{r}_\alpha(\tilde{s})$ is the continuous curve representing the reduced contour of a chain, from $\tilde{s} = 0$ (chain start) to $\tilde{s} = 1$ (chain end). The functional $\mathcal{P}\big[\mathbf{r}_\alpha(\bullet)\big]$ is a statistical weight for path $\mathbf{r}_\alpha(\tilde{s})$ of chain α in the absence of any field. In the Gaussian string model employed here it takes the form (compare eq 2.34):

$$\mathcal{P}\big[\mathbf{r}_\alpha(\bullet)\big] = \exp\left[-\frac{1}{4R_{\mathrm{g}}^2}\int_0^1 \left(\frac{\mathrm{d}\mathbf{r}_\alpha}{\mathrm{d}\tilde{s}}\right)^2 \mathrm{d}\tilde{s}\right] \tag{2.3}$$

where $R_{\mathrm{g}}{}^2$ symbolizes the mean squared radius of gyration of a polymer chain in the bulk and can be calculated from the following equation:

$$R_g{}^2 = C_\infty(N-1)l_{c\text{-}c}{}^2 \big/ 6 = N_K b_K^2 / 6. \tag{2.4}$$

C_∞ is the characteristic ratio for $N \gg 1$, a chemical constitution-dependent coefficient depending on local interactions along the chain, and $l_{c\text{-}c}$ is the length of chemical bond. Another way to calculate the radius of gyration is the Kuhn procedure, where the chain is mapped onto a random flight of N_K Kuhn steps, each of length b_K (compare eqs 2.86-2.89). An observant reader can easily note that, in the Gaussian model, the mean squared radius of gyration is the only characteristic conformational parameter of the polymer chain which is essential for the coarse-grained description.

We re-express the Boltzmann factor on the right-hand side of eq 2.1 in terms of a real monomer density field $\rho(\mathbf{r})$ and an energy field $w(\mathbf{r})$ by use of the inverse Fourier transform expression for a Dirac delta functional. With the field theoretic approach it is possible to replace the system of interacting chains with a system of noninteracting chains subject to a fluctuating field dictated by a generic free-energy functional representing the environment of a chain. This procedure is described in Appendix A. We define $Q[iw]$ as the configurational partition function of a single-chain subject to a field iw acting on its segments, divided by the partition function of an ideal chain. The grand partition function can then be written as

$$\Xi = C \int \mathcal{D}\rho(\mathbf{r}) \int \mathcal{D}[\beta w(\mathbf{r})] \exp\left(-\beta H[w(\mathbf{r}), \rho(\mathbf{r})]\right) \tag{2.5}$$

with

$$\mathcal{H}[w(\mathbf{r}), \rho(\mathbf{r})] = F\left[\rho(\mathbf{r})\right] - \int \mathrm{d}^3 r \rho(\mathbf{r}) iw(\mathbf{r}) - \frac{1}{\beta} \exp\left(\beta\mu N\right) \tilde{N} Z_{\text{free}} Q[iw] \tag{2.6}$$

where $Z_{\text{free}} = \int \mathcal{D}\mathbf{r}_\alpha(\bullet)\mathcal{P}\left[\mathbf{r}_\alpha(\bullet)\right]$ is the configurational partition function of a free chain.

The typical procedure of the SCF approach consists in invoking a saddle point integration with respect to w. The path integral is replaced by the value of the integrand at the corresponding saddle function in the complex plane. Frequently SCF treatments proceed further by performing a second saddle point approximation with respect to the monomer number density ρ. In Appendix A the whole procedure is described in detail. In the saddle point approximation, the effective Hamiltonian, eq 2.6, becomes

$$\bar{\mathcal{H}} = F\left[\rho(\mathbf{r})\right] - \int d^3 r \left\{ \rho(\mathbf{r}) \frac{\delta F\left[\rho(\mathbf{r})\right]}{\delta \rho(\mathbf{r})} \right\} - \frac{1}{\beta} \exp\left(\beta \mu N\right) \tilde{N} Z_{\text{free}} Q[iw] \tag{2.7}$$

From this we obtain the grand potential of our interfacial polymer

$$\Omega(\mu, V, T) = -\frac{1}{\beta} \ln \Xi = -\frac{1}{\beta} \ln \left[\exp(-\beta \bar{\mathcal{H}}) \right] = \bar{\mathcal{H}} \tag{2.8}$$

The extremization with respect to field w yields the condition (see Appendix A, eq A.38):

$$\rho(\mathbf{r}) = \exp\left(\beta \mu N\right) \tilde{N} Z_{\text{free}} \frac{Q[iw]}{\bar{n}} \langle \hat{\rho}(\mathbf{r}) \rangle \tag{2.9}$$

where $\bar{n}$ is the mean number of chains in the system. The brackets $\langle ... \rangle$ stand for statistical averages taken in a grand canonical ensemble of non-interacting chains subject to the external field iw. The approximation thus amounts to replacing the exact constraint $\hat{\rho}(\mathbf{r})$ in the fluctuating field by the more relaxed requirement $\rho(\mathbf{r}) = \langle \hat{\rho}(\mathbf{r}) \rangle$ for the mean field resulting from the saddle point approximation.

The saddle point approximation with respect to density ρ yields the field equation (see Appendix A, eq A.40):

$$w(\mathbf{r}) = -i \frac{\delta F\left[\rho(\mathbf{r})\right]}{\delta \rho(\mathbf{r})} \tag{2.10}$$

In place of the purely imaginary position-dependent field $w(\mathbf{r})$ we can use the real field $w'(\mathbf{r}) = iw(\mathbf{r})$. The effective field $w'(\mathbf{r})$ and the density $\rho(\mathbf{r})$ are associated with each other. The field $w'(\mathbf{r})$ or, equivalently, $Nw'(\mathbf{r})$, determines the density and all mean field profiles.[98]

In the derivation of SCF theory a central role is played by the restricted partition function (propagator) $q(\mathbf{r},s)$. The restricted partition function for a chain in the field $w'(\mathbf{r})$ is proportional to the probability that the segment at contour length s of the chain subject to the field finds itself at position $\mathbf{r}$, regardless of where in the system the chain may have started. It is reduced by the corresponding probability density in the bulk melt and obeys the initial condition $q(\mathbf{r},0) = 1$. The restricted partition function follows the Edwards diffusion equation for Gaussian chains (compare eq 2.46):

$$\frac{\partial q(\mathbf{r}, \tilde{s})}{\partial \tilde{s}} = R_g^2 \nabla_{\mathbf{r}}^2 q(\mathbf{r}, \tilde{s}) - \beta N w'(\mathbf{r}) q(\mathbf{r}, \tilde{s}) \tag{2.11}$$

The relation between $q(\mathbf{r}, s)$ and the single chain partition function in the presence of the field, $Q[w']$ is

$$Q[w'] = \frac{1}{V} \int d^3 r \; q(\mathbf{r}, 1) \tag{2.12}$$

The restricted partition function $q(\mathbf{r}, s)$ is related to the monomer density:

$$\frac{\bar{n} N}{V Q[w']} \int_0^1 d\tilde{s} \; q(\mathbf{r}, \tilde{s}) \; q(\mathbf{r}, 1 - \tilde{s}) = \rho(\mathbf{r}) \tag{2.13}$$

where $\bar{n} = \frac{1}{N} \int d^3 r \rho(\mathbf{r})$ is the total number of chains in the considered interfacial region. To uncover the structure and thermodynamic details of the inhomogeneous polymer problem, an integrodifferential system of equations needs to be solved. The integrodifferential system consists of the following equations: the partial differential equation, eq 2.11, the definition of the SCF, eq 2.10, and the segment balance equation, eqs 2.12 and 2.13. These must be solved numerically in the unknown propagator $q(\mathbf{r}, s)$, SCF $w'(\mathbf{r})$, and monomer density profile $\rho(\mathbf{r})$. The boundary conditions are controlled by the geometry of the problem and, as already pointed out, an initial condition $q(\mathbf{r}, 0) = 1$ is applied.[24,31,214,215]

3.2.2 Density Gradients Incorporated in the Free Energy Density

In the previous section we allowed for a generic excess Helmholtz energy functional depending on the monomer density profile $\rho(\mathbf{r})$ for the description of interchain interactions. In the current section we incorporate in this free-energy functional a square gradient term. The square gradient theory, or SGA, is a popular choice and proved to be a reliable method for predicting the microscopic and thermodynamic properties of inhomogeneous systems. SGA is based on a very simple basic conception. The interfacial monomer density profile of a pure fluid in gas-liquid equilibrium, $\rho(\mathbf{r})$, varies continuously from the bulk density of a vapor ρ_g to the bulk density of a liquid ρ_l. The Helmholtz energy is approximated by a functional Taylor expansion with

respect to the density profile, while the Taylor expansion is truncated after the quadratic term. The gradient expansion leads to a simple expression for the Helmholtz free energy of inhomogeneous systems

$$F[\rho(\mathbf{r})] = \int \left\{ f(\rho(\mathbf{r})) + \frac{1}{2}\kappa (\nabla \rho(\mathbf{r}))^2 \right\} d^3 r \qquad (2.14)$$

where $F[\rho(\mathbf{r})]$ represents the free energy (here excess Helmholtz energy relative to an ideal gas of chains) of the inhomogeneous system at temperature T and local monomer number density profile $\rho(\mathbf{r})$, the integration takes place over the entire volume V occupied by the system, and κ is the influence parameter. The first term on the right hand side within the integral corresponds to the local excess Helmholtz energy density of a homogeneous system of density equal to $\rho(\mathbf{r})$ at temperature T and the second (gradient) term incorporates a non-local correction to the excess Helmholtz energy because of the local density inhomogeneity. For all the apparent simplicity of the theory, the main difficulty lies in the definition and calculation of the influence parameter κ. It can be proven that this is related to the vertex function[216] and can be expressed in terms of the density-density correlation function. Theoretically it can be computed by its molecular definition, but the available theories for estimating its value perform poorly compared to experimental and simulation data. To circumvent this problem, one can reverse it and correlate experimental interfacial tension data with EoS parameters to figure out the value of the influence parameter. Here we wish to keep the model as rigorous as possible, while preserving its utility in predicting thermodynamic and structural observables. This led us to use the semi-empirical approach, based on a Sutherland potential, that was invoked by Poser and Sanchez with excellent results.[121] The main difference between our strategy for estimating the influence parameter and that of Poser and Sanchez[121] is that, in our case, the influence parameter is determined from the density profile derived from an atomistic molecular dynamics (MD) simulation of the free surface of molten polyethylene.

Past successes of SGA,[121,128,194,209,217] in conjunction with various EoSs, in describing surface thermodynamic properties motivated us to insert it in SCFT. Combining eq 2.14 and eq 2.10, the maximum term approximation with respect to the density field $\rho(\mathbf{r})$, based on the functional derivative of the excess Helmholtz energy F with respect to $\rho(\mathbf{r})$ leads to the following equation for the SCF:

$$w'(\mathbf{r}) = \frac{\partial f(\rho)}{\partial \rho}\bigg|_{\rho=\rho(\mathbf{r})} - \kappa \nabla^2 \rho\big|_{\rho=\rho(\mathbf{r})} \tag{2.15}$$

The expression for the grand potential by applying equation 2.14 in eq 2.7 becomes:

$$\Omega(\mu,V,T) = \int d^3r \left\{ f(\rho(\mathbf{r})) - \rho(\mathbf{r})\frac{\partial f(\rho)}{\partial \rho}\bigg|_{\rho=\rho(\mathbf{r})} - \frac{\kappa}{2}(\nabla\rho(\mathbf{r}))^2 \right\} - \frac{1}{\beta}\exp(\beta\mu N)\tilde{N}Z_{\text{free}}Q[w'] \tag{2.16}$$

3.2.3 Implementation of the Sanchez-Lacombe EoS to Calculate the Free-Energy

For a simple fluid, the homogeneous term of the excess Helmholtz energy in eq 2.14 can be derived from an EoS. In the literature different types of EoSs have been combined with SGA to investigate structural properties, thermodynamic stability and calculate interfacial tensions.[67,122,128,194,208,217–221] The SL, a lattice-based EoS with good performance in describing thermodynamic properties of polymer solutions and melts, involves three parameters. Generally, an EoS for a pure fluid relates pressure P, molecular density ρ_{m}, and temperature T. If the EoS is of the pressure-explicit form $P = P(\rho_{\text{m}},T)$ (as is the SL), the following expression gives the Helmholtz energy density A/V as a function of molecular density in the homogeneous fluid:

$$\frac{A}{V} = \rho_{\text{m}}k_{\text{B}}T\left[\ln\left(\frac{\rho_{\text{m}}\prod_i\Lambda_i^3}{Z_{\text{intra}}}\right) - 1\right] + \rho_{\text{m}}k_{\text{B}}T\int_0^{\rho_{\text{m}}}\frac{1}{\rho_{\text{m}}'}\left(\frac{P}{\rho_{\text{m}}'k_{\text{B}}T} - 1\right)d\rho_{\text{m}}' \tag{2.17}$$

In eq 2.17 Z_{intra} is the configurational integral of a single molecule over all but three translational degrees of freedom, whereas Λ_i is the thermal wavelength of atom i of the molecule; the product in the logarithmic term is taken over all such atoms. Clearly, the Helmholtz energy density for an ideal gas of molecules of the same temperature T and molecular density ρ_{m} is given by the first term on the right hand side of eq 2.17. As a result, the *excess* Helmholtz energy density relative to an ideal gas of molecules is given by:

$$f(\rho_{\text{m}}) = \rho_{\text{m}}k_{\text{B}}T\int_0^{\rho_{\text{m}}}\frac{1}{\rho_{\text{m}}'}\left(\frac{P}{\rho_{\text{m}}'k_{\text{B}}T} - 1\right)d\rho_{\text{m}}' \tag{2.18}$$

The Sanchez-Lacombe EoS is (compare eq 2.100):

$$\tilde{\rho}^2 + \tilde{P} + \tilde{T}\left[\ln(1-\tilde{\rho}) + \left(1 - \frac{1}{r_{SL}}\right)\tilde{\rho}\right] = 0 \tag{2.19}$$

where $\tilde{T}$, $\tilde{P}$ and $\tilde{\rho}$ are the reduced temperature, pressure, and density:

$$\tilde{T} = T/T^*, \quad T^* = \varepsilon^*/k_B \tag{2.20}$$

$$\tilde{P} = P/P^*, \quad P^* = \varepsilon^*/\upsilon^* \tag{2.21}$$

$$\tilde{\rho} = \frac{\rho_{mass}}{\rho_{mass}^*} = \rho_m r_{SL}\upsilon^* = \frac{\rho_{mass}}{M}r_{SL}\frac{RT^*}{P^*} = \rho\frac{r_{SL}}{N}\frac{k_B T^*}{P^*} \tag{2.22}$$

Here υ^* is the hard core volume of a Sanchez-Lacombe segment, ε^* is the attractive energy between Sanchez-Lacombe segments in adjacent sites of the lattice, while T^*, P^* and ρ_{mass}^* are the characteristic Sanchez-Lacombe temperature, pressure, and mass density, respectively. $r_{SL} = \dfrac{M}{\rho_{mass}^* N_A \upsilon^*}$ is the number of Sanchez-Lacombe segments constituting a molecule, $r_{SL}\rho_m$ is the segmental density (Sanchez-Lacombe segments per unit volume) with ρ_{mass} and M being the mass density and molar mass, respectively. As in Sections 3.2.1 and 3.2.2, ρ denotes the number density of chemical segments (monomers) and N denotes the number of chemical segments per molecule (chain length, e.g., number of methylenes and methyls, or of carbon atoms for linear polyethylene) and should be distinguished from the density in Kuhn segments or in SL segments. The quantities r_{SL} and N should be proportional to each other in a meaningful model. Equation 2.22 expresses the reduced density in terms of the segment density.

Combining eqs 2.18-2.22 leads to the excess Helmholtz energy density for a SL fluid in terms of its molecular density:

$$f(\rho_m) = -\frac{k_B T^*}{\upsilon^*}\left(\rho_m r_{SL}\upsilon^*\right)^2 + \rho_m r_{SL}k_B T\left[\left(\frac{1}{\rho_m r_{SL}\upsilon^*} - 1\right)\ln\left(1 - \rho_m r_{SL}\upsilon^*\right) + 1\right] \tag{2.23}$$

Considering eq 2.15, the excess Helmholtz energy density from eq 2.23 and bulk polymer expressions the final expressions for the SCF becomes

$$w'(\mathbf{r}) = k_{\mathrm{B}}T^* \left\{ 2\left(\frac{r_{\mathrm{SL}}}{N}\right)(\tilde{\rho}_1 - \tilde{\rho}(\mathbf{r})) - \tilde{T}\frac{r_{\mathrm{SL}}}{N}\ln\left(\frac{1-\tilde{\rho}(\mathbf{r})}{1-\tilde{\rho}_1}\right)\right\} - \kappa\nabla^2\rho\Big|_{\mathbf{r}} \tag{2.24}$$

In eq 2.21 we have used that the SCF is zero in a bulk liquid phase of equal chemical potential as our interfacial system. In that bulk liquid phase (homogeneous melt) the segment density is ρ_1 and the reduced mass density is $\tilde{\rho}_1$.

From eq 2.16, the grand potential of the interfacial system relative to a bulk phase of the same chemical potential, temperature, and spatial extent is

$$\begin{aligned}\Omega(\mu,V,T) - \Omega_{\mathrm{bulk}}(\mu,V,T) =\\ = P^*\int \mathrm{d}^3r\left\{\tilde{\rho}(\mathbf{r})\tilde{T} + [\tilde{\rho}(\mathbf{r})]^2 + \tilde{T}\ln(1-\tilde{\rho}(\mathbf{r})) + \tilde{P}_{\mathrm{s}} - \tilde{\kappa}\left(\upsilon^*\right)^{2/3}\left(\nabla\tilde{\rho}(\mathbf{r})\right)^2\right\}\\ - \frac{\rho_1 V}{\beta N}\exp\left(\beta N\frac{\partial f(\rho)}{\partial \rho}\Big|_{\rho=\rho_1}\right)Q[w']\end{aligned} \tag{2.25}$$

where $\tilde{P}_{\mathrm{s}}$ is the phase coexistence pressure at temperature T and $\tilde{P}_{\mathrm{s}} = P_{\mathrm{s}}/P^*$ and we have introduced a dimensionless influence parameter $\tilde{\kappa}$. Finally, the relation connecting the influence parameter κ in our derivation and $\tilde{\kappa}$ as described in Poser and Sanchez[121] is the following:

$$\kappa = 2\left(\frac{r_{\mathrm{SL}}}{N}\right)^2 P^*\left(\upsilon^*\right)^{8/3}\tilde{\kappa} \tag{2.26}$$

It should be noted that the influence parameter in eq 2.26 is in practice chain-length independent, because r_{SL} is proportional to chain length in the high molar mass regime, as can be seen from eq 2.22.

3.3 Models Examined

In eq 2.16 we intentionally left the field and grand potential depending on the functional of the excess Helmholtz energy density. In this chapter we examine a number of SCF models by varying the expression from which this excess Helmholtz energy density is obtained.

The first two models are based on the Helfand compressible model without (SCF_Helfand model) and with a square gradient correction term (SCF_Helfand+SGA model). The first model does not use any square gradient correction ($\tilde{\kappa}=0$), whereas in the second the gradient correction is inserted. The SCF_Helfand approximation has been used in the past at melt/solid

interfaces with remarkable success.[24,31,132] The Helfand excess free-energy density is given by the following equation

$$f(\rho(\mathbf{r})) = \frac{1}{2\kappa_T}\left(\frac{\rho(\mathbf{r})}{\rho_1} - 1\right)^2 \tag{2.27}$$

where κ_T is the isothermal compressibility and ρ_1 is the monomer density, both characterizing the bulk liquid polymer. The isothermal compressibility can be obtained from experimental data, but in this work it is calculated from the Sanchez-Lacombe EoS. It is worth mentioning that the compressibilities calculated from the Sanchez-Lacombe EoS are in excellent agreement with experiment. The compressibility for use in the Helfand model is here obtained from the following equation:

$$\kappa_T = \frac{1}{P^*\tilde{T}[\tilde{\rho}_1/(1-\tilde{\rho}_1)+1/r_{SL}]-2\tilde{\rho}_1} \tag{2.28}$$

The third SCF model we consider uses the excess Helmholtz energy density calculated by the Sanchez-Lacombe EoS (SCF_SL model). Equation 2.23 relates the molecular density with the excess Helmholtz energy density and is embedded in the SCF theory by eqs 2.24 and 2.25 without the taking into account the nonlocal gradient density term ($\tilde{\kappa} = 0$).

The fourth model we examine is the square gradient theory model of inhomogeneous systems developed by Poser and Sanchez (SGA-PS model), which is straightforwardly connected to our formulation. Poser and Sanchez used Square Gradient Theory in connection with the EOS of Sanchez and Lacombe, without an SCF treatment, i.e., without consideration of changes in chain conformation induced by the surface. We use an integrated form (eq 22 in ref 121) to calculate the density profiles for the SGA-PS model. We stress that the conformational effects introduced by the SCF treatment of the ideal Gaussian chain model are absent from the SGA-PS model.

Finally, the fifth model we consider combines SCFT with SGA, with the local excess Helmholtz energy term based on the Sanchez- Lacombe EoS (SCF_SL+SGA model). This is the most advanced model we examine, introduced for the first time in this work. The SCF felt by the chains, represented as Gaussian threads, is described by eq 2.24. The SCF_SL+SGA model encompasses entropic contributions created both by the density inhomogeneity and by the change in conformational distribution of polymer chains in the interfacial region.

Our intention in the calculations we present is to identify differences in performance between the new SCF_SL+SGA formulation and previous work, assess the importance of including surface-induced changes in the conformational distribution in the calculation, and compare model predictions with both experimental measurements and atomistic (MD) simulation results.

3.4 Calculation Details

3.4.1 Solution Method for the SCF Model

Given that a free polymer film such as the one shown in Figure 3.1 is homogenous along the xy plane and inhomogeneous along the z direction, being surrounded by gas phase in equilibrium with the polymer film on both sides, the problem can be reduced from three dimensions to one.
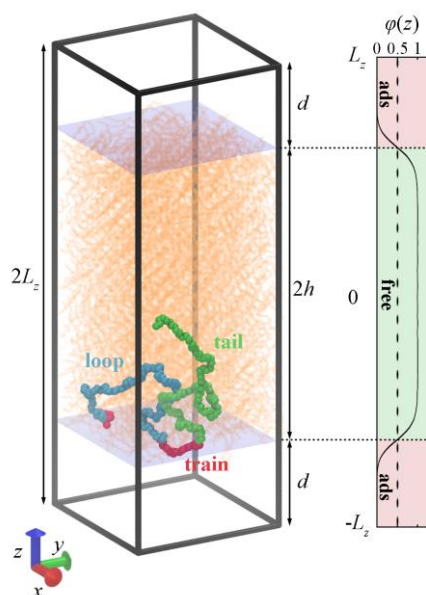
Figure 3.1. Schematic representation of the freely standing polyethylene film. The tagged chain consists of 260 CH_2 and CH_3 units extracted from a MD simulation frame. The thin orange lines outline the remaining chains in the simulation frame, to convey the picture of a field exerted on the tagged chain invoked in the SCF approach. The chain is depicted as a thread of spheres which represent segments belonging to trains (red), loops (blue) and tails (green). The simulation domain is of thickness $2L_z$ and the thickness of the film is $2h$, where h is the distance between the center of the film and the profile point where the local density reduced by the bulk liquid density becomes 0.5. The adsorption regions, of thickness d, are defined at the edges of the domain of analysis, where the liquid is in contact with gas phase. The visualization was made using VMD software.[222]

Consequently, the system domain $2\,L_z$ encompassing the film is defined in the direction z that is perpendicular to the film (L_z is the distance between the film midplane and the edge of the domain under examination).

The SCF equations, as presented in Section 3.2.3, are formulated for three-dimensional domains. For the purpose of modeling the planar film they are reduced to one spatial dimension, z. To be more definite, we collect below the SCF equations to be solved:

$$\frac{\partial q(z,\tilde{s})}{\partial s} = R_g^2 \nabla_r^2 q(z,\tilde{s}) - \beta N w'(z) q(z,\tilde{s}) \tag{2.29}$$

$$\frac{\bar{n}N}{VQ[w']} \int_0^1 d\tilde{s} \; q(z,\tilde{s}) \; q(z,1-\tilde{s}) = \rho(z) \tag{2.30}$$

$$w'(z) = \frac{\partial f(\rho)}{\partial \rho}\bigg|_{\rho=\rho(z)} - \kappa \frac{\partial^2 \rho}{\partial z^2}\bigg|_{\rho=\rho(z)} \tag{2.31}$$

$$Q[w'] = \frac{1}{2L_z} \int_{-L_z}^{L_z} dz \; q(z,1) \tag{2.32}$$

$$\frac{\bar{n}}{V} = \frac{1}{N(2L_z)} \int_{-L_z}^{L_z} dz \; \rho(z) \tag{2.33}$$

under the initial condition $q(z,0)=1$. We are investigating cases where the film thickness varies between 2 and 5 R_g so as to make comparisons with the results of atomistic simulations for films of similar thickness.[104] The molecular number bulk melt density, bulk vapor density and vapor pressure are calculated from the EOS (eq 2.19) by a Newton-Raphson scheme that equates the pressures and chemical potentials between the two phases. For high molar mass polymers the vapor pressure vanishes and the Dirichlet absorbing boundary conditions $q(-L_z,\tilde{s})=0$, $q(L_z,\tilde{s})=0$ for both sides of the film are appropriate.

The SCF eqs 2.29-2.33 are solved following a simple relaxation technique. An initial guess for the field $w'(z)$ is made (usually zero everywhere), which is then substituted into the Edwards diffusion equation. The equation is solved numerically to calculate the restricted partition function, $q(z,\tilde{s})$. Then the corresponding volume distribution of polymer, given by the monomer number density $\rho(z)$, is calculated from eq 2.30 and the resulting field $\tilde{w}'(z)$ is calculated through eq 2.31. Subsequently, new values for the field are estimated by mixing the old and the calculated field $w'^{\text{new}}(z) = (1-a_{\text{mix}})w'(z) + a_{\text{mix}}\tilde{w}'(z)$, where a_{mix} is the relaxation parameter (the fraction that we use from the calculated field in the new iteration). The

magnitude of a_{mix} is inversely related to the polymer chain length and determined empirically so that stability of the solution scheme is preserved. The field calculated by the relaxation technique serves as the field input for the next iteration. The whole procedure described above is repeated until convergence is achieved. The convergence criteria are based on monitoring the behavior of the surface tension. The iterative scheme was considered converged when the difference in surface tension between two sequential iterations was below 10^{-8} mN/m.

A central role in the above iteration scheme is played by the solution of the Edwards diffusion equation. The Edwards diffusion eq 2.29 is the most time demanding among all of the above equations to be solved. We used a Crank-Nicholson time implicit finite difference scheme to solve it with stability, which was introduced in ref 31. We take advantage of the symmetric tridiagonal matrices generated by this method to implement the tridiagonal matrix algorithm (TDMA), also known as the Thomas algorithm.[223] The solution can be obtained in $O(n)$ operations instead of $O(n^3)$ required by Gauss Elimination.

3.4.2 System Parameters -Surface Tension

The Sanchez-Lacombe parameters P^*, T^* and ρ^*_{mass} as listed in refs 224 and 225 have been used as input for all calculations reported here. The mass density values for the liquid ρ_l and gas phase ρ_g and for the equilibrium pressure P_s have been obtained from the equality of pressures and chemical potentials between gas and liquid phase based on the Sanchez-Lacombe EoS. A Newton-Raphson iteration scheme for calculating $\tilde{\rho}_g, \tilde{\rho}_l, \tilde{P}_s$ is outlined in the Supporting Information of ref 26. For high molar mass polymers, as already mentioned, the solution gives as $\tilde{P}_s = 0$ and $\tilde{\rho}_g = 0$. The isothermal compressibility κ_T needed for the Helfand model is calculated from eq 2.28. The Sanchez-Lacombe parameters used in this work are given in Table 3.1.

The influence parameter, κ, has a molecular theoretic definition related to the direct correlation function, which does not offer itself for practical calculations. We use eq 2.26, which was initially employed by Poser and Sanchez, translated to our model, to calculate the influence parameter. Use of a single reduced influence parameter $\tilde{\kappa}$ across all polymers and temperatures studied with the SCF_SL+SGA model allows us to obtain the influence parameter for each polymer based only on the parameters of the Sanchez-Lacombe EoS. Poser and Sanchez derived

the relation between the $\tilde{\kappa}$ value and the exponent n of a Sutherland-type potential, which, for the case of $n = 6$, leads to $\tilde{\kappa} = 0.5$. Poser and Sanchez obtained $\tilde{\kappa} = 0.55$ by fitting the surface tension of various polymers. Approximately the same value can be derived from eq 16 in the limit $r \rightarrow \infty$ in the work of Sgouros et al.[194] regarding a mesoscopic hybrid particle-field simulation approach to molten polyethylene surfaces.

The modified Edwards diffusion equation requires an additional quantity, namely the mean squared radius of gyration $\langle R_g^2 \rangle$. For long randomly coiled unperturbed chains, this can be calculated by eq 2.4. The characteristic ratio C_∞ depends on the nature of local interactions, dictated by the chemical details of the macromolecular chain. The temperature dependence of characteristic ratios is weak over the temperature range considered and was neglected in this work. In the literature one can find experimental and calculated values for C_∞. In this work we used experimental values, which are listed in Table 3.1.

Table 3.1. EoS Parameters and Characteristic Ratios*

polymer	T^*(K)	P^*(MPa)	ρ^*(kg/m^3)	C_∞
poly(dimethylsiloxane)(PDMS)	476	302	1104	5.8[226]
poly(vinyl acetate)(PVAc)	590	509	1283	8.6[227]
poly (n - butyl methacrylate) (PnBMA)	627	431	1125	7.9[227]
polyisobutylene (PIB)	643	354	974	6.7[228]
polyethylene (linear)(PE)	649	425	904	7.3[226]
poly(methyl methacrylate)(PMMA)	696	503	1269	8.2[226]
polystyrene (atatic) (PS)	735	357	1105	8.5[226]
poly(ethylene oxide)(PEO)	656	492	1180	5.5[226]

*Sanchez-Lacombe equation of state parameters taken from ref 224 except for PEO, where they are taken from ref 225.

The thermodynamic relation between the grand potential and surface tension for the case of a film of polymer melt bounded by gas is

$$\Omega(V,T,\mu) - \Omega_{\text{bulk}}(V,T,\mu) = \gamma S \tag{2.34}$$

where S is the total interfacial area of contact and γ is the polymer surface tension. The left hand side is calculated from the solution to the SCF model by eq 2.25, which in our one-dimensional problem reduces to

$$\left[\Omega(\mu, V, T) - \Omega_{\text{bulk}}(\mu, V, T) \right] / S =$$

$$= P^* \int_{-L_z}^{L_z} \mathrm{d}z \left\{ \tilde{\rho}(z)\tilde{T} + \left[\tilde{\rho}(z)\right]^2 + \tilde{T}\ln\left(1 - \tilde{\rho}(z)\right) + \tilde{P}_{\text{s}} - \tilde{\kappa}\left(\upsilon^*\right)^{2/3}\left(\frac{\partial\tilde{\rho}}{\partial z}\right)^2 \right\} \qquad (2.35)$$

$$- \frac{\rho_1 V}{\beta N}\exp\left(\beta N \left.\frac{\partial f(\rho)}{\partial \rho}\right|_{\rho = \rho_1} \right)Q[w']$$

Results for the surface density profile and surface tension are invariant to the precise value of L_z used (thick films) in all cases studied here.

3.4.3   MD Simulations

Our SCF findings are compared to density and conformational measures, some of which were retrieved from atomistic simulation trajectories of freely standing polyethylene films generated as in ref 104. The atomistic simulations were conducted using the Large-Scale Atomic-Molecular Massively Parallel Simulator (LAMMPS) package[229] with PE melts being described with the TraPPE united atom force field.[230,231] These simulations, in which long-range contributions to nonbonded interactions in the anisotropic environment of the film are handled with great care, have yielded predictions for the surface tension which are in excellent agreement with experiment over a variety of temperatures and chain lengths. The atomistic configurations represent thin films composed of $C_{100}H_{202}$ (C_{100}) and $C_{260}H_{522}$ (C_{260}) chains with lateral (normal) dimensions commensurate to $\sim 2\ R_{\text{g}}$ ($\sim 4\ R_{\text{g}}$). Additionally, an atomistic simulation was conducted on a $C_{520}H_{1042}$ (C_{520}) film with a thickness of $\sim 2\ R_{\text{g}}$. In-depth details regarding the MD simulations and simulated system characteristics can be found elsewhere.[104]

3.5   Results and discussion

3.5.1   Reduced Local Density Profiles

The current section deals with density profiles of polyethylene derived from field theoretic approaches and atomistic simulations. At the outset, the reduced local density profile, $\phi(z) = \rho(z)/\rho_1$ between liquid and gas phases of polyethylene at equilibrium is calculated by different methods. The SCF_Helfand and SCF_Helfand+SGA models, the SCF combined with the Sanchez-Lacombe equation of state without (SCF_SL) and with gradient correction (SCF_SL+SGA), and the Poser-Sanchez (SGA-PS) model are all compared to atomistic simulations (MD). The density profiles are shifted, so as to have the 0.5 point of the reduced

density profile for every model at the same position (10 Å). The reader can observe the difference among the sigmoidal curves that different models generate for the free surface of a C_{260} polyethylene melt at 450 K in Figure 3.2. Although plotting out the profiles reveals the structure and the exact shape of the curve produced by every model, it is more convenient to work with the surface thickness. The thickness of the profile can be quantified by two techniques. The first one is based on fitting the curve to a hyperbolic tangent sigmoid profile, given by:

$$\varphi(z) = \frac{1}{2}\left[1 - \tanh\left(2\frac{z-h}{w_{th}}\right)\right]$$ (2.36)

where w_{th} is the measure of the thickness of the sigmoidal curve and h is the value of z where the reduced density ϕ reaches 0.5. The second strategy for quantifying the surface thickness is based on drawing the tangent to the reduced density profile curve at $z = h$ and measuring the distance along the z direction between the intersections of this tangent with the lines $\phi = 0$ and $\phi = 1$. The estimate of the thickness is given by the following equation:

$$d_{th} = \frac{dz}{d\varphi}\bigg|_{\varphi(z)=0.5}$$ (2.37)

It is worth mentioning that when the profile follows the hyperbolic tangent, eq 2.36, exactly, then $d_{th} = w_{th}$. Division of these two estimates of the width by each other produces a factor $\lambda = w_{th}/d_{th}$ which is a measure of how well the reduced density profile can be fitted to a symmetric hyperbolic tangent curve described by eq 2.36. The λ value for symmetric curve is equal to 1. The values of λ, w_{th} and d_{th} are shown in Table 3.2.

The Gaussian chain model with the free-energy density given by the Helfand harmonic potential and no square gradient correction (SCF_Helfand) yields a very steep (thickness ~2 Å) and asymmetric (λ=0.936) profile. The SCF model with the field given by the more sophisticated Sanchez-Lacombe EoS (SCF_SL) gives a smoother profile than the Helfand model, with the low density tail more extended. The SCF_SL model is very symmetric ($\lambda = 0.983$), nonetheless the thickness of the profile is very small, below ~4 Å. Both of these profiles are unrealistic in comparison to the atomistic simulation profile, characterized by a

width of ~8 Å. This implies the necessity of the square gradient correction term. The gradient correction makes the profile wider and the profile gradient smoother.

Table 3.2. Thickness of the Reduced Density Profile Calculated by Two Different Methods for the Free Surface of a C_{260} Polyethylene Melt at 450 K According to Different Models and According to Molecular Simulation[a]

	thickness measure		
model	d_{th}(Å)	w_{th}(Å)	λ
SGA-PS	7.65	7.09	0.927
SCF_SL	3.69	3.63	0.983
SCF_SL+SGA	8.47	8.00	0.944
SCF_Helfand	1.99	1.86	0.936
SCF_Helfand+SGA	4.54	4.73	1.042
MD	8.13	7.90	0.971

[a]The factor λ is a measure of deviation of the profile shape from a hyperbolic tangent curve.

The reduced influence parameter $\tilde{\kappa}$ for the SCF_SL+SGA, SCF_Helfand+SGA and SGA-PS model was kept the same, equal to 0.55. This choice of the reduced influence parameter was made so that SCF_SL+SGA closely matches the atomistic density profile. Beginning with the SCF_Helfand+SGA model, although the interfacial width changes noticeably relative to the SCF_Helfand model, attaining a value of ~4.5 Å, it is still too small compared with atomistic simulation. The profile shape is quite different from that of MD, as evidenced from its λ value. The Poser-Sanchez model (SGA-PS) produces a profile of acceptable width of ~7 Å, but its asymmetry ($\lambda = 0.927$) is the highest among those of all models examined and clearly too high in comparison with the MD profile. The SGA-PS model yields a somewhat narrower profile than the ones obtained from SCF_SL+SGA or from atomistic simulation. The SCF_SL+SGA model is in very good quantitative agreement with the one obtained from the atomistic simulations, exhibiting an interface width ~8 Å and reasonable asymmetry. The Poser and Sanchez density profile departs from simulation results in the low-density region at the extremities of the film. It does not account for the restrictions that polymer chain conformations experience near surfaces, while the SCF_SL+SGA approach incorporates entropic changes associated with these restrictions. It would be worth noting that, even though all models are tested with the same value for the influence parameter $\tilde{\kappa} = 0.55$, optimized $\tilde{\kappa}$ values cannot reproduce precisely the full MD profiles, nor give fully satisfactory estimates of the surface

tension. The "best" $\tilde{\kappa}$ values for the SCF_Helfand+SGA and SGA_PS models in terms of reproducing the density profiles are 0.6 and 1.3, respectively.
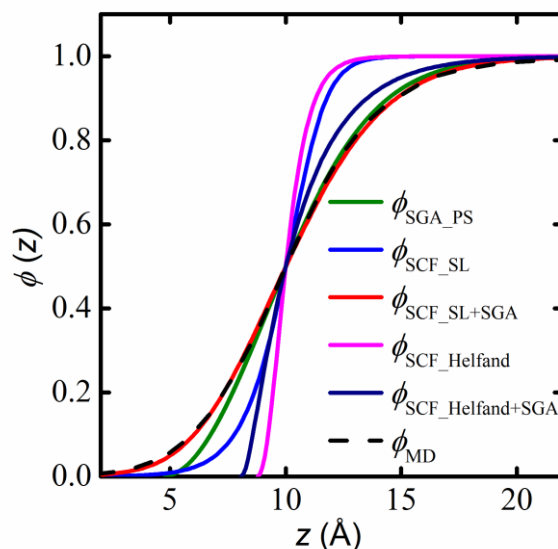
Figure 3.2. Local reduced density profiles obtained from theoretical models (lines) compared to that obtained from MD simulations (dashed line) for the free surface of a C_{260} polyethylene melt at 450 K. The reduced density profile of the SGA proposed by Poser and Sanchez (green), of the Helfand SCF compressible model without (magenta) and with (navy blue) square gradient approximation and the SCF with the free energy dictated by the Sanchez-Lacombe EoS with (red) and without (blue) gradient correction is discussed in the text. The profile coordinate where the reduced density becomes equal to 0.5 coincides for all models.

In Figure 3.3a we show the reduced density profile obtained from the SCF_SL+SGA calculations, for the C_{100} PE free film (FF) system at various temperatures. The Gaussian chain profiles and MD profiles are referred to the same thickness of the free film, with $z = 0$ located in the middle of the film. The vertical dashed line indicates the center of the free film, where the polymer reaches the bulk liquid density ρ_l, while the right and left boundaries of the film show the contact with the gas phase, where the bulk density reaches practically zero. The horizontal dashed line designates the points where the reduced density equals 0.5. The film thickness is defined as the distance between these points, and ranges from 4 R_g (400 K) to 4.5 R_g (500 K). In the MD simulation the system mass is kept constant; therefore, the film thickness increases with increasing temperature because of thermal expansion. To relate the conformational properties of the SCF method and MD, the film center will be held constant. It is apparent from Figure 3.3(a) that SCF with the gradient correction term follows quite faithfully the density profile produced by the atomistic simulations. With decreasing temperature, the profile becomes steeper. The

SCF reproduces the decrease in slopes of the profiles obtained by atomistic simulation in detail, across the entire temperature range studied.
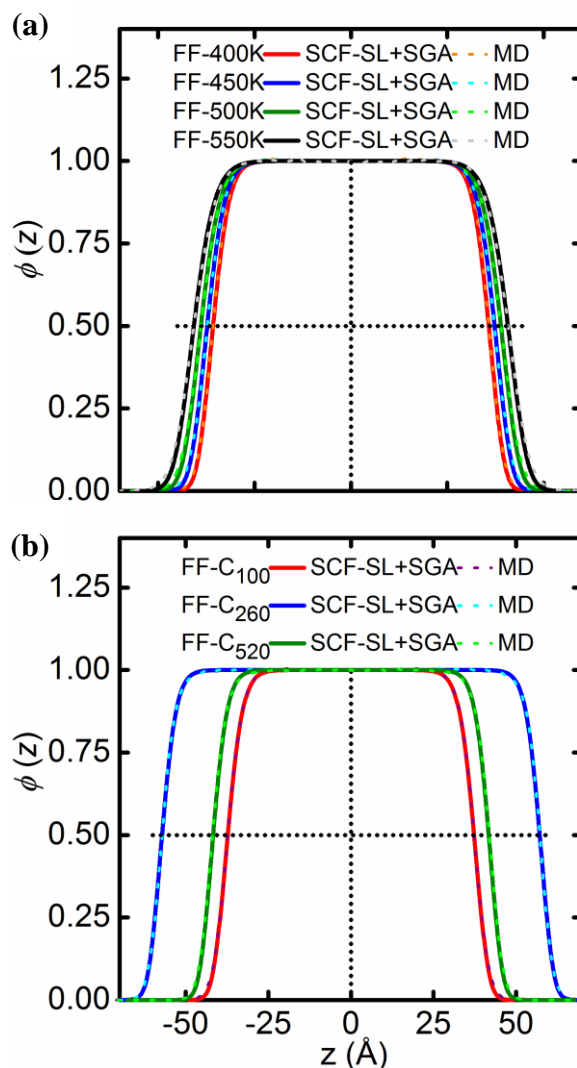
Figure 3.3. Reduced density profiles of freestanding polyethylene films at various temperatures for various chain lengths. **(a)** Results obtained for C_{100} from 400 K up to 550 K with a step of 50 K. The SCF approach combined with Sanchez-Lacombe and the SGA (lines) is compared with atomistic simulations (dashed lines). Each color refers to a different temperature. **(b)** Results for C_{100} (red), C_{260} (blue) and C_{520} (green) at 450 K from SCF (lines) and atomistic simulations (dashed lines). The vertical dotted lines indicate the center of the film and the line segments defined by the intersection of the horizontal dotted lines with the reduced density profiles are commensurate to the thickness of the films.

Another interesting comparison between the SCF_SL+SGA approach and detailed atomistic simulation concerns the change in reduced density profiles with chain length. In Figure 3.3b the reduced density profile obtained from the SCF_SL+SGA calculations is shown for the C_{100}, C_{260} and C_{520} PE free film (FF) system at the same temperature (450 K). The width of the interfacial region decreases very slightly with increasing chain length. Figure 3.3 undoubtedly

shows that there is an expansion of the interface region with increasing temperature, while an increase in chain length practically has no effect over the range of chain lengths examined here. Again we observe that the profile created from SCF_SL+SGA model matches the MD model very well.

3.5.2 End and Middle Segment Distributions

This section deals with the structure of segment profiles in more detail. The chain end segment distribution plays a major role for conformational, dynamic and thermodynamic properties, as Chevalier et al. have revealed.[232] Segregation of different segments along the chain has been shown by Jang et al.[195] to influence the configurational properties of freely standing films. It has been found that repulsive ($\varepsilon_{end} < \varepsilon_{middle}$) or neutral ($\varepsilon_{end} = \varepsilon_{middle}$) chain end groups tend to accumulate near the fluid−vacuum interface, while strongly attractive ones tend to reside in the bulk region and induce faster dynamics in the central region of the films. It is of interest, therefore, to examine if SCF_SL+SGA predictions for the end and middle segment populations at gas−liquid interfaces are consistent with atomistic simulations and how these populations depend on temperature and molar mass.

Generally the average density $\rho_s(\mathbf{r})$ at position $\mathbf{r}$ of chain segments lying at reduced contour length $\tilde{s}$ (the chain start being $\tilde{s} = 0$ and the end $\tilde{s} = 1$) along a continuous Gaussian thread is obtained as follows. Segment $\tilde{s}$ is envisioned as the junction of a chain section of reduced contour length $\tilde{s} = 0$ with the complementary chain section having contour length $1 - \tilde{s}$. The reduced density of these segments is therefore proportional to the product of the propagators of the two chain sections:

$$\varphi_{\tilde{s}}(\mathbf{r}) = \frac{\rho_{\tilde{s}}(\mathbf{r})}{\rho_{\tilde{s},\text{bulk}}} = \frac{\bar{n}N}{VQ[w']\rho_{\tilde{s},\text{bulk}}} q(\mathbf{r},\tilde{s})q(\mathbf{r},1-\tilde{s}) \tag{2.38}$$

The middle segment reduced density $\varphi_{\text{middle}} = \varphi_{1/2}$ is calculated by setting $\tilde{s} = 1/2$ and $\rho_{1/2,\text{bulk}} = \rho_1/N$. The reduced density of a chain end segment is a case of particular interest.[131] In the homopolymer case the ends are indistinguishable and therefore the total chain end segment density can be calculated as a sum of the first and last segment density $\rho_{end} = \rho_0 + \rho_1$ (see also eq 2.56). The reduced end segment density φ_{end} can be obtained by dividing at every point the

end segment density by $\rho_{end,bulk} = \rho_{0,bulk} + \rho_{1,bulk} = 2\rho_1 / N$. The bulk reduced density for both end and middle segments equals unity.
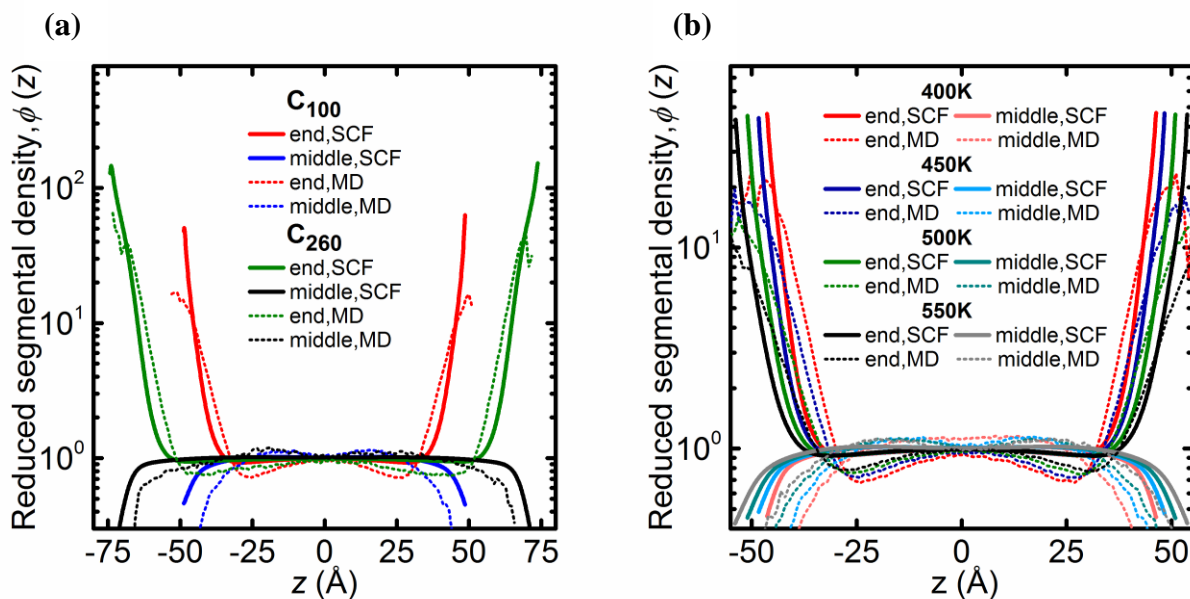
Figure 3.4. Profile of the reduced end segment and middle segment distributions **(a)** Profiles of the reduced end segment density and the reduced middle segment density in free films of molten polyethylene composed of chains of 100 (ends: red, middle: blue) and 260 (ends: green, middle: black) skeletal carbon atoms at 450 K. Solid lines show results from the SCF_SL+SGA approach, while dashed lines show the corresponding results from atomistic MD simulation. **(b)** Profile of the reduced end segment and middle segment distributions, for free films of molten polyethylene composed of chains of 100 skeletal carbon atoms at various temperatures (400-550 K). Solid lines: SCF_SL+SGA results, dotted lines: MD simulation results.

Figure 3.4a shows the comparison between the reduced density profiles of the end segments and the middle segments for freely standing PE films consisting of C_{100} and C_{260} chains at $T = 450$ K. Figure 3.4b shows the reduced density profiles of films composed of C_{100} chains over a temperature range, from $T = 400$ K to $T = 550$ K. Results from the SCF_SL+SGA approach are compared with the corresponding results from atomistic simulations. In the atomistic simulations the chain ends and middle segments were represented with the same Lennard-Jones parameters and the thickness of the films was set to 4 R_g. Even though we treated both end and middle monomers as not differing chemically, nonetheless we found, as expected,[104,131,195] near the surfaces of the film the population of end groups to be significantly enhanced with an effective selective attraction of end groups to the surface due solely to chain connectivity. The SCF_SL+SGA model end segment profiles generally agree well with those from detailed atomistic simulation qualitatively and quantitatively. The weak depletion of chain ends observed in the atomistic simulations deeper in the film is not well reproduced by the SCF

calculation, probably because the local conformational stiffness of chains is not captured by the Gaussian thread model invoked by SCF. In general, the SCF model's end segment density profile seems to rise more steeply than the MD model profile at the extreme edges of the film. The performance of the SCF model improves with increasing molar mass of the melt, as one would expect, because the Gaussian thread model is primarily a model for high molar mass chains.

The reduced density of the middle segments is lower than that of end segments at the edges of the film by about 2 orders of magnitude. The SCF model yields broader and steeper reduced middle segment density profiles compared to MD. This overestimation is seen in both the temperature and chain length dependence. This difference is clearer in the small molar mass polymer system and appears to be less pronounced for the higher molar mass system. Again, it seems to be associated with local stiffness effects which are not fully represented by the Gaussian thread model and are most pronounced for low molar masses. The expectation is that in higher molar mass systems the SCF model will be more accurate in predicting the middle segment profile. Even though the SCF model is not appropriate for low molar mass systems, it seems to capture the tendencies for segregation of end segments and middle segments in good agreement with atomistic simulation. In both approaches as applied to polyethylene, there is no enthalpic profit to be gained by end segments when they are exposed to the surfaces instead of a bulk region of the same density.[107,195]

3.5.3   Structure of Adsorbed Polymer Layer

Entire polymer chains in the free film can be distinguished into "adsorbed" and "free," depending on whether they have segments in the low-density surface regions. It is useful to check whether the SCF_SL+SGA model can capture this distinction as observed in atomistic simulations. Comparisons between SCFT and atomistic simulation regarding the segment density profiles of free and adsorbed chains and of the various parts (trains, loops, and tails) in which adsorbed chains can be partitioned according to their configuration relative to the surfaces have been conducted by Daoulas et al.[24] at polymer melt/solid interfaces. Sgouros et al.[104] conducted MD simulations of freely standing films and distinguished the adsorbed chains into 4 categories depending on the positions of their ends relative to the free surfaces. They treated as "adsorbed" a segment at the liquid-vacuum interface if it lay in a certain region. The definition of this region where a segment and, more generally, a molecule is considered as "absorbed"

plays a fundamental role in the calculation. At solid-liquid interfaces the region of adsorbed segments is defined so as to contain only the first peak of the density profile next to the solid (see ref 24). At the gas-liquid interface, following ref 24, we will consider as "adsorbed" all segments lying at a distance larger than h from the center of the film along the z direction (see Figure 3.1, domains of thickness d). Both in SCF and molecular dynamic calculations, a monomer-segment is defined as adsorbed when it finds itself within this low-density region of the gas/ polymer interphase. In this way it is ensured that both field theoretic and atomistic representations employ the same characteristic length for identifying adsorbed segments. As in sections 3.5.1 and 3.5.2, the film midplane will be placed at $z = 0$ and comparisons will be made between films of the same thickness for freely standing films composed of C_{100} and C_{260} polyethylene chains.

The reduced volume fraction profile of segments belonging to adsorbed molecules, $\varphi_{ads}(z)$, is obtained after decomposing the Gaussian chain propagator, $q(z, \tilde{s})$ in two parts, q_{ads} and q_{free}, representing the two states of the polymer chain, adsorbed and free, respectively.[233] The q_{free} propagator is calculated from the Edwards diffusion equation using the self-consistent field of the converged solution with initial conditions $q_{free}(z,0) = 1$ for $|z| \leq h$ and $q_{free}(z,0) = 0$ for $h < |z| < L_z$ and boundary condition $q_{free}(\pm h, \tilde{s}) = 0$. The q_{ads} part is easily obtained after subtracting from the total propagator $q(z,s)$ the term corresponding to the free state of chains, $q_{ads} = q - q_{free}$. The reduced segment density profile of the free, $\varphi_{free}(z)$, and the adsorbed polymer can be obtained from:

$$\varphi_{free}(z) = \frac{\bar{n}N}{VQ[w']\rho_1} \int_0^1 q_{free}(z,\tilde{s}) q_{free}(z, 1 - \tilde{s}) \mathrm{d}s \tag{2.39}$$

$$\varphi(z) = \varphi_{ads}(z) + \varphi_{free}(z) \tag{2.40}$$

We can now separate the adsorbed segments into loops, trains and tails, following their traditional definitions.[24,233,234] A train is a chain section consisting exclusively of adsorbed segments and bounded by free segments, whereas a tail is a terminal section consisting exclusively of free segments and terminating in an adsorbed segment. A loop, on the other hand, is an internal chain section consisting of free segments and terminating in adsorbed segments. In
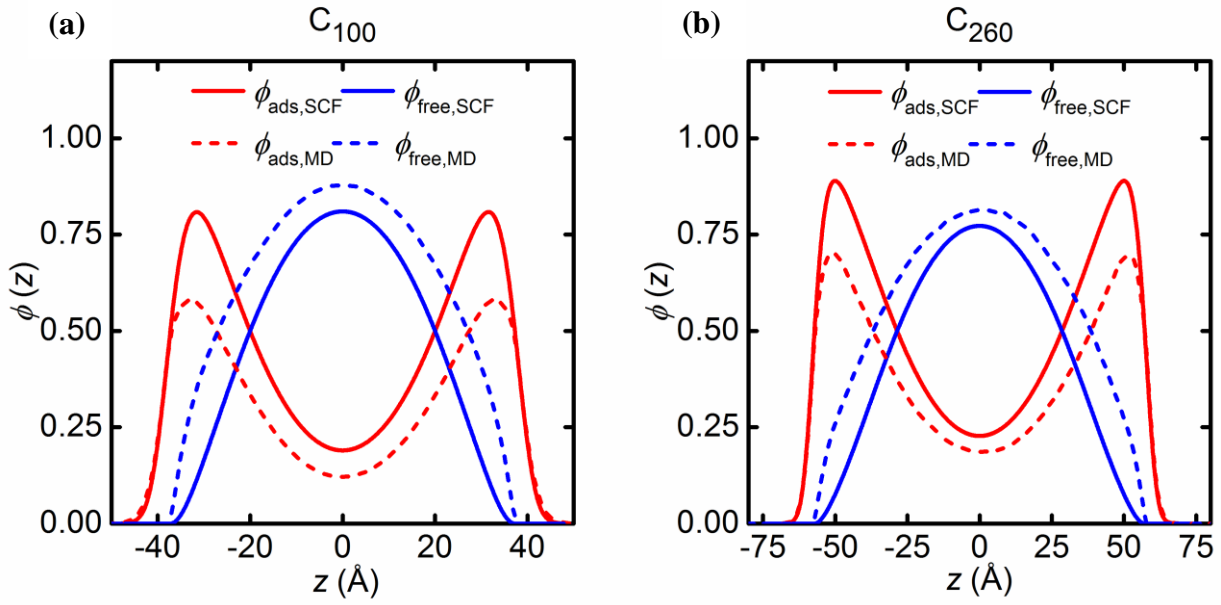
Figure 3.5. Volume fraction profiles of segments belonging to adsorbed and free chains (presented with red and blue color respectively) as derived by SCF theory implementing the Sanchez-Lacombe excess free-energy density combined with the square gradient approximation for freely standing films of **(a)** C_{100} and **(b)** C_{260} melts. The dashed lines display the corresponding atomistic simulation results.

the SCF formulation, a segment belonging to a loop is viewed as the junction point of two adsorbed subchains.

$$\varphi_{\text{loop}}(z) = \frac{\bar{n}N}{VQ[w']\rho_1} \int_0^1 q_{\text{ads}}(z,\tilde{s}) q_{\text{ads}}(z,1-\tilde{s}) d\tilde{s} \qquad (2.41)$$

A segment belonging to a tail, on the other hand, is viewed as a junction point between a free and an adsorbed subchain:

$$\varphi_{\text{tails}}(z) = \frac{2\bar{n}N}{VQ[w']\rho_1} \int_0^1 q_{\text{free}}(z,\tilde{s}) q_{\text{ads}}(z,1-\tilde{s}) d\tilde{s} \qquad (2.42)$$

where the factor of 2 takes care of the presence of two ends.[233] In polymer films it is possible to encounter segments belonging to "bridges", i.e., chains adsorbed on both surface regions, which span the film. Here the thickness of the film is large enough for the presence of bridges to be insignificant.

Figure 3.6 illustrates the $\varphi_{\text{tails}}(z)$ (and $\varphi_{\text{loops}}(z)$) profiles as obtained from atomistic simulations and calculated from eqs 2.41 and 2.42 for the SCF_SL+SGA model for the C_{100} and C_{260} melts. By definition the adsorbed chain profile contains tail, loop, and train distributions; for this reason the adsorbed profile of SCF seems to contain cumulatively more loops and tails
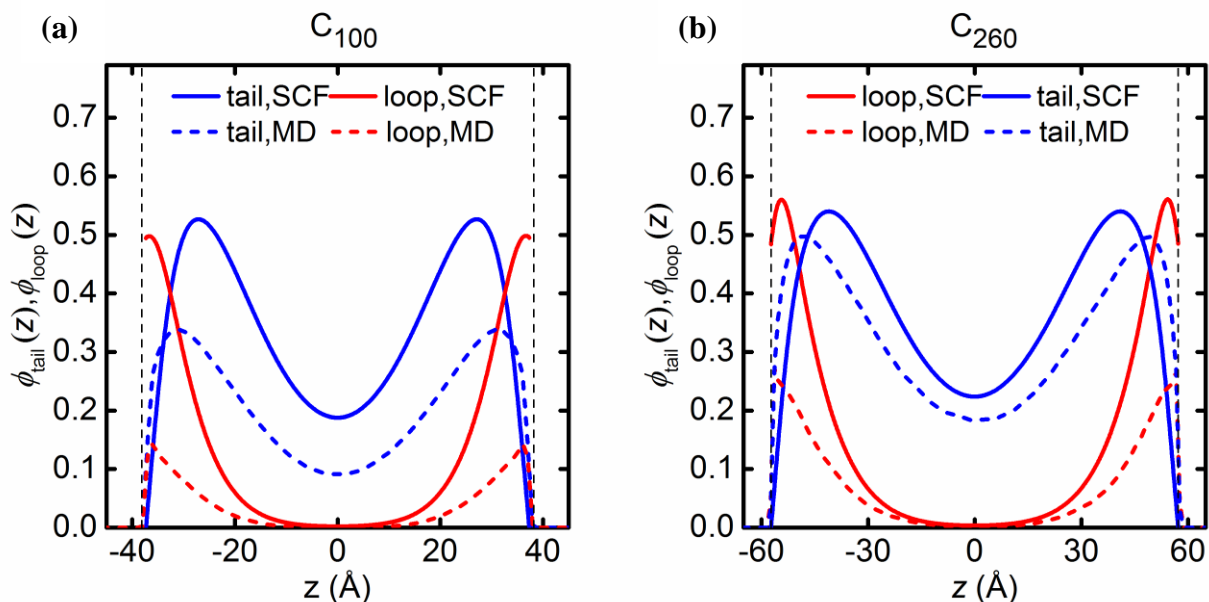
Figure 3.6. Volume fraction profiles of segments belonging to tails $\varphi_{\text{tails}}(z)$, and loops, $\varphi_{\text{loops}}(z)$, as derived by the SCF_SL+SGA approach (solid line) implementing the Gaussian thread connectivity model for **(a)** C_{100} and **(b)** C_{260} melts. The dashed lines show the corresponding atomistic simulation results for the tails and loops, respectively. The vertical, thin dashed line marks the boundary of the region where the polymer is considered as adsorbed for both SCF and atomistic model simulations.

than atomistic simulations, because they add up to a greater amount of adsorbed chains according to Figure 3.5. In the C_{100} system the loop reduced density profile reaches 0.49 (0.14), while the tail reduced profile for the same chain length exhibits a maximum at 0.53 (0.34) according to the SCF calculation (atomistic simulation, respectively). In the C_{260} system the loop-reduced density profile reaches 0.56 (0.27), whereas the tail-reduced profile has a maximum at 0.54 (0.50) according to the SCF (atomistic simulation) and the minimum in the middle of film differs between the two calculations 0.23 (0.19). The atomistic simulation yields a loop profile which increases significantly from C_{100} to C_{260}, indicating an expected tendency for longer chains to form more loops. In the SCF model the maximum in the loop profile does not increase at the same rate from C_{100} to C_{260}, implying a convergence between the SCF model and atomistic simulations for very long chain PE. It is apparent that, with increasing chain length, the correspondence of loop and tail profiles between the SCF approach and atomistic MD becomes more reliable. This trend is expected to improve further as the molecular weight increases further and the chain can be represented better by a Gaussian connectivity model. The tail-reduced segment profiles obtained from the SCF calculation and MD simulation in the case of the C_{260} system are quite close, whereas for the C_{100} system there is considerable disparity. The degree of agreement gives the impression that it does not depend on the film thickness. We

remind the reader that for both C_{100} and C_{260} the film thickness is $\sim 4R_g$ ($\sim$75 and $\sim$114 Å, respectively).

3.5.4   Chain Shape Profiles

The presence of the gas/liquid interface affects the global chain conformational characteristics in the liquid state. The orientation and intrinsic shape of chain segment clouds in the various parts of the interphase depart from those in the bulk melt. The motivation for exploring these chain conformational properties as a function of the molecular structure is that they are intimately connected to macroscopic thermodynamics and dynamics. Theodorou introduced a method to calculate the number of chains passing through a surface drawn parallel to the interface anywhere within the film.[235] The methodology, originally developed for a lattice fluid SCF model, was extended by Daoulas et al. and implemented in the continuous Gaussian thread model to calculate the number of chains per unit surface passing through a plane at z_0 parallel to the interface.[24] Based on these two approaches, we calculate the probability that a chain starting anywhere in the system will intersect a given plane at z_0. From this we obtain the average number per unit surface of chains passing through that plane.

The probability p_{int} of a chain that started anywhere in the system to intersect a given plane at z_0 is equal to the complement of the probability that the chain does not intersect the given plane. Calculation of the latter can be translated into imposing the Dirichlet boundary condition $q = 0$ at the dividing plane at z_0, splitting the domain into two regions; solving the Edwards diffusion equation in the two separate subdomains $z < z_0$ and $z > z_0$ using the converged $w(z)$, and thus obtaining the q_{shape,z_0} propagator for chains that do not intersect the plane. The probability p_{int} can be evaluated by the following equation:

$$p_{\text{int}}(z_0) = 1 - \frac{\int_{-L_z}^{z_0} q_{\text{shape},z_0}(z,1)dz + \int_{z_0}^{L_z} q_{\text{shape},z_0}(z,1)dz}{\int_{-L_z}^{L_z} q(z,1)dz} \tag{2.43}$$

The numerator on the right hand side is written in this way to emphasize that the plane perpendicular to z_0 is not contained in the integral. After evaluating the probability p_{int} we can

obtain the number of chains $n_{ch}(z_0)$ that intersect the plane at z_0 per unit surface by multiplying p_{int} by the total number of chains in the system:

$$n_{ch}(z_0) = p_{int}(z_0)\frac{1}{N}\int_{-L_z}^{L_z}\rho(z)dz \qquad (2.44)$$

Working with a variety of z_0 values we derive, through eq 2.44, $n_{ch}(z)$, a conformation-dependent quantity readily obtainable from the SCF_SL+SGA model, which allows us to make direct comparisons with atomistic simulations. Figure 3.7 displays the profile of $n_{ch}(z)$ from the SCF_SL+SGA model and MD simulations. For comparing the two models, the profile for each
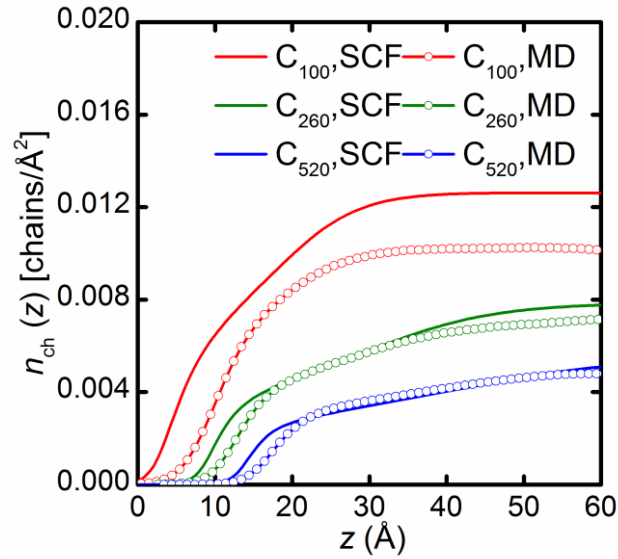
Figure 3.7. Profile of the average number of chains per unit surface that intersect a plane at z, $n_{ch}(z)$, from SCF_SL+SGA model (solid lines) and MD (lines with points) for C_{100} (red) C_{260} (green) and C_{520} (blue). The MD and SCF profiles have been shifted so that their reduced density profiles align at ϕ=0.5.

chain length is shifted so that the reduced density profiles are aligned at $\varphi = 0.5$. Overall, $n_{ch}(z)$ from SCF_SL+SGA is in good qualitative agreement with MD, both of them exhibiting a reduced number of chain intercepts in the vicinity of the free surface and saturating to a bulk value in the bulk regions of the films. The saturated bulk value obtained for C_{100} from SCF_SL+SGA is considerably higher than the one computed from MD; similar behavior has been reported by Daoulas et al.[24] Nevertheless, with increasing chain length the correspondence

between SCF and MD improves. Moreover, there is a significant deviation between MD and SCF_SL+SGA at the extremities of the interface, because the latter overestimates n_{ch}.

An additional quantity for assessing the orientation and intrinsic shape of chains is the chain shape profile, $n_s(z)$, which measures how many times, on average, a chain passing through a plane parallel to the interface at z intersects that plane. This quantity was introduced by Theodorou for a lattice model.[54] In this work we derive this quantity for the continuum model as follows. By inverting n_{ch} we obtain the average surface area occupied in plane z_0 by a chain passing through that plane, $a_{ch}(z_0) = 1/n_{ch}(z_0)$, which assumes an asymptotic value in the bulk melt. Multiplying a_{ch} by the density of segments and by a height per segment, we have an estimate of the mean number of segments that a chain passing through a plane at z occupies on that plane; in other words, the mean number of intersections of the chain contours with a considered z-plane. We form the quantity $n_s(z)$, which gives us an idea of the average chain shape profile along the z axis:

$$n_s(z) = \rho(z) a_{ch}(z) \Delta l \left(\frac{N-1}{N} \right) = \frac{\phi(z) \rho_1 \Delta l}{n_{ch}(z)} \left(\frac{N-1}{N} \right) \qquad (2.45)$$

In eq 2.45 Δl is the average projection on the z-axis of the distance connecting two segments, taken here as $\Delta l = l / 2$, with l being the chemical bond length, because ρ counts chemical segments per volume. The factor $(N-1)/N$ is the ratio of the number of bonds to the number of segments in the system. We apply it because we wish $n_s(z)$ to count intersections per chain going through the z-plane, rather than segments per chain going through the z-plane. We will call $n_s(z)$ the average "width" of chains going through the z-plane. A high value of $n_s(z)$ signifies a tendency for chains at z to extend flat in directions parallel to the surface, while a low value of it indicates that chains are oriented normal to the surface. The chains per area passing through a surface $n_{ch}(z)$ and the reduced density $\phi(z)$ can be calculated easily by eqs 2.44 and 2.30, respectively. Regarding the factor $\rho_1 \Delta l(N-1)/N$, Δl is not readily accessible from the SCF approach. However the need for the quantity Δl can be circumvented by considering the reduced chain shape with respect of the chain shape in the bulk $n_{s,bulk}$.
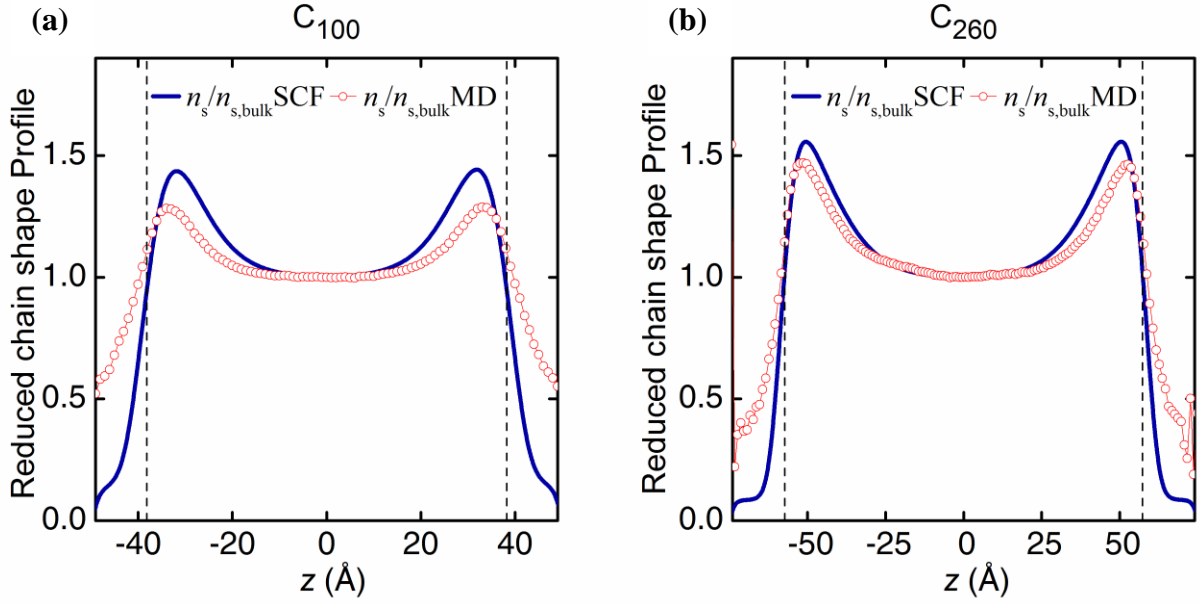
Figure 3.8. Reduced chain shape profiles $n_s (z)/ n_{s,bulk}$ as derived by the SCF_SL+SGA model (blue lines) for polyethylene free films consisting of (**a**) 100 and (**b**) 260 carbon atoms. The temperature is 450 K. The red open circles symbols show the corresponding MD results. The dashed lines indicate the position where the polymer density equals half of its bulk density.

Figure 3.8 illustrates the reduced chain shape profiles, $n_s(z)/ n_{s,bulk}$, for free molten polymer films of C_{100} and C_{260}, compared directly with the corresponding results from atomistic simulation. Taking into consideration the above analysis, the low values of $n_s(z)$ observed in the graphs of Figure 3.8 in the vicinity of the free surface betray a tendency for chain ends to protrude from the melt into the gas region, terminal segments adopting a predominantly normal orientation to the interface. As we move towards the center of the film, the chain width $n_s(z)$ increases, with chain segment clouds tending to orient flat on the surface. The chain width goes through a maximum and then decays to its asymptotic bulk melt value.

Generally, agreement between SCF theory and simulation as regards the chain width is very satisfactory. SCF tends to produce narrower chain width profiles than the simulation, which fully includes local chain stiffness and fluctuations. An evident discrepancy between SCF_SL+SGA and MD is that the first predicts a lower number of z-plane chain intersections in the low-density region of the interface. This behavior is strongly correlated to the profiles n_{ch} in Figure 3.7, where the chains per area—which are inversely proportional to n_s—according to by SCF_SL+SGA are much more than that according to MD at the interfaces. Over the remaining domain SCF_SL+SGA predicts higher chain widths. This shortcoming is intrinsic to the

Gaussian string model, the chains being fully flexible and thus allowing for a larger number of chain intersections along z-planes. Although the locations of maxima of the reduced chain shape profiles compare well between SCF_SL+SGA and MD, the ones from MD are closer to the gas/liquid interfaces. It is clear in Figure 3.8 that the agreement between SCF_SL+SGA and atomistic simulations again improves with increasing chain length.
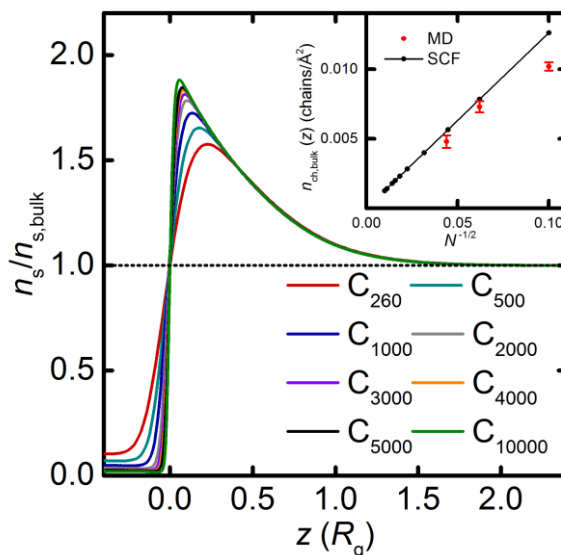
Figure 3.9. Reduced chain shape profiles from SCF_SL+SGA for various chain lengths varying from 100 to 10000 monomers per chain. Each chain length is represented by a different color. The MD and SCF profiles have been shifted so that their reduced density profiles align with ϕ=0.5 at $z = 0$. The inset displays the dependence of $n_{ch,bulk}$ on the inverse square root of the chain length according to the SCF_SL+SGA model (circles) and according to atomistic MD (diamonds).

Figure 3.9 depicts the profile of the reduced chain width over a broad range of chain lengths, with the distance z reduced by the bulk radius of gyration for each chain length. As already seen in Figure 8, the chain width features a pronounced peak near the interface, indicating high chain flattening in this region. The position of the peak is chain length independent and is located at ~15 Å from the extremities of the films. Upon moving towards the bulk region of the film the pronounced peak decays and the reduced chain shape saturates to its bulk value corresponding to chains of unperturbed shape and random orientation. Clearly, the characteristic length for the decay is influenced by the degree of polymerization, being proportional to the radius of gyration R_g (note that the abscissa is in R_g units). More specifically, in all cases examined here the distance between the position where ϕ=0.5 and the point where the profile saturates to unity equals ~ $1.6R_g$. In the inset of Figure 3.9 is displayed

the average number of chains passing through a plane positioned in the bulk liquid region of the film (e.g., the film midplane) against the inverse square root of the chain length, $N^{-1/2}$. A perfect linear correlation is seen in the SCF_SL+SGA results, characteristic of unperturbed, randomly oriented conformations. The MD deviates from the linearity for small chain lengths but comes very close to the SCF_SL+SGA estimates, both in slope and in actual values, for high molecular weights, underlining the increasing validity of the Gaussian approximation with increasing chain length.

3.5.5 Surface Tension of Various Polymers

As pointed out above, the reduced influence parameter $\tilde{\kappa}$ for use with the SCF_SL+SGA approach was obtained by fitting the atomistic simulation density profile of polyethylene films composed of C_{100}, C_{260} and C_{520} chains. At these chain lengths, altering the chain length has small impact on the density profile. We use the same reduced influence parameter ($\tilde{\kappa} = 0.55$) to perform calculations for higher molecular weight polyethylenes and for polymers of different chemical constitution for any chain length and temperature. In this section we utilize the SCF_SL+SGA approach to calculate the surface tension of various polymer melts. Poser and Sanchez fitted their theory (SGA_PS) to experimental surface tension data, obtaining the same reduced influence parameter as we use. The role of the reduced influence parameter is central, as it treated as a universal parameter for all chemical constitutions and is the sole interface-related parameter in the SCF_SL+SGA approach. (The remaining, chemical constitution-dependent parameters are T^*, P^*, ρ^* of the SL EoS and the characteristic ratio is C_∞, all are listed in Table 3.1).

In Table 3.3 is shown the surface tension for polymer melts as predicted by the SCF_SL+SGA with reduced influence parameter $\tilde{\kappa} = 0.55$, using the Sanchez-Lacombe EoS parameters and the characteristic ratios listed in Table 3.1. Calculated values are compared against experimental values for the same temperatures.

Agreement between SCF_SL+SGA and experiment is generally very good. As expected,[236] with the SCF approach inserted in the theoretical model, the conformational entropy effects in the vicinity of the free surface are taken into account. A direct consequence is a general increase of the surface tension relative to what would be predicted by SGA alone. Indeed, in comparing our model against the Poser and Sanchez model (SGA-PS) we find that there is a small increase of 5-15% in surface tension using the same parameters. The

incompressible model used by Hong and Noolandi results in a similar increase in surface tension relative to the Poser and Sanchez model, although they used a different continuum approach and a different method to calculate the influence parameter.[91]

Table 3.3. Surface Tension of Polymers at Various Temperatures in mN/m

polymer	SCF_SL+SGA			experimental*		
	413K	423K	453K	413K	423K	453K
poly(dimethyl siloxane)(PDMS)	13.8	13.2	11.5	14.1	13.6	12.2
poly(vinyl acetate)(PVAc)	28.8	27.8	26.2	28.6	27.9	25.9
poly (n - butyl methacrylate) (PnBMA)	28.5	27.7	25.4	24.1	23.5	21.7
poly isobutylene (PIB)	26.7	26.2	23.9	25.8	25.1	23.1
polyethylene (linear)(PE)	31.7	31.0	28.9	28.8-30.0	28.1	26.5-27.7
poly(methyl methacrylate)(PMMA)	37.0	36.2	33.6	32.0	31.2	29.9
polystyrene (atatic) (PS)	31.8	31.0	29.0	32.1	30.8	29.2
poly(ethylene oxide)(PEO)	34.3	33.4	30.9	33.8	33.0	30.7

*Experimental values obtained from ref 91. Experimental and calculated values refer to the same molar mass.

In Figure 3.10 the surface tension is plotted against temperature for all polymers except for poly(methyl methacrylate) (PMMA) and poly(n- butyl methacrylate)(PnBMA). The maximum error between experimental values and those calculated through the SCF_SL+SGA approach is nearly the same as the uncertainty in the measurements, approximately 2% on average. Predictions for PMMA and PnBMA are not so successful, differing by 15% from experimental values. One would tend to associate this limited success of the model in the case of methacrylates with the polarity of these polymers. Nevertheless, the calculation for PVA, which exhibits a polarity close to that of PMMA, performs very well in comparison to the experimental data. In our opinion, further investigation is needed into the manner in which methacrylates contribute to enthalpic or entropic components of surface tension. SGA alone also does not work very well for these two polymers, as evidenced by the predictions of the Poser-Sanchez model.[121] The nice overall agreement of SGA-SL+SGA predictions for the surface tension with experiment is mainly due to the high quality of the Sanchez-Lacombe equation of state. Contributions to γ from the density profile are dominant, while those due to perturbation of the chain conformational distribution, as treated with SCF theory, amount to 8-19%.

Surface tensions for a variety of polymer melts over a broad temperature range can be captured by the SCF_SL+SGA model. An interesting aspect of these calculations is that PE and PS exhibit similar behavior, although their SL parameters and radii of gyration are quite

dissimilar. Generally, an increase in T^*, P^*, ρ^* and C_∞ brings about an increase in surface tension. The PE P^* is high enough to counterbalance the higher values in other parameters of PS.
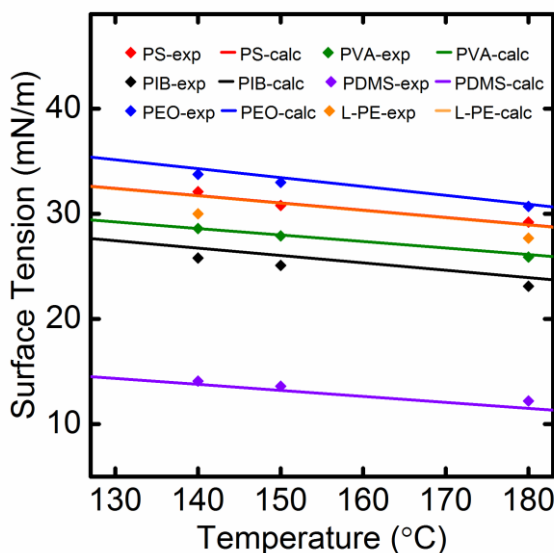
Figure 3.10. Surface tensions of various polymers with symbols depicting the experimental values and with lines corresponding to calculations from the SGA-SL+SGA model.

The surface entropy, $-\mathrm{d}\gamma/\mathrm{d}T$, of the polymer melts is shown in Table 3.4. The corresponding temperature derivative, as calculated from the Poser and Sanchez theory which includes the square gradient correction but no conformational entropy effects, is illustrated along with our results. Generally there is significant improvement in the calculation of the surface entropy relative to experimental measurements in relation to SGA alone. SGA ignores the effect of restrictions posed by the interface on the orientations and conformations of polymer molecules, which result in lowering the surface entropy. Although the SCF_SL+SGA approach increases the complexity of calculations in comparison to the pure SGA approach, it is physically more complete and brings considerable improvement.

The performance of SCF_SL+SGA is demonstrated by the lower deviations between model and experiment in the calculation of both γ and $-\mathrm{d}\gamma/\mathrm{d}T$.

91

Table 3.4. Surface Entropy Calculated Values from SCF_SL+SGA and Estimates from Previous Works

Polymer	SGA-PS (mN m^{-1} K^{-1})	SCF_SL+SGA (mN m^{-1} K^{-1})	Expt. (mN m^{-1} K^{-1})	Deviation from expt.	
				SGA-PS	SCF_SL+SGA
PE (linear)	0.0820	0.0692	0.057	44%	21%
PIB	0.0725	0.0700	0.066	10%	6%
PS	0.0722	0.0693	0.072	0%	4%
PVA	0.0920	0.0621	0.066	39%	6%
PMMA	0.0914	0.0865	0.076	20%	14%
PnBMA	0.0826	0.0787	0.059	40%	33%
PEO	0.0975	0.0849	0.076	28%	12%
PDMS	0.0609	0.0570	0.048	27%	19%

Experimental and Poser-Sanchez (SGA-PS) values retrieved from ref 121.

3.6 Concluding Remarks

In this chapter, we have coupled two theoretical methodologies to determine equilibrium properties of free surfaces of polymer melts: SCFT based on a Gaussian thread representation of chains, and square gradient theory based on the Sanchez-Lacombe EoS. We are motivated by the idea that including both cohesive interactions and chain conformational distributions in the model can account for energetic as well as local and nonlocal entropic effects on the structure and thermodynamics of the liquid-gas interface, allowing us to describe it in a quantitative way. To validate our results we have used surface tension measurements for a variety of polymers over a range of temperatures, as well as atomistic simulation results for linear polyethylene.

The free energy functional used to describe intermolecular interactions exhibits a dependence on both local density and its spatial gradient. The grand canonical ensemble, which is more appropriate for describing vapor-liquid equilibrium in an open system capable of exchanging molecules with the bulk liquid and vapor phases, is used to derive the thermodynamic field exerted on a chain and the grand partition function. From the latter the surface tension is readily obtained. We exploit the generalized excess free-energy functional description to implement the realistic EoS introduced by Sanchez and Lacombe. Density gradients are incorporated in the formulation through the SGA. In SGA a central role is played by the influence parameter, i.e. by the coefficient that multiplies the square gradient density term. We have followed the reduced influence parameter procedure suggested by Poser and Sanchez and used the same value of reduced influence parameter for all polymers we studied.

This value was extracted by matching the atomistically calculated surface density profile of polyethylene at one temperature.

The conformational component of the free energy, which takes into account the chain connectivity, was described by the fully flexible Gaussian thread model which is the basis of most continuous-space formulations of SCFT, employing the modified Edwards diffusion equation. Even though SCF treatments have been used in several works to describe interfacial polymeric systems, to the best of our knowledge it is the first time that SCF is employed in the framework of a continuum approach for a free polymer surface problem. The continuous Gaussian thread model is elegant and convenient for describing the conformational properties of high molar mass polymer chains, introducing a single, readily measurable or predictable additional parameter (R_g) into the picture. The need to compare the theoretically calculated results against the outcomes of atomistic simulations, which become very demanding computationally at large length scales, forced us to implement the Gaussian thread model even for smaller length chains.

We have tested various SGA and SCF models and the reduced density profiles at vapor-gas interfaces that arose from them, and found that the model employing an excess Helmholtz energy density based on the Sanchez-Lacombe EoS coupled with a square density gradient term (SCF_SL+SGA) achieves best agreement with atomistic simulation results. On one hand, SCFT models which consider only the local density to describe chain interactions produce steeper profiles, which demonstrates the necessity for using a gradient expansion. On the other hand, SGA-based models, although capable of generating smoother and more realistic profiles, do not incorporate entropic effects associated with the change of chain conformational/orientational distributions in response to the constraints present at the surfaces, thus overestimating the surface entropy. Density (total, end segment and middle segment) and conformational profiles (adsorbed and free chains, loops and tails, chain shapes) as calculated by the SCF_SL+SGA were found to agree very well with the corresponding profiles from detailed molecular simulation, the agreement improving with increasing chain length. Differences between SCF_SL+SGA and MD reflect the fact that the former does not incorporate conformational stiffness at a local level. The free film density profiles obtained from the SCF_SL+SGA model and MD simulations were investigated over a range of temperatures and chain lengths, with the theoretical predictions exhibiting excellent agreement with simulation.

The converged solution of the SCF_SL+SGA theory was used to determine end and middle segment density profiles, based on the treatment introduced by Wu et al[131]. As is well known for homopolymers where the ends are of the same chemical constitution as the middle segments, chain ends were found to dominate the surface profile. The magnitude of this effect and the extent of the interfacial region dominated by the end segments can be estimated with accuracy by our SCF approach, as comparison with atomistic simulations shows. In addition, the temperature dependence of this effect is correctly captured by the theory.

Following previous works of Semenov[233] and Daoulas et al.,[24] we have applied our SCF model to characterize the structure of polyethylene chains adsorbed to the free surface. The volume region used to characterize a chain segment as free or adsorbed is defined using the plane where the reduced segment density equals 0.5 as a boundary. Some discrepancy appears between SCF_SL+SGA and MD in the profiles of segments belonging to adsorbed and free chains, which is less significant for C_{260} chains than it is for C_{100} chains. SCF qualitatively follows the atomistic results. The same behavior is seen in the loop and tail distributions of adsorbed chains.

An important structural feature of polymer melts at surfaces is the flattening of chains due to their preferential orientation parallel to the surface. Inspired by past works[24,235] we have extended the continuum model to evaluate the reduced chain shape profile, which provides a direct quantitative measure of chain flattening. Both atomistic and field theoretic results show a relationship between the chain length and extent of the chain flattening region. In free polyethylene films of chains as short as C_{260} the shape profile from SCF_SL+SGA almost coincides with that from MD. The range of the flattening effect is in good agreement between theory and simulation, being on the order of $1.6R_g$.

A challenge for our formulation was its application to calculate the surface tension of various polymers. The reduced influence parameter used to reproduce the atomistically calculated reduced density profile for the polyethylene surface was used for all polymers examined. The SCF conformational entropy contribution added by the SCF treatment in the Gaussian thread approximation increases the surface tension by 5-10%. A nice feature of our SCF model is that it accounts for two distinct length scales simultaneously: i) a monomeric one, set by the range of monomer interactions, governing properties of the liquid-vapor interface; ii) a polymeric one, set by the radius of gyration, governing structural properties at the chain level.

For most polymers this approach yields results for both surface tension and surface entropy that are in excellent agreement with experiments.

4 Structure and Thermodynamics of Grafted Silica/PNCs

Polymer/matrix nanocomposites (PNCs) are materials with exceptional properties.[237] They offer a plethora of promising applications in key industrial sectors. In most cases, it is preferable to disperse the nanoparticles (NPs) homogeneously across the matrix phase. However, under certain conditions NPs might lump together and lead to a composite material with undesirable properties. A common strategy to stabilize the NPs is to graft on their surface polymer chains of the same chemical constitution as the matrix chains. There are several unresolved issues concerning the optimal molar mass and areal density of grafted chains that would ensure best dispersion, given the nanoparticles and the polymer matrix. We propose a model for the prediction of key structural and thermodynamic properties of PNC and apply it to a single spherical silica (SiO_2) nanoparticle or planar surface grafted with polystyrene chains and embedded at low concentration in a matrix phase of the same chemical constitution. Our model is based on self-consistent field theory, formulated in terms of the Edwards diffusion equation. The properties of the PNC are explored across a broad parameter space, spanning the mushroom regime (low grafting densities, small NPs and chain lengths), the dense brush regime, and the crowding regime (large grafting densities, NP diameters, and chain lengths). We extract several key quantities regarding the distributions and the configurations of the polymer chains, such as the radial density profiles and their decomposition onto contributions of adsorbed and free chains, the chains/area profiles, and the tendency of end segments to segregate at the interfaces. Based on our predictions concerning the brush thickness, we revisit the scaling behaviors proposed in the literature and we compare our findings with experiment, relevant simulations, and analytic models, such as Alexander's model for incompressible brushes.

4.1 Background

Solid particles with polymer chains anchored on their surface hold a central place in nanocomposite materials research,[134,135] since they are widely used in a variety of scientific and industrial applications such as sensing and therapy in biotechnology and biomedicine, wettability of membranes, surface activation, and interfacial electronic modulation.[136] Usually, grafted polymer chains are used to stabilize inorganic nanoparticles (NPs) inside a host polymer matrix. When NPs are properly dispersed inside the polymeric material, they lead to mechanical reinforcement and improvement of viscoelastic properties in comparison to the pure material.

4.1.1 Dispersion of NPs

The state of dispersion of NPs inside a polymer matrix depends on solid-solid and solid-polymer interactions as well as on entropic effects. In most cases, the embedded NPs tend to stick to each other due to attractive forces between them.[137] Addressing this behavior, a widely used methodology is to graft homopolymer chains on the NP surface. Under certain conditions, the entropic cost related to the configurational restriction of grafted chains when the particles get closer to each other is able to keep the particles separated.

The key factors influencing NP separation are their size, the molecular weight of grafted chains, and the surface grafting density. Trombly et al.[238] studied the effect of curvature of the solid surface on polymer mediated interactions among grafted NPs and demonstrated that the dependence of their separation on the grafting density becomes weaker with increasing particle curvature.

We say that matrix chains wet the grafted polymer brush when they are able to interpenetrate with grafted chains and therefore diffuse inside the space occupied by the polymer brush. Such a situation leads to a well-dispersed set of NPs. It has been seen that, in most cases, matrix chains are able to wet the polymer brush when their molecular weight is less than that of the grafted chains.[136] Depending on the grafting density, when matrix chains are longer than the grafted chains, it is harder for them to penetrate into the interfacial region due to the higher entropy loss they experience. This is known as "autophobic dewetting". One way to reduce the possibility for autophobic dewetting is to disperse smaller NPs.[42] When grafted chains are

attached to smaller particles, they have more available space, thus the penetration of matrix chains is facilitated and the corresponding conformational entropy cost becomes smaller.

As mentioned before, another important parameter for nanoparticle dispersion is the solid surface grafting density. When grafting density is lower than a threshold value, the particle cores are no longer screened by the grafted chains surrounding them, so they attract each other, leading to aggregation. This is known as "allophobic dewetting". Sunday et al.[136] derived experimentally a phase diagram demonstrating the regions where autophobic, allophobic dewetting, and complete wetting occurs.

4.1.2 Previous Works

Major experimental work has been conducted to understand the behavior of polymer grafted NPs and their influence on the properties of the composite material.[75–78,80,81,83,239–242] Experimentalists are also interested in studying the interactions among grafted inorganic NPs in the absence of a host polymer matrix (particle-solids).[243–245] Most of the experimental work up to now has been concentrated on medium grafting densities (< 0.2 nm^{-2}).[83] However, silica particles with higher grafting densities (around 1.0nm^{-2}) coated with asymmetric block copolymers have also been synthesized.[240]

Atomistic molecular dynamics simulations have been performed by Ndoro et al.[138], while Meng et al.[139] and Kalb et al.[246] have performed coarse-grained molecular dynamics simulations representing the polymer chains by the Kremer-Grest bead-spring model. Using the same coarse-grained model, Ethier and Hall[247] studied the structure and entanglements of grafted chains on an isolated polymer-grafted NP. Various additional studies employing particle-based simulation methods exist in the literature addressing nanoparticles in a polymer melt or solution,[248–250] as well as isolated nanoparticles.[251–254] Dissipative particle dynamics (DPD)[141] and density functional theory (DFT)[142] simulations addressing systems of polymer brushes are also reported. Vogiatzis et al.[255] devised a hybrid particle-field approach called *FOMC* (Fast Off-lattice Monte Carlo) which is a coarse-grained class of Monte Carlo simulations, where the nonbonded interactions are described by a mean-field inspired Hamiltonian.

Another popular approach for investigating the structure and thermodynamics of polymer grafted NPs and brushes is self-consistent field theory (SCFT).[43,144,145,147–150,152,153,256,257] It invokes a mathematical transformation from a system of

interacting chains to an equivalent system of independent chains, where each chain interacts with a chemical potential field, *w*, created by the rest of the chains.[258] SCFT is a strong modeling tool for describing equilibrium properties of interfacial systems involving polymer melts or solutions. Besides the fact that it is accurate in high density and large molar mass systems, it is able to derive directly the free energy of the investigated system. For a detailed explanation of SCFT and the transition from particle-based to field-theoretic formulations, the reader is referred to the relevant monograph by Fredrickson.[259]

4.1.3   Current Research Approach

In the present chapter we employ SCFT to investigate the structure and thermodynamics of systems comprising atactic polystyrene (PS) chains grafted on a single spherical nanoparticle or planar surface made of silica (SiO_2), immersed in a PS melt. The chemical constitution of the system under study is identical to the one investigated with *FOMC* by Vogiatzis et al.[255] The range of molecular parameters (nanoparticle size, surface grafting density, molar masses of grafted and matrix chains) has been chosen so as to encompass that of experimental investigations of SiO_2/PS nanocomposite systems.[260] It is mentioned here that no adjustment of parameters has been undertaken to fit with experiment or *FOMC*; rather, the actual physical parameters of silica and polystyrene have been used. The main virtue of *FOMC* is that it can directly sample chain conformations. On the other hand, the main advantage of SCFT in relation to *FOMC* is that it can directly calculate the free energy, enthalpy and entropy of mixing between the NP and the polymer matrix and the potential of mean force between two nanoparticles immersed in a host polymer matrix.[150,261,262]

The calculations were performed by employing the SCFT in one dimension (radial distance or normal distance coordinates) by taking advantage of the symmetry of the nanoparticle/planar surface. This one-dimensional treatment is expected to perform fairly well at moderate to large grafting densities and molecular weights of grafted chains. As in previous work,[24] our SCFT model has finite compressibility. We apply the Gaussian string model to describe chain conformations, which punishes stretching of chain contours, since stretched contours have fewer available conformations, thus reducing the entropy. Nonbonded interactions in the polymer are calculated from an expression giving the free energy density as a function of the polymer local segment density. Polymer/solid interactions are accounted for by Hamaker integration.

That SCFT calculations are computationally inexpensive in one dimension allowed us to perform an extensive and dense grid search over a broad parameter space spanning: i) the radii of the NP, $R_{NP} = 2^0$ nm to 2^{14} nm, as well as $R_{NP} \to \infty$ (planar surfaces); ii) the molar mass of the grafted chains, $M_g = 1.25$ kg/mol to 100 kg/mol; iii) the grafting densities $\sigma_g = 0.1$ nm^{-2} to 1.6 nm^{-2}. These calculations provide useful quantitative understanding of the limiting cases of sparse/dense grafting of short/long chains, on surfaces with low/high curvature, as well as of the intermediate transition regimes.

In particular, throughout our calculations, we extracted the density profiles of the grafted and matrix chains, which provide a direct picture of their conformations across the parameter space. The density profiles of the matrix chains are decomposed into contributions from "adsorbed" and "free" chains, the categorization of which is based on distance-based criteria; these results unveil the tendency of the matrix chains to penetrate the brush emanating from the nanoparticle/flat surface. The shape of polymer chains is investigated in terms of the number of chains passing through a unit surface[24,235,263] and provides a measure of "crowding" phenomena and of the tendency of the chain ends to segregate at the matrix-grafted interface. Subsequently, the distributions of the grafted chains are analyzed in terms of their corresponding brush thickness, wherein we compare our findings to correlations that are reported in the literature.[255,264] The brush thickness exhibits a rather complicated behavior across the transition regime from spherical nanoparticle to flat surface, which we try to describe through a scaling equation. Finally, the thermodynamics of these systems is examined in terms of the grand potential across the parameter space and a direct comparison with the Alexander model at fixed density[265,266] (which is similar to the dry part of the two-layer model)[267,268] is performed regarding the stretching free energy of grafted chains.

Before presenting the main results, we first validate our model and implementation by comparing our density profiles against $FOMC$[255] across the same regime of grafting densities and chain molar masses that was investigated by Vogiatzis et al.[255] This comparison is made for profiles obtained via both the Sanchez-Lacombe (SL) equation of state coupled with square-gradient theory (SGT) for nonbonded interactions, that we have adopted herein, and the Helfand (HLF) free energy density using the same compressibility employed by Vogiatzis et. al.[255]; the latter model is typically used in most field theory-inspired simulations.

4.2   Model and Theoretical Formulation
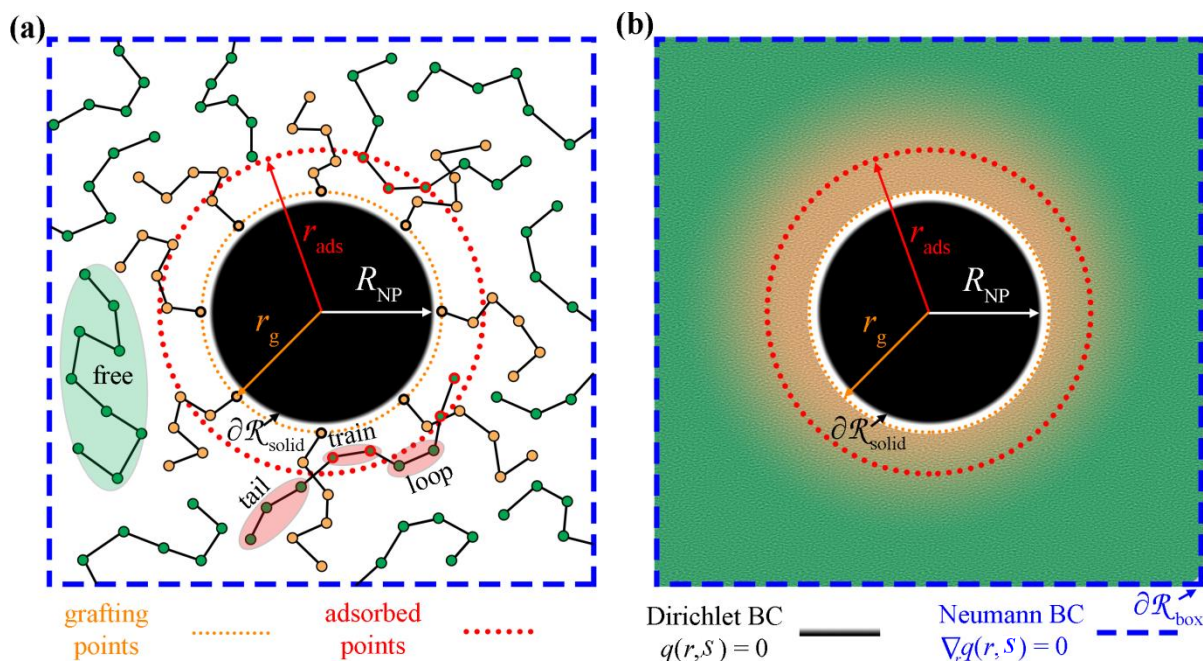
Figure 4.1. (a) A particle-based representation of a nanoparticle with grafted chains at r_g (orange) embedded in a polymer matrix (green chains). **(b)** In unidimensional SCFT, the chains are replaced by a density field and the grafting points are smeared normal to the radial direction. r_{ads} depicts a critical distance based on which the matrix chains are categorized as adsorbed (e.g., see red circles in (a)) or free.

In Figure 4.1(a), we depict the geometry of the three-dimensional region $\mathcal{R}$ of the system that we wish to model. Grafted polymer chains (circles with orange fill) are chemically anchored at the grafting points, r_g (orange arrow), which are located at a small distance (circle of small orange dots) from the surface of the NP (black) of radius R_{NP} (white arrow). On the surface of the NP, $\partial\mathcal{R}_{solid}$, Dirichlet boundary conditions are imposed. The red dotted circle of radius r_{ads} (red arrow) defines the region where the segments of matrix chains (green circles connected by black line) are considered to be "adsorbed" (red circles with a green fill). These can be additionally subdivided into tails, loops and trains.[26,104] Those matrix chains whose segments lie exclusively at a distance larger than r_{ads} from the NP center are called "free" (black circles with a green fill). Across the edges of the simulation box, $\partial\mathcal{R}_{box}$ (dashed blue lines), Neumann boundary conditions with zero flux are applied.

In SCFT, the degrees of freedom associated with the positions of chain segments are replaced by a spatially varying chemical potential field, as illustrated in Figure 4.1(b).This field governs the chain conformations and thus the segment density. At the same time, the field is

dictated by the polymer segment density, so the field must be self-consistent and correctly describe the thermodynamic properties of the polymer. Furthermore, Figure 4.1(b) depicts the smearing of grafting points normal to the radial direction.

4.2.1 Iterative Procedure for Obtaining the Self-Consistent Field

4.2.1/a General Algorithm

When the Gaussian chain model is applied to describe bonded interactions along the polymer chain, the propagation of matrix and grafted chains in three-dimensional space is described by the Edwards diffusion equation in the presence of a chemical potential field, w'_{ifc}; note that "ifc" stands for "interface":[182]

$$\frac{\partial}{\partial s}q_c(\mathbf{r},s) = \frac{R_{\text{G},c}{}^2}{N_c}\nabla_{\mathbf{r}}^2 q_c(\mathbf{r},s) - \beta w'_{\text{ifc}}(\mathbf{r})q_c(\mathbf{r},s) \qquad \left(c = \text{m, g}\right) \tag{4.1}$$

where $R_{\text{G},c}{}^2 = C_\infty l_{\text{C-C}}{}^2 N_c / 6$ is the ensemble averaged squared radius of gyration of a chain[193] in its unperturbed state (bulk melt) with $C_\infty = \gamma b_{\text{K}}/l_{\text{c-c}}$ being Flory's characteristic ratio, b_{K} the Kuhn length, $l_{\text{C-C}}$ the length of the skeletal C-C bond and γ is a geometric factor depending on bond-angles along the chain backbone.[193] q_c is the restricted partition function, s is the variable spanning the contour of the chains, measured in skeletal bonds, and c denotes the kind of the chains; i.e., c = m for matrix, and c = g for grafted chains. Based on the resulting q_c, one can compute the spatial density distributions of the chain segments, which in turn dictate an updated chemical potential field. This procedure is repeated until the input field in eq 4.1 becomes equal to the resulting field; thus the field becomes self-consistent. A detailed derivation of the equations is presented in the appendix B.1.

The iterative convergence procedure can be summarized as follows:

1. Equation 4.1 is solved for the matrix chains $\forall \mathbf{r} \in \mathcal{R}$ for $0 < s < \max\left(N_{\text{m}}, N_{\text{g}}\right)$ with N_{m} and N_{g} being the length of the matrix and grafted chains, respectively. The initial condition is set to $q_{\text{m}}(\mathbf{r},0) = 1$ across the polymer domain, whilst Dirichlet, $q_{\text{m}}(\mathbf{r},s) = 0$ and Neumann ($\nabla_{\mathbf{r}}q_{\text{m}}(\mathbf{r},s) = 0$) boundary conditions are imposed at the solid surface and system box boundaries, respectively (see Figure 4.1).

2. Subsequently, eq 4.1 is solved for the grafted chains for $0 < N < N_g$, $\mathbf{r} \in \mathcal{R}$ and $\mathbf{r} \neq \mathbf{r}_{gi_g}$ where $\mathbf{r}_{gi_g}$ is the grafting point of the i_gth grafted chain, $0 \leq i_g \leq n_g$. The boundary conditions are the same as those for the matrix chains. In contrast, the initial condition is given by the following equation[257]:

$$q_g(\mathbf{r}_{gi_g}, 0) = \frac{N_g}{\rho_{seg,bulk}} \sum_{i_g=1}^{n_g} \frac{\delta(\mathbf{r} - \mathbf{r}_{gi_g})}{q_m(\mathbf{r}_{gi_g}, N_g)} \tag{4.2}$$

with $\rho_{seg,bulk}$ being the segment density in the bulk region of the polymer melt and $\delta(\mathbf{r})$ being the Dirac delta function.

3. With $q_c(\mathbf{r}, N)$ known, the reduced densities, $\varphi_c = \rho_c / \rho_{seg,bulk}$, can be calculated by the following convolution integral:

$$\varphi_c(\mathbf{r}) = \frac{1}{N_c} \int_0^{N_c} ds \; q_c(\mathbf{r}, s) \; q_m(\mathbf{r}, N_c - s) \quad (c = \mathrm{m, g}) \tag{4.3}$$

Note that in both m and g chains the second term of the convolution integral is q_m (for details appendix B.1.3).

4. Having calculated the density profiles of matrix and grafted chains, an EoS must be used to determine the free energy density functional and the corresponding chemical potential field:

$$w'_{ifc}(\mathbf{r}) = w'(\mathbf{r}) - w'_{bulk} = \left.\frac{\partial f[\rho, \nabla\rho]}{\partial \rho}\right|_{\rho=\rho(\mathbf{r})} - \left.\frac{\partial f[\rho, \nabla\rho]}{\partial \rho}\right|_{\rho=\rho_{seg,bulk}} - \nabla \cdot \frac{\partial f[\rho, \nabla\rho]}{\partial \nabla\rho} + U_s(\mathbf{r}) \tag{4.4}$$

with $f[\rho, \nabla\rho]$ being the excess (relative to an ideal gas of chains) Helmholtz energy density of intermolecular interactions as a function of the local segment density and its gradient, U_s being the field exerted on a segment by the solid surface, and $\rho = \rho_m + \rho_g$ being the total segment density. Note that subtracting w'_{bulk} from w' guarantees that the chemical potential field is zero in the bulk phase.

5. To inspect the convergence, the maximum difference between the fields of the previous and the current iteration, $\Delta w'^{max}_{ifc} = \max\left(\{\|w'^{new}_{ifc}(\mathbf{r}) - w'_{ifc}(\mathbf{r})\|, \forall \mathbf{r} \in \mathcal{R}\}\right)$, is estimated, therefore:

a. If $\Delta w_{\mathrm{ifc}}'^{\max}$ is smaller than a tolerance value, $\Delta w_{\mathrm{ifc}}'^{\mathrm{tol}}$, the simulations are considered converged and the procedure halts.

b. If not, the algorithm cycles back to step (1) wherein the Edwards equation is reevaluated in the presence of the mixed field for numerical stability purposes:

$$w_{\mathrm{ifc}}'(\mathbf{r}) \rightarrow \left(1 - a_{\mathrm{mix}}\right) w_{\mathrm{ifc}}'(\mathbf{r}) + a_{\mathrm{mix}} w_{\mathrm{ifc}}'^{\mathrm{new}}(\mathbf{r}) \tag{4.5}$$

with $a_{\mathrm{mix}} \in [0,1]$ being a relaxation parameter.

The above algorithm is generic and applicable to arbitrary system geometries.

4.2.1/b Solving SCFT in one Dimension

By taking advantage of the spherical symmetry of the NP or the translational symmetry in the case of planar surfaces, one can evaluate the SCFT equations in an one-dimensional domain. In 1D, the grafting points become delocalized throughout the surface near the solid substrate, suggesting a smeared distribution of grafting points, which practically ignores the presence of a grafting point at a specific surface point; e.g., in Figure 4.1b the grafting points have been smeared across a spherical cell highlighted by an orange dotted circle. In doing so, eq 4.2 for the initial condition of the grafted chains can be written as follows:

$$q_{\mathrm{g}}(h_{\mathrm{g}},0) = \frac{S_{\mathrm{solid}}}{S_{h_{\mathrm{g}}}} \frac{\sigma_{\mathrm{g}} N_{\mathrm{g}}}{\rho_{\mathrm{seg,bulk}}} \frac{\delta\left(h - h_{\mathrm{g}}\right)}{q_{\mathrm{m}}\left(h_{\mathrm{g}}, N_{\mathrm{g}}\right)} \tag{4.6}$$

where $\sigma_{\mathrm{g}} = n_{\mathrm{g}} / S_{\mathrm{solid}}$ is the grafting density, S_{solid} is the surface area of the solid, and $S_{h_{\mathrm{g}}}$ is the surface area over which grafting points are smeared. To make eq 4.6 applicable for both spherical and planar geometries, it has been written in terms of h and h_{g}, which denote the segment-surface and the grafting point-surface distance, respectively. Consequently, in spherical geometries, $h \equiv r - R_{\mathrm{NP}}$; this relation is ill-defined in planar geometries, since $r, R_{\mathrm{NP}} \rightarrow \infty$. The three-dimensional delta function $\delta\left(\mathbf{r} - \mathbf{r}_{\mathrm{g},i_{\mathrm{g}}}\right)$ is approximated as $\delta\left(h - h_{\mathrm{g}}\right) / S_{h_{\mathrm{g}}}$ for all i_{g}.

For *planar surfaces* with area S_{solid}, the Edwards diffusion equation is evaluated across the normal direction with respect to the surface, and the differential $d\mathbf{r}$ of the spatial integration equals the volume of the layer, $d\mathbf{r} \rightarrow S_{\mathrm{solid}} dh$. The delta function in eq 4.6 is set to the inverse

discretization step in the h direction; i.e., $\delta(h - h_g) \simeq 1/\Delta h$, with Δh being the width of the intervals in which h is subdivided in the numerical solution.

For s*pherical nanoparticles,* with area equal to $S_{solid} = 4\pi R_{NP}^2$, the Edwards equation can be evaluated across a radial direction (normal to the surface). The differential d$\mathbf{r}$ for spatial integration is equal to the volume of the spherical cell, d$\mathbf{r} \rightarrow 4\pi(R_{NP}+h)^2dh$. The delta function in eq 4.6 is again set to the inverse width of the intervals in which length is subdivided in the radial direction; i.e., $\delta(h - h_g) \simeq 1/\Delta h$.

Throughout this chapter, we present the overall mathematical formulation in three dimensions; one can derive the corresponding expression in spherical and planar geometries by employing the aforementioned relations.

4.2.2 Grand Potential

The thermodynamics of the polymer-grafted NP and planar surfaces immersed in the matrix are described by a grand potential, defined relative to a bulk melt phase of matrix chains, each of length N_m, occupying a volume equal to the polymer-accessible volume of the system, and a set of n_g isolated end-pinned unperturbed chains, each of length N_g. The temperature T is the same between the system under study and the reference system:

$$\Delta\Omega = \Omega - \Omega_{bulk} - A_{bulk} = \Delta\Omega_{coh} + \Delta\Omega_{field} + \Delta\Omega_m + \Delta A_g + U_s \tag{4.7}$$

where $\Delta\Omega_{coh}$ is the cohesive interaction component (relative to the bulk melt chains) arising due to segment-segment interactions in the polymer,

$$\Delta\Omega_{coh} = \int_{\mathcal{R}} d\mathbf{r}\left\{ f\left[\rho(\mathbf{r}), \nabla\rho(\mathbf{r})\right] - f\left[\rho_{seg,bulk}, \mathbf{0}\right]\right\} \tag{4.8}$$

$\Delta\Omega_{field}$ is the interaction energy between the density field and the chemical potential field,

$$\Delta\Omega_{field} = -\int_{\mathcal{R}} d\mathbf{r}\left\{\rho(\mathbf{r})w'(\mathbf{r}) - \rho_{seg,bulk}w'_{bulk}(\mathbf{r})\right\} \tag{4.9}$$

U_s is the contribution of the potential energy exerted from the solid,

$$U_s = \int_{\mathcal{R}} d\mathbf{r}\left\{\rho(\mathbf{r})u_s(\mathbf{r})\right\} \tag{4.10}$$

$\Delta\Omega_m$ describes the translational and conformational entropy (relative to the bulk melt entropy) of noninteracting matrix chains subject to a chemical potential, $N_m \mu_m$,

$$\Delta\Omega_m = -\frac{\rho_{seg,bulk} V}{\beta N_m} \left(Q_m \left[w' - w'_{bulk} \right] - 1 \right) \tag{4.11}$$

and ΔA_g is associated with the conformational entropy of n_g grafted chains subject to the field $w' - w'_{bulk}$,

$$\Delta A_g = -\frac{1}{\beta} \sum_{i_g=1}^{n_g} \ln Q_g \left[\mathbf{r}_{g,i_g} ; w' \right] - \frac{1}{\beta} \sum_{i_g=1}^{n_g} \ln \frac{r_{ref,q=0}}{r_{g,i_g,q=0}} \tag{4.12}$$

The partition function, $Q_g \left[\mathbf{r}_{g,i_g} ; w' - w'_{bulk} \right] = q_m \left[\mathbf{r}_{g,i_g}, N_g ; w' - w'_{bulk} \right]$, appearing in the first term of eq 4.12 depends on the position of the grafting point, and therefore on the discretization of space. In order to overcome this technical issue and normalize ΔA_g with respect to the distance of the grafting point from the surface where Dirichlet boundary conditions, $q_c(\mathbf{r},N) = 0$, are imposed, we have introduced the second term in eq 4.12. Based on the observation that the chain propagator, q_m, decreases linearly close the Dirichlet boundary, adding the second term ensures that ΔA_g is discretization independent; i.e., for a set $r_{ref,q=0}$, ΔA_g is independent of the position of the grafting point, while, if $r_{g,i_g,q=0} = r_{ref,q=0}$, the contribution of this term vanishes. This allows for comparisons for different spatial discretization and slightly altered grafting positions.

Our formalism is based on the works by Daoulas et al.[24] and Schmidt et al.[269], which have been extended to systems of arbitrary geometry comprising polymer chains grafted on solid surfaces. Furthermore, it was generalized so that any suitable equation of state can be applied to describe the non-bonded interactions among chain polymer segments. In depth information regarding our mathematical formulation can be found in the appendix sections B.1.1-B.1.3.

4.2.3 Free Energy Densities

In this work we employed two models for the investigation of the polymer-matrix nanocomposites/brushes: i) the Helfand free energy density, and ii) the Sanchez-Lacombe free energy density in conjunction with density gradient theory.

4.2.3/a Helfand's Free Energy Density

The Helfand free energy density and its first derivative with respect to the density are the following:

$$f_{\text{EoS}}^{\text{HFD}}\left(\rho(\mathbf{r})\right) = \frac{1}{2\kappa_T}\left(\frac{\rho(\mathbf{r})}{\rho_{\text{seg,bulk}}} - 1\right)^2 \tag{4.13}$$

$$\left.\frac{\partial f_{\text{EoS}}^{\text{HFD}}(\rho)}{\partial \rho}\right|_{\rho=\rho(\mathbf{r})} = \frac{1}{\kappa_T \rho_{\text{seg,bulk}}}\left(\frac{\rho(\mathbf{r})}{\rho_{\text{seg,bulk}}} - 1\right) \tag{4.14}$$

with κ_T being the isothermal compressibility of the polymer at temperature T.

4.2.3/b Sanchez-Lacombe Free Energy Density

The SL-EoS is the following:

$$\tilde{\rho}^2 + \tilde{P} + \tilde{T}\left[\ln(1-\tilde{\rho}) + \left(1 - \frac{1}{r_{\text{SL}}}\right)\tilde{\rho}\right] = 0 \tag{4.15}$$

$\tilde{\rho} = \rho_{\text{mass}} / \rho^*$, $\tilde{T} = T / T^*$ and $\tilde{P} = P / P^*$ are the reduced density, temperature and pressure; ρ^*, T^* and P^* are the corresponding characteristic SL parameters; r_{SL} is the number of SL segments constituting a molecule. The mass density ρ_{mass} for each chain length is derived from the vapor-liquid equilibrium of a Sanchez-Lacombe fluid (see Supplemental material section S1 in ref 26). The compressibility of the SL-EoS as a function of chain length and temperature is given by the following equation:

$$\kappa_{T,\text{SL}}^{-1} = \tilde{T}P^*\tilde{\rho}_{\text{bulk}}^2\left(\frac{1}{1-\tilde{\rho}_{\text{bulk}}} + \frac{1}{\tilde{\rho}_{\text{bulk}}r_{\text{SL}}N_{\text{m}}} - \frac{2}{\tilde{T}}\right) \tag{4.16}$$

with $\tilde{\rho}_{\text{bulk}} = \rho_{\text{mass,bulk}} / \rho^*$.

The corresponding free energy density and its first derivative with respect to the density are the following:

$$f_{\text{EoS}}^{\text{SL}}\left(\rho(\mathbf{r})\right) = P^*\left[\tilde{T}\tilde{\rho} - \tilde{\rho}^2 + \tilde{T}(1-\tilde{\rho})\ln(1-\tilde{\rho})\right] \tag{4.17}$$

$$\left.\frac{\partial f_{\text{EoS}}^{\text{SL}}(\rho)}{\partial \rho}\right|_{\rho=\rho(\mathbf{r})} = k_{\text{B}}T^*\left(\frac{r_{\text{SL}}}{N}\right)\left\{-2\tilde{\rho}(\mathbf{r}) - \tilde{T}\ln\left(1-\tilde{\rho}(\mathbf{r})\right)\right\} \tag{4.18}$$

The reader is reminded that the Sanchez-Lacombe model has a firm theoretical basis in a mean field statistical mechanical analysis of a lattice fluid composed of chains and voids, reminiscent of Flory-Huggins theory with voids playing the role of solvent molecules. [192,270]

4.2.4 Square Gradient Term

A more realistic treatment of inhomogeneous systems is achieved by including nonlocal contributions to the Helmholtz energy density. A common form assumed for $f[\rho(\mathbf{r}), \nabla\rho(\mathbf{r})]$ is the one presented in eq 4.19:[26,67,194,217,271]

$$f[\rho(\mathbf{r}), \nabla\rho(\mathbf{r})] = f_{\text{EoS}}(\rho(\mathbf{r})) + \frac{1}{2}\kappa(\nabla\rho(\mathbf{r}))^2 \tag{4.19}$$

with κ being the influence parameter. In other words, the excess Helmholtz energy density in an inhomogeneous polymer phase is equal to that of a homogeneous polymer phase with the same local density plus a square gradient term arising from density inhomogeneities at the considered location. For this special form, eq 4.4 for the self-consistent field becomes:

$$w'_{\text{ifc}}(\mathbf{r}) = \left.\frac{\partial f_{\text{EoS}}(\rho)}{\partial\rho}\right|_{\rho=\rho(\mathbf{r})} - \left.\frac{\partial f_{\text{EoS}}(\rho)}{\partial\rho}\right|_{\rho=\rho_{\text{seg,bulk}}} - \kappa\nabla^2\rho\Big|_{\rho=\rho(\mathbf{r})} + U_s(\mathbf{r}) \tag{4.20}$$

4.3 Calculation Details

The system considered in the present study consists of polystyrene (PS) chains grafted on a silica (SiO_2) NP or planar surfaces, in contact with a polymer melt of the same chemical constitution as the grafted chains. All calculations were carried out in the grand canonical ensemble at a temperature equal to $T = 500$ K.

The PS-SiO_2 interactions are described with the Hamaker potential[272] using the interaction parameters, A_{PS} and A_{SiO_2}, and the effective radii, σ_{PS} and σ_{SiO_2}, presented in Table 4.1 Given that the repulsive term of the Hamaker potential increases steeply at short distances, we opted to replace the Hamaker potential below a segment-surface distance, $h_{\text{HS}} \sim 0.4$ nm, where $U_s(h_{\text{HS}}) = 5\,k_B T$, with a hard sphere wall. To impose the hard sphere wall, the coordinate of the first node of the simulation domain was set at a distance h_{HS} from the surface. As a result, the region below h_{HS} becomes inaccessible to the polymer chains.

As Chantawansri et al.[144] observed, in the context of SCFT there is a special difficulty in the case of polymer chains whose one end is grafted to the solid surface. The grafted chains propagator is subject to a Dirac delta function initial condition as shown in eq 4.6. In addition to that, the denominator on the right-hand side of eq 4.6 is problematic, since the chain propagator of matrix chains goes to zero close to the solid surface. A usual approach to bypass these issues is to reposition the grafting points to a surface close to the solid instead of right on top of it.[273–275] Regarding the numerical implementation of the delta function, smearing of the grafting points in the direction normal to the surface takes place by treating the grafting point density as a Gaussian distribution[144] or as a rectangular function. In the three-dimensional analog of our in-house code named *RuSseL,* where we employ a Finite Element Method numerical scheme, the initial condition of the grafting points is evaluated exactly upon the desired points of the domain and the delta function is again evaluated as the inverse volume assigned to the node.[275] Guided by these studies, in the present work we set the location of the grafting points at the discretization nodal point which is nearest to the hard-sphere wall. Furthermore, a smearing of the grafting points was introduced, so that they degenerate into a grafting "spherical shell" with radius slightly larger than that of the NP itself (Figure 4.1, orange arrow) and thickness Δh.

Unless otherwise stated, the nonbonded interactions are described by the SL EoS in conjunction with square gradient theory (eqs 4.17 and 4.19). We employed the characteristic SL parameters for PS[270] and the influence parameter from the relation: $\kappa = 2(r_{\mathrm{SL}}/N)^2 P^* \left(\upsilon^*\right)^{8/3} \tilde{\kappa}$, with the reduced influence parameter being set to $\tilde{\kappa} = 0.55$, same as in Chapter 3 and ref 26.

The Edwards diffusion equation was solved with a finite difference scheme with spatial discretization $\Delta h = 0.05$ nm, and contour length discretization $\Delta s = 0.25$ segments. The rectangle integration method has been employed to evaluate the convolution integrals, since other higher-order methods such as Simpson integration can produce artifacts in the presence of grafting points. The field mixing fraction, a_{mix}, for the iterative convergence of the field in eq 4.5 was optimized for each chain length so as to enhance the efficiency of our evaluations. The tolerance value for the convergence was set to $\Delta w_{\mathrm{ifc}}'^{\mathrm{tol}} = 10^{-5} k_{\mathrm{B}} T$. In all cases, the system dimensions were at least 10 nm larger than the edge of the brush of the grafted chains in order to avoid finite size effects.

The simulations were realized with *RuSseL*; an in-house developed code which is designed to run calculations based on SCFT in both one and three dimensional systems, using the finite

differences and finite element method, respectively.[275] The evaluations were performed across a broad parameter space concerning R_{NP}, σ_g and M_g: $R_{NP} = \{1, 2, 4, 8, 16, 32, 64, 128, 256, 512, 1024, 2080, 4096, 8192, 16384\}$ nm, $\sigma_g = \{0.1, 0.4, 0.8, 1.2, 1.6\}$ nm^{-2} and, $M_g = \{1.25, 2.5, 5, 10, 20, 40, 80\}$ kg/mol. According to ref 255, as long as the matrix chains are longer than the grafted ones, the latter are not perturbed considerably; thus, unless otherwise stated, $M_g = M_m$. The diagrams were designed using relevant software.[276]

Table 4.1. Parameters of the calculations

	parameter	value	reference
system	T	500 K	255
	P	0 atm	-
	$r_{ref,q=0}$	0.05	-
	$r_{g,i_g,q=0}$	0.05	-
chain stiffness	b_k	1.83	255
	$l_{c\text{-}c}$	0.154 nm	-
	γ	0.829	193
	$m_{monomer}$	52.08 g/mol	-
Hamaker	h_{HS}	~0.4 nm	-
	σ_{PS}	0.37 nm	255
	σ_{SiO2}	0.30 nm	255
	A_{PS}	$5.84 \cdot 10^{-20}$ J	255
	A_{SiO_2}	$6.43 \cdot 10^{-20}$ J	255
SL	T^*	735 K	270
	P^*	357 MPa	270
	ρ^*	1105 kg/m^3	270
	$\tilde{\kappa}$	0.55	26
Helfand	$\kappa_{T=500K}$	1.07 (GPa)$^{-1}$	255
Edwards diffusion	Δh	0.05 nm	
	Δs	0.25 segs	
	$\Delta w_{ifc}'^{tol}$	$10^{-5}\, k_B T$	-

4.4 Results

4.4.1 Radial Density Profiles

The radial segment density profile distributions of matrix and grafted chains can be employed as a measure of the particle-polymer interactions and reveal how these interactions are affected by the grafting density and the molecular weight of matrix and grafted chains.

4.4.1/a Comparisons with FOMC

Figure 4.2 depicts the reduced radial segment density profiles of matrix and grafted chains from *FOMC*, SCF_Helfand and SCF_SL+SGA. Beyond a certain distance from the solid surface, our model results in practically identical radial density profiles to those obtained by *FOMC*. This holds for both the Helfand and the SL+SGA Hamiltonian. The agreement becomes better as the grafting density or the molecular weight of chains increases. This is reasonable, since SCFT is more accurate in systems of longer chains and higher density.

Nevertheless, there is a discrepancy near the surface of the NP, which could be related to the fact that SCFT cannot describe in detail the packing of chain segments or the anchoring of grafted segments at discrete points close to the surface, while *FOMC* invokes not an atomistic, but rather a coarse-grained model. Another observation is that the SCF_SL+SGA model provides smoother radial density profiles for grafted chain segments in comparison to *FOMC* or SCF_Helfand. This mainly has to do with the incorporation of the square gradient term in the description of nonbonded interactions, which does not affect the long-ranged segment interactions, but rather the smoothness of the density profiles in the region near the solid surface. In addition, SCFT features a depletion region ranging from the solid surface up to a distance equal to $h_{HS} = 4$ Å (the position of the aforementioned hard-sphere wall), wherein the repulsive interactions from the Hamaker potential are very strong.

It is stressed at this point that the density profiles obtained from our SCF_SL+SGA model are closer to the corresponding ones obtained from atomistic molecular dynamics simulations[138,277–279] than *FOMC*. If one averages out the oscillations of the atomistic density profiles, then their smeared analogues come out very close to the density profiles of SCF_SL+SGA (and especially close to Helfand) in terms of the position of the peak and the width of the depletion zone near the solid surface. [138,277–279] Interestingly, the peak of the density profiles appears to become less pronounced in atomistic simulations with increasing grafting

density, presumably due to excluded volume effects.[138,279] Hereafter, all presented results are obtained with the SCF_SL+SGA model, since it is more realistic and reproduces the experimentally measured surface tension of PS.[26] It is also mentioned that no fitting of parameters with respect to experiment or *FOMC* has been performed to describe this silica-polystyrene interfacial system, but the actual physical parameters of silica and polystyrene have been used.
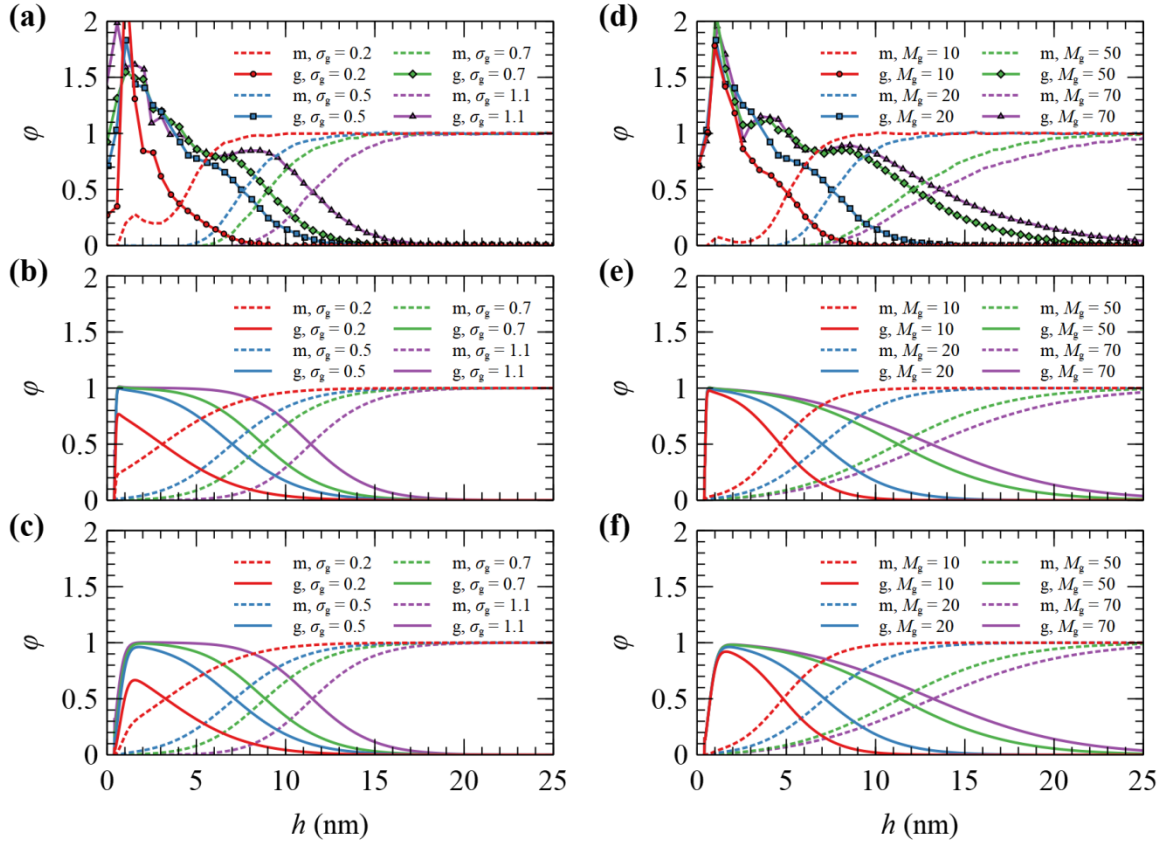
Figure 4.2. Radial density distribution for matrix (m) and grafted (g) chains on a NP with $R_{NP} = 8$ nm, from *FOMC*[255] (top), SCFT with Helfand (middle), and SCFT with SL+SGT (bottom). In **(a, b, c)** $M_g = 20$ kg/mol, $M_m = 100$ kg/mol, and σ_g varies from 0.2 to 1.1 nm^{-2}. In **(d, e, f)** $\sigma_g = 0.5$ nm^{-2}, $M_m = 100$ kg/mol and M_g varies from 10 to 70 kg/mol.

4.4.1/b Radial Density Profiles from the Sanchez-Lacombe EoS: Exploration of the R_{NP}, σ_g, M_g Parameter Space

Figure 4.3 presents the reduced radial density profiles of grafted (φ_g) and matrix (φ_m) chains across the (R_{NP}, σ_g, M_g) parameter space. In all cases grafted and matrix chains have the same molar mass, $M_m = M_g$. Overall, the radial density profiles of grafted chains expand with increasing σ_g, M_g, and R_{NP}. Concerning the latter, with increasing particle radius (i.e., decreasing

curvature), the grafted chain segments have less available space to explore near the surface, so they experience crowding and extend further towards the bulk phase.

The radial density profiles exhibit a rather rich behavior which could be classified into three distinct regimes:

(i) *Mushroom regime*. In the region of low σ_g, M_g and R_{NP}, the radial density profiles of the grafted chains become very suppressed and their density peaks are much lower than the bulk density. That the grafted chains are short and the distance between them is relatively large implies that they cannot experience the presence of each other. In other words, the density distributions of individual chains do not overlap and therefore chains tend to form mushroom-like structures[280]; this effect is expected to be more pronounced at small R_{NP}, since the chains would have more available space thanks to the increased curvature. Matrix chains, on the other hand, can penetrate the polymer brush readily and reach the surface of the NP. However, in the one-dimensional model employed herein, the inevitable smearing of grafting points may prevent us from accurately predicting the density profiles of grafted chain segments in this regime. Our subsequent work with the three-dimensional analog of *RuSseL* will investigate the mushroom regime more realistically, transcending the limitations of the one-dimensional approximation.[275]

(ii) *Dense brush regime*. With increasing σ_g, M_g and R_{NP} the radial density profiles become more pronounced and feature extended regions with bulk densities; e.g., see Figure 4.3 for $\sigma_g \geq 0.8$ nm^{-2} and $R_{NP} \geq 64$ nm. Towards the matrix phase, the radial density profiles feature a characteristic sigmoid shape[26] suggesting stretched brushes. The profiles of grafted and matrix chains intercept at reduced densities $\varphi_m = \varphi_g \simeq 0.5$. The presence of chemically grafted chains on the particle surface inhibits the penetration of matrix chains into the solid-polymer interfacial region and the strength of this exclusion of matrix chains increases with increasing σ_g, R_{NP}, and M_g.

(iii) *Crowding regime*. In the extreme case of high grafting densities ($\sigma_g \geq 1.6$ nm^{-2}) and low curvatures (e.g., $R_{NP} \geq 64$ nm), the crowding experienced by the grafted chain segments reaches a level where their densities exceed the bulk densities somewhat (see dashed grey line in the plots of Figure 4.3). In other words, the compressing forces imposed by the stretching of grafted chains overcome the tendency of the equation of state to maintain bulk reduced densities at unity; hence, the densities exceed this level. In this regime matrix chains are unable to reach the surface of the NP, even for the shortest grafted chains ($M_g = 1.25$ kg/mol) studied herein.
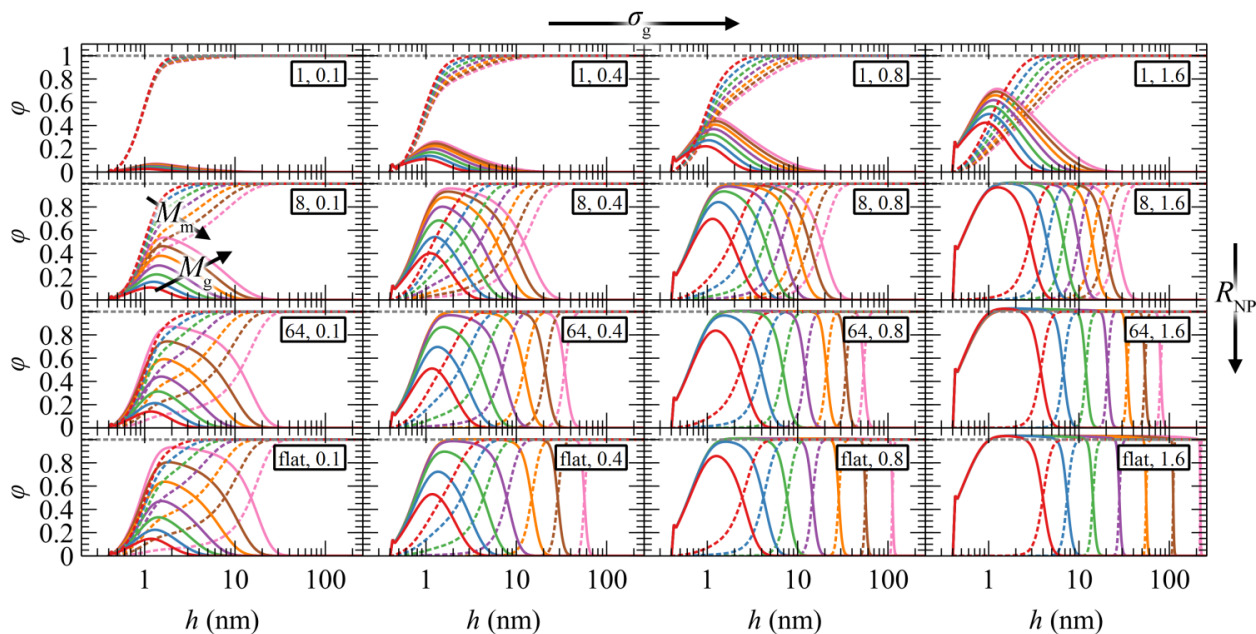
Figure 4.3. φ profiles of g (solid lines) and m (dashed lines) chains with molar mass equal to 1.25 (red), 2.5 (blue), 5 (green), 10 (violet), 20 (orange), 40 (brown) and 80 (pink) kg/mol. In all cases, $M_m = M_g$. Legend in rectangles: R_{NP}(nm), σ_g(nm^{-2}).

In Figure 4.3, for given σ_g and R_{NP}, the radial density profiles are shifted by about a constant amount along the abscissa whenever the M_g is doubled; this effect becomes more pronounced with increasing R_{NP}. Given that the radial density profiles are presented in semi-log plots, this observation leads to the conclusion that the edges of the profiles follow a $\sim M_g^n$ power-law for constant σ_g and R_{NP}. This scaling exponent exhibits a complicated dependence on σ_g and R_{NP}, which is explored below (see section 4.4.5).

Regarding the total reduced density profiles, even though they are practically insensitive to M_g (except under very crowded conditions), they are somewhat enhanced near the surface with increasing σ_g and deviate from unity across the brush region under conditions of intense chain crowding.

4.4.2 Structure of Adsorbed Polymer Layer

The chains cannot propagate against the solid surface; as a consequence, their conformation is dictated by configurational entropy effects different from those prevailing in the bulk melt. Furthermore, the presence of the NP or the planar surface brings about an attraction of the polymer segments—which belong either to grafted or matrix chains—towards the solid surface. The strength of this attraction, in relation to the cohesive interactions of the polymer, determines

the wetting behavior of the melt on the solid surface. Low, moderate, and high energy surfaces lead to low, high (e.g., treated silica[281]) and perfect (e.g., untreated silica[281]) wetting conditions which may alter the local configurations of the grafted and matrix chains relative to what is dictated by entropic phenomena.
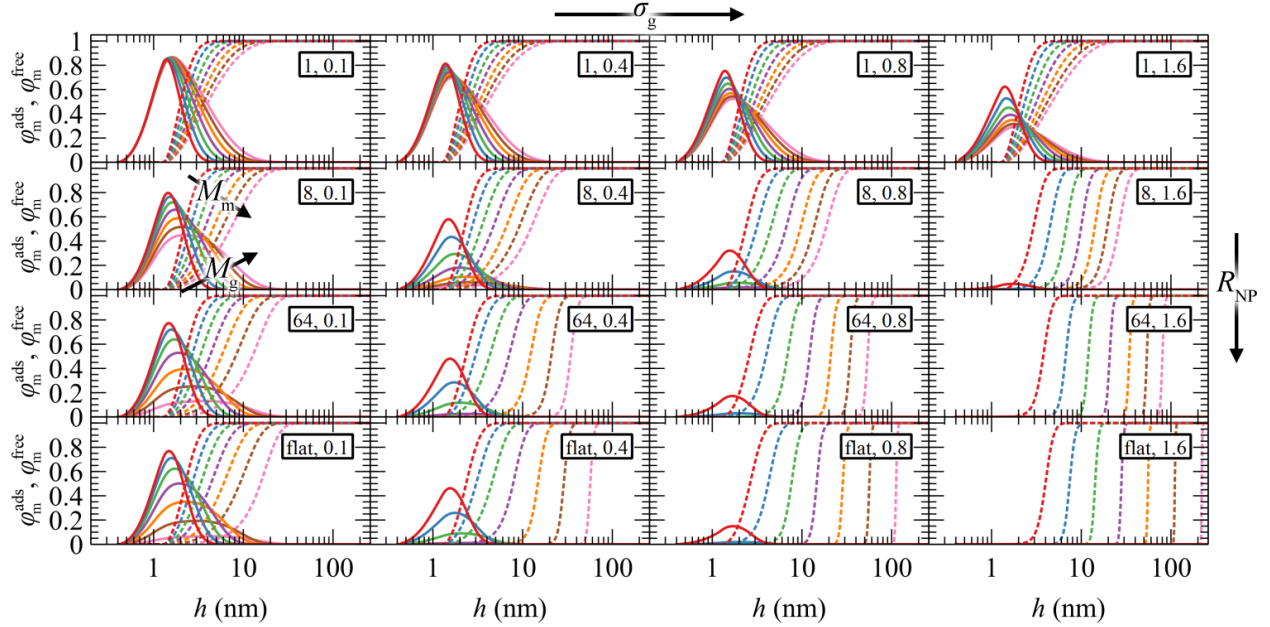
Figure 4.4. φ_m^{ads} (solid lines) and φ_m^{free} (dashed lines) profiles of adsorbed and free matrix chains with molar mass equal to 1.25 (red), 2.5 (blue), 5 (green), 10 (violet), 20 (orange), 40 (brown) and 80 (pink) kg/mol. In all cases, $M_g = M_m$. Legend in rectangles: R_{NP}(nm), σ_g(nm^{-2}).

In order to investigate these effects, a distinction is made between "adsorbed" and "free" chains. By definition, grafted chains are adsorbed, therefore the aforementioned distinction concerns primarily the matrix chains. The value of the characteristic distance of closest approach to the NP surface, below which a matrix chain is characterized as adsorbed, is set at $h_{ads} = 1.28$ nm. This is where the tail of the Hamaker potential emanating from the solid starts, i.e., where the Hamaker potential assumes a value equal to $\sim -0.005\ k_B T$. It should be emphasized at this point that the distinction between "adsorbed" and "free" chains is not based on chain dynamics, but rather on a geometric criterion revealing the tendency/ability of matrix chains to penetrate the brush and experience the potential exerted by the solid surface.

The reduced density of free matrix chains can be derived from the convolution integral of eq 4.21.

$$\varphi_m^{free}(\mathbf{r}) = \frac{1}{N_m} \int_0^{N_m} ds\ q_m^{free}(\mathbf{r}, s)\ q_m^{free}(\mathbf{r}, N_m - s) \tag{4.21}$$

where $q_{\mathrm{m}}^{\mathrm{free}}$ is the propagator of the free matrix chains that can be obtained by solving the Edwards diffusion equation (eq 4.1) with an additional constraint that the matrix chains are not allowed to access segment-surface distances smaller than h_{ads}. In practical terms, an additional boundary condition is applied: $q_{\mathrm{m}}^{\mathrm{free}}(\mathbf{r}, N) = 0$, $\forall \mathbf{r} : \min\left(\|\mathbf{r} - \mathbf{r}_{\mathrm{l}}\|, \mathbf{r}_{\mathrm{l}} \in \partial \mathcal{R}_{\mathrm{solid}}\right) \le h_{\mathrm{ads}}$, whilst the other boundary conditions remain the same. Subsequently, the reduced density of the segments of adsorbed matrix chains is obtained as $\varphi_{\mathrm{m}}^{\mathrm{ads}}(\mathbf{r}) = \varphi_{\mathrm{m}}(\mathbf{r}) - \varphi_{\mathrm{m}}^{\mathrm{free}}(\mathbf{r})$.

Figure 4.4 presents the reduced radial density profiles of free ($\varphi_{\mathrm{m}}^{\mathrm{free}}$) and adsorbed ($\varphi_{\mathrm{m}}^{\mathrm{ads}}$) matrix chains across the (R_{NP}, σ_{g}, M_{g}) parameter space. The reduced radial density profiles of segments belonging to free chains assume a value equal to unity in the bulk, while going by definition to zero when approaching h_{ads}. According to Figure 4.4, the matrix chains can easily penetrate the brush of grafted chains in the mushroom regime. With increasing σ_{g} and R_{NP}, the matrix chains experience noticeable resistance in penetrating the brush, while $\varphi_{\mathrm{m}}^{\mathrm{ads}} \to 0$ upon transitioning to the crowding regime.

4.4.3 Chains/Area Profiles

In three dimensions, the chains/area can be defined as the number of chain segments which cross *at least once* a surface $\partial \mathcal{R}_{h_0}$. A meaningful choice for $\partial \mathcal{R}_{h_0}$ would be a surface which is parallel to the surface of the solid ($\partial \mathcal{R}_{\mathrm{solid}}$) at distance h_0; $\min\left(\|\mathbf{r}_1 - \mathbf{r}_2\|, \mathbf{r}_1 \in \partial \mathcal{R}_{h_0}, \mathbf{r}_2 \in \partial \mathcal{R}_{\mathrm{solid}}\right) = h_0$. Refs [24,26,282] include a detailed explanation of the chains/area calculation in one dimension; in this work we present a more general formalism in three dimensions which is compatible with smooth surfaces of arbitrary shape. To compute the chains/area we use the following eq 4.22.

$$p_{\mathrm{int},c}(h_0) = 1 - \frac{\int\limits_{\mathcal{R}} q_{c,h_0}^{\mathrm{shape}}(\mathbf{r}, N_c) \mathrm{d}\mathbf{r}}{\int\limits_{\mathcal{R}} q_c(\mathbf{r}, N_c) \mathrm{d}\mathbf{r}} \tag{4.22}$$

Initially, we estimate the probability $p_{\mathrm{int},c}$ using eq 4.22, with $q_{c,h_0}^{\mathrm{shape}}$ being the propagator of a type "c" chain arising from solving Edward's diffusion equation (eq 4.1) with an additional constraint that the chains cannot propagate past the surface, $\partial \mathcal{R}_{h_0}$. To impose this constraint, we apply the Dirichlet boundary condition to all of the nodes that belong to this surface;

$q_c(\mathbf{r}, N) = 0, \; \forall \mathbf{r} \in \partial \mathcal{R}_{h_0}$. Subsequently, the number of chains ($n_{\text{ch},c}$) of type c that pass at least once through $\partial \mathcal{R}_{h_0}$ per unit area of the surface is calculated as follows:

$$n_{\text{ch},c}(h_0) = p_{\text{int},c}(h_0) \frac{1}{S_{h_0}} \frac{1}{N_c} \int_{\mathcal{R}} \rho_c(\mathbf{r}) d\mathbf{r} \tag{4.23}$$

where S_{h_0} is the surface area of $\partial \mathcal{R}_{h_0}$, and $\dfrac{1}{N_c} \displaystyle\int_{\mathcal{R}} \rho_c(\mathbf{r}) d\mathbf{r}$ is the total number of type-c chains.

At this point, we define a reference chain which obeys the Gaussian model and has infinite length. Given this definition, the reference chain will cross any shell-surface at least one time. Therefore, since the number of grafted chains equals $n_g = \sigma_g \, 4\pi R_{\text{NP}}^2$, the number of these reference chains passing through a surface separated by h from the surface of the solid per unit area of that surface is given by the following eq 4.24.

$$n_{\text{ch},g}^{\text{ref}} = \frac{n_g}{4\pi (R_{\text{NP}} + h)^2} = \sigma_g \left(\frac{R_{\text{NP}}}{R_{\text{NP}} + h} \right)^2 \tag{4.24}$$

In Figure 4.5(a), we present n_{ch} for the matrix and the grafted chains, while Figure 4.5(b) illustrates $n_{\text{ch},g} / \sigma_g$ for the grafted chains across the considered parameter space (R_{NP}, σ_g, M_g). In both panels, the corresponding $n_{\text{ch},g}^{\text{ref}}$ are represented by dotted lines.. In the flat geometry $n_{\text{ch},g}^{\text{ref}} = \sigma_g$ throughout the domain, while for finite curvatures, $n_{\text{ch},g}^{\text{ref}}$ decreases with distance from the surface according to eq 4.24, since the polymer chains have more available space to perform their walk.

The behavior of the chains per area profiles with increasing grafting density or molar mass is consistent with the reduced radial density profiles of Figure 4.4. For low nanoparticle radius, the chains per area profiles seem to be insensitive to the grafting density, a picture that is consistent with the mushroom regime. Higher grafting density or molar mass leads to a gradual extension of grafted chains towards the bulk region and a simultaneous exclusion of matrix chains from the solid-melt interface. For larger NPs and grafting densities, the crowding phenomena inside the interfacial region intensify and push the grafted chain segments further towards the bulk region.
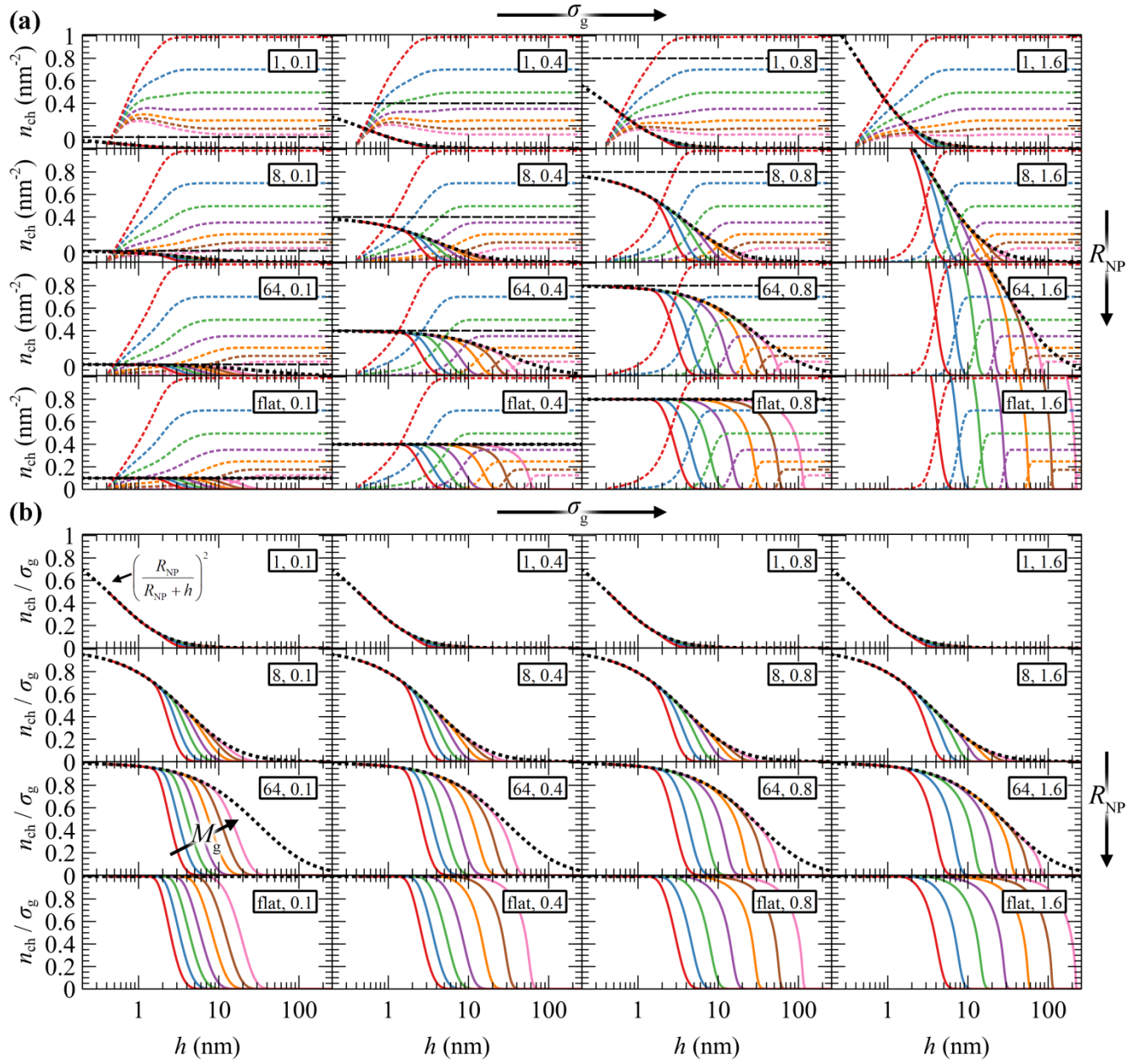
Figure 4.5. Profiles of **(a)** n_{ch} of m (dashed lines) and g (solid lines) chains, **(b)** n_{ch}/σ_g of g chains. M_g equals to 1.25 (red), 2.5 (blue), 5 (green), 10 (violet), 20 (orange), 40 (brown) and 80 (pink) kg/mol. In all cases, $M_g = M_m$. Legend in rectangles: R_{NP}(nm), σ_g(nm^{-2}). The dotted lines depict $n_{ch,g}^{ref}/\sigma_g$ for the reference chain from eq 4.24.

As expected, in the planar geometry case the number of grafted chains per area on the surface of the solid equals the grafting density throughout a broad region of the profile and starts to deviate upon approaching the region where ends terminate, where the number of grafted chains per area decreases. It is also noted that, since the hard sphere wall is located at ~0.4 nm from the solid surface, the maximum $n_{ch,g}$ assumed by the chains is $n_{ch} = \sigma_g R_{NP}^{2}/\left(R_{NP} + h_{HS}\right)^{2}$, albeit $n_{ch} = \sigma_g$ upon extrapolation towards $h \rightarrow 0$.

4.4.4 Chain End Segregation at the Interface

The reduced density of the sth segment, $\varphi_{c,N}$, of a chain of kind c located at $\mathbf{r}$ can be retrieved by the following expression:

$$\varphi_{c,s}(\mathbf{r}) = \frac{1}{N_c} q_c(\mathbf{r},s)\, q_m(\mathbf{r},N_c-s) \tag{4.25}$$

Normalizing this quantity with the corresponding density in the bulk phase ($\varphi_{c,N}^{\text{bulk}} = 1/N_c$; since $q = 1$ in the bulk), we obtain a quantity of particular interest, which denotes the tendency of a region to attract or repel these segments.

Figure 4.6 depicts the reduced radial density profiles of the end segments of grafted and matrix chains across the investigated parameter space. As expected, the density of free ends of grafted chains increases with increasing σ_g as well as with increasing R_{NP}, since there is less space for the grafted chains to develop their conformations. With increasing grafting density the radial density profiles of the chain ends are shifted towards the bulk region. In the crowding regime where σ_g and R_{NP} are high, the chain ends are segregated far from the surface, suggesting that the grafted chains are stretched. These profiles resemble those obtained for incompressible brushes, such as those in ref 283, and with the more extreme case of Alexander's model,[265,266] in which all chain ends are by definition concentrated at the edge of the brush, h_{edge}, the position of which is denoted by the vertical dotted lines in Figure 4.6 (for more details see appendixB.3). In the mushroom regime, the chain ends from Alexander's model are segregated much closer to the solid wall as compared to our model and this is attributed to the following factors: i) Alexander's model requires constant segment density of the grafted polymer, equal to that of the bulk melt; therefore, in the mushroom regime—where interpenetration between the matrix and grafted chains becomes significant—it needs to squeeze the profiles of grafted chain segments in order to maintain this bulk density and conserve the amount of material at the same time, ii) the segments in our model experience an additional repulsive interaction which is modeled by a hard sphere wall located at $h_{\text{HS}} \sim 0.4$ nm. Clearly, Alexander's model with fixed density is not appropriate for the mushroom regime and generally in regimes where the matrix chains can penetrate the brush. Nevertheless, Alexander's model is expected to perform very well under bad solvent conditions (e.g., polymer/vacuum interphases) which lead to collapsed brushes across the solid surface.
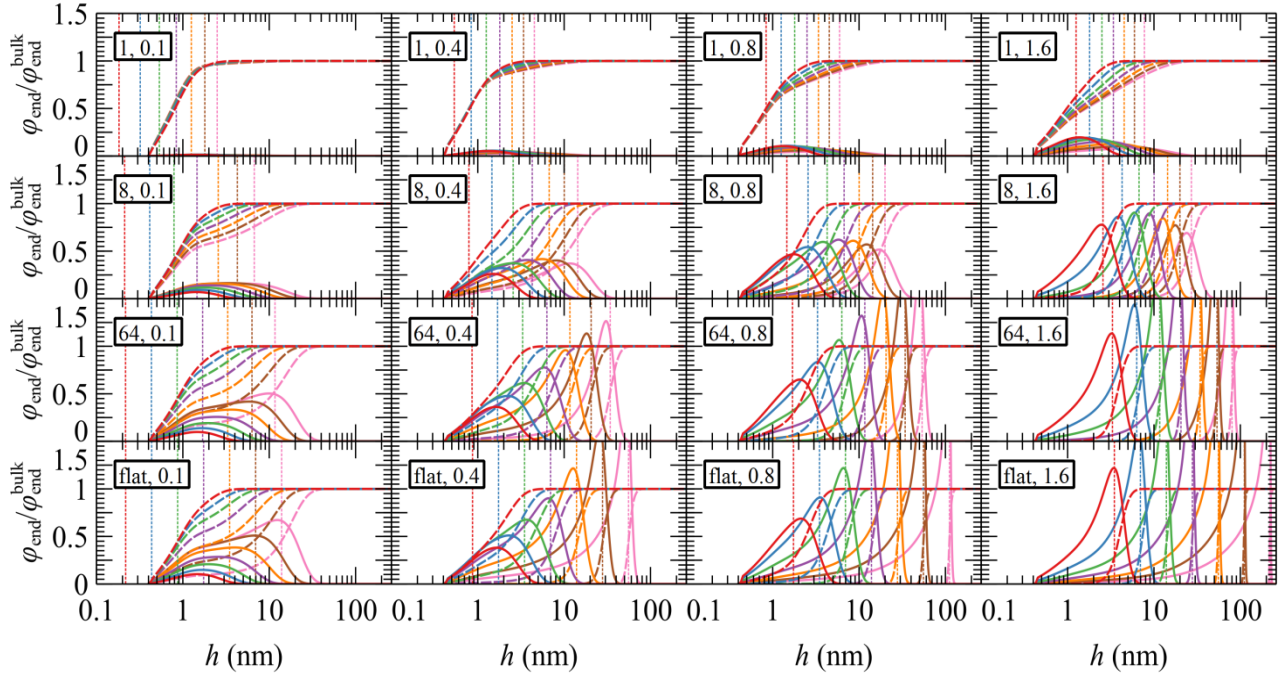
Figure 4.6. φ_{end} profiles of g (solid lines) and m (dashed lines) chains with molecular weight equal to 1.25 (red), 2.5 (blue), 5 (green), 10 (violet), 20 (orange), 40 (brown) and 80 (pink) kg/mol. The vertical dotted lines illustrate predictions for the position of chain ends from Alexander's model for the corresponding M_g, σ_g and R_{NP}. In all cases, $M_g = M_m$. Legend in rectangles: R_{NP}(nm), σ_g(nm^{-2}).

4.4.5 Scaling of Grafted Polymer Layers

As was mentioned in section 4.4.1/b, the expansion of the grafted polymer brushes features a complicated dependence on σ_g, R_{NP} and M_g. In the present section, an attempt will be made to analyze this dependence in terms of the mean brush thickness, $\left\langle h_g^2 \right\rangle^{1/2}$, which is directly related to the radial density profiles.[284] In particular, the mean brush thickness is a functional of the density profile illustrating the mean distance of the segments of grafted chains from the solid surface. It can be estimated from the following expression:

$$\left\langle h_g^2 \right\rangle^{1/2} = \left[\frac{\int_{\mathcal{R}} d\mathbf{r} \left[h(\mathbf{r}) \right]^2 \rho_g(\mathbf{r})}{\int_{\mathcal{R}} d\mathbf{r} \rho_g(\mathbf{r})} \right]^{1/2} \tag{4.26}$$

with $h(\mathbf{r})$ being the radial distance between a segment located at $\mathbf{r}$ and the solid surface. Another measure for quantifying brush thickness is the characteristic distance $h_{99\%}$ which is the distance between the *center of the nanoparticle* and a surface, $\partial \mathcal{R}_{h_{99\%}}$, which is parallel to the surface of the nanoparticle and encloses 99% of grafted chain segments:

$$\int_{\mathcal{R}_{99\%}} d\mathbf{r}\rho_g(\mathbf{r}) = 0.99 N_g n_g \qquad (4.27)$$

with $\mathcal{R}_{99\%}$ being the three-dimensional domain between $\partial\mathcal{R}_{solid}$ and $\partial\mathcal{R}_{h_{99\%}}$.

The scaling behavior of the polymer brushes shows quite a similar behavior to star polymers. According to Daoud and Cotton,[264] the radius of a star polymer (R_{star}) in a solvent exhibits a power-law dependence of the form: $R_{star} \sim N_{star}{}^n f_{star}{}^m \upsilon^k$, where N_{star} is the number of segments constituting a branch, f_{star} is the number of branches, $\upsilon = 0.5 - \chi$ is the monomer excluded volume parameter, χ is the Flory-Huggins parameter and n, m and k are the corresponding scaling exponents.[4,191,285] They[264] classified the behavior of the stars into three distinct regimes:

1. $N_{star} \gg f_{star}{}^{1/2}\upsilon^{-2}$, $R_{star} \sim N_{star}{}^{3/5} f_{star}{}^{1/5}\upsilon^{1/5}b_k$;

2. $f_{star}{}^{1/2}\upsilon^{-2} \gg N_{star} \gg f^{1/2}$, $R_{star} \sim N_{star}{}^{1/2} f_{star}{}^{1/4}b_k$;

3. $f_{star}{}^{1/2} \gg N_{star}$, $R_{star} \sim N_{star}{}^{1/3} f_{star}{}^{1/3}b_k$,

with b_k being the Kuhn length. By substituting $f_{star} \to \sigma_g$ and $N_{star} \to M_g$, and by ignoring the contribution of the core of the NP to the brush, the model by Daoud and Cotton[264] could be applied to describe the scaling of the polymer brushes via the following eq 4.28,

$$\langle h_g{}^2 \rangle^{1/2} = M_g{}^n \sigma_g{}^m l_g \qquad (4.28)$$

where l_g is a quantity with dimensions $(kg/mol)^{-n} nm^{2m+1}$.

Figure 4.7 illustrates evaluations for NPs with $R_{NP} = 8$ nm, from *RuSseL*, from *FOMC*[255] (blue "+") and from small angle neutron scattering (SANS)[260] measurements (red "×"). Overall, eq 4.28 can describe accurately the scaling of the PS brushes on SiO$_2$ nanoparticles with $R_{NP} = 8$ nm, since both $\langle h_g{}^2 \rangle^{1/2}$ and $\langle h_{99\%} \rangle$ appear to be proportional to $\sim M_g{}^{0.5}\sigma_g{}^{0.25}$. Note that the evaluations from *RuSseL* appear shifted with respect to *FOMC*. This is attributed to the fact that, in *FOMC*, the increased density near the solid increases the weight of smaller h_g in the integration of eq 4.26; thus, it leads to decreased overall $\langle h_g{}^2 \rangle^{1/2}$. In addition, $\lim_{M_g \to 0}\langle h_g{}^2 \rangle^{1/2} \sim 0$ in *RuSseL*, since the length of grafted chains goes to zero. For the same reasons, the $h_{99\%}$ points
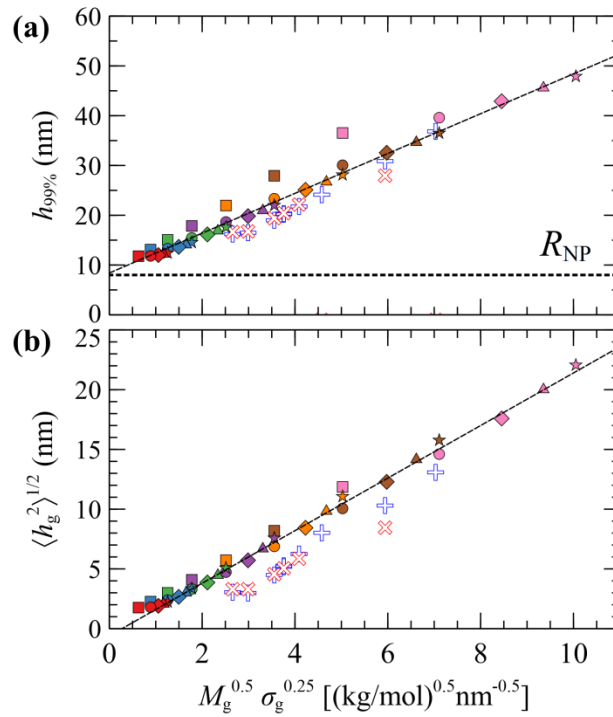
Figure 4.7. Evaluations of **(a)** $h_{99\%}$ and **(b)** $\langle h_g^2 \rangle^{1/2}$ as a function of $M_g^{0.5}\sigma_g^{0.25}$ for $R_{NP} = 8$ nm, from *FOMC* (+),[255] SANS measurements (×),[260] and *RuSseL*; in the latter, colors denote chains with $M_g = 1.25$ (red), 2.5 (blue), 5 (green), 10 (violet), 20 (orange), 40 (brown) and 80 (pink) kg/mol, and shapes denote grafting densities, $\sigma_g = 0.1$ (□), 0.4 (O), 0.8 (◇), 1.2 (△) and 1.6 (☆) nm^{-2}. The dashed lines are guides to the eye.

obtained with *RuSseL* lie slightly higher than *FOMC* and SANS values, while the minimum value of $h_{99\%}$ is equal to the radius of the nanoparticle. In the mushroom regime (square points in Figure 4.7), the evaluations from *RuSseL* deviate from the linear behavior and this could be a consequence of the fact that the one-dimensional model employed herein cannot capture accurately the behavior of chain segments for low grafting densities, i.e., the smearing of grafting points might be a poor approximation in this region. In our subsequent work, the mushroom regime will be thoroughly examined with the three-dimensional version of *RuSseL*.

In the following we test these scaling laws across the full parameter space explored herein. Figure 4.8(a-e) displays evaluations of $\langle h_g^2 \rangle^{1/2}$ plotted versus $M_g^{0.5}\sigma_g^{0.25}$ for NP with radius 1, 4, 16 and 64 nm as well as for flat surfaces, for various M_g and σ_g. An interesting behavior is manifested in these plots, which reveals three distinct regimes: i) for NP with small R_{NP} (e.g., Figure 4.8 (a)) the curves for specific M_g (same colors) are disconnected and feature a very weak slope; ii) for NP with intermediate sizes $R_{NP} = 4$-8 nm (e.g., Figure 4.8(b))
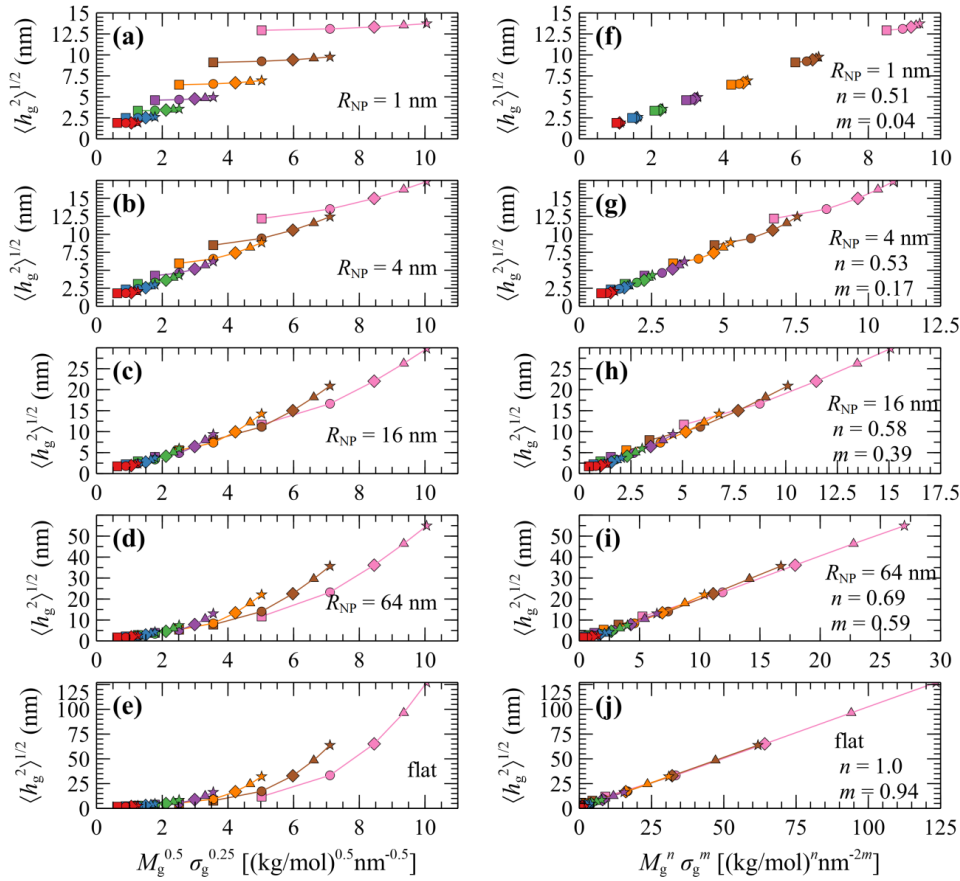
Figure 4.8. Evaluations of the mean brush thickness $\left\langle h_\text{g}^2 \right\rangle^{1/2}$ as a function of **(a-e)** $M_\text{g}^{0.5}\sigma_\text{g}^{0.25}$ and **(f-j)** $M_\text{g}^n \sigma_\text{g}^m$, where n, m are the optimized exponents from Figure 4.10a. Colors denote chains with M_g = 1.25 (red), 2.5 (blue), 5 (green), 10 (violet), 20 (orange), 40 (brown) and 80 (pink) kg/mol. Shapes denote grafting densities, σ_g = 0.1 ($\square$), 0.4 (O), 0.8 ($\diamond$), 1.2 ($\triangle$) and 1.6 ($\star$) nm^{-2}. In all cases, $M_\text{g}=M_\text{m}$.

the curves for specific M_g connect with each other, suggesting that the $\sim M_\text{g}^{0.5}\sigma_\text{g}^{0.25}$ correlation is fairly accurate in the description of this regime;[255] iii) for NP with larger sizes $R_\text{NP} > 8$ nm (e.g., Figure 4.8(c-e)) the curves appear disconnected as in the case of small NPs, the difference now being that the slope for each individual M_g curve appears to be stronger. The aforementioned analysis suggests that even though the $\sim M_\text{g}^{0.5}\sigma_\text{g}^{0.25}$ correlation appears to describe the brush scaling with reasonable accuracy for $R_\text{NP} \sim 4$-8 nm, it becomes inaccurate for NP with relatively large or small radius.

In view of these observations, one can optimize the n and m exponents for each R_NP to retrieve the power-law in eq 4.28. According to Figure 4.3, for constant R_NP and σ_g, the radial density profiles expand by a roughly constant factor when doubling M_g; thus, it is reasonable to assume that $\left\langle h_\text{g}^2 \right\rangle^{1/2} \sim M_\text{g}^n$ with n being a function of (R_NP, σ_g). Figure 4.9 presents the optimized

n	σ_g (nm^{-2})					
	0.1	0.4	0.8	1.2	1.6	fit
1	0.51	0.50	0.50	0.50	0.49	0.51
2	0.51	0.51	0.50	0.50	0.49	0.51
4	0.52	0.52	0.52	0.51	0.50	0.53
8	0.53	0.55	0.54	0.53	0.52	0.55
16	0.55	0.59	0.59	0.57	0.55	0.58
32	0.57	0.66	0.65	0.63	0.61	0.62
64	0.58	0.73	0.72	0.70	0.68	0.69
128	0.60	0.79	0.79	0.77	0.75	0.76
256	0.61	0.84	0.85	0.84	0.82	0.83
512	0.61	0.87	0.90	0.89	0.88	0.89
1024	0.62	0.89	0.93	0.93	0.92	0.94
2048	0.62	0.90	0.95	0.95	0.95	0.96
4096	0.62	0.91	0.96	0.97	0.97	0.98
8192	0.62	0.91	0.96	0.98	0.98	0.99
16384	0.62	0.92	0.97	0.98	0.98	0.99
flat	0.62	0.92	0.97	0.98	0.99	1.00

(leftmost label for rows: R_{NP} (nm))

Figure 4.9. Optimized n exponents of the power-law in eq 4.28 for set σ_g and R_{NP}. The rightmost column depicts the fit with eq 4.29.

n exponent from fitting *RuSseL* results to a power law $\langle h_g^2 \rangle^{1/2} \sim M_g^{\,n}$ over all R_{NP} and σ_g. The reader is reminded that the 1D model employed here might not be able to describe accurately the chain configuration at low grafting densities or molecular weights of grafted chains due to the inevitable smearing of grafting points. For this reason we decided to not take into account the cases corresponding to values of $\sigma_g R_g^2 < 3$, and $\sigma_g = 0.1$ nm^{-2} (which excluded the larger part of cases corresponding to the mushroom regime) when fitting the scaling exponents for the master equation, eq 4.28.

For large σ_g, the exponent n presents a stronger dependence on R_{NP} than σ_g; thus, for simplicity, one could treat n as being independent of σ_g and instead being function of only R_{NP}. Consequently, the data for $\sigma_g > 0.1$ nm^{-2} were fitted to a sigmoid function of the form:

$$n = n_{min} \left[\frac{1}{2} \tanh \left(n_s \ln \left(R_{NP} / R_d \right) \right) + \frac{3}{2} n_{max} \right] \tag{4.29}$$

with $n_{min} = 0.5$ and $n_{max} = 1$ being the minimum and maximum values of n, $R_d = 126.5$ nm and $n_s = 0.4$. Subsequently, with n set, one can optimize the exponent of σ_g with respect to R_{NP} aiming at aligning the data points for a given R_{NP}. Figure 4.8(f-j), displays evaluations of $\langle h_g^2 \rangle^{1/2}$ using the optimized n and m exponents in Figure 4.10(a). Using the optimized n and m exponents, $\langle h_g^2 \rangle^{1/2}$ increases linearly with $M_g^{\,n} \sigma_g^{\,m}$ over the full range of R_{NP} (from 1 nm to ∞).
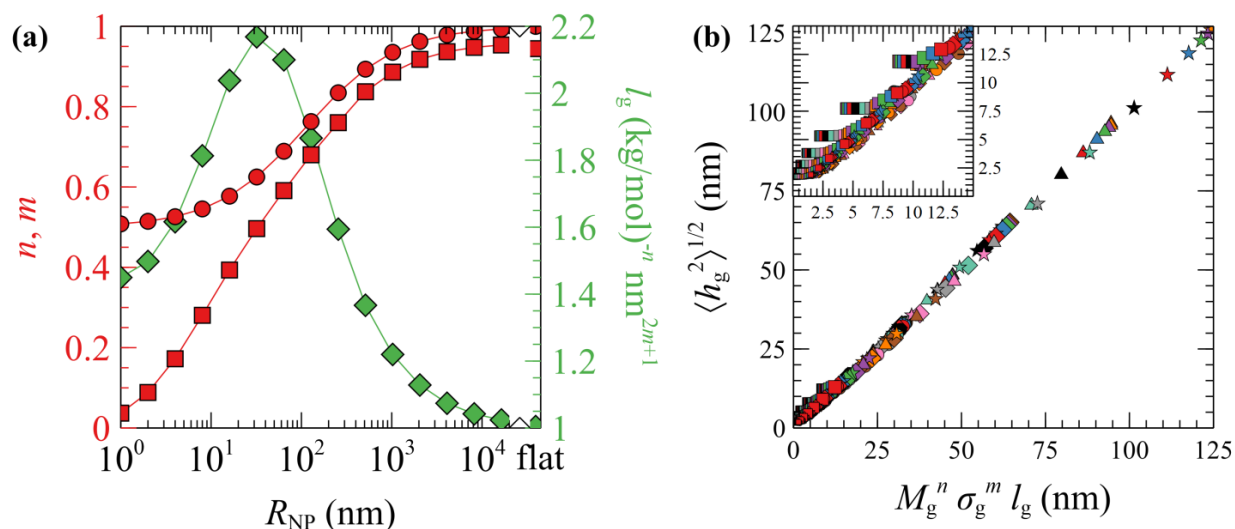
Figure 4.10. (a) The optimized n (circles) and m (squares) exponents of eq 4.28 and l_g (diamonds) as functions of R_{NP}. The rightmost data points correspond to flat surfaces. **(b)** Evaluations of eq 4.28 using the n, m and l_g parameters in (a). Colors denote chains with $M_g = 1.25$ (red), 2.5 (blue), 5 (green), 10 (violet), 20 (orange), 40 (brown) and 80 (pink) kg/mol. Shapes denote grafting densities, $\sigma_g = 0.1$ (□), 0.4 (O), 0.8 (◇), 1.2 (△) and 1.6(☆) nm^{-2}. The size of the symbols increases slightly with R_{NP}. The inset in (b) depicts a zoomed region of the master curve. In all cases, $M_g = M_m$.

In addition, the curves in Figure 4.8 can be collapsed onto the master curve shown in Figure 4.10(b), where $\left\langle h_g^2 \right\rangle^{1/2}$ is plotted against eq 4.28 with l_g being the slope of the individual curves in Figure 4.8(f-j) (see green diamonds in Figure 4.10(a)). Overall, the data points in Figure 4.10(b) are in good quantitative agreement with eq 4.28, with the exception of the low M_g, σ_g regime where $\left\langle h_g^2 \right\rangle^{1/2}$ plateaus; see zoomed region in the inset of Figure 4.10(b). The plateaus of $\left\langle h_g^2 \right\rangle^{1/2}$ in the limit of small σ_g and M_g could be artifacts of SCFT; our subsequent investigations with *RuSseL* in 3D will clarify the phenomena that manifest themselves in this regime.

Several key points can be retrieved by analyzing the scaling behavior of the brushes. Across the mushroom regime (small R_{NP} or small σ_g), $\left\langle h_g^2 \right\rangle^{1/2}$ is independent of σ_g and R_{NP} and scales as $M_g^{0.5}$. This is a characteristic property of the mushroom regime in which the grafted chains do not interact with each other and behave as (reflected) ideal/unperturbed chains. With increasing R_{NP} and increasing σ_g the n and m exponents increase, while in the limit of large R_{NP} and σ_g (crowding regime) the exponents reach unity indicating linear scaling, $\left\langle h_g^2 \right\rangle^{1/2} \sim M_g^1 \sigma_g^1$; this kind of scaling is characteristic of the incompressible Alexander brushes;[265,266] for more details see appendixB.3.
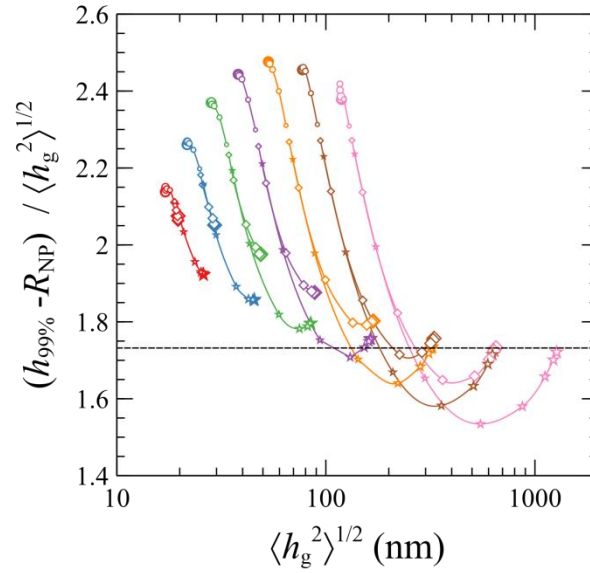
Figure 4.11. Ratio $\left(h_{99\%} - R_{NP}\right)/\left\langle h_g^2\right\rangle^{1/2}$ vs $\left\langle h_g^2\right\rangle^{1/2}$. Colors denote chains with M_g = 1.25 (red), 2.5 (blue), 5 (green), 10 (violet), 20 (orange), 40 (brown) and 80 (pink) kg/mol. Shapes denote grafting densities, σ_g = 0.1 (O), 0.8 ($\Diamond$), and 1.6 ($\star$) nm^{-2}. Increasing marker sizes correspond to larger R_{NP}.

In Figure 4.11, we demonstrate the $(h_{99\%} - R_{NP})$ to mean brush thickness ratio against the mean brush thickness. In the Alexander model, this ratio is constant and equal to $3^{1/2}$ and corresponds to the horizontal dashed line. Regarding our SCFT results, for small grafted chain lengths, the ratio is higher than the one of Alexander for all grafting densities and nanoparticle radii. For higher chain lengths, a minimum is manifested, while in the dense brush regime the ratio reaches the Alexander value as a limiting case. Overall, for small grafting density (0.1 nm^{-2}) the dependence on the nanoparticle radius (ratio increasing with increasing R_{NP}) features opposite trends as compared the one for larger grafting densities (ratio decreasing with increasing R_{NP}).

4.4.6   Thermodynamics

4.4.6/a Contributions to the Grand Potential

In Figure 4.12, the plots (a-e) depict the individual grand potential terms (eqs 4.8-4.12) over the parameter space (R_{NP}, σ_g, M_g). Regarding the cohesive interaction term per unit solid surface ($\Delta\Omega_{coh} / S_{solid}$ in Figure 4.12(a)), it decreases steeply in the vicinity of small R_{NP} and this is attributed to the fact that when high curvatures are involved (small R_{NP}), the surface of the spherical cells where we integrate $\Delta\Omega_{coh}$ is larger than the surface S_{solid} of the NP by which we

normalize all energy quantities, by a factor, $\left(R_{NP}+h\right)^2/R_{NP}{}^2$. At low grafting densities (mushroom regime, circles in Figure 4.12(a)), $\Delta\Omega_{coh}/S_{solid}$ appears to be insensitive to M_g for M_g up to 80 kg/mol; i.e., all different colored lines with circular markers collapse onto the same curve in Figure 4.12(a). With increasing grafting density (squares and stars in Figure 4.12(a)), $\Delta\Omega_{coh}/S_{solid}$ deviates notably with increasing M_g and increasing R_{NP}. This is attributed to ρ_g exceeding $\rho_{seg/bulk}$ due to chain crowding and this enhances the cohesion of the brush when the SL-EoS is used. In detail, the minimum of $f(\rho)-f(\rho_{bulk})$ for SL is about –0.5 mJ/m^3 for reduced densities slightly larger than one; thus, the accumulation of these negative values over the integration of larger and larger brushes due to crowding leads to the eventual decrease of $\Delta\Omega_{coh}/S_{solid}$.

Similarly, the field term ($\Delta\Omega_{field}/S_{solid}$ in Figure 4.12(b)) presents the same qualitative behavior as $\Delta\Omega_{coh}/S_{solid}$ for the exact same reasons: i) steep initial decline due to high curvature; ii) accumulation of negative values by integrating over gradually larger brushes.

Considering the solid-polymer interaction term (U_s/S_{solid}), it is practically insensitive to chain molar mass; i.e., in Figure 4.12c the energies for different chain molar masses do not exhibit noticeable variations with each other, irrespectively of NP size. With increasing grafting density it is clear that the cohesion between the solid and the polymer is enhanced because of the increased density of polymer segments close to the surface.

In all cases, the entropy term associated with the partition function of matrix chains ($\Delta\Omega_m/S_{solid}$ in Figure 4.12(d)) appears to be rather weak. It shifts upwards by a constant amount with increasing grafting density, because grafted chains claim more space in the interfacial region, leaving the matrix chains with fewer available conformations.

Concerning the entropy term associated with the grafted chains ($\Delta A_g/S_{solid}$ in Figure 4.12(e)), it exhibits a rather interesting behavior: in the mushroom regime ($\sigma_g = 0.1$ nm^{-2}), $\Delta A_g/S_{solid}$ appears to be flat and roughly equal to zero, indicating that for low grafting densities there is no entropic penalty with increasing R_{NP} associated with chain conformations. On the contrary, for larger σ_g (squares and stars), $\Delta A_g/S_{solid}$ increases with R_{NP} for R_{NP} up to ~100 nm and plateaus to finite values in the limit of flat surfaces. This response is attributed to the

stretching of the grafted chains due to crowding phenomena. A direct manifestation of this effect is presented in Figure 4.12 that depicts the segregation of the grafted chain ends towards the matrix phase in crowded conditions.
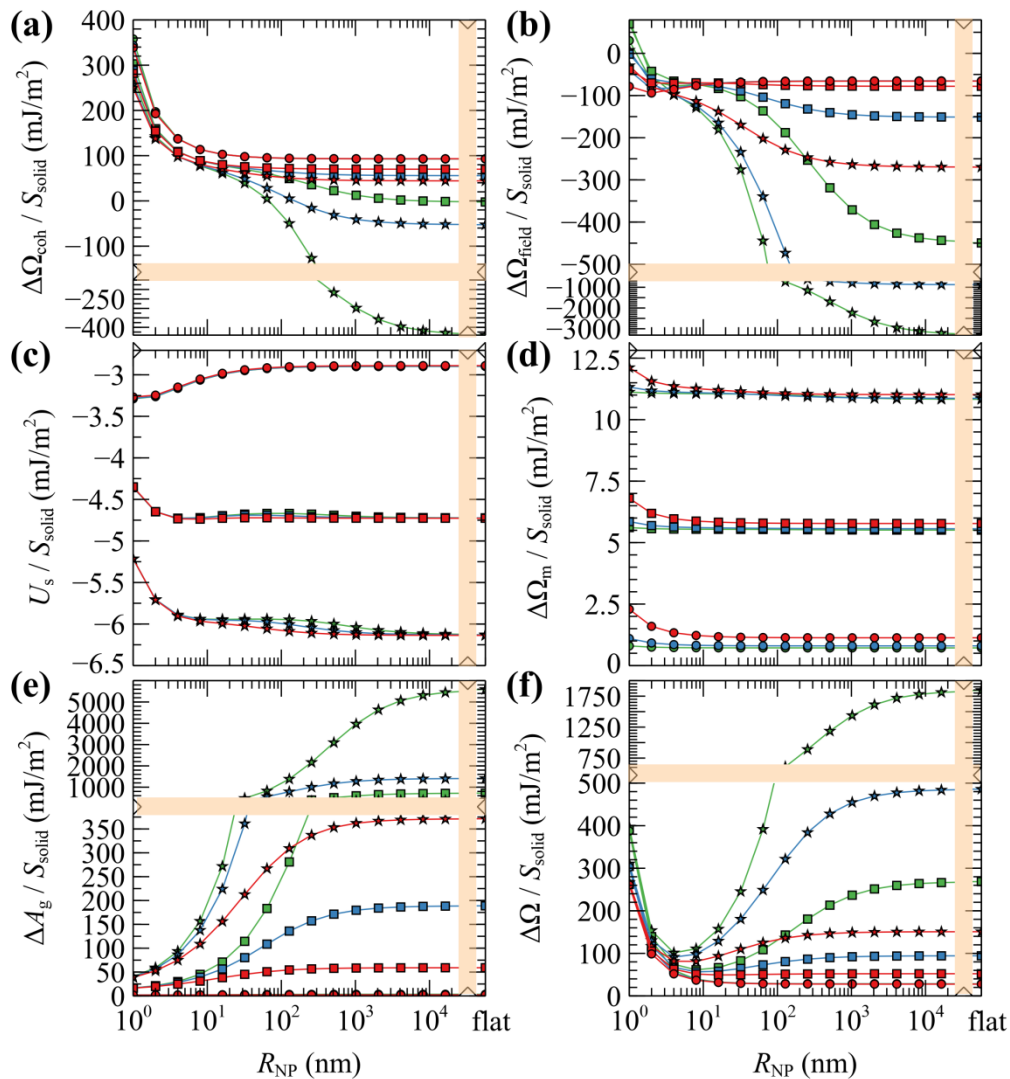
Figure 4.12. Partial contributions to the grand potential per unit area **(a-e)** from eqs 4.8-4.12. Total grand potential per unit area. **(f)** Colors denote chains with $M_g = 5$ (red), 20 (blue) and 80 (green) kg/mol. Shapes denote grafting densities, $\sigma_g = 0.1$ (O), 0.8 ($\square$) and 1.6 ($\star$) nm^{-2}. In all cases, $M_g = M_m$. The rightmost data points correspond to flat surfaces. Bands denote scale changes along the axes.

The total grand potential from eq 4.7 is illustrated in Figure 4.12(f). Across the mushroom regime ($\sigma_g = 0.1$ nm^{-2}, circles) $\Delta\Omega / S_{solid}$ exhibits a monotonic decrease and plateaus to a value commensurate to the surface tension of PS for $R_{NM} \geq 100$ nm which is about $\gamma_{PS} \sim 25.9$ mN/m at $T = 500$ K;[26] note that, in the limiting case $\sigma_g \rightarrow 0$ and $R_{NP} \rightarrow \infty$, and in the absence of the Hamaker potential, $\gamma_{PS} \equiv \Delta\Omega / S_{solid}$. With increasing σ_g, the grand potential

features a minimum at $R_{NP} \sim 10$ nm, after which it increases in a way suggesting the domination of the stretching term in Figure 4.12(e).

4.4.6/b Contributions to Chain Stretching

The entropy term associated with the grafted chains in Fig. 4e does not reflect the total conformational contribution to the grand potential, since the partition function in eq 4.12 is evaluated in the presence of the field. Therefore, in terms of SCFT, the free energy associated with the conformations of the grafted chains can be estimated by the following eqs 4.30 and 4.31

$$A_{conf}^{g} = \Delta A_{g} + \Delta A_{field}^{g} \tag{4.30}$$

with ΔA_{field}^{g} being the field experienced by the grafted chains:

$$\Delta A_{field}^{g} = -\int_{\mathcal{R}} d\mathbf{r} \left\{ \sum_{i_g=1}^{n_g} \rho_{g,i_g}(\mathbf{r}) w_{ifc}'(\mathbf{r}) \right\} \tag{4.31}$$

with ρ_{g,i_g} being the segment density associated with the i_g^{th} grafted chain.

At this point, it is worth analyzing and comparing the conformational free energy of grafted chains with the stretching free energy obtained by the density profiles of the grafted chain ends. In the one-dimensional model employed herein, the grafted chain conformations are reflected random walks starting at h_g. Assuming that the system finds itself in the dense brush, rather than in the mushroom regime, the number of conformations of a chain such that the end-to-end vector projection normal to the solid surface is between h and $h+\Delta h$, is the same as in the unperturbed melt. It will be proportional to $f_{end}(h)dh$, where the probability density $f_{end}(h)$ is given by eq 4.32 in the context of the Gaussian chain model.

$$f_{end}(h) = \left(\frac{3}{2\pi \left\langle R_{end,g}^{2} \right\rangle} \right)^{1/2} \exp\left(-\frac{3 h^2}{2 \left\langle R_{end,g}^{2} \right\rangle} \right), \quad h > 0 \tag{4.32}$$

Note that this is based on the approximation that a grafted chain will access all conformations accessible to it at given value of the end-to-end distance. In reality, as is obvious from the profiles in Figure 4.5 and Figure 4.6, grafted chains are more stretched near their grafted end and less stretched near their free end. Based on eq 4.32, the Helmholtz energy contribution, A_{chain}, of a Gaussian chain grafted at $\mathbf{r}_{i_g}$ whose end lies at point r, is given by eq 4.33 within an additive

constant. In eqs 4.32 and 4.33 $\left\langle R_{\text{end,g}}^{2} \right\rangle$ is the mean square end-to-end distance of an unperturbed chain of length N_{g}.

$$A_{\text{chain}}(\mathbf{r}) = \frac{3k_{\text{B}}T}{2} \frac{\left(\mathbf{r} - \mathbf{r}_{i_{\text{g}}}\right)^2}{\left\langle R_{\text{end,g}}^{2} \right\rangle} \tag{4.33}$$

Let $\rho_{\text{g,end}} = \varphi_{\text{g,end}}\rho_{\text{seg,bulk}}$ be the local number density (segments per unit volume) of free ends of grafted chains; note that each grafted chain contributes one free end. Consecutively, integrating $\rho_{\text{g,end}}$ across the domain results to the total number of chains; $\int_{\mathcal{R}} \rho_{\text{g,end}}(\mathbf{r})\mathrm{d}\mathbf{r} = n_g$. The total stretching free energy of grafted chains in our system within an additive constant equals $A_{\text{stretch}}^{\text{g}} = \int_{\mathcal{R}} \rho_{\text{g,end}}(\mathbf{r}) A_{\text{chain}}(\mathbf{r}) \, \mathrm{d}\mathbf{r}$, and it can be approximated across the dense brush regime as

$$A_{\text{stretch}}^{\text{g}} \sim \int_{\mathcal{R}} \rho_{\text{g,end}}(h) A_{\text{chain}}(h) \, 4\pi \left(R_{\text{NP}} + h\right)^2 \mathrm{d}h \tag{4.34}$$

in spherical and

$$A_{\text{stretch}}^{\text{g}} \sim \int_{\mathcal{R}} \rho_{\text{g,end}}(h) A_{\text{chain}}(h) \, S_{\text{solid}}\mathrm{d}h \tag{4.35}$$

in planar geometries.

In the special case of Alexander's model in which all chain ends are segregated at the edge of the film, $\rho_{\text{g,end}} = \sigma_{\text{g}}\delta(h - h_{\text{edge}})$, thus eq 4.34 becomes:

$$A_{\text{stretch}}^{\text{g}} \sim S_{\text{solid}}\sigma_{\text{g}} A_{\text{chain}}(h_{\text{edge}}) \tag{4.36}$$

with h_{edge} given by eq B.56 in the appendix B.3. In Figure 4.13, we demonstrate a comparison between the stretching energy term obtained by the Alexander model (lines) and our SCFT model (markers); the latter is calculated either from: (a) $A_{\text{conf}}^{\text{g}}$ given by eq 4.30, or (b) $A_{\text{stretch}}^{\text{g}}$ given by eqs 4.34 and 4.35. We mention at this point that the Alexander model, which we develop in our SI, is similar to the h_{dry} region that Mydia et al.[267] report in the context of their two-layer theoretical model for the description of nanoparticle brushes. In that work,[267] the authors state that in curved surfaces and for constant grafting density, the free energy associated with the stretching of grafted chains does not increase indefinitely with increasing length of grafted chains, but it rather saturates at a maximum value. This is well expected, since at some

point the grafted chains cannot experience the presence of each other due to the curvature of the solid surface and therefore they become unperturbed. It must be pointed out, however, that in the case of planar surfaces, the grafted chains experience the presence of each other indefinitely due to confinement and thus $A_{\text{stretch}}^{\text{g}}$ increases monotonically with N_{g} in this regime. Our model is consistent with this behavior: $A_{\text{stretch}}^{\text{g}}$ and $A_{\text{conf}}^{\text{g}}$ are about to form a plateau with increasing N_{g} across the small R_{NP} regime, whereas in the limit of flat surfaces they appear to increase indefinitely with N_{g}.
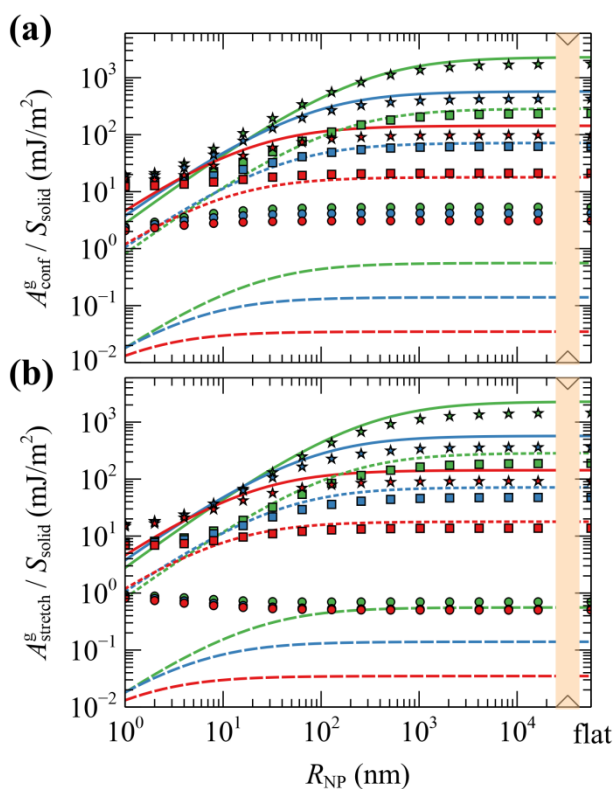
Figure 4.13. Evaluations of **(a)** $A_{\text{conf}}^{\text{g}}$ and **(b)** $A_{\text{stretch}}^{\text{g}}$. Markers correspond to evaluations from our model, whereas lines correspond to $A_{\text{stretch}}^{\text{g}}$ from the model of Alexander. Colors denote chains with $M_{\text{g}} = 5$ (red), 20 (blue) and 80 (green) kg/mol. Shapes/lines denote grafting densities, $\sigma_{\text{g}} = 0.1$ (O / dashes), 0.8 ($\square$ / dots) and 1.6 ($\star$/ Solid lines) nm^{-2}. In all cases, $M_{\text{g}} = M_{\text{m}}$. The rightmost data points correspond to flat surfaces.

We can see that for larger grafting densities, our SCFT results and Alexander's model are in good agreement for all chain lengths in describing the conformational entropy of grafted chains as a function of the nanoparticle radius. A large discrepancy between the two models occurs for low grafting density; there, the totally stretched chains assumption of the Alexander model and the requirement to maintain bulk density everywhere result in suppressed grafted

chains and thus lower $A_{\text{stretch}}^{\text{g}}$ (compare the evaluations of Alexander's model at low grafting densities in Figure 4.6). On the contrary, in the mushroom regime the profiles of grafted chains obtained with our model appear broader and this is reflected in the increased contribution to the conformational component of the free energy. $A_{\text{stretch}}^{\text{g}}$ is consistently lower than $A_{\text{conf}}^{\text{g}}$ — especially at low σ_{g}—and this is attributed to approximations in eqs 4.34 and 4.35 not sufficing in the regime; this effect will be investigated in detail in our subsequent work with *RuSseL* in three dimensions.

4.5 Concluding Remarks

The conformation and shape of chains grafted on a solid surface immersed in a homopolymer melt of the same chemical constitution as the grafted chains are complex and depend on a number of molecular parameters. In this work, we have explored a broad parameter space for a system of a single grafted nanoparticle immersed in a homopolymer matrix. Adopting a self-consistent field theory modeling approach, the Edwards diffusion equation is solved by means of an implicit finite-difference algorithm in one dimension, introducing a smearing approximation for grafting points and taking advantage of the spherical symmetry of the problem. The parameterization is chosen so as to correspond to a particular chemical constitution (silica/polystyrene), which is readily accessible experimentally.[260]

The spatial distributions and the conformations of grafted and matrix chain segments have been derived for different surface grafting densities, nanoparticle radii and chain lengths of grafted chains, taken equal to those of matrix chains. In order to better describe the results of our work, we define three different regimes: the mushroom regime, the dense brush regime, and the crowding regime. The behavior of the system in each of these regimes is well described and quantified in multiple ways, namely through the chains/area profiles, the distribution of matrix and grafted chain ends, as well as the segment density profiles of adsorbed and free matrix chains. It is clear that with increasing grafting density and chain molar mass, the grafted chains need to stretch towards the bulk in order to adjust to their conformational restriction[255,260,264]. As a result, it is more difficult for the matrix chains to penetrate into the interfacial region.

The dependence of the brush thickness is examined with respect to all the aforementioned parameters in order to thoroughly investigate and clarify the behavior reported

in the literature. The scaling law, $\sim N_{star}^{1/2} f_{star}^{1/4}$, proposed by Daoud and Cotton for star polymers in the intermediate regime, $f_{star}^{1/2} \upsilon^{-2} \gg N_{star} \gg f^{1/2}$, is accurate over a specific range of nanoparticle radii, specifically from 4 nm to 8 nm. For larger nanoparticles, the scaling exponents exhibit a complicated behavior and thus a more general equation must be implemented, which treats the exponents of the molecular weight and grafting density as functions of nanoparticle radius. Adjusting also the pre-exponential factor of the scaling law, a master curve can be obtained, which provides a faithful description of SCFT predictions for the brush height given the molecular weight of grafted chains, the grafting density and the radius of the nanoparticle. This master curve seems to be quite accurate, especially in the region of high molecular weight and grafting density. In the mushroom regime, the brush height exhibits a weak dependence on the grafting density and nanoparticle radius and is proportional to the square root of the molecular weight. In the crowding regime the brush scales linearly with grafting density and molecular weight, while the density profiles of grafted chains, and in general the overall behavior of the brushes, compares well with Alexander's model for incompressible brushes.

In calculating the free energy of the system, the term associated with the conformational entropy of grafted chains does not depend on nanoparticle radius for low grafting densities and molar masses (Figure 4.4(e)). The same plot reflects that with increasing grafting density or molar mass the chains need to stretch and therefore entropy increases. This entropy contribution of the grafted chains becomes dominant for high grafting densities and molar masses. The stretching free energy of grafted chains has been estimated with two different ways (1: from the configurational partition function of grafted chains and 2: from the density profiles of the grafted chain ends) and a good agreement with the Alexander model was observed in the limit of large grafting densities. The corresponding entropic term of matrix chains has a minor contribution to the total free energy.

Future prospects of this study include the investigation of the structure and thermodynamics of isolated NP and comparison against those of a NP embedded in polymer matrices; such comparisons allow for the prediction of meaningful thermodynamic quantities such as the solvation free energy of the nanoparticle. A more detailed investigation can be performed across the mushroom regime for low σ_g and R_{NP} via the three-dimensional finite element version of *RuSseL* developed in ref 275, which treats the grafted chains as single

entities, each one emanating from a single grafting point, avoiding the smearing approximation. Through the same three-dimensional finite element scheme, the potential of mean force between grafted NPs immersed in the melt can be predicted as a function of their center-to-center distance.

5 A Self-Consistent Field Finite Element Method

A method is formulated, based on combining self-consistent field theory with the finite element method (SCFFEM), for studying structural and thermodynamic features of three dimensional inhomogeneous polymeric systems. Initially, this approach is tested on a planar polyethylene/ vacuum and a polyethylene/ graphite system, where the whole methodology is parameterized by atomistically detailed molecular simulations. These systems have been studied previously with one dimensional SCF methods. The new, three-dimensional SCFFEM approach is used to predict reduced density profiles and interfacial free energies, yielding very favorable agreement with previous SCF results, thus validating the SCFFEM methodology. The primary objective of this work is to investigate the system behavior by implementing the finite element method. We apply an *h-*, *r-*, *p-* refinement technique to optimize the finite element mesh. Furthermore, we introduce two new criteria for accurate convergence and an innovative successive substitution scheme. The resulting scheme is employed to analyze a more complicated system consisting of polystyrene brushes grafted on silica walls immersed in polystyrene. Up to now, the grafted chains in such systems have always been subjected to a smearing technique. With the three-dimensional SCFFEM approach we can distinguish the positions where individual grafted chains are tethered from positions on the surface which do not bear grafted chains. We compare the reduced density profiles and end segment distributions along various lines connecting two parallel planar silica surfaces capping a polystyrene melt in a sandwich geometry and bearing surface-grafted polystyrene chains at prescribed areal density. The lines are drawn perpendicular to the silica surfaces at various positions relative to the grafting points. The structural properties and grand potential contributions of the system are obtained for a broad range of grafting

densities, molar masses and swelling ratios, and are compared to experimental data, theoretical models, and earlier one-dimensional (smeared) SCF studies.

5.1   Background

The fascinating and complex behavior of polymers near solid surfaces challenges the limitations of atomistic simulations, due to the broad spectra of time and length scales involved.[31] On one hand, one of the most common approaches invoked for studying equilibrium properties of polymer/solid interfaces at the molecular level is the Self Consistent Field Theory (SCFT).[26,133,197,215,286] On the other hand, the Finite Element Method (FEM) is an important and widespread technique in the field of integrodifferential equations which govern a lot of applications of physics and engineering.[287–289] In this chapter, we aim to combine these tools in order to develop the ability to calculate the free energy and the structure of complex three-dimensional (3D) multi-nanoparticle configurations of polymer nanocomposites.

As we already proved in the previous chapters, SCFT constitutes a rather successful framework in the study of the structure and the thermodynamic description of an interfacial polymer system. Mathematically, the SCFT model is derived through a complicated variational problem, possessing many unsatisfactory features, such as the existence of saddle-points, nonlinearity, multi-solutions, and multi-parameters. Solving this problem analytically requires rough approximations, compelling analytic solutions to be quite limited in applicability, because they demand the system to have very particular properties.[155] In most cases of interest, numerical methods are required to solve the set of integro-differential equations.

The numerical methods for solving the SCFT model mainly consist of four components, namely: (a) screening initial values[290–292], (b) solving time-dependent partial differential equations (PDEs), (c) evaluating (monomer) density operators, and (d) finding saddle-points via iterative methods.[293,294] By far the second component i.e. solving the time-dependent PDE is the most CPU consuming process in applying the SCFT algorithm. The time-dependent PDEs can be solved with either frequency domain approaches (e.g. spectral, pseudo spectral methods)[144,290] or real space approaches (e.g finite difference, finite volume, finite element methods).[275] The simplicity of finite difference methods and the high spatial accuracy achieved by spectral methods made them an excellent choice for many applications till now. Nonetheless, the majority of the systems which have been addressed with these methods exhibit a simple or

symmetric geometry and limitations on the boundary conditions. These hindrances can be overcome with the FEM.

5.1.1 Numerical Methods Comparison

FEM is used to solve partial differential equations (PDEs) in a variety of scientific and engineering problems.[295,296] Despite the fact that FEM belongs to real space approaches, it is quite similar in philosophy to spectral algorithms. The basic idea is to assume that the unknown variables can be approximated by a linear combination of trial functions (a.k.a. basis functions). The essential difference from spectral methods is that in FEM, the domain of interest is divided into a finite number of sub-intervals, while the basis functions are locally defined in each interval. Practically, the basis functions are usually chosen to be simple polynomials of fixed degree, which are non-zero only over a couple of neighboring sub-intervals. In contrast, spectral methods use global basis functions in which basis function is a polynomial (or trigonometric polynomial) of high degree which is non-zero, except at isolated points, over the entire computational domain.[297]

The choice of the finite element method is beneficial for various reasons compared to spectral methods. FEM converts the strong form of the differential equation into a linear system of equations, which is usually sparse, since only a handful of basis functions are non-zero in a given sub-interval. It can also be implemented in irregularly shaped systems and multi-dimensional domains; the sub-intervals become triangles or tetrahedra, which are easily fitted in complex geometries. The main weakness of FEM is low accuracy (for a given number of degrees of freedom) because each basis function is a polynomial of low degree.[297] The accuracy weakness though can be surpassed either by improving the resolution of certain regions of the domain, or by increasing the degree of the interpolation polynomials.[298]

5.1.2 FEM History

The mathematical roots of the finite element method date back at least half a century. Approximate methods for solving differential equations using trial solutions are even older in origin. Lord Rayleigh and Ritz used trial functions to approximate solutions of differential equations.[289] Galerkin used the same concept for the solution of PDEs.[297] The drawback of the earlier approaches, compared to the modern finite element method, is that the trial functions must apply over the entire domain of the problem of concern. Only when Courant in the

1940s[299] introduced the concept of piecewise-continuous functions in a subdomain did the finite element method have its real start. In the late 1940s, aircraft engineers were dealing with the invention of the jet engine and the needs for more sophisticated analysis of airframe structures to withstand larger loads associated with higher speeds. The term finite element was first used by Clough[300] in 1960 in the context of plane stress analysis and has been in common usage since that time.

The finite element method is computationally intensive, due to the large amount of required operations on large matrices. In the early years, applications were performed using mainframe computers, which, at the time, were considered to be powerful high-speed tools for use in engineering analysis. NASTRAN was the first structural analysis software tool, which implemented the available FEM technology. [298] It was originally developed for NASA in the late 1960s under United States government funding for the aerospace industry. In the years since the development of NASTRAN, many commercial software packages have been introduced for finite element analysis. In today's computational environment, most of these packages can be used on desktop computers and engineering workstations to obtain solutions to large problems in static and dynamic structural analysis, heat transfer, fluid flow, electromagnetics, and seismic response. [289]

5.1.3 Previous Works

Although FEM is a workhorse for solving computational problems in all branches of engineering, few studies have been published on applications to molecular problems, and especially in conjunction with SCF. Ackerman et al [156] used the FEM as an alternative to the standard spectral and pseudo-spectral methods for SCF calculations. They investigated the details of the implementation on block copolymer systems of self-assembled structures in complex geometries. Huayi Wei et al[155] proposed a linear surface FEM to solve the SCFT model and studied the self-assembly behaviors of block copolymers on general curved surfaces. An essential point missing from both works is that they mainly illustrate confinement effects for specific geometries, without being concerned about how representative of the real world the system is. The extension of SCF computational framework to more realistic polymeric systems remains a problem to be explored.

Another limitation of previous works is that they are mainly focused on block copolymer systems. Even though SCF approaches to polymer melts at interfaces have been validated

against detailed atomistic simulations, few researchers have addressed structural and thermodynamic properties through SCFT for realistic polymeric systems and interfaces. Daoulas et al.[24] determined the equilibrium properties, calculated polymer volume fraction profiles for a polymer melt (polyethylene) adsorbed on a solid substrate (graphite) and compared it with atomistic simulations. Theodorou et al.[31] calculated the adhesion tension of the above system through SCFT, which is in good agreement with the adhesion tension estimated by atomistic MD simulations. More recently, we[26] implemented SCFT for free surfaces of molten polymers (linear polyethylene films) and compared the results against atomistic simulations and experiment over a variety of temperatures and chain lengths. All the above works were based on the one-dimensional representation of the interfacial systems, but they form a basis for validating the new three-dimensional FEM approach.

Our goal is the implementation of the SCFFEM to more complex systems containing grafted polymer chains. Polymer brushes, i.e., chains grafted either on spherical nanoparticles or on planar surfaces, have gained attention because of their uses in a variety of applications such as flocculation control, wetting control, biocompatible surfaces, tunable and switchable surfaces, lubrication, and templates for microelectronic devices.[301–304] Various methods for the experimental synthesis of such systems are reported in the literature.[305,306] The system of a polymer brush grafted to a planar surface in contact with a melt of chemically identical chains is useful for understanding polymer brushes grafted on spherical nanoparticles immersed in polymer melts. Although numerous experimental results and several theoretical works[307] on polymer grafting on solid substrates have been published, the lack of well-developed characterization methods for thin polymer films do not allow an accurate study and identification of the grafted layers as polymer brushes.[301–304]

Important molecular parameters for this system are the Kuhn segment length of the chains, b_K, the lengths (in Kuhn segments) of the grafted, N_g, and matrix, N_m, chains, and the surface grafting density (chains per unit area), σ_g. The case of planar polymer brushes exposed to low molecular weight solvent was studied theoretically by de Gennes[5] and Alexander.[6] They used a scaling approach where a constant density was assumed throughout the brush: all the brush chains were assumed to be equally stretched to a distance from the substrate equal to the thickness of the brush. Aubouy et al.[308] extracted the phase diagram of a planar brush exposed to a high molecular weight chemically identical matrix. Their scaling analysis is based on the assumption of a steplike concentration profile and on imposing the condition that all chain ends

lie at the same distance from the planar surface. Five regions with different scaling laws for the height, h, of the brush were identified.

A numerical self-consistent field (SCF) calculation has also been reported,[8] where the density profile is no longer assumed to be a step profile and the end points of the chains are distributed throughout the brush. Analytical equations based on a similar model were developed by Milner et al.[309] and by Zhulina et al.[310] In the wetting state, the grafted and matrix chains are intermixed along the full extent of the brush. If the matrix chains are not able to penetrate the region occupied by the grafted chains, then the corona collapses and the brush is dewetted. A detailed study of moderately stretched planar brushes exposed to moderately long melt chains was performed by Ferreira et al.[11] who found that the domain where attraction exists between two grafted layers in a melt and therefore partial wetting is expected, scales as $\sigma_g (N_g)^{1/2} > (N_g / N_m)$. This scaling law indicates that flat surfaces grafted with sparse polymer brushes in a long chain polymer melt could exhibit entropic attraction, provided that the molecular weight of the matrix chains is large enough.

5.1.4 Current Research Approach

The present chapter aims to combine one of the most captivating theoretical frameworks for the estimation of the interfacial properties of solid polymer interfaces, self-consistent field theory, with one of the widely used numerical methods, namely the finite element method, in a manner that will enable the implementation of SCFT in complex three-dimensional geometries. The chapter can be divided in two parts. Firstly, in order to validate the SCFFEM method and assess its computational requirements, the works of Daoulas et al.[2] ,Theodorou et al [31] and our work[26] are used as a reference point and the same problem is solved in three dimensions. The primary aim is to calculate various thermodynamic and structural characteristics of the free surface polyethylene melt system and the polyethylene melt/graphite interfacial system, such as the surface and adhesion tension and the reduced density profiles of polymer segments. Additionally the behavior of the aforementioned systems is examined with SCFFEM as well as how the mesh refinement affects the accuracy of the solution. In the second part, the structure of atactic polystyrene melt (matrix) is investigated, confined between two silica plates which bear grafted with polymer chains of the same chemical constitution (atactic polystyrene). Removing the incompressibility assumption and imposing Dirichlet boundary conditions at the solid surfaces allows to investigate systems with additional complexity. So far, the grafted chains have been

always subjected to a smearing technique. For the first time, to our knowledge, we can distinguish the positions where the grafted chains are tethered, from positions not attached to grafted chains and compare the reduced density profiles in the vicinity of these different positions. The intention is to compare our approach against previous works and calculate various thermodynamic and structural characteristics of grafted chain systems with variable grafting density, chain length and grafted/matrix chain length ratio. The SCF calculations are vigorously compared against atomistic simulation results and experimental data.

5.2 Model System and Theoretical Formulation

5.2.1 Finite Element Method

5.2.1/a Weak Formulation

The SCF approach has been employed to describe polymer melt interfaces in previous chapters. Here we will focus primarily on novel points introduced by the finite element analysis. The finite element method (FEM), sometimes referred to as finite element analysis (FEA), is a computational method for finding approximate solutions of boundary value problems in engineering. Two main approaches are used for the derivation of the finite element formulation: the Method of Weighted Residuals (MWR) and the variational approach. The latter, also called the "Energy Approach", was popular in the past, but now is rather rarely used. The MWR is an approximate technique which utilizes trial functions satisfying the prescribed boundary conditions and an integral formulation to minimize error, in an average sense, over the problem domain.

The Edwards diffusion equation can be seen as a time dependent differential equation whose independent variable is the propagator q and the contour length s plays the role of time. We will adopt the more familiar in Finite Element Analysis notation for eq 4.1:

$$\dot{q} - k\nabla_{\mathbf{r}}^2 q + \omega q = 0 \tag{5.37}$$

where $\dot{q} = \dfrac{\partial}{\partial s} q(\mathbf{r}, s)$, $k = \dfrac{R_{\mathrm{G},c}{}^2}{N_c}$ and $\omega = \beta w'_{\mathrm{ifc}}$. Eq 5.37 is called the strong form of the partial differential equation. We can proceed by multiplying and integrating both sides of eq 5.37 with an arbitrary function $W(\mathbf{r})$, which is defined over the entire domain Ω. The symbol Ω here

denotes the volume of the closed domain $\mathcal{R}$. These calculations result in the following weighted residual form:

$$\int_\Omega W(\mathbf{r})\left(\dot{q} - k\nabla_\mathbf{r}^2 q + \omega q\right)\mathrm{d}\Omega = 0 \qquad (5.38)$$

The three dimensional weak form of the WRM is obtained by applying the divergence theorem in the above weighted integral. In one dimension, the divergence theorem is equivalent to integration by parts, and in two dimensions it is equivalent to Green's theorem. The form obtained is called weak form due to its lower differentiability requirements compared to the original weighted residual form or the strong form:

$$G(W,q) = \int_\Omega W(\mathbf{r})\left(\dot{q} + \omega q\right)\mathrm{d}\Omega + k\int_\Omega \left(\nabla_\mathbf{r} W\right)\cdot\left(\nabla_\mathbf{r} q\right)\mathrm{d}\Omega - k\int_\Gamma W(\mathbf{r})\nabla_\mathbf{r} q\,\mathrm{d}\Gamma \qquad (5.39)$$

The symbol Γ denotes the surface area that bounds the domain. A differential volume within the domain will be denoted as $\mathrm{d}\Omega$ and an elementary surface area as $\mathrm{d}\Gamma$. The implementation of the weak formulation is beneficial for three reasons. The highest order of the Laplacian operator disappears, a symmetry is introduced in the second term of the residual, and gradient boundary conditions are inserted via the third term.

The main concept of FEM is the transformation of the original partial differential equation (PDE) into a discrete set of linear equations. Solving these equations, an array q_i is obtained, containing approximations of the continuous solution q of the differential equation at a finite number of points, referred to as interpolation points. An approximation field of the solution can be constructed by means of these interpolation points. The fundamental idea of this approximation field comprises the assumption that the unknown q can be approximated by a sum of $n+1$ "trial functions" $\varphi_i(\mathbf{r},s)$ and therefore be calculated by the following equation:·

$$q(\mathbf{r},s) \simeq \sum_{i=0}^{n} q_i\varphi_i(\mathbf{r},s) \qquad (5.40)$$

The trial functions are continuous over the domain of interest, respect the specified boundary conditions, and are selected to satisfy the "physics" of the problem in a general sense. The integral statements[287] in eqs 5.38 and 5.39 allow an approximation to be made if, in place of any function $W(\mathbf{r})$, we use a finite set of approximate functions w_j:

$$W \simeq \sum_{j=0}^{n} w_j \qquad (5.41)$$

Inserting the above approximations into Eq. 5.39, demands the residual to be equal to zero, the residual form becomes a function of the unknown q_i given by:

$$G = \int_{\Omega} \sum_{i=0}^{n}\sum_{j=0}^{n} w_j \varphi_i \dot{q}_i \mathrm{d}\Omega - \int_{\Omega} \sum_{i=0}^{n}\sum_{j=0}^{n} \omega w_j \varphi_i q_i \mathrm{d}\Omega + \int_{\Omega} \sum_{i=0}^{n}\sum_{j=0}^{n} (\nabla w_j)\cdot(\nabla \varphi_i q_i)\mathrm{d}\Omega - \int_{\Gamma} \sum_{i=0}^{n}\sum_{j=0}^{n} w_j \nabla \varphi_i q_i \mathrm{d}\Gamma \quad (5.42)$$

Clearly, almost any set of independent functions w_j could be used for the purpose of weighting and, according to the choice of function, a different name can be attached to each method. Thus, the various common choices are: the pseudo-spectral or collocation method (method of selected points), the method of moments, the least square method and Galerkin's method.[288][297] Among them, the most popular choice is Galerkin's method (Bubnov- Galerkin) in which the original trial (or basis) functions are used as weighting functions ($w_i = \varphi_i$).[287] This method, as we shall see, frequently leads to symmetric matrices and is adopted in our finite element work exclusively.[297]

5.2.1/b Domain Discretization

A convenient technique to construct the approximate trial functions is obtained by dividing the domain to be analyzed into small regular shaped regions. The division into elements and nodes is a fundamental part of the finite element method. Domain discretization in elements describes what we will refer to as the finite element mesh or simply the mesh of the domain. Using the above subdivision, a simple set of local continuous polynomial functions may be defined for the approximation of the solution. Such functions are called shape functions and they are usually of class C_0, meaning that they are continuous themselves, but their first derivative is only piecewise continuous with the discontinuities located at the nodes.

The domain Ω can be decomposed into N_{el} finite element sub-domains, Ω_e, connected at appropriate nodes (N_{nod}). Let the eth element have $N_{nod,e}$ nodes with global coordinates $\mathbf{r}^{k,e}$ ($k=1,..$, $N_{el,e}$) and let the Lagrangian shape functions $N_i(\xi)$ ($i=1,..$, $N_{nod,e}$) be polynomials of ξ, chosen such that $N_i(\xi)$ evaluates to one at the ith node and to zero at all the other nodes of the element. At the juncture between two elements, the internal gradients are equal and opposite,

thus selfequilibrating, which means that the last term of eq 5.42 becomes zero. The total volume of the set of elements approximates the total volume of our domain:

$$\Omega \approx \Omega_h = \sum_{e=1}^{N_{el}} \Omega_e \qquad (5.43)$$

where Ω_h is the approximation of the domain created by the set of elements, Ω_e. Any integral over Ω can therefore be approximated as a sum of integrals over the elements:

$$\int_\Omega (\bullet) d\Omega \approx \int_{\Omega_h} (\bullet) d\Omega = \sum_{e=1}^{N_{el}} \int_{\Omega_e} (\bullet) d\Omega \qquad (5.44)$$

By further proceeding in this analysis, we encounter one of the central issues in the three-dimensional FEM, which is the query for the optimum type of element to be used. Three types of elements are commonly used in modeling three-dimensional structures: tetrahedral, hexahedral (also known as bricks) and prism (also known as wedges or pentahedra) elements. Due to their flexibility in discretizing arbitrary complex geometries and the associated degree of automation in the mesh generation procedure, the use of tetrahedral elements becomes practically unavoidable in complex finite element analysis.
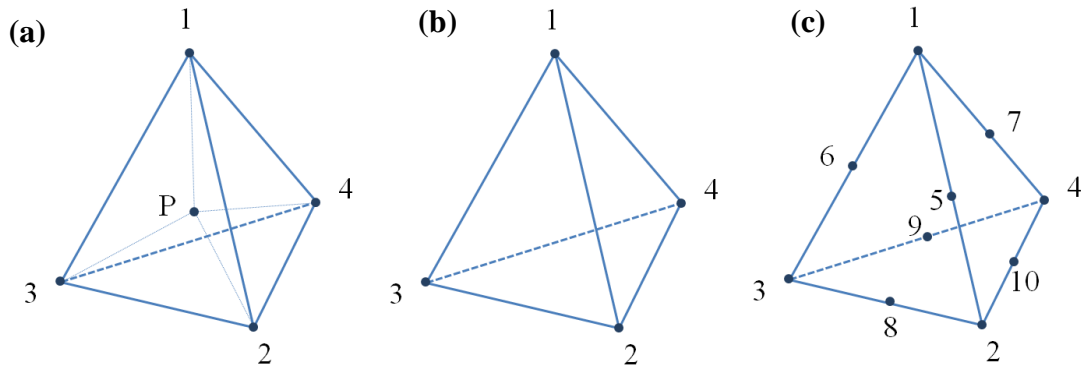
Figure 5.1. Tetrahedral element **(a)** A four-node tetrahedral element, showing an arbitrary interest point P defining four sub-volumes. **(b)** The linear or first order tetrahedron element: also called the 4-node tetrahedron. **(c)** The quadratic or second order tetrahedral element: also called the 10-node tetrahedron.

A tetrahedral element is depicted in Figure 5.1(a) in relation to a global Cartesian coordinate system. We introduce the concept of volume coordinates using Figure 5.1(a). Point P is an arbitrary point in the tetrahedron defined by the four nodes. As indicated by the dotted lines, point P and the four nodes define four other tetrahedra having volumes:

$$V_1 = V_{P234}, \quad V_2 = V_{P134}, \quad V_3 = V_{P124}, \quad V_4 = V_{P123} \qquad (5.45)$$

Figure 5.1(b) shows a typical 4-node tetrahedron. Its geometry is fully defined by giving the location of the four corner nodes [$\mathbf{r}_i=(x_i,\ y_i,\ z_i)$, $i=1,2,3,4$] with respect to the Cartesian coordinate system. The natural volume coordinates of the element are then defined as:

$$L_a = V_a / V_{el}, \quad a = 1, 2, 3, 4 \tag{5.46}$$

where V_{el} is the volume of the element. The nodal basis functions $N_i\left(\mathbf{L}^e\right)$ for each element e are the following:

(i) 4 shape functions for first order tetrahedral elements (Figure 5.1(b)) given by:

$$N_a = L_a, \ a = 1, 2, 3, 4 \tag{5.47}$$

(ii) 10 shape functions for second order tetrahedral elements (Figure 5.1(c)) given by:

- Vertex nodes

$$N_1 = L_1\left(2L_1 - 1\right), \ N_2 = L_2\left(2L_2 - 1\right), \ N_3 = L_3\left(2L_3 - 1\right), \ N_4 = L_4\left(2L_4 - 1\right) \tag{5.48}$$

- Mid-edge nodes

$$N_5 = 4L_2L_1, \ N_6 = 4L_3L_1, \ N_7 = 4L_4L_1,$$
$$N_8 = 4L_2L_3, \ N_9 = 4L_3L_4, \ N_{10} = 4L_4L_2 \tag{5.49}$$

The relation between volume coordinates $\mathbf{L} = \left(L_1, L_2, L_3, L_4\right)$ and $\boldsymbol{\xi} = (\zeta, \eta, \xi)$ can be easily derived and the transformation of nodal basis functions $N_i\left(\mathbf{L}^e\right)$ to $N_i\left(\boldsymbol{\xi}^e\right)$ for each element e is described further in appendix C.2.

According to the eq 5.40 the relation between local and global coordinates within the e-th element is given by:

$$\mathbf{r}^e = \sum_{I=1}^{N_{nod,e}} \mathbf{r}^I N_I\left(\boldsymbol{\xi}^e\right), \ q^e = \sum_{I=1}^{N_{nod,e}} N_I\left(\boldsymbol{\xi}^e\right) q^I(s) \tag{5.50}$$

where $\mathbf{r}^I$ and $q^I(s)$ are the values of $\mathbf{r} = (x, y, z)$, q respectively, at node I of the particular element e examined. Note that the "time dependence" of $q^I(s)$, will be discussed later. Derivatives for isoparametric elements may be constructed using the following chain rule.

$$\frac{\partial N_I}{\partial \xi_i^e} = \frac{\partial N_I}{\partial r_j} \frac{\partial r_j}{\partial \xi_i^e} = \frac{\partial N_I}{\partial r_j} J_{ij}^e \tag{5.51}$$

Accordingly, the Jacobian matrix of the transformation from natural (reduced, element-based, ξ^e) to real (spatial, $\mathbf{r}$) coordinates $\mathbf{J}^e$ is the matrix with the following entries:

$$J_{ij}^e = \frac{\partial r_i}{\partial \xi_j^e} = \sum_{I=1}^{N_{\text{nod},e}} \frac{\partial N_I\left(\xi^e\right)}{\partial \xi_j^e} r_i^I \tag{5.52}$$

In formulating element characteristic matrices, various derivatives of the shape functions with respect to the global coordinates are required. In isoparametric elements, both element geometry and variation of the shape functions are expressed in terms of the natural coordinates of the parent element, so some additional mathematical complication arises. By using eq 5.51 we can calculate derivatives of the shape functions with respect to the real coordinates by the following equation:

$$\frac{\partial N_I}{\partial r_j} = \sum_{i=1}^{N_{\text{nod},e}} J_{ij}^{e,-1} \frac{\partial N_I}{\partial \xi_i^e} \tag{5.53}$$

The matrix $\mathbf{J}^{e,-1}$ is the inverse matrix of $\mathbf{J}^e$. Hence, $\mathbf{J}^{e,-1}$ is the Jacobian matrix of transformation from real (spatial) to natural coordinates. We can express the integral form of the eq 5.44 in terms of the local shape functions by using the eq 5.52:

$$\int_{\Omega_e} (\bullet) d\Omega = \int_e (\bullet)\left|\mathbf{J}^e\right| d\xi \tag{5.54}$$

5.2.1/c Matrix Representation

Up to this point, we made a distinction between weight functions, trial functions and shape functions. As mentioned above, in Galerkin's Method, the first two are by definition the same. In finite element representation, the shape function plays the role of trial function within every element *e*. This choice allows us to re-express the residual function of eq 5.42 by using eq 5.44 and 5.52 in matrix representation:

$$\mathbf{M\dot{q}} + \mathbf{Kq} - \mathbf{Wq} = \mathbf{0} \tag{5.55}$$

where

$$M_{IJ} = \sum_{e=1}^{N_{\text{el}}} M_{IJ}^e = \sum_{e=1}^{N_{\text{el}}} \sum_{I=1}^{N_{\text{nod},e}} \sum_{J=1}^{N_{\text{nod},e}} \int_e N_I\left(\xi^e\right) N_J\left(\xi^e\right)\left|\mathbf{J}^e\right| d\xi \tag{5.56}$$

$$K_{IJ} = \sum_{e=1}^{N_{el}} K_{IJ}^e = \sum_{e=1}^{N_{el}} \sum_{I=1}^{N_{nod,e}} \sum_{J=1}^{N_{nod,e}} \left(\sum_i \sum_j \sum_l \int_e \frac{\partial N_I(\xi^e)}{\partial \xi_j^e} k \frac{\partial N_J(\xi^e)}{\partial \xi_l^e} \left(J^{e,-1}\right)_{ji} \left(J^{e,-1}\right)_{li} \right) \left|\mathbf{J}^e\right| d\xi \quad (5.57)$$

$$W_{IJ} = \sum_{e=1}^{N_{el}} W_{IJ}^e = \sum_{e=1}^{N_{el}} \sum_{I=1}^{N_{nod,e}} \sum_{J=1}^{N_{nod,e}} \omega^J \int_e N_I(\xi^e) N_J(\xi^e) \left|\mathbf{J}^e\right| d\xi \quad (5.58)$$

where ω^J is the value of the field in the nodal point J and $\mathbf{q}$ is a column vector with the values of the propagator q at every nodal point at the considered "time" s. In order for the integral of eq.5.42 to be well defined, the fourth term of the equation associated with the surface integral between adjacent elements must vanish. This occurs under the condition that shape functions are continuous, while the first derivatives may be discontinuous in Ω. The derivation of this matrix form is presented in appendix C.5.

5.2.1/d Gauss Quadrature Integration

The integration procedure is of high importance when we deal with the FEM. From the above discussion, it is clear that the weak form introduces integrals which are usually too complicated to be evaluated analytically, thus numerical integration is preferred. In this section we consider the effect of the numerical integration on the acquired FEM solution.

The Gauss Quadrature method is the most commonly used numerical integration scheme in FEA, and exploits the isoparametric concept introduced in section 5.2.1/b. In numerical analysis, a quadrature rule approximates the definite integral of a function g, as a weighted sum of the values of the function at specified points within the domain of integration. Consequently, another source of error is introduced. The general formula of the numerical integration of an arbitrary function $g(\mathbf{r})$ over a domain Ω_e (according to eq 5.54) is expressed by:

$$I = \int_{\Omega_e} g(\mathbf{r}) d\Omega = \int_e g(\xi) \left|\mathbf{J}^e\right| d\xi = \sum_{m=1}^{N_{gp}} g(\lambda_m) w_m \left|\mathbf{J}_m^e\right| + \varepsilon \quad (5.59)$$

where N_{gp} denotes the number of integration points, λ_m denotes the location of the integration point m, $g(\lambda_m)$ is the value of the function g at the integration points, w_m is the associated weight factor of the integration point and ε is the error associated with the quadrature used. The locations of the integration points are chosen in a way such that maximum accuracy is obtained. The order of the numerical integration must offer exact results when integrating polynomials

(i.e., solution equal to the one obtained from analytical integration) and ensure the non-singularity of the resulting matrices.[287,288,298] A thorough study of numerical integration in the context of the FEM can be found in ref 311. In Zienkiewicz's work, [287] an 1-points rule as well as a 4-points and 15-points rules are derived for a unity tetrahedron. The Gauss quadrature technique used to calculate the volume integral is presented in eqs 5.56, 5.57 and 5.58.

5.2.1/e Transient Equation

We now elaborate on the derivative $\dot{\mathbf{q}}$ and apply the overall procedure for transient implementation. We can deal with this derivative as a "time derivative" of the nodal propagator matrix with the backward difference approximation presented below:

$$\dot{\mathbf{q}} \cong \frac{1}{\Delta s}(\mathbf{q}^{s+\Delta s} - \mathbf{q}^s) \tag{5.60}$$

Where $\mathbf{q}^{s+\Delta s}$ is the column vector containing the values of the propagator q at every nodal point at the next "time step" $s,$ whereas $\mathbf{q}^s$ contains the values of the propagator at the current time-step. In this method, we evaluate the nodal propagators at "time" $s+\Delta s$ based on the state of the system at "time" s. It is clear that these two states of the system depend on how small the time-step Δs is. Substituting and rearranging, eq 5.55 becomes:

$$\mathbf{M}\mathbf{q}^{s+\Delta s} + \Delta s\mathbf{K}\mathbf{q}^{s+\Delta s} - \Delta s\mathbf{W}\mathbf{q}^{s+\Delta s} = \mathbf{M}\mathbf{q}^s \tag{5.61}$$

The initial condition is the given either by eq4.1 or by eq 4.2

5.3   Calculation Details

5.3.1   Model Geometry

Figure 5.1 illustrates a rectangular parallelepiped domain $\mathcal{R}$ in which we solve our SCFT formulation. The parallelepiped domain has volume V and consists of points (x, y, z) with $x \in [-L_x/2, L_x/2]$, $y \in [-L_y/2, L_y/2]$, $z \in [-L_z/2, L_z/2]$. Although this is a three dimensional domain, under some conditions (imposition of periodic boundary conditions in the *x*- and *y*-directions, absence of grafted chains) the solution is expected to depend only on one direction (*z*) due to its symmetry. The parallelepiped domain chosen offers itself for comparisons against one-dimensional solutions based on smearing. The primary goal is to investigate the consistency of results obtained by three-dimensional SCFFEM with previous works based on other methods and

understand physically the behavior of the considered systems. The formulation of the current section is generic and refers to a grafted/matrix polymer system, but it can also be implemented in ungrafted solid/polymer and vacuum/polymer systems. In a solid/polymer or vacuum/polymer system, the absence of grafted chains causes the propagator q_g to vanish and thus only the three eqs 4.1, 4.3 and 4.4 are required for the SCF solution. For additional simplicity, q_m and φ_m can be replaced by q and φ, respectively. On the other hand, a system containing grafted chains, exposed to a melt of matrix chains, requires the solution of two different diffusion equations (one for the matrix and one for the grafted chains), which increases the complexity and computational
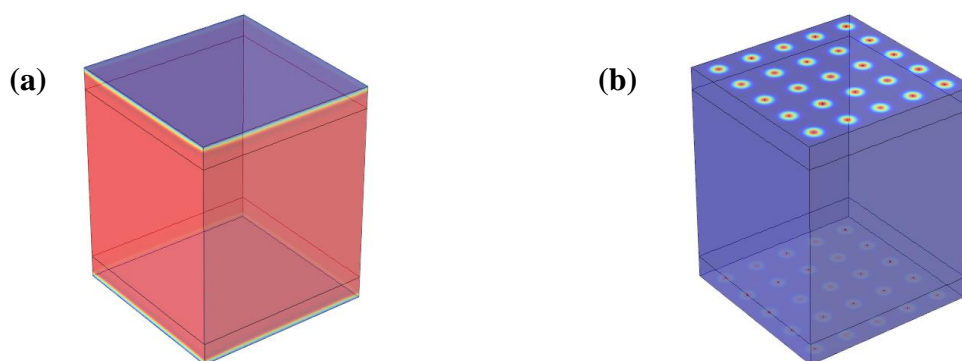
Figure 5.2. The Edwards diffusion equation domain. **(a)** The matrix chain Edwards diffusion equation domain. The parallelepiped domain of dimensions in 8×8×10 nm is shown, with the origin positioned at its center. On the solid surfaces (blue), Dirichlet boundary conditions are applied, while on the lateral surfaces (red), Neumann boundary conditions (*x*- and *y*- derivatives of the propagator equal to zero) hold. **(b)** The grafted chain Edwards diffusion domain. The parallelepiped simulation domain has the same dimensions as in (a) and contains 50 grafted chains; 25 grafted to the top and 25 to the bottom. The grafting ends are represented as 3D delta functions. Again, Dirichlet boundary conditions are imposed on the solid surfaces and Neumann boundary conditions hold on the lateral surfaces.

requirements of the problem. Furthermore, in such a system we have to calculate the reduced segment density for both matrix and grafted chains. It is worth mentioning that, despite the fact that both grafted and matrix chains share the same domain, the initial conditions for matrix and grafted chain propagators differ. The initial condition $q_m(\mathbf{r},0)=1$, is assigned to the matrix chain propagator, while for the grafted chain propagator the initial value is equal to zero in the whole domain, except for the positions of the grafting (eq 4.2). Dirichlet boundary conditions equal to zero are assigned to the top and bottom surfaces of the box/domain for both grafted and matrix chain propagators.

As Chantawansri et al.[144] observed, in the context of SCFT there is a special difficulty in the case of polymer chains whose one end is grafted to the solid surface. As shown in eq 4.2, the grafted chain propagator is subject to a Dirac delta function initial condition. The complication increases when we have to deal with the limit near zero, caused by the Dirichlet boundary condition of the matrix chain propagator appearing in the denominator of the initial condition for grafted chains. A usual approach to bypass these issues is to reposition the grafting points to a surface close to the solid, instead of right on top of it.[273–275] In 1D, the numerical implementation of the delta function resulted in a smearing of the grafting points. In our three-dimensional FEM implementation, the initial condition of the grafting points is evaluated exactly upon the desired points of the domain and the delta function is again evaluated as the inverse volume assigned to the node; thus, the smearing of the grafted point disappears. (Figure 5.2(b))

5.3.2 Mesh

The main weakness of the FEM compared to spectral methods is the accuracy of the method. This drawback, though, can be surpassed by using three different strategies.[297] The first is to subdivide each element to improve the spatial resolution uniformly over the whole domain. This strategy is usually called "h-refinement", because h is the common symbol for the size or average size of a subdomain. The second alternative is to subdivide only in regions of steep gradients where high resolution is needed, called "r-refinement". The third option is to keep the subdomains fixed while increasing p, the degree of the polynomials in each subdomain. This strategy of "p-refinement" is precisely the one employed by spectral methods.

The mesh that was initially employed to discretize the domain contained equally sized elements and the mesh densities were coarse (Figure 5.3(a-c)). For such meshes, negligible time is consumed between iterations. The resolution of the mesh was low, given the steepness of the solution and therefore the accuracy of the acquired results was rather poor. The mesh gradually became finer (Figure 5.3(d-h)) in order to achieve convergence with acceptable accuracy (h-refinement). The final mesh was extremely fine at the top and bottom surfaces, compared to the mesh near the center (bulk polymer) (Figure 5.3(i)) (r-refinement). Finally, aiming to investigate the behavior of the system, we compared the use of both first and second order tetrahedral elements, corresponding to linear and quadratic Lagrange shape functions (p-refinement).[312]
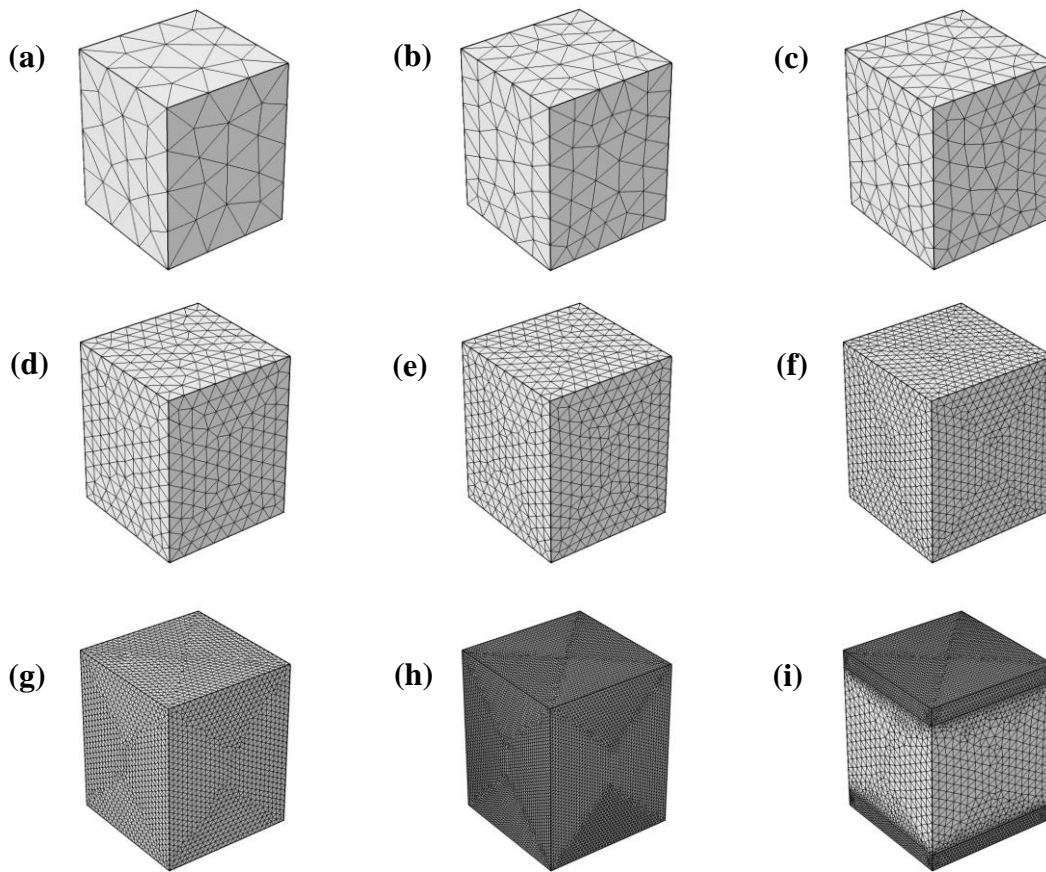
Figure 5.3. The difference between mesh densities applied. **(a-c)** Meshes contain equally sized elements and coarse mesh densities (from 438 to 3,062 elements). **(c-h)** Meshes contain equally sized elements and finer mesh densities (from 10,327 to 1,387,473elements). **(i)** A more efficient mesh, which is finer at the boundaries and coarser in the middle.

Nine types of meshes were used in order to benchmark the discretization of the system. The meshes were generated with the commercial software, COMSOL Multiphysics. The average element size, h_{avg}, which is defined as the average length of all the edges of tetrahedral elements contained in the domain, the average element volume, V_{el}, the number of nodes, N_{nod}, and the number of elements, N_{el}, of the meshes, for both quadratic and linear shape functions, are presented in Table 5.1. For comparison purposes, the average element size of quadratic elements has been considered to be equal to half the actual value (two nodal points are assigned to each edge). Considering that the volume of the domain is equal to 640 nm^3 and knowing the total number of elements, the average element volume can be easily calculated. The average element size and average element volume are perceptible parameters, because they can be associated with size parameters of other methods (e.g finite difference method). The number of mesh points

which the domain is comprised of is directly correlated with the mesh resolution and is the most important aspect to consider when benchmarking a FEM model. As mentioned above, every quadratic tetrahedral element consists of ten nodal points, whereas a linear tetrahedral element consists of four nodal points; this is the reason why meshes with the same number of elements can consist of different numbers of mesh points.

Table 5.1. Mesh parameters

average element size(Å)	average element volume(Å^3)	linear tetrahedral element		quadratic tetrahedral element	
		mesh points	elements	mesh points	elements
30	1461.19	131	438	793	438
19	404.55	377	1,582	2,572	1,582
15	209.01	676	3,062	4,720	3,062
10	61.97	2,033	10,327	15,357	10,327
8	31.14	3,901	20,552	28,644	20,552
5.5	9.87	11,733	64,819	84,473	64,819
3.5	2.52	44,425	253,950	339,085	253,950
2	0.46	236,885	1,387,473		

The calculations have been initially performed with the COMSOL Multiphysics[313] commercial package, which was linked to a Matlab[314] interface. To solve the Edwards diffusion equation, we used the coefficient form corresponding to a general and multipurpose PDE. The spatially dependent chemical potential field was inserted as an absorption coefficient through an external three dimensional interpolation function. Although this method worked properly for simple systems, as the complexity increased, the interpolation function did not exhibit the desired accuracy. The poor accuracy resulted in low flexibility, especially in grafted chain systems. We finally managed to develop an in-house finite element code, which we call *RuSseL*, and we use COMSOL Multiphysics exclusively as a mesher.

5.3.3   Validation System

The first system that we considered consists of polyethylene (PE) chains in the presence or absence of graphite. Polyethylene – graphite sandwiches and freely standing films of polyethylene are both appropriate systems for verifying our methodology. Theodorou et al.,[31] Lakkas et al.[26] and Daoulas et al.[22] worked on these systems comparing their results with atomistic simulations. Since all previous works were performed at *T*=450 K, the same temperature will be assumed during the SCF calculations of the present work. The bulk density

of the polymer is ρ_{mass}=766 kg/m^3, from which ρ_0 is readily obtained. The compressibility appearing in the SCF equations, κ_T, will be considered equal to the isothermal compressibility of the atomistically studied bulk polymer. Taking into account our atomistic simulations and experimental data,[315] we employ $\kappa_T = 1.43$ GPa^{-1}.

The mean squared radius of gyration of a chain can be calculated as $R_g = l_{c\text{-}c}\left[C_N(N-1)/6\right]^{1/2}$, where C_N is Flory's characteristic ratio, N the number of skeletal bonds and $l_{c\text{-}c}$ their bond length. The bond length used in the atomistic simulations is $l_{c\text{-}c} = 1.54$ Å and we set C_N for the molecular weight of interest, following the work of Karayiannis et al.[316] A crucial step in implementing the field-theoretic representation of the PE/graphite system is the definition of the polymer/substrate interaction potential, $U_s(\mathbf{r})$. In this direction, we follow the work of Daoulas et al.[24], where a square-well potential was used. The depth of the square well potential was determined under the requirement that the field-theoretic model have the same adsorption energy per unit surface as the atomistic one. The potential energy field exerted by a semi-infinite graphite phase on a polyethylene segment can be approximated reasonably well by a square well potential whose width is equal to w=4.5 Å and depth is equal to u_0= $-1.65k_BT$ at T=450 K.[24]

In the case of the capped polyethylene film, the grand potential is directly related to the adhesion tension:

$$\Omega(V,T,\mu) - \Omega_{\text{bulk}}(V,T,\mu) = S_{\text{solid}}(\gamma_{\text{sp}} - \gamma_s) \tag{5.62}$$

Where γ_{sp} is the interfacial tension between the graphite and the molten polymer, γ_{sp} is the surface free energy of a pure graphite surface, and S_{solid} is the total surface area of contact between polymer and graphite (both faces).

5.3.4 Grafted Chain System

In the present chapter, we will study a system of chains which are grafted on the surface of a solid of planar geometry. A polystyrene/silica interface with grafted polystyrene chains, for which density profiles have been computed by both coarse grain atomistic simulation[317] and lattice-based self-consistent field theory,[318] would constitute a convenient test system. The objective is to validate the SCF/FEM approach in presence of grafted chains in a planar

geometry. We employ the planar geometry in order to compare our system with atomistic simulations performed by several authors.[319,320]
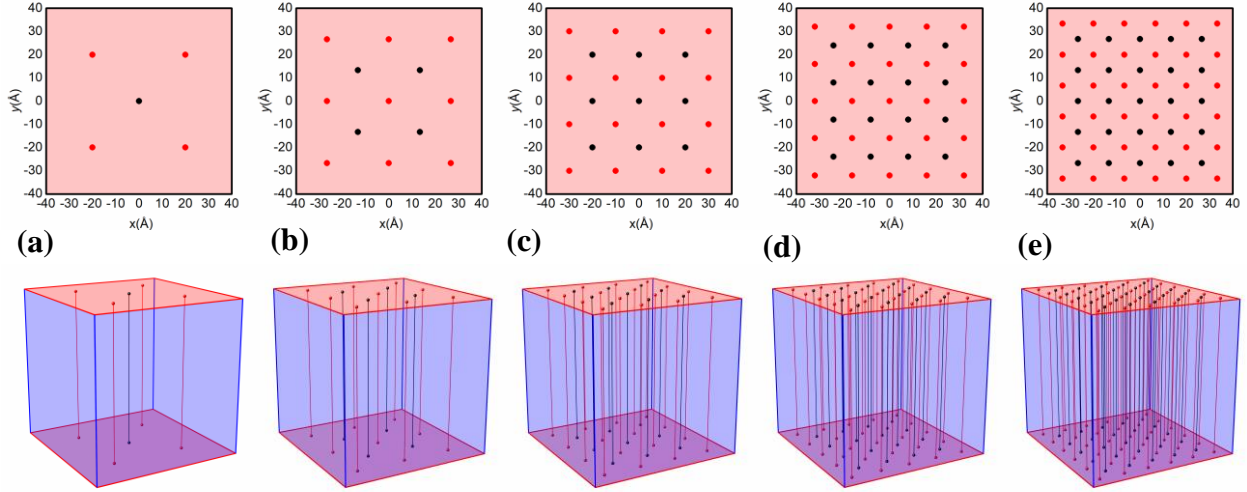
Figure 5.4. Representation of the system under various grafting densities. Each solid surface has an area of 64 nm^2 with dimensions of 8×8 nm. The two solid surfaces are mirror images of each other. Red colored points (•) and black colored points (•) denote the grafting positions of chains (g-points) and the centers of squares formed by the grafting positions (c-points), respectively. The surface grafting density increases implicitly in each panel from left to right, with values equal to; σ_g = 0.06 nm^{-2} **(a)**, 0.14 nm^{-2} **(b)**, 0.25 nm^{-2} **(c)** , 0.39 nm^{-2} **(d)**, 0.56 nm^{-2}**(e)**. Profiles are accumulated separately along the red and blue straight lines shown in the bottom part of the picture.

The system consists of polystyrene (PS) chains grafted on a silica (SiO$_2$) planar surface, in contact with a polymer melt of the same chemical constitution as the grafted chains. In this special case where the chemical composition of the grafted and matrix chains are identical, the entropic contributions to the free energy dominate the thermodynamics.[308] Previous experimental[76] and computational works[57,277,321] have been performed considering polystyrene (PS) chains grafted on a silica (SiO$_2$) plates, embedded in polystyrene melt. Herein, all calculations were carried out in the grand canonical ensemble at a temperature equal to T = 500 K. The PS-SiO$_2$ interactions are described with the Hamaker potential[272] using the interaction parameters, A_{PS} and A_{SiO_2}, and the effective radii, σ_{PS} and σ_{SiO_2}, presented in Table 5.2. Note that, in the representation used, each PS repeat unit is mapped to two segments.

The calculations were performed with *RuSseL 3D*; an in-house developed code which is designed to run calculations based on SCFT in three dimensional systems, using the finite element method.[275] The initial condition of the grafting points is evaluated exactly on the desired points of the domain and the delta function is evaluated as the inverse volume assigned to the node.[275] The main advantage of FEM is expected to be that each grafting point is explicitly

attached on a single node of the spatial mesh. In the 3D calculation, we expect to obtain different structural results (e.g., density profiles) as we move across the z axis for different (x,y) values. To explore this, we define the g-points (black dots in Figure 5.4) on the surfaces, which correspond to the grafting points, and the c-points (red dots in Figure 5.4) as the centers of the squares defined on each silica surface by the g-points. By symmetry, the lines connecting pairs of corresponding g- or c- points on the two surfaces are normal to the surfaces, i.e., parallel to the z axis (Figure 5.4). The structural properties for both grafted and matrix chains are evaluated along these lines, which connect opposing g- and c-points. The evaluations along these different lines were performed across a broad parameter space spanned by surface grafting density σ_g, grafted chain length N_g, and swelling ratio N_m/N_g. Specifically, values of $\sigma_g = \{0.06, 0.14, 0.25, 0.40, 0.56\}$ nm^{-2}, $M_g = \{5, 10, 15, 20, 25\}$ kg/mol (or $N_g = \{100, 200, 300, 400, 500\}$ monomer segments) and $N_m/N_g = \{0.25, 0.5, 1.0, 2.0, 3.0\}$ were explored. According to ref 255, as long as the matrix chains are longer than the grafted ones, the latter are not perturbed considerably. The results were plotted using relevant software.[322]

Table 5.2. Parameters of the calculations

	parameter	value	reference
system	T	500 K	255
	b_K	1.83 nm	255
chain stiffness	$l_{c\text{-}c}$	0.154 nm	-
	γ	0.829	193
	$m_{monomer}$	52.08 g/mol	-
	h_{HS}	~0.4 nm	-
	σ_{PS}	0.37 nm	255
Hamaker	σ_{SiO2}	0.30 nm	255
	A_{PS}	$5.84 \cdot 10^{-20}$ J	255
	A_{SiO2}	$6.43 \cdot 10^{-20}$ J	255
Helfand	κ_T	3.97 (GPa)$^{-1}$	
	$\rho_{mass,bulk}$	953 kg/m^3	255
Edwards diffusion	Δs	0.5 segs	
	s	200 segs	-

5.4 Results

5.4.1 Capped/Free Interfaces

The present section discusses the structure of vacuum/melt (VM) and solid/melt (SM) interphases and the surface and adhesion tension, respectively, calculated from both our one dimensional (SCFFD: *RuSseL1D*)[323]and three-dimensional code (SCFFEM: *RuSseL3D*). The results obtained from these systems will be used as a proof of the efficiency of the SCFFEM methodology. In order to achieve the same results with SCFFEM as those achieved via SCFFD, extremely high density meshes are required, making the calculations time consuming. For that reason, a study of the behavior of the system has been undertaken to accelerate the whole process without significant accuracy cost.

5.4.1/a Validation of SCFFEM

Figure 5.5 presents the reduced density profile $\varphi(\mathbf{r})$ obtained with the three-dimensional SCFFEM[275] method for a free-standing thin film of polyethylene melt at 450 K. The corresponding solution of the planar thin film problem with the one- dimensional finite differences method (SCFFD)[26], using exactly the same parameters, is presented with red points. This is the converged solution using the actual value of the isothermal compressibility of molten polyethylene, following the statistical mechanical approach developed by Daoulas et al.[24], based on a simplified, Helfand-type effective Hamiltonian for polymer-polymer interactions with no gradient correction. The finite element mesh of the converged solution consists of 418,064 elements and 587,575 nodal points, while the Finite differences solution utilized 2,000 points. The results for all nodal points in the three-dimensional mesh collapse onto a single curve, and this is expected, since the problem is in fact one-dimensional.

The density profile exhibits qualitatively the expected shape, also seen in atomistic simulations. It starts off at zero at the extreme edge of the film and rises in a sigmoidal fashion as one moves towards the bulk polymer region, assuming its bulk value at a position less than $0.25 \left\langle R_\mathrm{g}^{2} \right\rangle^{1/2}$ from the extreme edge. As we have shown in chapter 3, the square gradient theory combined with a free energy density given by a more sophisticated Sanchez-Lacombe EoS is needed to obtain quantitatively realistic density profiles. However, for validation purposes this model is sufficient.
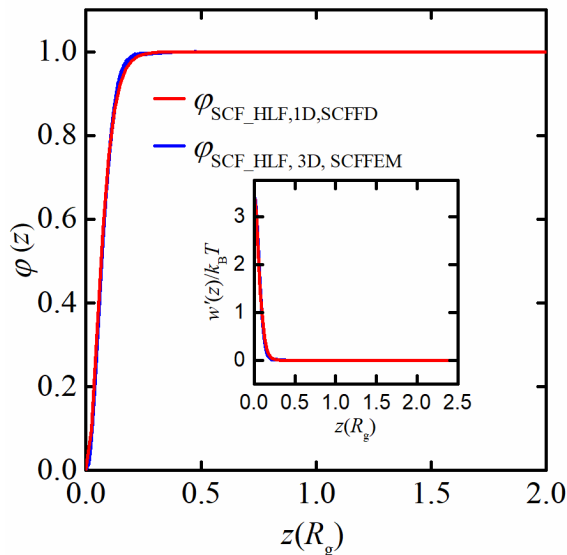
Figure 5.5. Reduced segment density profile φ (**r**) in a planar thin film of molten polyethylene as a function of distance z normal to the film as obtained by our three-dimensional Finite Element Method (SCFFEM, *RuSseL3D*) and as obtained by a one-dimensional finite difference solution of the same problem (SCFFD, *RuSseL1D*). The film edge is on the left and the middle of the film, where bulk conditions prevail, is on the right. The case which refers to the real compressibility, $\kappa_T = 1.43$ GPa^{-1}, converged in real time with *Russel3D*. In the inset, we demonstrate the self-consistent field per segment, w' $(z)/$ $k_B T$ in a planar thin film of molten polyethylene, plotted as a function of distance z normal to the film.

Setting the value of γ_{sp} equal to zero in eq 5.62 we can calculate the surface tension of the polyethylene free film. The asymptotic value of the surface tension obtained from the solution of the SCFFD problem is 63.99 mJ/m^2, while the corresponding surface tension obtained from the SCFFEM is 63.51 mN/m. This supports the equivalence of the two techniques and validates the methods we have developed. The experimentally[131,324] measured surface tension of PE at 450 K is γ_s= 28.1 mJ/m^2, which is in good agreement with the surface tension estimated by our atomistic MD simulations and results from the SCF_SL-SGA model, but not with the SCFFEM and SCFFD presented here. The reason for this discrepancy between SCF values and experimental ones is the use of the Helfand approximation[90] in the effective Hamiltonian of the SCFFEM and SCFFD calculations. While this approximation is satisfactory for systems where the local density does not depart significantly from its bulk value, it is not appropriate for free surfaces, where the local density drops down to zero.

The corresponding converged solution for the self-consistent field w'(**r**) in the case of the freely standing polyethylene film is shown in the inset of Figure 5.5. The finite element and finite difference solutions are practically coincident, confirming the correctness of the SCFFEM approach. Again, excellent agreement between the three-dimensional finite element and the one-

dimensional finite difference results is observed, confirming that both the formulation and the computational implementation of the new SCFFEM methodology are correct.
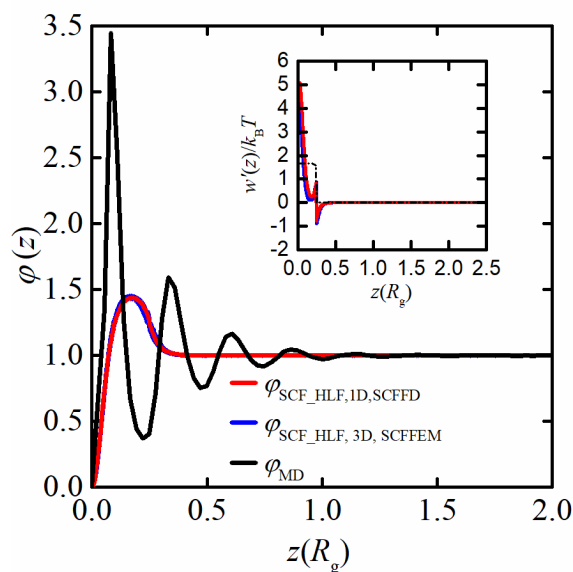
Figure 5.6. Polymer volume fraction profile $\varphi(z)$ in a planar thin film of molten polyethylene between graphite plates plotted as a function of distance z, measured in R_g units, normal to the film as obtained by our three-dimensional Finite Element Method (SCFFEM, *RuSseL3D*) and as obtained by a one-dimensional finite difference solution of the same problem (SCFFD, *RuSseL1D*). The case which refers to the real compressibility $\kappa_T = 1.43$ GPa^{-1} converged in real time in *Russel3D*. The profile from our SCFFEM calculation coincides with that calculated by Daoulas et al.[24] and Theodorou et al.[31] from a SCFFD calculation. The black line displays the atomistic simulation data calculated by Kritikos et al.[325] In the inset, the self-consistent field per segment $w'(z)/k_BT$ is plotted as a function of distance z normal to the film.

The next challenge was to validate the new method for the case of a planar thin film of molten polyethylene in contact with graphite plates ("capped" film).[2] In order to solve this graphite/polymer system, we made an initial estimation of the field, based on the solution for the freely standing film of polyethylene (discussed above). The finite element and the finite differences system discretization parameters are the same with the corresponding ones of the free polymer standing film. The solutions we get from the 3D Finite Element method and the 1D Finite Difference method are identical, as presented in Figure 5.6. Furthermore, the solutions of both techniques are compared with molecular dynamics results obtained by Sgouros.[104] As Daoulas et al. pointed out in their work,[24] the SCF calculation cannot reproduce the oscillatory behavior of the segment density close to the solid surface, whose characteristic length is commensurate with the segment diameter and is readily observed in atomistic simulations. It does, however, reproduce the increased segment density near the attractive solid surface.

Qualitatively, the SCF approach provides a smeared picture of the polymer density variations inside the area subjected to the effect of the potential $U_s(\mathbf{r})$.

The interaction potential between the polymer and the substrate, $U_s(\mathbf{r})$, was tuned[24] in order to reproduce the total energy of adsorption and the characteristic length scale of the density variations. The value of the adhesion tension obtained from the solution of the SCFFD problem was 71.86 mN/m, almost identical to the value of 71.84 mN/m obtained from SCFFEM. In addition, the adhesion tension is in good agreement with the adhesion tension estimated by atomistic MD simulations, 70 ± 10 mN/m. Following the work of Theodorou et al.[31] and Girifalco and Good[52] and considering that experimental data on interfacial thermodynamic properties of the polyethylene/ graphite system are not readily available, the adhesion tension can be expressed in terms of the geometric mean of the surface tensions of the liquid and the solid as follows:

$$\gamma_s - \gamma_{sp} \simeq 2\Phi(\gamma_s\gamma_p)^{1/2} - \gamma_p \tag{5.63}$$

The experimentally measured surface tension of PE at 450 K is $\gamma_p = 28.1$ mJ/m^2, and that of graphite[326] is $\gamma_s = 115$ mJ/m^2. On the basis of these values, the experimental estimate of the adhesion tension, taking the interaction parameter $\Phi = 1$, is $(\gamma_s - \gamma_{sp}) = 85.6$ mJ/m^2.

5.4.2   Study of the Behavior of the Solution

5.4.2/a h-,r-and p- Refinement

In Figure 5.7 the reduced density profile $\varphi(z)$ is illustrated in a planar thin free standing polyethylene film a function of distance z in Å normal to the film as obtained by SCFFEM, in 3D, with varying mesh density applied, compared with the solution obtained by SCFFD, in 1D. As shown in the previous section 5.4.1/a, the profiles become identical, proving the direct correspondence between two methods. Herein we use the SCFFD volume fraction profile solution as a reference to compare with the solution obtained by SCFFEM with various mesh densities. The system we use to explore this feature is the free standing polymer film described in section 5.3.3. The difference between the solutions illustrated in Figure 5.7 indicates the accuracy achieved in the SCFFEM solution.

A discrepancy between density profiles is clear in Figure 5.7(a-c). The coarser meshes which correspond to these densities are illustrated in Figure 5.3. These mesh densities are definitely inappropriate for the considered system. The SCFFEM solution fails to even capture
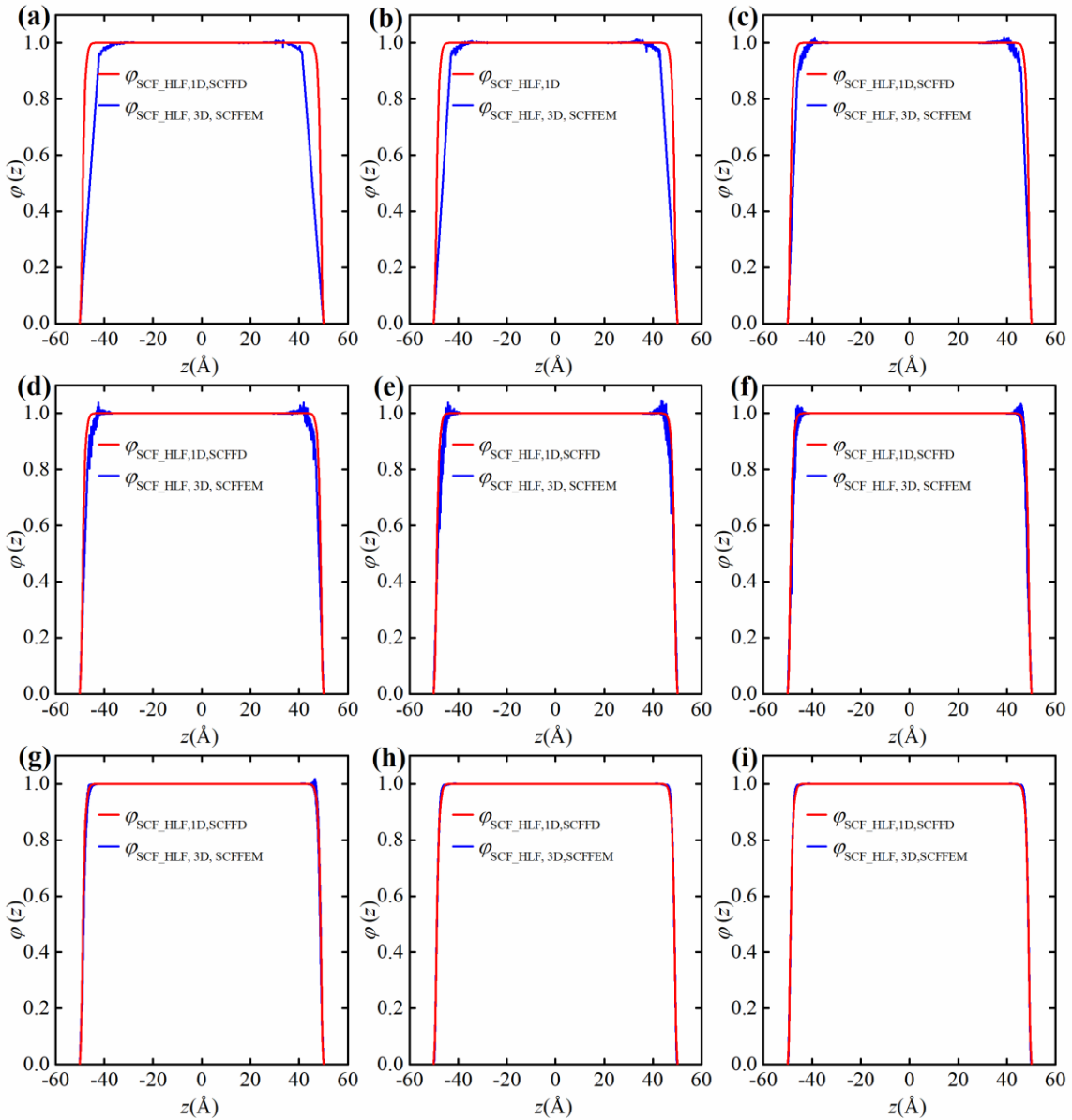
Figure 5.7. Polymer volume fraction profile $\varphi(z)$ in a planar thin free standing polyethylene film plotted as a function of distance z normal to the film, in Å, as obtained by the three-dimensional SCFFEM method (blue line) with varying mesh density, compared with the solution obtained by one-dimensional SCFFD (red line). The difference in volume fraction profile solutions illustrated indicates the accuracy achieved in SCFFEM The plots **(a-h)** corresponds to uniform meshes with parameters listed in Table 5.1.Moving from left to right and from top to bottom the mesh density increases. The plot **(i)** corresponds to a more efficient mesh, which is finer at the boundaries and coarser in the middle, and therefore provides better accuracy in solutions with steep gradients. The actual meshes used are depicted in Figure 5.3.

the position where the density begins to fall from its bulk value as the vacuum is approached.

Proceeding to the plots shown in Figure 5.7(d-f) we see that, as the mesh density increases

(compare mesh depictions in Figure 5.3), the disparity between the 3-D SCFFEM and the 1-D

SCFFD solutions subsides. SCFFEM can now capture the position of the polymer vacuum interface with accuracy. Nonetheless, noise is encountered in the strongly curved area of the reduced density profile. The noise, which is experienced in the finite element solution, is due to the fact that all nodal points in the three-dimensional mesh are projected onto a single curve.

For the solutions obtained from SCFFEM and presented in Figure 5.7(g-h) extremely fine meshes were used, which consumed a great deal of computational time compared to the finite difference scheme. On the other hand, the noise is drastically reduced and the profiles become nearly overlapping. An interesting observation which can be made in Figure 5.7(h) is that, despite the symmetry of the system, the profiles are not perfectly symmetric. This is a common issue encountered in the finite element method when the domain is unable to be discretized into elements with the same shape and volume. The finer the mesh becomes, the more time consuming is the solution of the Edwards's equation. To overcome this problem, a more sophisticated meshing scheme was applied. Concerning the profiles presented in Figure 5.7(h) and Figure 5.7(i), although they seem identical, a much different mesh was applied to retrieve each one of them. The mesh applied in Figure 5.7(i) was coarser in the bulk region, but retained a much finer density near the vacuum edges where the gradients are steeper (see Figure 5.3). Without losing the desired accuracy, we take advantage of the finite element method, which allows us to change the mesh resolution between domains without much effort.

Having established that a mesh which is finer at the boundaries and coarser in the middle yields the same solution as a finer mesh in the whole domain, a question arises. How coarse should the inner mesh be? Herein we describe a method for choosing the optimal mesh density for the inner domain. For h_{avg} equal to 2 Å near the surfaces, higher accuracy is provided in solutions with steeper gradients. In the middle there is no need for the mesh to be so dense, since the gradients become zero. Keeping the h_{avg} constant near the surfaces and increasing in at the bulk region, the time needed for a single iteration decreases (for linear and quadratic interpolation functions). As illustrated in Figure 5.8, with increasing average element size of the inner mesh (mesh becoming coarser), the time decreases sharply and reaches a plateau. The point where the plateau begins corresponds to the optimum h_{avg}. Below this point, the gain in speed is negligible compared to the accuracy we lose.

The above procedure is commonly referred to as *h-r* refinement. Increasing the degree of element method applied in this work, *p*-refinement can be implemented by changing from first
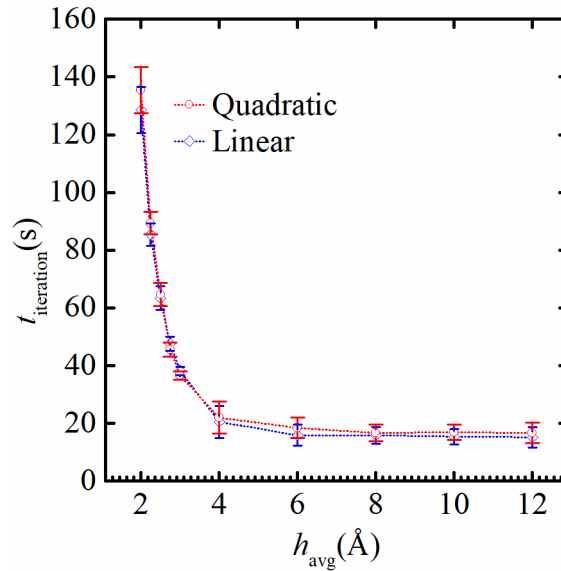
Figure 5.8. The method for the construction the mesh, which is finer at the boundaries and coarser in the middle. For h_{avg} equal to 2 Å, better accuracy is provided near the surfaces where the solution has steeper gradient. In the middle there is no need for the mesh to be so dense. Keeping the h_{avg} constant equal to 2 Å near the surfaces and increasing it in the bulk region, the time needed for a single iteration decreases (for both linear and quadratic interpolation functions).

to second or higher degree tetrahedral elements. In Figure 5.9(a), the time needed for a single iteration ($t_{iteration}$) is plotted versus the number of mesh nodal points for both linear and quadratic interpolation. For the same number of mesh nodes, the time consumed for a single iteration is roughly the same with quadratic as with linear elements, the latter exhibiting slightly higher speed. It is evident that the number of nodal points affects the time spent for an iteration, which is reasonable given the eqs 5.56-5.58, where we can see that the size of the matrices depends on the number of nodal points. Figure 5.9(b) depicts the effect of the number if mesh elements in the speed of iterations for first and second order tetrahedral elements. The meshes are presented in Table 5.1, where it is noticeable that a mesh comprising the same number of first order elements can have considerably smaller number of nodal points than another with second order elements. This difference increases when the mesh becomes denser. Figure 5.9(c) demonstrates how the average element size (h_{avg}) affects the time needed for a single iteration for both linear and quadratic tetrahedral elements. The time for a single iteration and h_{avg} exhibit an inverse dependence. As h_{avg} approaches zero, $t_{iteration}$ goes to infinity. Note that h_{avg} can be directly compared to the spatial domain discretization of the 1D finite difference method. For a mesh with h_{avg} roughly equal to 0.2 nm (corresponding to approximately 235,000 nodal points), the

3D SCFFEM needed 120 to 130 seconds for one iteration, while for the same iteration, 1D SCFFD needs 0.002s.
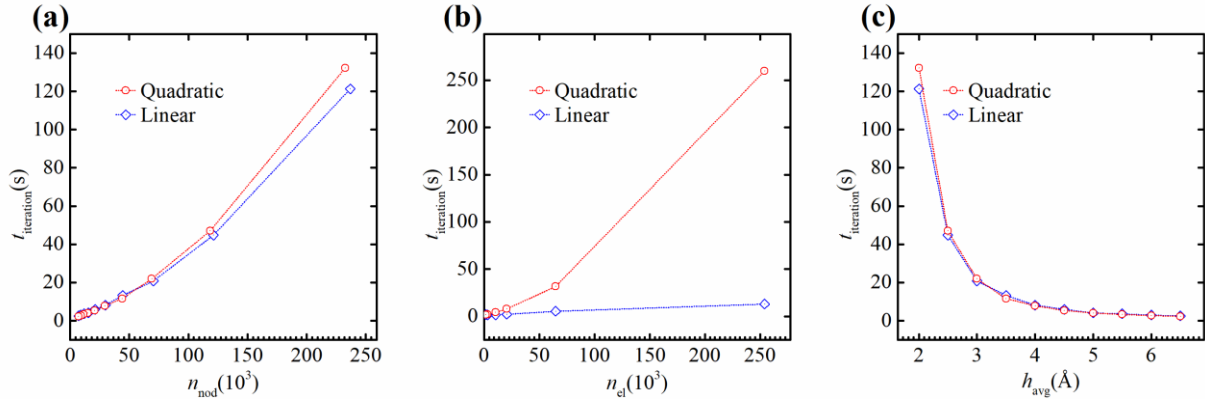
Figure 5.9. Time needed for a single iteration for linear and quadratic interpolation functions versus **(a)** number of nodal points, **(b)** number of elements and **(c)** average element size. The parameters of the meshes are presented in Table 3.1.

5.4.2/b Mesh Convergence Criterion

As mentioned in the above section, the calculations performed with SCFFEM used a high density mesh. The size of the matrices increased with the number of elements and so did the time needed for a single iteration. On the other hand, we use as convergence criterion the difference of the relative $\Delta\Omega$ change between two sequential iterations, which is required to be below a tolerance (in our case, $10^{-5}k_BT$). We can see that, despite the fact that the same convergence criterion is satisfied in all graphs presented in Figure 5.7, clearly not all curves exhibit the same accuracy. Considering the fact that the iterations needed for the solution to converge can vary and increase abruptly, especially when dealing with realistic compressibilities, a criterion for mesh quality is required.

In Figure 5.10 we address the system presented in section 5.3.3, but the real compressibility demand is relaxed. The experimentally measured compressibility of PE at 450 °C is 1.43 GPa^{-1}. Herein, the compressibility was altered to a value 10 and 100 times higher than the real one. The system of equations was solved for all the mesh densities described in subsection 5.4.2/a. The increase in compressibility results in a decreased surface tension, which is calculated by eq 5.62, and in the number of iterations needed for the system to converge. In order to compare the results from different compressibility values, the variable $\gamma_{calc}/\gamma_{conv}$ is introduced, where γ_{calc} is the surface tension calculated by eq 5.62 and γ_{conv} is the surface tension calculated from both SCFFD and SCFFEM (when an extremely dense mesh is applied).

When the mesh density increases, $\gamma_{calc}/\gamma_{conv}$ converges to 1. The field relaxation parameter a_{mix} is constant and the same for all the systems.
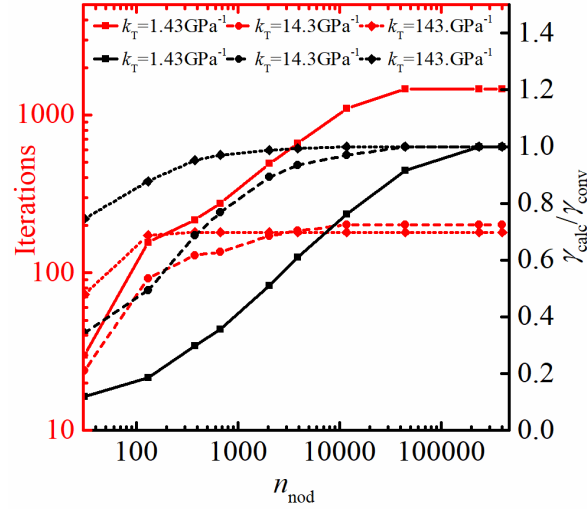
Figure 5.10. Iterations needed for the system to converge versus number of nodal points for 3 different compressibility values: $\kappa_T=143.$ GPa^{-1} (red line-rectangle), 14.3 GPa^{-1} (red dash-circle) and 1.43 GPa^{-1} (red dots-diamond). "Reduced calculated surface tension" ($\gamma_{calc}/\gamma_{conv}$) versus number of nodal points for the same compressibility values: $\kappa_T=143.$ GPa^{-1} (black line-rectangle), 14.3 GPa^{-1} (black dash-circle) and 1.43 GPa^{-1} (black dots-diamond).

The discrepancy between density profiles shown at Figure 5.7 gives rise to a difference in the "reduced calculated surface tension" ($\gamma_{calc}/\gamma_{conv}$), presented in Figure 5.10. The ratio $\gamma_{calc}/\gamma_{conv}$ varies from 0.2 to 1, 0.5 to 1, 0.8 to 1 for a value of 143.0 GPa^{-1}, 14.3 GPa^{-1} and 1.43 GPa^{-1}, respectively. The more compressible the model is, the more sharply the surface tension converges to γ_{conv}. As the number of nodal points increases, the ratio $\gamma_{calc}/\gamma_{conv}$ reaches a plateau, indicating a satisfying precision of the model. The higher the compressibility, the lower the number of nodes (implying a coarser mesh) required to converge to the solution. The quantity $\gamma_{calc}/\gamma_{conv}$ can be considered as a reliable accuracy convergence criterion for more complicated models. Another parameter depicted in Figure 5.10 is the number of iterations needed for the system to converge. It is clear that the number of iterations required increases with increasing mesh density. This feature becomes an additional burden for the SCFFEM to be taken into account. It is obvious that the number of required iterations also reaches a plateau, and this can be an indicator for the accuracy convergence criterion, since the plateau in number of iterations occurs a bit before that in the reduced calculated surface tension.

5.4.2/c Initial Field Value

Understanding the behavior of the successive substitution scheme is important for developing a concrete converging technique for SCFFEM. A central role in the scheme is played by the initial value of the field inserted in the Edwards diffusion equation. For compressibility values closer to the real one, feeding the field generated by the convolution integration back into the Edwards diffusion equation causes divergence of the successive substitution scheme. Mixing the old field with a small fraction of the new one makes the system stable and leads to convergence. We take advantage of the relaxation technique and study two possible ways to reach the solution.
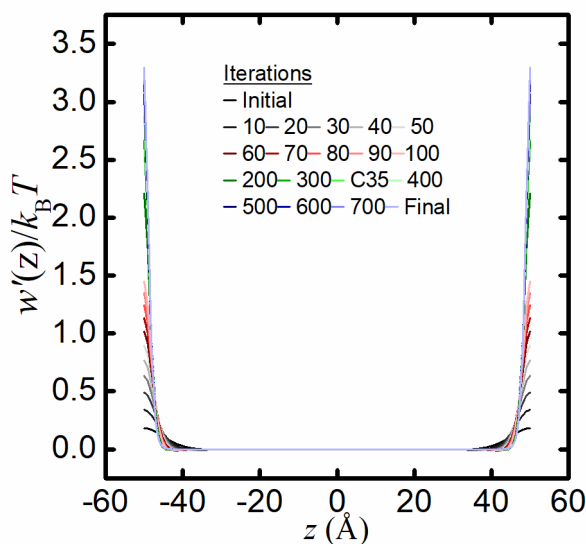
Figure 5.11. First continuation scheme   Evolution of the field during the converge procedure with a value of compressibility: $\kappa_T = 1.43 \times 10^{-9}\,\text{Pa}^{-1}$ and with constant field relaxation parameter, $a_{\text{mix.}} = 0.005$. As can be seen in the graph, the initial field is zero everywhere and 700 iterations are needed for convergence. When second order tetrahedral elements are used (not shown), a continuation scheme with respect to the compressibility is required; approximately the same number of iterations is needed at each individual "compressibility step".

   The first continuation scheme begins with zero or random initial value of the field. The mixing parameter is kept constant and depends on the chain length, the compressibility, the characteristic ratio and the bulk polymer segment density. Figure 5.11 depicts the fluctuations of the field projected to dimension z, for the experimentally measured compressibility of PE at 450 °C. The initial field $w'(z)/k_BT$ is zero everywhere in the domain, and in approximately 100 iterations it reaches the value of 1.5 near the surfaces. In order to reach the value of 3.41 on the surfaces (converged value), approximately 700 iterations are required. An interesting observation concerning this technique is that, if we use quadratic elements to discretize the domain, the system diverges. In order to achieve convergence with the second order tetrahedral

elements, the continuation scheme must begin with high melt compressibility and continue by gradually reducing the compressibility to its correct value. This approach demands convergence at every compressibility step and was proven to be too time consuming for realistic compressibilities, since, in every compressibility step, a large number of iterations is required to achieve convergence.
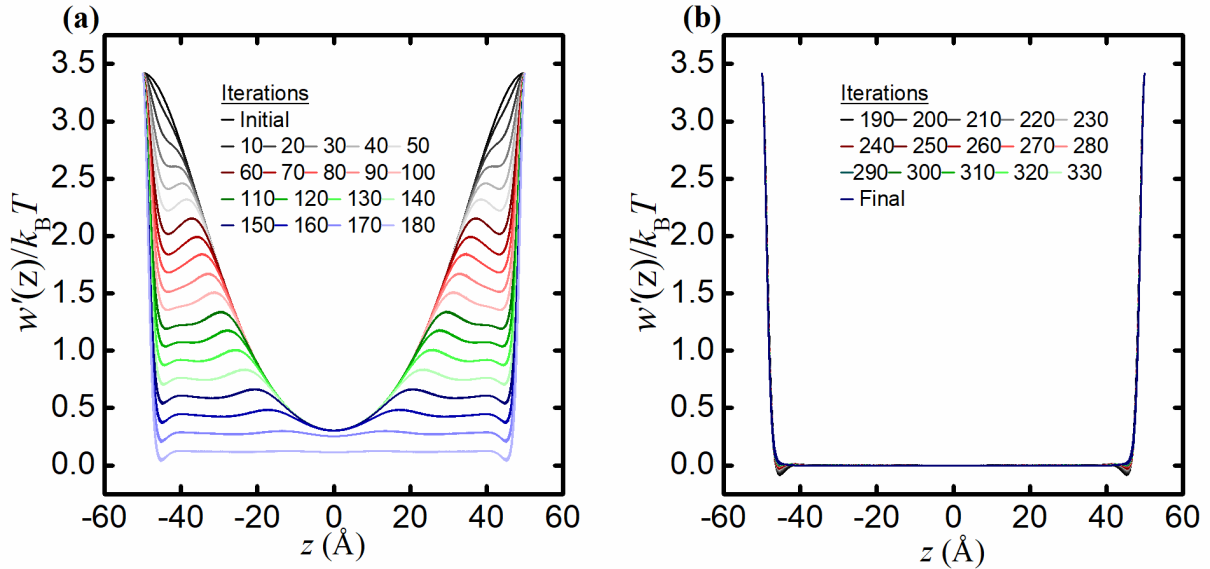
Figure 5.12. Second continuation scheme   **(a)** Evolution of the field during the convergence procedure with a value of compressibility: $\kappa_T = 1.43\times10^{-9}\mathrm{Pa}^{-1}$, using variable a_{mix}. Initial field calculated from the first iteration with zero field as input and $a_{\mathrm{mix}}=1$.   180 iterations are needed for a_{mix} to reach 0.005 and the field profile to stabilize. **(b)** After a_{mix} reaches the value of 0.005, nearly another 200 iterations are needed for the system to converge.

A second, more direct approach was implemented in order to save computation time. In this technique, as initial guess for the field we used the field configuration calculated from the first iteration. The first iteration had zero field as input and $a_{\mathrm{mix}}=1$. The initial field configuration is presented in Figure 5.12(a); it differs from zero. Near the surfaces it reaches from the beginning the converged value, but it exhibits smoother gradients than the converged field in the rest of the domain. In this direct approach, the relaxation parameter does not remain constant. Starting with extremely small mixing fractions for the new field, we attempt to converge to the solution. The initial mixing fraction was set equal to 0.5×10^{-131}. In every iteration, the mixing fraction was multiplied by a factor of 10. When the mixing fraction reaches the same value as in the previous technique, it is kept constant. This procedure bypasses the intermediate compressibility steps and reaches the target compressibility with quite remarkable performance. The convergence following this strategy, which we call the "straightforward approach," is

shown in Figure 5.12(a). After a_{mix} reaches the value of 0.005, nearly another 200 iterations are needed for the system to converge. This process is depicted in Figure 5.12(b).

5.4.3 Grafted Chain System

The current section presents structural and thermodynamic properties of polymer grafted surfaces in contact with chemically identical matrix chains. The SCFFEM is a three-dimensional method, as it is shown in Figure 5.13. Although we use it in a planar geometry for demonstration purposes, the capabilities for implementation in more complicated geometries are indisputable. The grafted chain system is captured with small elements, demonstrating how adaptable and flexible the FEM method can be. As declared in section 2.2.1, the initial condition is adjusted for every grafted chain. The number of matrix chains can fluctuate, but the number of grafted chains in the system remains constant, since they are chemically grafted to the solid surface.
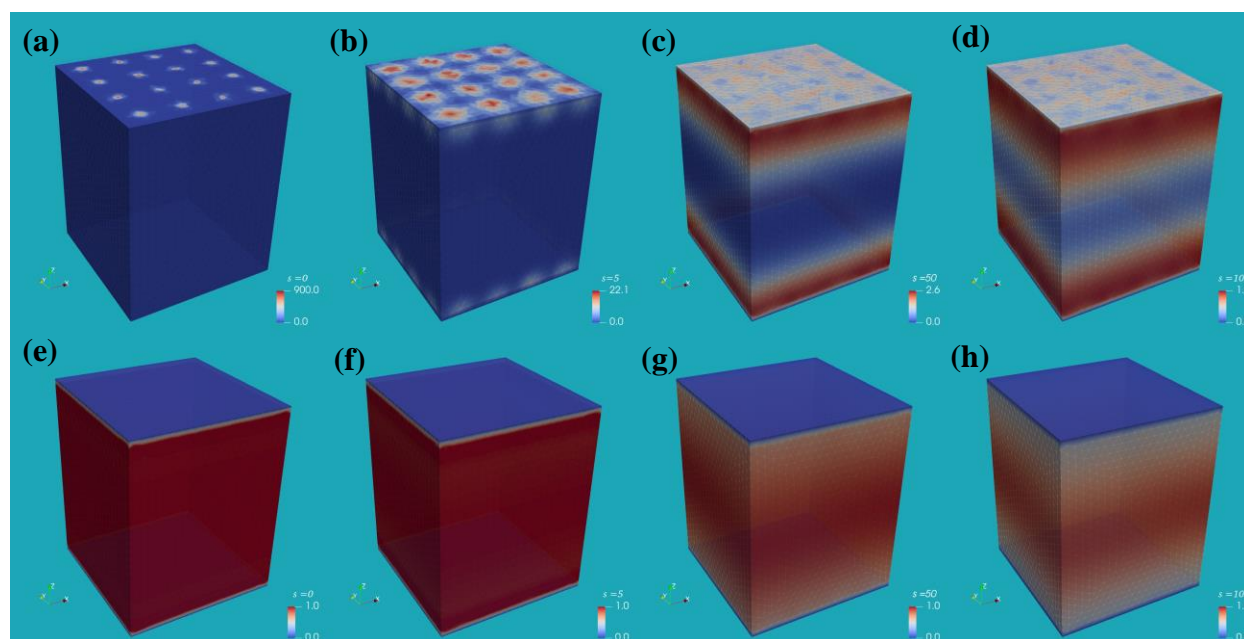
Figure 5.13. The grafted chain "diffusion" equation against matrix chain "diffusion" equation at several reduced contour length steps. We illustrate the probability of finding a segment of a grafted(q_{g}) **(a-d)** and a matrix(q_{m}) **(e-h)** chain initially and after 5, 10, 100 contour length steps, respectively, throughout the volume of the domain.

In Figure 5.13, we illustrate the probability of finding a segment of a grafted and of a free chain after various contour length steps in the volume of the domain. It is obvious that 16 chains are grafted to each substrate surface, resulting in a grafting density of 0.25 nm^{-2}. The probability of finding the grafted segment of a grafted chain (corresponding to contour length equal to zero) is zero everywhere inside the domain except for the positions of the grafted points. As the contour length steps increase, the probability diffuses from the surfaces to the

center. In contrast to the grafted chains, matrix chains begin with zero probability of finding a segment at the interface and equal to 1 everywhere else. The two systems of chains are connected to each other through the chemical potential field, which determines the way in which the propagator of both kinds of chains behaves.

5.4.3/a Reduced Density Profiles

Figure 5.14 depicts the reduced density profiles of PS grafted chains in the presence of a Hamaker potential exerted by the silica walls, as a function of σ_g, M_g, and N_m/N_g. The behavior of grafted chains can be classified into three distinct regimes depending on the combinations of σ_g and N_g: The structural behavior of both grafted and matrix chains varies with position, as we move along directions perpendicular to the interface. In previous SCF works addressing grafted chain systems, the grafted chains were handled via a smearing technique, hence it was not possible to distinguish how these reduced density profiles vary as one moves laterally (along the *x* and/or *y* directions). The results obtained from the one dimensional model,where the grafting points are smeared, are demonstrated with dashed lines in Figure 5.4. As illustrated in Figure 5.4, the grafting points (g-points) denote the positions where the grafted chains are tethered to the silica surface, while the central points (c-points) denote the centers of squares formed by adjacent grafted points. It is expected that the density profiles of grafted chains, along the *z*-direction, are maximal at the g-points and minimal at the c-points. In addition the profiles corresponding to the smeared grafting points assume values between the profiles at g-points and c-points.

In the left column of Figure 5.14, a wide range of reduced segment densities is illustrated. As we move downwards along this column in the figure, the grafting density increases, while the molecular weight of grafted chains, M_g, and the swelling ratio, N_m/N_g, are kept constant. The mushroom regime is depicted in the first three graphs (Figure 5.14(a-c)), where the matrix chains are seen to reach the solid wall. In Figure 5.14(c), the regime between mushroom and dense brush is displayed. The number of matrix chains which reach the interfacial regions is small and localized in the vicinity of m-points. In Figure 5.14(d), a dense brush is formed on each surface, with small interpenetration of the matrix chains. In Figure 5.14(e) grafted chains have completely expelled the matrix chains. At low grafting densities, the matrix chains of the melt penetrate the brush and there is a broad brush-matrix polymer

interface. With increasing grafting density, a gradual growth of an almost pure layer of grafted chains on the substrate is observed.

The most striking result emerging from the left-hand side column of Figure 5.14 is that the reduced density profiles of grafted chains connecting two opposing g-points exhibit a sharp peak near the interfaces. When the grafting density increases, the peak of the density profiles becomes less pronounced. It is important to note that the decrease in the peaks is reasonable, since at low grafting densities the chains behave like mushrooms and therefore they look like reflected random coils with strong presence near the solid surfaces, whereas at high grafting densities crowding forces them to extend further into the bulk. Our findings appear to be in good agreement with the reported literature. Ndoro et al.[138] report a peak which exceeds the bulk density by at least a factor of 1.4. In addition, according to Ndoro et al.[138] the total monomer number density profiles exhibit a peak equal to 1.9 times the bulk density, while this peak decreases with increasing grafting density. Vogiatzis et al.'s [143] findings appear to support our conclusions; they observed a similar behavior in studying the structural features of polystyrene brushes grafted on spherical silica nanoparticles immersed in polystyrene. In that work, they used a Monte Carlo methodology based on a mean-field Hamiltonian.

In the central column of Figure 5.14, a wide range of chain lengths is illustrated. Moving downwards, the chain length increases, while σ_g and N_m/N_g are kept constant. The peak exhibited by the reduced density of grafted chains starting from g-points is fixed at 1.6 for all chain lengths. The matrix chains reach the solid wall even for higher values of N_g. With increasing N_g, the density of matrix chain segments decreases, whereas the one of grafted chain segments increases. Moreover, the reduced density of grafted chain segments at c-points and g-points near the surfaces is quite different for small N_g, while, with increasing N_g, this difference is reduced. If we now turn to the matrix chain segment profiles at c-points and g-points near the surfaces, they tend to translate downwards almost uniformly with increasing N_g; an almost constant difference is observed between c-profiles and g-profiles of matrix chains for all grafted chain lengths.

For further investigation, a comparison between graphs with the same $\sigma_g N_g$ product but different values of σ_g and N_g is revealing. Plots of Figure 5.14(c) and Figure 5.14(j) display results for $\sigma_g=0.25\text{nm}^{-2}$, $M_g=10.4\text{kg/mol}$ and $\sigma_g=0.06\text{nm}^{-2}$, $M_g=41.7\text{kg/mol}$, respectively. Note that $N_m=N_g$ in both cases. Although they belong to the same region according to ref 237, the
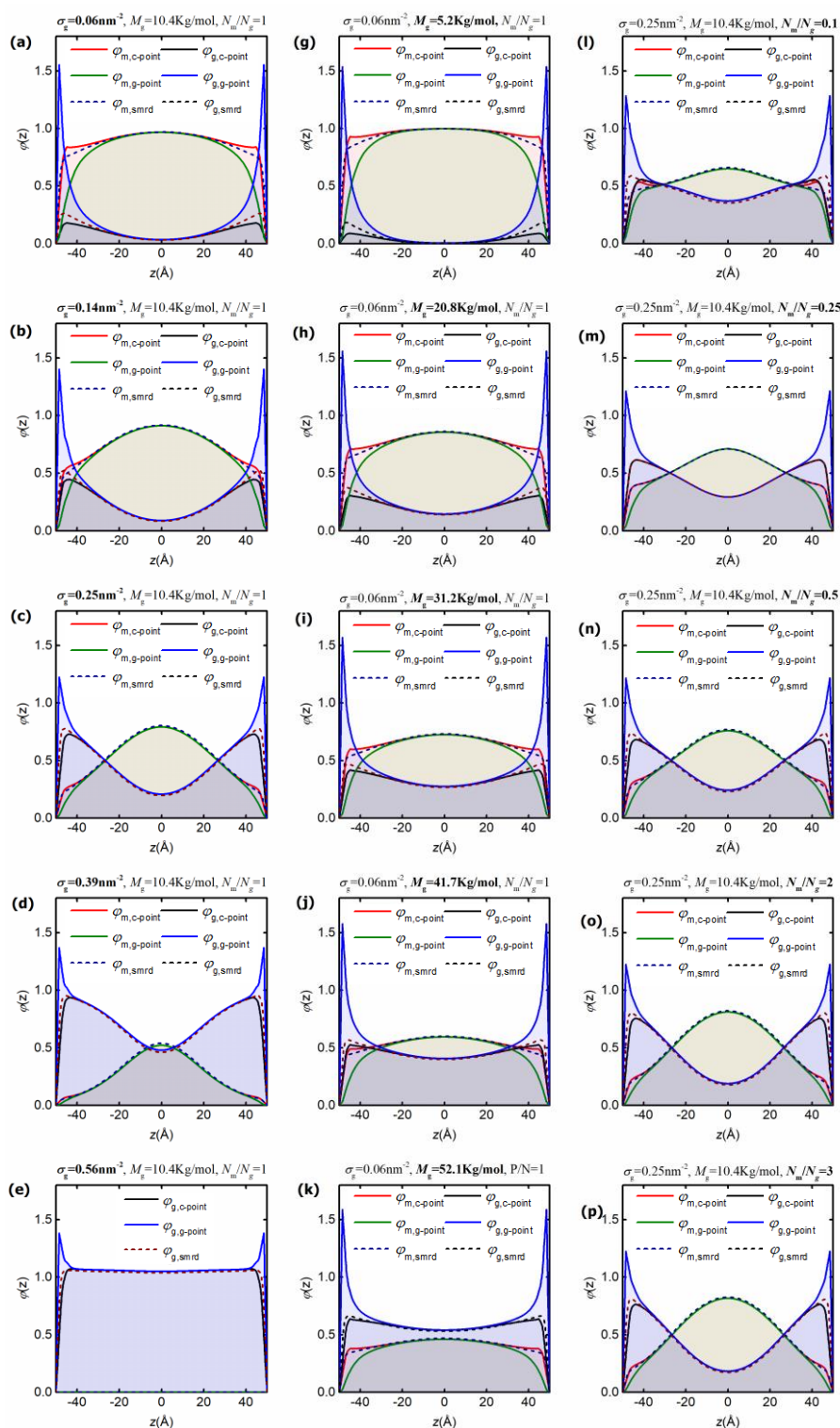
Figure 5.14. Reduced density profiles of PS grafted and matrix chains as a function of σ_g, M_g and N_m/N_n Profiles of matrix chains move across a direction perpendicular to the interface starting from c-points(red) and g-points (green). Profiles of grafted chains move across a direction perpendicular to the interface starting from c-points (black) and g-points (blue). With dashes the results for reduced density profiles of PS grafted and matrix chains as obtained from the smeared 1-D model (SCFFD).

density profiles differ. The matrix chains penetrate the region occupied by the grafted chains more easily in the system with higher grafting density. The brush thickness of the system with lower molecular weight of grafted chains appears to be smaller. Moreover, in the higher N_g system the matrix chains seem to have the same density throughout the domain, while in the lower N_g system the matrix chains dominate the bulk region and are absent from the interfaces.

In the right hand-side column of Figure 5.14, a wide range of swelling ratios N_m/N_g is illustrated. Moving downwards, the swelling ratio increases, while σ_g and N_g are kept constant. In Figure 5.14(l), it is interesting to see that the reduced profiles starting from c-points are almost identical for the matrix and grafted chains. Smaller matrix chains can easily move and penetrate into the region occupied by the grafted chains. With increasing swelling ratio (Figure 5.14(l-n)), this penetration ability of the matrix chains decreases. Experimental,[136] SCF,[307] and molecular dynamics (MD)[327] works on planar polymer brushes, in a chemically identical matrix, have shown that the matrix wets the polymer brush only when the melt chains are shorter than the chains of the brush. When the matrix chains become shorter than grafted chains (Figure 5.14(o-p)), the density profiles remain unchanged. The increase in the swelling ratio seems to have no effect on the matrix segments penetrating the brush. It is experimentally observed[328] that "autophobic dewetting" occurs when the brush and the matrix share the same length. Longer melt chains spontaneously dewet the brush, because the gain in mixing entropy cannot overcome the conformational entropy loss associated with the matrix chains penetrating the brush.

5.4.3/b Reduced End – Middle Segment Distribution

Figure 5.15 depicts the reduced density profiles of the end segments of grafted and matrix chains on lines connecting c-points and g-points across the investigated parameter space. Of particular interest is that, in all graphs, the end segments of both grafted and matrix chains appear to prefer to be near the c-points rather than the g-points. As expected, there is no difference in the bulk region between end segments starting from c-points or g-points.

With increasing grafting density and keeping the remaining parameters constant (Figure 5.15(a- e)), there is a rise in the reduced density profiles of the grafted chain ends in the whole domain. At higher grafting densities the grafted chain end profiles are shifted towards the bulk region, confirming that the chain ends are segregated far from the surface, suggesting that the grafted chains are stretched. The matrix chain ends appear to dominate in the bulk region, even at higher grafting densities. As anticipated, near interfaces the matrix chain ends reach
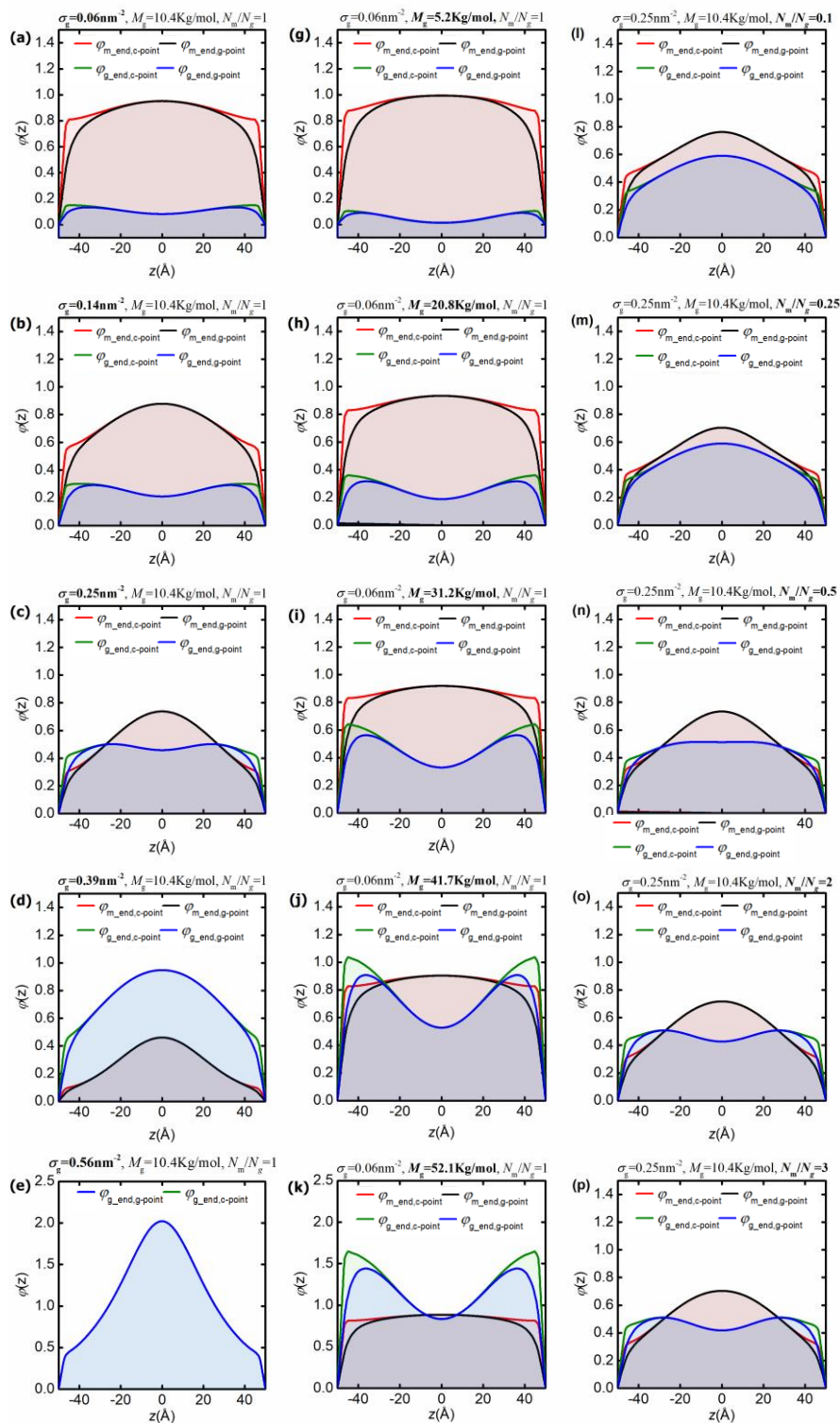
Figure 5.15. End segment distributions of PS grafted chain systems as a function of σ_g, N_g and N_m/N_g. Profiles of matrix chains are moving across a direction perpendicular to the interface starting from c-points (red) and g-points (green). Profiles of grafted chains are moving across a direction perpendicular to the interface starting from c-points (black) and g-points (blue).

more easily c-points than g-points. The presence of matrix chain ends at the interfaces decreases with increasing grafting density.

As shown in Figure 5.15(g-k), with increasing molecular weight of grafted and matrix chains, and retaining the (low) grafting density and swelling ratio constant, the grafted chain ends increase near interfaces more sharply than in the bulk region. Interestingly, for high values of molecular weight, the grafted chain ends seem to prefer the interface rather than the bulk region. The reduced density of matrix chain ends assumes an approximately constant value in the whole domain. Again, a preference of matrix chain ends exists for c-points rather than g-points.

Plots of Figure 5.15(c) and Figure 5.15(j) display results with the same $\sigma_g N_g$. In both cases, $N_m=N_g$. The grafted chain ends vary throughout the whole domain in the system with lower grafting density, exhibiting a peak near 1.0, while in the system with higher grafting density the grafted end chain profile is smoother. The opposite behavior is revealed for the matrix chain ends. In the higher N_g system the matrix chain ends seem to have the same density throughout the domain, while in the low N_g system, the matrix chain ends dominate in the bulk region and are absent near the interfaces.

Figure 5.15(l-p) illustrate how the swelling ratio affects the chain end profiles. Our findings are consistent with previous results[136,307,327] confirming that the smaller the matrix chains are, the more easy it is for them to penetrate into the region occupied by the grafted chains. The above statement is proved by the fact that, when the swelling ratio is lower than 0.5, the matrix chain ends extend in the whole domain, indicating a presence of matrix chains in the brush region. As the swelling ratio increases, the matrix chain ends are pushed towards the bulk region. Finally, with increasing swelling ratio, the grafted chain ends have an enhanced presence near the interfaces.

5.4.3/c Contributions to the Grand Potential

Figure 5.16(a) presents the individual grand potential terms against the grafting density, σ_g. The cohesive interaction term per unit solid surface ($\Delta\Omega_{coh} / S_{solid}$) is practically insensitive to grafting density. The solid-polymer interaction term (U_s / S_{solid}) remains constant for all grafting densities, while the entropy term associated with the partition function of matrix chains ($\Delta\Omega_m/S_{solid}$) exhibits a minor increase, which becomes larger at larger grafting densities, because

grafted chains claim more space in the interfacial region, leaving the matrix chains with fewer available conformations. With increasing grafting density, the entropy term associated with the grafted chains $\Delta A_g/S_{\text{solid}}$ and the field term $\Delta\Omega_{\text{field}}/S_{\text{solid}}$ vary notably, especially for larger grafting densities. This is attributed to ρ_g exceeding $\rho_{\text{seg/bulk}}$ due to chain crowding and enhances the cohesion of the brush. $\Delta A_g/S_{\text{solid}}$ increases steeply in the vicinity of higher grafting densities. This response is attributed to the stretching of the grafted chains due to crowding phenomena. The total grand potential $\Delta\Omega/S_{\text{solid}}$, being a sum of all the above terms, increases with increasing grafting density. According to Figure 5.16(d) the SCFFEM and SCFFD exhibit similar quatitative behavior.
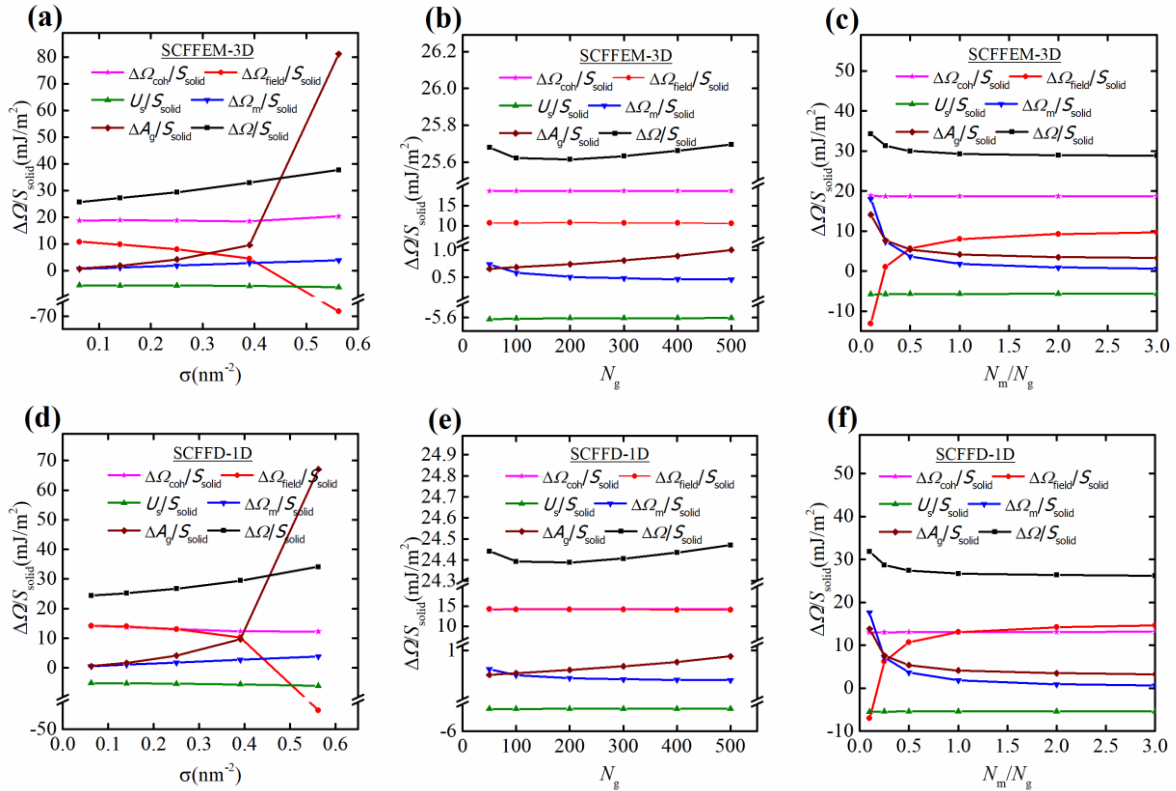
Figure 5.16. Partial contributions to the grand potential per unit area over the parameter space (σ_g, N_g, N_m/N_g). Grand potential terms against: **(a)** the grafting density , σ_g, keeping constant N_g=100, N_m/N_g=1, **(b)** the grafted chainlength , N_g, keeping constant σ_g=0.625nm^{-2}, N_m/N_g=1, **(c)** the swelling ratio , N_m/N_g keeping constant σ_g=0.25nm^{-2}, N_g=100,obtained from SCFFEM-3D. **(d-f)** The partial contributions to the grand potential per unit area over the same parameter space (σ_g, N_g, N_m/N_g) as obtained from SCFFD-1D.

Figure 5.16(b) illustrates the individual grand potential terms against the grafted chainlength , N_g. Again, the cohesive interaction term per unit solid surface ($\Delta\Omega_{\text{coh}} / S_{\text{solid}}$) is practically insensitive to chain length. Similar behavior is exhibited by the field term, $\Delta\Omega_{\text{field}}/S_{\text{solid}}$, and the solid-polymer interaction term, U_s / S_{solid}. The grafting density is rather

small and therefore these terms are not affected by the change in chainlength. The entropy term associated with the partition function of matrix chains ($\Delta\Omega_{\mathrm{m}}/S_{\mathrm{solid}}$) exhibits a monotonic decrease, which is evident from eq 4.11, since N_{m} appears in denominator and at the same time the partition function Q_{m} is rather insensitive to N_{m} . This can be also explained by the fact that with increasing N_{m} the number of matrix chains per unit surface decreases. These values correlate favorably with figure 5b of Sgouros et al.,[321]in which the dependence of $\Delta\Omega_{\mathrm{m}}$ with N_{g} is illustrated for constant $N_{\mathrm{m}}/N_{\mathrm{g}}$=1. The entropy term associated with the grafted chains ($\Delta A_{\mathrm{g}}/S_{\mathrm{solid}}$) increases, indicating that there is an entropic penalty with increasing grafted chain length associated with grafted chain conformations. The most remarkable result to emerge from this plot is the behavior of total grand potential $\Delta\Omega/S_{\mathrm{solid}}$, exhibiting an initial decline due to the $\Delta\Omega_{\mathrm{m}}/S_{\mathrm{solid}}$ term, a minimum at chainlength equal to 200 skeletal bonds, and finally an increase due to $\Delta A_{\mathrm{g}}/S_{\mathrm{solid}}$. The one dimensional model results in the same exact prediction wherein the minimum is located at N_{g} =200 as illustrated in Figure 5.16(e).

Figure 5.16(c) shows the individual grand potential terms against the swelling ratio $N_{\mathrm{m}}/N_{\mathrm{g}}$. As in the two previous plots, the cohesive interaction term per unit solid surface and the solid-polymer interaction term remain almost constant with increasing swelling ratio. Unexpectedly, with increasing swelling ratio, the entropy term associated with the grafted chains and the entropy term associated with the partition function of matrix chains present the same qualitative behavior; initial decrease and eventual relaxation to a plateau value. This behavior is attributed to the stretching of the grafted chains due to crowding phenomena, because matrix chains are shorter and thus exhibit a larger number of available conformations when in the lower swelling ratio regime. With increasing swelling ratio, the matrix chains cannot easily penetrate grafted chains and they exhibit fewer available conformations due to increase in their chain length. $\Delta\Omega_{\mathrm{field}}/S_{\mathrm{solid}}$ increases with increasing swelling ratio and this is attributed to the increase of segment density near interfaces. $\Delta\Omega/S_{\mathrm{solid}}$ exhibits a monotonic decrease and finally reaches a plateau, which is in agreement with previous findings in the literature[321] as well as with the SCFFD-1D model as shown in Figure 5.16(f)

5.5   Concluding Remarks

In this chapter we have coupled one theoretical methodology with one of the most important and widespread numerical techniques, in order to determine the equilibrium properties of polymer melts at interfaces: self-consistent field theory (based on a Gaussian thread representation of

chains) and the finite element method. To validate the results of our SCFFEM approach, we have used the system of a free standing molten polyethylene film and the interface between molten polyethylene and graphite as reference systems, which we are also studying with atomistic and mesoscopic simulations and for which a solution using one- dimensional finite differences (SCFFD) is available. Moreover, we compared the results against previous authors' implementations.[24,31]

The results and assessment of the computational requirements of our new SCFFEM approach, for a polymer free surface and for a planar solid/polymer interface, were validated through the calculation of the surface and the adhesion tension. We prove that SCFFEM gives identical solutions with SCFFD and MD. Although the problem we solve was in fact one-dimensional, our *RuSseL* code solves it in all three dimensions, without any bias in any dimension.

An objective of this chapter was to develop a finite element computational methodology to explore the most critical parameter for finite element method: the mesh density and composition. At first, we investigated how the mesh density affects our solution and what is the optimum mesh density to accomplish the desired accuracy. For our realistic PE system with real compressibility, a mesh with average element size equal to 2 Å is needed. This mesh proved to be time consuming and we took advantage of the flexibility of the finite element method by applying a coarser mesh to the domain where no steep solution gradients are exhibited. We developed a technique to decide what the ideal mesh for this domain is. Additionally, we compared the time for a single iteration needed for both linear and quadratic elements, with respect to the number of nodal points, the number of elements, and the average element size. These tests revealed that first order tetrahedral elements enable faster convergence than second order tetrahedral elements for the same number of nodal points.

Furthermore, we analyzed the stability of the integrodifferential system of equations in order to find out its behavior and convergence requirements. As a first attempt, we chose to adjust the compressibility of the system. Different meshes were applied for various compressibilities. We introduced the "reduced surface tension" as a reliable criterion for system convergence with the desired accuracy. The number of iterations required for the system to converge was used as a second criterion for the obtained accuracy. In order to comprehend the behavior of the successive substitution scheme, different initial field configurations were tried.

In the classical approach, the relaxation parameter remained constant, while in our new "straight forward approach", the relaxation parameter changed at each iteration. The latter calculation proved to be quite efficient, since it reduced the total computation time with negligible cost in accuracy.

Next, we considered a system of grafted chains in a planar geometry. A polystyrene/silica interface with grafted polystyrene chains constitutes a convenient system. Implementation of the SCF-FEM approach in systems containing grafted chains at specific points of the solid surfaces was far from a trivial undertaking. As pointed out in Section 5.3, in the presence of grafted chains, two Edwards diffusion equations have to be solved, one for the matrix melt chains and one for the grafted chains. In each iteration, the equation for the matrix chains has to be solved first, as it is necessary for the evaluation of the initial conditions of grafted chains.

Until now, a smearing in grafted chains was applied. We distinguish the grafting positions on the surfaces from those without grafted chains. On the one hand, "g-points" designate the positions where the grafted chains are tethered to the silica interface. On the other hand, "c-points" designate the centers of the squares formed by adjacent grafting points. Reduced density profiles along lines connecting opposing g- and c- points were derived, considering a parameter space comprising N_g, σ_g and N_m/N_g.

The reduced density of grafted chains on lines connecting two opposing g-points exhibits a peak near the surfaces. When the grafting density increases, the peak of the density profiles becomes less pronounced. This is in good agreement with previous works.[138,143] With increasing molecular weight, the peak value remains unchanged. The matrix chains reach the solid wall even for higher values of N_g and their profiles at the c-points and g-points near the interfaces exhibit a constant difference for all values of N_g. Systems with the same $\sigma_g N_g$ product, although belonging to the same region according to ref 237, exhibit dissimilar density profiles. Finally, by varying the swelling ratio, we have shown that the matrix wets the polymer brush only when the melt chains are shorter than the chains of the brush. Our findings corroborate previous results. [136,307,327].

The end segment distributions of grafted and matrix chains along lines connecting c-points and g-points were also investigated across the same parameter space. Of fundamental interest is the fact that end segments of both grafted and matrix chains appear to prefer to be near the c-points, rather than g-points. With increasing grafting density, it was revealed that grafted chain

ends spread in the whole domain. As expected, for higher grafting densities, the grafted chain ends prefer the bulk region. As might have been expected, for small swelling ratio values, matrix chain ends extend in the whole domain, confirming that the smaller the matrix chains are, the easier it is for them to penetrate into the region occupied by the grafted chains.

Regarding the contribution to the grand potential, the present chapter investigates the individual grand potential terms, defined in the previous chapter, against grafting density, chain length, and swelling ratio. With increasing grafting density, $\Delta A_{\mathrm{g}}/S_{\mathrm{solid}}$ and $\Delta\Omega_{\mathrm{field}}/S_{\mathrm{solid}}$ deviate notably, especially at larger grafting densities. This is attributed to chain crowding and enhances the cohesion of the brush and the stretching of the grafted chains. The total $\Delta\Omega/S_{\mathrm{solid}}$ increases with increasing grafting density. With increasing chain length, $\Delta\Omega_{\mathrm{m}}/S_{\mathrm{solid}}$ exhibits a monotonic decrease, which is justified from eq 4.11. This can be also associated with the fact that with increasing N_{m} the number of matrix chains per unit surface decreases. The $\Delta A_{\mathrm{g}}/S_{\mathrm{solid}}$ increases, indicating that there is an entropic penalty associated with grafted chain conformations. The $\Delta\Omega/S_{\mathrm{solid}}$ term exhibits a minimum at chainlength equal to 200 skeletal bonds. With increasing swelling ratio, $\Delta A_{\mathrm{g}}/S_{\mathrm{solid}}$ and $\Delta\Omega/S_{\mathrm{solid}}$ decrease and reach a plateau value due to crowding phenomena. Matrix chains are shorter and thus exhibit a higher number of available conformations in the lower swelling ratio regime. $\Delta\Omega/S_{\mathrm{solid}}$ exhibits a monotonic decrease and eventually reaches a plateau which is in agreement with previous findings reported in the literature.[321]

6 Main Conclusions and Innovations

The present Thesis addresses three major theoretical challenges in the field of field-theoretic calculations, and especially in self-consistent field theory of polymers. First, by including nonlocal terms from square gradient theory into SCFT of a free film polymer system, we obtained critical insight into its local segment-level structure and increased accuracy in predictions of polymer surface tension. Then, having verified the novel SCFT with SGA methodology, we have used it as a stepping stone to access the structural and thermodynamic properties of PNC and at the same time we reexamined the scaling features of grafted polymer layers, against experimental measurements and relevant theoretical predictions. Last but not least, prompted by the need to develop a better quantitative understanding of structure and interactions in polymer-matrix NC, we developed a new computational approach, based on SCFT combined with FEM for dealing with inhomogeneous polymer systems containing interfaces in three dimensions. The main contribution of this thesis was to build up a field theoretic approach based on the SCFT capable of providing fundamental understanding and giving answers to specific nanocomposite design-related problems, to prove its thermodynamic consistency, and to validate it against available experimental measurements. In the following we briefly summarize the innovations introduced by the dissertation at three levels: methodology, physical insight, and computational tools.

6.1   Methodological Advances

- Formulation of grand partition function which relies on *a generic excess Helmholtz energy functional*, in such a way that any suitable equation of state can be applied to describe the non-bonded interactions among chain polymer segments. In conjunction with the aforementioned free energy functional, a square gradient term was introduced based on Square Gradient Theory, which allows to describe non-local effects and leads to more accurate estimates of density profiles and surface tensions. The formulation can be implemented in systems of arbitrary geometry consisting of either only free polymer chains or both grafted and free (matrix) polymeric chains.

- Derivation of a *closed form expression for the free energy density* by employing a lattice-based EoS, proposed by Sanchez-Lacombe, to calculate the grand potential and density-dependent field in SCFT. Moreover, we have reexpressed the dimensionless influence parameter to benefit from the advantages of the non-local term approximation and transformed the SCFT formulation, enabling estimation of the influence parameter for each polymer based only on the parameters of the Sanchez-Lacombe EoS

- Quite a long time ago, Theodorou[235] introduced a method to calculate the *number of chains passing through a surface* drawn parallel to the interface anywhere within the film. The methodology, originally developed for a lattice fluid SCF model, was extended by Daoulas et al.[24] and implemented in the continuous Gaussian thread model. The contribution of this thesis consists in deriving the necessary expressions for calculating the reduced chain shape quantity, allowing direct comparison of SCFT results with atomistic simulations in terms of the conformational properties of chains. Additionally, we have reformulated this quantity in a way that is applicable to spherical geometries as well.

- Derivation of a *thermodynamic relation* between the grand potential and surface tension for the case of a film of polymer melt bounded by gas capable of yielding the surface tension for various polymers. This relation proved to be very accurate for calculating the surface tension as obtained from SGT density profiles, giving a more generic character to the formulation.

- Development of two techniques for evaluating the thickness of the reduced free polymer density profile capable of quantifying the *sigmoid profiles* obtained by various models. These two distinct strategies allowed measuring how symmetric, smooth, and wide a density profile is.

- Development of a numerical formulation for *Vapor-Liquid Equilibrium of a Sanchez-Lacombe Fluid* based on the Newton-Raphson method capable of calculating the densities and (common) chemical potential of both phases, as well as the vapor pressure. That calculation was incorporated in all models, even if in the simple Helfand model by calculating the isothermal compressibility of the liquid.

- Development of a separate technique capable of classifying chain segments in free standing polymer chains into *adsorbed* or *free*. We modified this technique to GNP immersed molten polymer matrices to describe how matrix chains can penetrate the grafted chains.

- Derivation of the *segment balance equations* dealing with the grafted and the matrix chains in the presence of the external field of the solid(s). We related the reduced grafted chain density with grafted and matrix chain propagators, allowing the calculation of grafted chain density profiles.

- Transformation of SCF equations from Cartesian to *spherical polar coordinates* so that they can be utilized in the case of a spherical nanoparticle with uniformly smeared grafting points on its surface.

- Quantification of exponents of the *power-law* applied to describe the *scaling of the height of polymer brushes* with surface grafting density, grafted and free chain lengths, allowing us to evaluate the mean brush thickness and obtain a unique perspective on various brush regimes. Moreover, we introduced the measure brush thickness ratio, enabling us to make additional comparisons between the SCFT model and Alexander's model for incompressible melts.

- Derivation of *thermodynamic contributions* to the grand potential for the case of chains grafted on NP or planar surfaces in contact with a polymer melt capable of clarification of the enthalpic and entropic parts of energy. Likewise, the stretching free energy of grafted chains has been estimated with two different ways: from the configurational partition function of grafted chains and from the density profiles of the grafted chain ends.

- A rigorous and efficient three dimensional finite element method based on tetrahedral elements for solving Edwards's diffusion equation has been developed. Tetrahedral elements are appropriate for arbitrary complex geometries and compatible with fully automatic mesh generations. The results from the new, three-dimensional finite element method are in excellent agreement with previous results based on a one-dimensional method. Moreover, in the three-dimensional formulation we employ a rigorous initial condition on the grafting points, evaluating the required delta function as the inverse volume assigned to the node. Previous efforts resulted in smearing of the grafted points, an approximation that is lifted with our new, three-dimensional FEM technique.

- Development of a *h-,r-,p-refinement technique* capable of obtaining the ideal mesh density for finite element solution. The contribution of this thesis consists in deriving two criteria for obtaining the desired mesh density (one based on system iterations and a second one based on the grand potential/surface tension obtained), in discovering the optimal element size for bulklike domains that are represented more coarsely, and in the comparison of time needed for a single iteration between linear and quadratic element meshes.

- A precise and timesaving iteration method was established by implementing an improved procedure for guessing the initial field imported into the Edwards diffusion equation and by tuning the relaxation parameter between iterations. This "*straight forward approach*" was successfully validated, with significant reduction in the time needed for the system to converge.

6.2   Physical Insight Obtained

By using the methodologies described above we have extended our understanding of materials in the following ways:

- The model employing *an excess Helmholtz energy density* based on the Sanchez-Lacombe equation of state coupled with a square density gradient term achieves best agreement with atomistic simulation results.

- The SCF-SGA model *combines* SCF models, which consider only the local density in describing chain interactions and produce steeper profiles, and SGA-based models, which, although capable of generating smoother and more realistic density profiles, do not incorporate entropic effects associated with the change of chain conformational/orientational distributions in response to the constraints present at the surfaces, thus overestimating the surface entropy.

- As is well known for homopolymers where the ends are of the same chemical constitution as the middle segments, *chain ends* were found to segregate to the interfaces. The magnitude of this effect and the extent of the interfacial region dominated by the end segments can be estimated with accuracy by our SCF approach, as comparison with atomistic simulations shows. In addition, the temperature dependence of this effect is correctly captured by the theory.

- Some discrepancy appears between SCF_SL+SGA and MD in the profiles of segments belonging to *adsorbed and free chains*, which is less significant for C260 chains than it is for C100 chains. The reason for this discrepancy is that the Gaussian thread model employed does not fully capture local stiffness effects. SCF qualitatively follows the atomistic results. The same behavior is seen in the loop and tail distributions of adsorbed chains.

- An important structural feature of polymer melts at surfaces is the *flattening of chains* due to their preferential orientation parallel to the surface. Both atomistic and field theoretic

results show a relationship between the chain length and extent of the chain flattening region. In free polyethylene films of chains as short as C260 the shape profile from SCF_SL+SGA almost coincides with that from MD. The range of the flattening effect is in good agreement between theory and simulation, being on the order of $1.6R_g$.

- The *reduced influence parameter* found to reproduce the atomistically calculated reduced density profile for the polyethylene surface was used for all polymers examined. The SCF conformational entropy contribution added by the SCF treatment in the Gaussian thread approximation increases the surface tension by 5-10%.

- A nice feature of SCF-SGA model is that it accounts for *two distinct length scales simultaneously*: i) a monomeric one, set by the range of monomer interactions, governing properties of the liquid-vapor interface; ii) a polymeric one, set by the radius of gyration, governing structural properties at the chain level.

- For most polymers SCF_SL+SGA yields results for both *surface tension and surface entropy* that are in excellent agreement with experiments

- *It is clear that with increasing grafting density and chain molar mass, the grafted chains on* a solid surface exposed to melt of the same chemical constitution as the grafted chains need to stretch towards the bulk in order to adjust to their conformational restriction.[255,260,264] As a result, it is more difficult for the matrix chains to penetrate into the interfacial region.

- The *scaling law* for the corona thickness, $h \sim N_{star}^{1/2} f_{star}^{1/4}$, proposed by Daoud and Cotton for star polymers in the intermediate regime, $f_{star}^{1/2} \upsilon^{-2} \gg N_{star} \gg f^{1/2}$, over a specific range of nanoparticle radii, specifically from 4 nm to 8 nm. For larger nanoparticles, the scaling exponents exhibit a complicated behavior, and thus a more general equation must be implemented, which treats the exponents of the molecular weight and grafting density as functions of nanoparticle radius.

- Adjusting also the *pre-exponential factor of the scaling law*, a master curve can be obtained, which provides a faithful description of SCFT predictions for the brush height in linear polymer melts of the same chemical constitution and length as the grafted chains, given the molecular weight of grafted chains, the grafting density, and the radius of the nanoparticle.

- In calculating the free energy of the system, the *term associated with the conformational entropy* of grafted chains does not depend on nanoparticle radius for low grafting densities and molar masses (Figure 4.12). The same plot reflects that, with increasing grafting density or molar mass, the grafted chains need to stretch and therefore the free energy penalty associated with chain stretching increases. This entropy contribution of the grafted chains becomes dominant for high grafting densities and molar masses.

- The *stretching free energy* of grafted chains has been estimated in two different ways (1: from the configurational partition function of grafted chains and 2: approximately from the density profiles of the grafted chain ends) and a good agreement with the Alexander model was observed in the limit of large grafting densities. The corresponding entropic term of *matrix chains has a minor contribution to the total free energy.*

- The reduced density of grafted chains across a line connecting two opposite g-points exhibits *a peak near* the surfaces. When the grafting density increases, the peak of the density profiles becomes less pronounced. This is in good agreement with previous works.[138,143] With increasing grafted chain molecular weight the peak value remains fixed. For low surface grafting densities (mushroom regime), the matrix chains reach the rigid wall even for higher values of N_g and their profiles at c-points and g-points near the interfaces exhibit a constant difference for all values of N_g.

- Systems with same $\sigma_g N_g$, although belonging the same region according to ref 237, may exhibit dissimilar density profiles.

- By adjusting the *swelling ratio* N_m/N_g, the matrix is found to wet the polymer brush only when the melt chains are shorter than the chains of the brush. Our findings corroborate previous results. [136,307,327]

- Of fundamental interest is the fact that, at low grafting densities according to ref 237, *end segments for both grafted and matrix chains* appear to prefer to be near the c-points rather than g-points. With increasing grafting density that grafted chain ends spread across larger parts of the domain. As expected, for higher grafting densities the grafted chain ends prefer to segregate in the vicinity of the bulk region. As might have been expected, matrix chain ends at small swelling ratios extend throughout the whole domain, confirming that smaller the matrix chains are more easily capable of penetrating grafted chains.

- With increasing grafting density, $\Delta A_g/S_{solid}$ and $\Delta \Omega_{field}/S_{solid}$ deviate notably, especially for larger grafting densities. This is attributed to chain crowding and enhances the cohesion of the brush and the stretching of the grafted chains due to crowding phenomena. In addition, the grand potential per unit area, $\Delta\Omega/S_{solid}$ increases with increasing grafting density.

- With increasing grafted chain length, while keeping σ_g and N_m/N_g constant, the entropy term associated with the partition function of matrix chains ($\Delta\Omega_m/S_{solid}$) exhibits a monotonic decrease, and this result correlates well with figure 5b of Sgouros et al.,[321] in which the dependence of $\Delta\Omega_m$ on N_g is illustrated, for constant $N_m/N_g=1$.

- With increasing grafted chain length, while keeping σ_g and $N_m/N_g, L_z$ constant, the $\Delta A_g/S_{solid}$ increases indicating that there is an entropic penalty associated with chain conformations. For the system with opposing grafted surfaces $\sigma_g=0.06nm^{-2}$, $N_m/N_g=1$ and $L_z=10$ nm, the $\Delta\Omega/S_{solid}$ exhibiting a minimum at value of 200 skeletal bonds chain length.

- With increasing swelling ratio N_m/N_g, while keeping σ_g and N_g constant, $\Delta A_g/S_{solid}$ and $\Delta\Omega/S_{solid}$ decrease and reach a plateau value due to crowding phenomena, because matrix chains are smaller and more broadly distributed in the lower swelling ratio regime.

$\Delta\Omega/ S_{\text{solid}}$ exhibits a monotonic decrease, reaching a plateau, which substantiates previous findings in the literature.[321]

6.3 Computational Tools

In the framework of the present thesis the following computer codes have been developed:

- RuSseL-1D, the one-dimensional version of our in-house code, has been developed to address polymeric interfaces through Self-Consistent Field calculations. RuSseL can be used for a wide variety of systems in planar and spherical geometries, such as free films, cavities, adsorbed polymer films, polymer-grafted surfaces, and nanoparticles in melt and vacuum phases. The code includes a wide variety of functional potentials for the description of solid–polymer interactions, allowing the user to tune the density profiles and the degree of wetting by the polymer melt. Based on the solution of the Edwards diffusion equation, the equilibrium structural properties and thermodynamics of polymer melts in contact with solid or gas surfaces can be described. We have extended the formulation of Schmid to investigate systems comprising polymer chains, which are chemically grafted on the solid surfaces. A full ducementation can be foundin ref 323.

- RuSseL-3D, the three-dimensional version of our in-house code, is capable of addressing a great variety of systems in complex geometries, such as nanoparticles in melt and vacuum phases, nanotubes, free, supported, or capped polymer films, polymer-grafted interfaces, and every nanostructure anyone can imagine. It is based on the finite element method for solving the Edwards diffusion equation. It is compatible with COMSOL Multiphyshics for mesh generation, features an input parser, uses a BDF solver, and is connected with MUltifrontal Massively Parallel sparse direct Solver (MUMPS) for large linear systems. It is capable of using first and second order tetrahedral elements, but fully versatile to use hexahedra or pyramids as elements, if desired. It can compute initial values for grafted chains at specific points and it is capable of applying Neumann and Dirichlet boundary conditions. An extension for periodic boundary conditions is in the making.

6.4 Side Projects

In order to address the main challenges of this PhD thesis, several other sub-problems have been resolved:

- A mesoscopic simulation approach has been developed for liquid−gas interfaces of weakly and strongly entangled polymer melts and implemented for linear polyethylene at 450 K. A combined particle and field-theoretic treatment has been adopted based on aggressive coarse-graining, each polymer bead representing ∼50 carbon atoms, with effective bonded interactions extracted from atomistic simulations. Non bonded interactions in the mesoscopic model are dictated by an equation of state (here the Sanchez−Lacombe) in conjunction with a variant of gradient theory; the discrete square gradient theory. The dynamics of free films has been examined in the presence and in the absence of topological constraints (modeled by slip-springs) to unveil the impact of the latter on chain self-diffusion, to assess their contribution to the interfacial free energy, and to explore how this contribution can be removed by invoking a compensating potential. The molar mass dependence of surface tension; which arises from bonded contributions among beads in the mesoscopic chains, has been extracted over a broad range of molar masses (10^3−10^6 g/mol), in excellent agreement with experiment. Two approaches for computing the surface tension have been adopted, based on stress profiles and based on changes in free energy with interfacial area, leading to consistent results. The predicted density profiles, conformations, and orientational tendencies of the mesoscopic chains have been retrieved from the simulations and shown to reproduce very well the corresponding results from atomistic simulations. An annealing scheme has been developed with the purpose of accelerating transitions of metastable states into more stable biphasic states such as spherical and cylindrical droplets, free films, and spherical and cylindrical bubbles, which minimize the free energy of the periodic model system. Results for the phase diagram as a function of polymer volume fraction conform to the predictions of atomistic simulations of simpler systems.

- The investigation of single and opposing silica plates, either bare of grafted, in contact with vacuum or melt phases, using self-consistent field theory. Solid–polymer and solid–solid nonbonded interactions have been described by means of a Hamaker potential, in

conjunction with a ramp potential. The cohesive nonbonded interactions have been described by the Sanchez-Lacombe or the Helfand free energy densities. We first built our thermodynamic reference by examining single surfaces, either bare or grafted, under various wetting conditions in terms of the corresponding contact angles, the macroscopic wetting functions (i.e., the work of cohesion, adhesion, spreading and immersion), the interfacial free energies and brush thickness. Subsequently, we derived the potential of mean force (PMF) of two approaching bare plates with melt between them, each time varying the wetting conditions. We then determined the PMF between two grafted silica plates separated by a molten polystyrene film. Having allowed the grafting density and the molecular weight of grafted chains to vary between the two plates, we tested how asymmetries existing in a real system could affect steric stabilization induced by the grafted chains. Additionally, we derived the PMF between two grafted surfaces in vacuum and determine how the equilibrium distance between the two grafted plates is influenced by their grafting density and the molecular weight of grafted chains. Finally, we provided design rules for the steric stabilization of opposing grafted surfaces (or fine nanoparticles) by taking account of the grafting density, the chain length of the grafted and matrix chains, and the asymmetry among the opposing surfaces.

7   Research Outlook

The mathematical formulation and the computer codes developed in the present thesis have been designed in a rigorous and versatile way, ensuring their applicability to a wide class of problems. The following paragraphs discuss some interesting potential applications and future research directions.

7.1   SCFT Combined with SGA

Based on the SCF, and its combination with square gradient theory that was developed for free polymer surfaces and films several other problems can be addressed:

- Disjoining pressure of thin liquid films on the order of a few nanometers in thickness and bounded on both the sides by air or vapor can immediately be calculated from the Self-consistent field with square gradient term formalism (e.g., SCF_SL+SGA). The first results on the estimation of the disjoining pressure are highly promising.

- Binary blends of linear polymer with well-separated molecular weights. An accurate description of polymer interfaces is important because phase separation and immiscibility are the rule rather than the exception for polymer mixtures. In commercial phase-separated polymer blends the interfacial tension is a crucial factor in the adhesive bonding between phases. In addition, the interfacial tensions of polymer blends are of interest for such applications as enhanced oil recovery. The input parameters can be extracted from previous works and the computer code must be extended to include two different polymers.

7.2   Structure and Thermodynamics of Grafted Silica/PNCs

Based on the spherical methodology for grafted nanoparticles, a broad range of materials (pure and composite) can be addressed, by simply providing as an input to the method the melt compressibility and the squared radius of gyration of the grafted or matrix chain polymer. Among the limitless possibilities, several other problems can be addressed:

- Block copolymers for use in self-assembly nanoparticles structures. In comparison to the homopolymer case, block copolymers introduce additional complexities due to new interactions and confinement effects. Graft block copolymers (GBCPs) can be used to achieve nano-structured polymers with ultra-small nanodomains and diverse morphologies without sacrificing materials properties that are critical for processing and functions. The bulk properties of GBCPs can conversely be tuned either by selecting a variety of sidechains or through adjusting the backbone length with minimal interference with the nanostructures. However, major modifications in computer code must be extended to include these interactions.

- Potential of mean force between two bare or surface-grafted nanoparticles in a polymer melt. By calculating the PMF, it is possible to identify the thermodynamically most stable configuration of multi-nanoparticle systems. The investigation of single and opposing silica plates, either bare or grafted, in contact with vacuum or melt phases, using self-consistent field theory addressed by Sgouros et al.,[321] can be used as a guide in such an effort. The 1D computer code developed in Ref 323 could be extended in 2D as well, in order to provide additional validations and facilitate the calculations with the 3D version of the code.

7.3   SCFFEM Methodology

The methodology and tools developed based on the SCFFEM model introduced in Chapter 5 can be used for predicting the equilibrium of arbitrary polymer systems. Possible areas of application of SCFFEM computational methodology can include:

- Systems comprising more than two nanoparticles bearing grafted chains and embedded inside a polymer matrix. In such systems, we can address the interactions among

nanoparticles as a function of their volume fractions and the grafting chain distributions (homogeneus, biased) across their surfaces. Various representative ordered and disordered configurations of the nanoparticle centers at a variety of nanoparticle volume fractions could be considered. For each configuration, one could estimate the free energy, as well as the density and conformational distributions of matrix and grafted chains. An interesting concept for examination is to determine how the lowest free energy configuration changes when a nonuniform distribution of grafting points on the surfaces of the spherical nanoparticles is adopted.

- The study of materials made up of self-assembled SiO_2 spheres bearing surface-grafted chains, in the absence of matrix homopolymer. These "matrix-free hairy nanoparticle assemblies", also known as "particle-solids", combine excellent optical and mechanical properties. The objective of such a computational investigation would be to predict the particle configuration which minimizes the free energy, including the pair distribution function of nanoparticle centers, the crystal structure adopted, if present, and even the effects of polydispersity in the particles.

Appendices

A   Grand Partition Function and Saddle Point Approximation

A.1   Edwards diffusion equation

Following Edwards[187] we consider the continuous-space curve $\mathbf{r}(s)$ followed by a chain represented by the Gaussian thread model with root mean square effective bond length b. By definition of the propagator, eq. 2.41, if $\mathbf{r}'$ is the position vector of the chain at contour length s_1, $0 < s_1 < s$, the following condition is satisfied:

$$G(\mathbf{r}, \mathbf{r}_0; s) = \int d^3 r' \, G(\mathbf{r}, \mathbf{r}'; s - s_1) \, G(\mathbf{r}', \mathbf{r}_0; s_1) \tag{A.1}$$

For $w(\mathbf{r}) = 0$, $G(\mathbf{r}, \mathbf{r}_0; s)$ becomes the probability density of the end-to-end vector of a field-free Gaussian chain:

$$G(\mathbf{r}, \mathbf{r}_0; s) = G_0(\mathbf{r} - \mathbf{r}_0; s) = \left(\frac{3}{2\pi s b^2}\right)^{3/2} \exp\left[-\frac{3(\mathbf{r} - \mathbf{r}_0)^2}{2 s b^2}\right] \Theta(s) \tag{A.2}$$

with $\Theta(n)$ being the Heaviside step function: $\Theta(s) = 1$ for $s > 0$ and $\Theta(s) = 0$ for $s < 0$. Expressing the exponential term in eq A.2 as a Fourier transform, we write:

$$G_0(\mathbf{r} - \mathbf{r}_0; s) = \frac{1}{(2\pi)^3} \int d^3 k \, \exp\left[i\mathbf{k} \cdot (\mathbf{r} - \mathbf{r}_0)\right] \exp\left(-s\frac{k^2 b^2}{6}\right) \Theta(s) \tag{A.3}$$

Differentiating both sides with respect to s,

$$\frac{\partial}{\partial s} G_0(\mathbf{r} - \mathbf{r}_0; s) = \frac{1}{(2\pi)^3} \int d^3 k \, \exp\left[i\mathbf{k} \cdot (\mathbf{r} - \mathbf{r}_0)\right] \exp\left(-n\frac{k^2 b^2}{6}\right)\left[-\frac{k^2 b^2}{6}\Theta(s) + \delta(s)\right] \tag{A.4}$$

or

$$\frac{\partial}{\partial s} G_0(\mathbf{r} - \mathbf{r}_0; s) = \frac{b^2}{6} \nabla_{\mathbf{r}}^2 G_0(\mathbf{r} - \mathbf{r}_0; s) + \delta(\mathbf{r} - \mathbf{r}_0)\, \delta(s) \tag{A.5}$$

Thus, the Edwards diffusion equation, is satisfied for $w(\mathbf{r}) = 0$.

Consider now the more general case $w(\mathbf{r}) = 0$. By virtue of the factorization eq A.1 we can write:

$$G(\mathbf{r}, \mathbf{r}_0; s + \Delta s) = \int d^3 r' \, G(\mathbf{r}, \mathbf{r}'; \Delta s) \, G(\mathbf{r}', \mathbf{r}_0; s) \tag{A.6}$$

The first Green function refers to a very small piece of chain, of length Δs, which starts at $\boldsymbol{r}'$ and ends at $\boldsymbol{r}$. The defining equation, eq 2.41, for $G(\boldsymbol{r}, \boldsymbol{r}'; \Delta s)$ contains in its numerator the term

$$-\frac{1}{k_B T} \int_s^{s+\Delta s} ds_1 w[\boldsymbol{R}(s_1)] \cong -\frac{1}{k_B T} \, w \, (\boldsymbol{r}) \, \Delta s \tag{A.7}$$

Then,

$$G(\boldsymbol{r},\boldsymbol{r}';\Delta s) = \exp\left[-\frac{1}{k_B T} \, w(\boldsymbol{r}) \, \Delta s \right] G_0(\boldsymbol{r} - \boldsymbol{r}';\Delta s) \tag{A.8}$$

Substituting eq A.8 in eq A.7 we obtain

$$G(\boldsymbol{r}, \boldsymbol{r}_0; \, s + \Delta s) = \exp\left[-\frac{1}{k_B T} \, w(\boldsymbol{r}) \, \Delta n \right] \int d^3 r' \, G_0(\boldsymbol{r} - \boldsymbol{r}'; \, \Delta s) \, G(\boldsymbol{r}', \boldsymbol{r}_0; \, s) \tag{A.9}$$

For small Δs, $G_0(\boldsymbol{r} - \boldsymbol{r}'; \Delta s)$ is sharply peaked at $\boldsymbol{r} - \boldsymbol{r}' = \boldsymbol{0}$. Expanding $G(\boldsymbol{r}', \boldsymbol{r}_0; s)$ with respect to $\boldsymbol{r}'' = \boldsymbol{r} \text{ - } \boldsymbol{r}'$ we obtain:

$$\int d^3 r' \, G_0(\boldsymbol{r} - \boldsymbol{r}'; \, \Delta s) \, G(\boldsymbol{r}', \boldsymbol{r}_0; \, s) = \int d^3 r'' \, G_0(\boldsymbol{r}''; \, \Delta s) \, G(\boldsymbol{r} - \boldsymbol{r}'', \boldsymbol{r}_0; \, s) =$$

$$= \int d^3 r'' \, G_0(\boldsymbol{r}''; \, \Delta s) \left(1 \, - \, \sum_\alpha r''_\alpha \frac{\partial}{\partial r_\alpha} + \frac{1}{2} \sum_\alpha \sum_\beta r''_\alpha r''_\beta \frac{\partial^2}{\partial r_\alpha \partial r_\beta} \right) G(\boldsymbol{r}, \boldsymbol{r}_0; \, s) \tag{A.10}$$

with indices $\alpha, \beta \in \{1, 2, 3\}$ being used to denote the components of a vector. Now,

$$\int d^3 r'' \, G_0(\mathbf{r}''; \, \Delta s) \, r''_\alpha = 0 \quad \text{and} \quad \int d^3 r'' \, G_0(\mathbf{r}''; \, \Delta s) \, r''_\alpha \, r''_\beta = \frac{1}{3} (\Delta s \, b^2) \, \delta_{\alpha\beta} \tag{A.11}$$

as r''_α, r''_β are components of the end-to-end vector of a Gaussian chain. Thus, we obtain

$$\int d^3 r' \, G_0(\boldsymbol{r} - \boldsymbol{r}'; \, \Delta s) \, G(\boldsymbol{r}', \boldsymbol{r}_0; \, s) = \left(1 + \frac{\Delta s \, b^2}{6} \nabla_r^2 \right) G(\boldsymbol{r}, \boldsymbol{r}_0; \, s) \tag{A.12}$$

Combining Eqs. A.9 and A.12 we obtain:

$$G(\boldsymbol{r}, \boldsymbol{r}_0; \, s + \Delta s) = \exp\left[-\frac{1}{k_B T} \, w(\boldsymbol{r}) \, \Delta s \right] \left(1 + \frac{\Delta s \, l^2}{6} \nabla_r^2 \right) G(\boldsymbol{r}, \boldsymbol{r}_0; \, s) \tag{A.13}$$

Subtracting $G(\boldsymbol{r}, \boldsymbol{r}_0; s)$ from both sides, we obtain

Appendix A. Grand Partition Function and Saddle Point Approximation

$$G(\mathbf{r}, \mathbf{r}_0; s+\Delta s) - G(\mathbf{r}, \mathbf{r}_0; s)=\exp\left[-\frac{1}{k_B T}\ w(\mathbf{r})\ \Delta s\right]\left(1+\frac{\Delta s\ b^2}{6}\nabla_r^2\right)G(\mathbf{r}, \mathbf{r}_0; s) - G(\mathbf{r}, \mathbf{r}_0; s)$$

or

$$\frac{\partial}{\partial s}G(\mathbf{r}, \mathbf{r}_0; s)\ \Delta s=\exp\left[-\frac{1}{k_B T}\ w(\mathbf{r})\ \Delta s\right]\left(1-\exp\left[\frac{1}{k_B T}\ w(\mathbf{r})\ \Delta s\right]+\frac{\Delta s\ b^2}{6}\nabla_r^2\right)G(\mathbf{r}, \mathbf{r}_0; s)\text{ In}\qquad\text{the}$$

limit $\Delta s \to 0$ one obtains

$$\left(\frac{\partial}{\partial s}\ -\ \frac{b^2}{6}\nabla_r^2\ +\ \frac{1}{k_B T}\ w(\mathbf{r})\right)G(\mathbf{r}, \mathbf{r}_0; s) = 0 \tag{A.14}$$

To account for the singularity at $s=0$, we use Eq A.8 for small s:

$$G(r,r';s) = \exp\left[-\frac{1}{k_B T}\ w(\mathbf{r})\ s\right]G_0(r-r';s) \tag{A.15}$$

upon differentiation of which, for a smoothly varying field $(l\,|\,\nabla_r w(\mathbf{r})\,|\,/(k_B T) << 1)$ one obtains

$$\left(\frac{\partial}{\partial s}-\frac{b^2}{6}\nabla_r^2+\frac{1}{k_B T}\ w\left(r\right)\right)G\left(r,r_0;s\right)=\delta\left(r-r_0\right)\delta\left(s\right) \tag{A.16}$$

A.2   Grand partition Function of an Ensemble of Chains Subjected to a Field

Following Schmid,[98] we re-express the Boltzmann factor on the right-hand side of eq 2.1 in terms of a real density field $\rho(\mathbf{r})$ and an energy field $w(\mathbf{r})$ by use of the inverse Fourier transform expression for a Dirac delta functional:

$$\exp\left(-\beta F\left[\hat{\rho}(\mathbf{r})\right]\right)= \int\mathcal{D}\rho(\mathbf{r})\ \delta[\rho(\mathbf{r})-\hat{\rho}(\mathbf{r})]\ \exp\left(-\beta F\left[\rho(\mathbf{r})\right]\right) \tag{A.17}$$

and

$$\delta[\rho(\mathbf{r})-\hat{\rho}(\mathbf{r})]= C\int\mathcal{D}\left[\beta w(\mathbf{r})\right]\exp\left\{i\int d^3 r\beta w(\mathbf{r})[\rho(\mathbf{r})-\hat{\rho}(\mathbf{r})]\right\} \tag{A.18}$$

with C being a normalization constant.[198] Combining eqs A.17 and A.18,

$$\exp\left(-\beta F\left[\hat{\rho}(\mathbf{r})\right]\right)=C\int\mathcal{D}\rho(\mathbf{r})\ \int\mathcal{D}\left[\beta w(\mathbf{r})\right]\exp\left\{i\int d^3 r\beta w(\mathbf{r})[\rho(\mathbf{r})-\hat{\rho}(\mathbf{r})]\right\}\exp\left(-\beta F\left[\rho(\mathbf{r})\right]\right) \tag{A.19}$$

Using eq A.19 within eq 2.1,

$$
\begin{aligned}
\Xi &= \sum_{n=0}^{\infty} \frac{1}{n!} \exp\left[\frac{\mu N n}{k_B T}\right] \tilde{N}^n \int \prod_{\alpha=1}^{n} \mathcal{D}\mathbf{r}_\alpha(\bullet) \mathcal{P}\left[\mathbf{r}_\alpha(\bullet)\right] \times \\
&\quad \times C \int \mathcal{D}\rho(\mathbf{r}) \int \mathcal{D}[\beta w(\mathbf{r})] \exp\left\{i\int d^3 r \beta w(\mathbf{r})[\rho(\mathbf{r}) - \hat{\rho}(\mathbf{r})]\right\} \times \\
&\quad \times \exp\left(-\beta F[\rho(\mathbf{r})]\right) \\
&= C \sum_{n=0}^{\infty} \frac{1}{n!} \exp\left[\frac{\mu N n}{k_B T}\right] \tilde{N}^n \int \prod_{\alpha=1}^{n} \mathcal{D}\mathbf{r}_\alpha(\bullet) \mathcal{P}\left[\mathbf{r}_\alpha(\bullet)\right] \times \\
&\quad \times \int \mathcal{D}\rho(\mathbf{r}) \int \mathcal{D}[\beta w(\mathbf{r})] \exp\left(i\int d^3 r \beta w(\mathbf{r})\rho(\mathbf{r})\right) \times \\
&\quad \times \exp\left(-\beta F[\rho(\mathbf{r})]\right) \exp\left(-i\int d^3 r \beta w(\mathbf{r})\hat{\rho}(\mathbf{r})\right)
\end{aligned}
\tag{A.20}
$$

The last factor within the functional integral of eq A.20 incorporates the density operator $\hat{\rho}(\mathbf{r})$. Introducing the definition for $\hat{\rho}(\mathbf{r})$, eq 2.2, we obtain

$$
\begin{aligned}
\exp\left(-i\int d^3 r \beta w(\mathbf{r})\hat{\rho}(\mathbf{r})\right) &= \exp\left[-i\int d^3 r \beta w(\mathbf{r}) N \sum_{\alpha=1}^{n} \int_0^1 \delta\left(\mathbf{r} - \mathbf{r}_\alpha(\tilde{s})\right) d\tilde{s}\right] \\
&= \exp\left[-\sum_{\alpha=1}^{n} i\int d^3 r \beta N w(\mathbf{r}) \int_0^1 \delta\left(\mathbf{r} - \mathbf{r}_\alpha(\tilde{s})\right) d\tilde{s}\right] \\
&= \prod_{\alpha=1}^{n} \exp\left[-i\int d^3 r \beta N w(\mathbf{r}) \int_0^1 \delta\left(\mathbf{r} - \mathbf{r}_\alpha(\tilde{s})\right) d\tilde{s}\right]
\end{aligned}
\tag{A.21}
$$

Combining eqs A.20 and A.21,

$$
\begin{aligned}
\Xi &= C \sum_{n=0}^{\infty} \frac{1}{n!} \exp\left[\frac{\mu N n}{k_B T}\right] \tilde{N}^n \int \mathcal{D}\rho(\mathbf{r}) \int \mathcal{D}[\beta w(\mathbf{r})] \exp\left(i\int d^3 r \beta w(\mathbf{r})\rho(\mathbf{r})\right) \times \\
&\quad \times \exp\left(-\beta F[\rho(\mathbf{r})]\right) \times \\
&\quad \times \int \prod_{\alpha=1}^{n} \mathcal{D}\mathbf{r}_\alpha(\bullet) \mathcal{P}\left[\mathbf{r}_\alpha(\bullet)\right] \prod_{\alpha=1}^{n} \exp\left[-i\int_0^1 d\tilde{s} \int d^3 r \beta N w(\mathbf{r}) \delta\left(\mathbf{r} - \mathbf{r}_\alpha(\tilde{s})\right)\right]
\end{aligned}
\tag{A.22}
$$

or

Appendix A. Grand Partition Function and Saddle Point Approximation

$$\Xi = C \sum_{n=0}^{\infty} \frac{1}{n!} \exp\left[\frac{\mu N n}{k_{\mathrm{B}} T}\right] \tilde{N}^n \times$$

$$\times \int \mathcal{D}\rho(\mathbf{r}) \int \mathcal{D}[\beta w(\mathbf{r})] \exp\left(-\beta F[\rho(\mathbf{r})] + \int d^3 r \beta \{i w(\mathbf{r})\rho(\mathbf{r})\}\right) \times \qquad \text{(A.23)}$$

$$\times \prod_{\alpha=1}^{n} \left\{ \int \mathcal{D}\mathbf{r}_\alpha(\bullet) \mathcal{P}[\mathbf{r}_\alpha(\bullet)] \exp\left[-i \int_0^1 d\tilde{s} \ \beta N w(\mathbf{r}_\alpha(\tilde{s}))\right] \right\}$$

Following Edwards[187] we introduce the notation $Q[iw]$ to indicate the partition function of a single chain subject to the field iw acting on its segments, *relative* to the partition function of a field-free chain. Then,

$$\int \mathcal{D}\mathbf{r}_\alpha(\bullet) \mathcal{P}[\mathbf{r}_\alpha(\bullet)] \exp\left[-i \int_0^1 d\tilde{s} \ \beta N w(\mathbf{r}_\alpha(\tilde{s}))\right] =$$

$$= \left\{ \int \mathcal{D}\mathbf{r}_\alpha(\bullet) \mathcal{P}[\mathbf{r}_\alpha(\bullet)] \right\} Q[iw] = Z_{\mathrm{free}} \ Q[iw] \qquad \text{(A.24)}$$

where $Z_{\mathrm{free}} = \int \mathcal{D}\mathbf{r}_\alpha(\bullet) \mathcal{P}[\mathbf{r}_\alpha(\bullet)]$ is the configurational partition function of a free chain. With this notation,

$$\Xi = C \sum_{n=0}^{\infty} \frac{1}{n!} \exp\left[\frac{\mu N n}{k_{\mathrm{B}} T}\right] \left(\tilde{N} Z_{\mathrm{free}}\right)^n$$

$$\int \mathcal{D}\rho(\mathbf{r}) \int \mathcal{D}[\beta w(\mathbf{r})] \left(Q[iw]\right)^n \exp\left(-\beta F[\rho(\mathbf{r})] + i \int d^3 r \beta w(\mathbf{r})\rho(\mathbf{r})\right) \qquad \text{(A.25)}$$

or

$$\Xi = C \int \mathcal{D}\rho(\mathbf{r}) \int \mathcal{D}[\beta w(\mathbf{r})] \exp\left(-\beta F[\rho(\mathbf{r})] + i \int d^3 r \beta w(\mathbf{r})\rho(\mathbf{r})\right) \times$$

$$\times \left\{ \sum_{n=0}^{\infty} \frac{1}{n!} \exp\left[\frac{\mu N n}{k_{\mathrm{B}} T}\right] \left(\tilde{N} Z_{\mathrm{free}}\right)^n \left(Q[iw]\right)^n \right\} \qquad \text{(A.26)}$$

Now, the summation over different n can be performed, yielding

$$\sum_{n=0}^{\infty} \frac{1}{n!} \exp\left[\frac{\mu N n}{k_{\mathrm{B}} T}\right] \left(\tilde{N} Z_{\mathrm{free}}\right)^n \left(Q[iw]\right)^n = \exp\left\{ \exp\left[\frac{\mu N}{k_{\mathrm{B}} T}\right] \tilde{N} Z_{\mathrm{free}} Q[iw] \right\} \qquad \text{(A.27)}$$

The grand partition function of eq A.26 is written as

$$\Xi = C \int \mathcal{D}\rho(\mathbf{r}) \int \mathcal{D}[\beta w(\mathbf{r})] \, \exp\left(-\beta F[\rho(\mathbf{r})] + i\int d^3r \beta w(\mathbf{r})\rho(\mathbf{r})\right) \times$$
$$\times \exp\left\{\exp\left[\frac{\mu N}{k_B T}\right]\tilde{N}Z_{free}Q[iw]\right\} \tag{A.28}$$

or equivalently:

$$\Xi = C \int \mathcal{D}\rho(\mathbf{r}) \int \mathcal{D}[\beta w(\mathbf{r})] \, \exp\left(-\beta H[w(\mathbf{r}), \rho(\mathbf{r})]\right) \tag{A.29}$$

with

$$H[w(\mathbf{r}), \rho(\mathbf{r})] = F[\rho(\mathbf{r})] - i\int d^3r w(\mathbf{r})\rho(\mathbf{r}) - \frac{1}{\beta}\exp(\beta\mu N)\tilde{N}Z_{free}Q[iw] \tag{A.30}$$

It is remarkable that the effective "Hamiltonian" $H[w(\mathbf{r}), \rho(\mathbf{r})]$ incorporates a term proportional to $\exp\left[\dfrac{\mu N}{k_B T}\right]$ and to $Q[iw]$, rather than to μN and to $\ln Q[iw]$, because of the grand canonical formulation adopted.

A.3   Saddle Point Approximation

We now replace the functional integral appearing in eq A.29 for Ξ with its dominant term, obtained by setting

$$\frac{\delta H}{\delta w} = 0 \tag{A.31}$$

From eq A.30 we obtain

$$\frac{\delta H}{\delta w} = -i\rho(\mathbf{r}) - \frac{1}{\beta}\exp(\beta\mu N)\tilde{N}Z_{free}\frac{\delta Q[iw]}{\delta w} \tag{A.32}$$

Now, by definition[187]

$$Q[iw] = \frac{\int \mathcal{D}\mathbf{r}_\alpha(\bullet)\mathcal{P}[\mathbf{r}_\alpha(\bullet)]\exp\left[-\int_0^1 d\tilde{s} \,\, (\beta i N w(\mathbf{r}_\alpha(\tilde{s})))\right]}{\int \mathcal{D}\mathbf{r}_\alpha(\bullet)\mathcal{P}[\mathbf{r}_\alpha(\bullet)]} \tag{A.33}$$

which can be rewritten as

Appendix A. Grand Partition Function and Saddle Point Approximation

$$Q[iw] = \frac{\int \mathcal{D}\mathbf{r}_\alpha(\bullet)\,\mathcal{P}\big[\mathbf{r}_\alpha(\bullet)\big]\exp\left[-\int d^3r \int_0^1 d\tilde{s}\,\,\delta(\mathbf{r}-\mathbf{r}_\alpha(\tilde{s}))(\beta iN w(\mathbf{r}))\right]}{\int \mathcal{D}\mathbf{r}_\alpha(\bullet)\,\mathcal{P}\big[\mathbf{r}_\alpha(\bullet)\big]} \tag{A.34}$$

The functional integrals are taken over the path of one chain, labeled α. The latter form, eq A.34, has been used in eq A.24.

From eq A.34,

$$\frac{\delta Q[iw]}{\delta w} =$$

$$= \frac{\int \mathcal{D}\mathbf{r}_\alpha(\bullet)\,\mathcal{P}\big[\mathbf{r}_\alpha(\bullet)\big]\left(-\beta iN \int_0^1 d\tilde{s}\,\,\delta(\mathbf{r}-\mathbf{r}_\alpha(\tilde{s}))\right)\exp\left[-\int d^3r \int_0^1 d\tilde{s}\,\,\delta(\mathbf{r}-\mathbf{r}_\alpha(\tilde{s}))(\beta iN w(\mathbf{r}))\right]}{\int \mathcal{D}\mathbf{r}_\alpha(\bullet)\,\mathcal{P}\big[\mathbf{r}_\alpha(\bullet)\big]} \tag{A.35}$$

$$= -\beta iNQ[iw]\frac{\int \mathcal{D}\mathbf{r}_\alpha(\bullet)\,\mathcal{P}\big[\mathbf{r}_\alpha(\bullet)\big]\left(\int_0^1 d\tilde{s}\,\,\delta(\mathbf{r}-\mathbf{r}_\alpha(\tilde{s}))\right)\exp\left[-\int d^3r \int_0^1 d\tilde{s}\,\,\delta(\mathbf{r}-\mathbf{r}_\alpha(\tilde{s}))(\beta iN w(\mathbf{r}))\right]}{\int \mathcal{D}\mathbf{r}_\alpha(\bullet)\,\mathcal{P}\big[\mathbf{r}_\alpha(\bullet)\big]\exp\left[-\int d^3r \int_0^1 d\tilde{s}\,\,\delta(\mathbf{r}-\mathbf{r}_\alpha(\tilde{s}))(\beta iN w(\mathbf{r}))\right]}$$

Recalling that $\hat{\rho}(\mathbf{r}) = N\sum_{\alpha=1}^n \int_0^1 \delta(\mathbf{r}-\mathbf{r}_\alpha(\tilde{s}))d\tilde{s}$, eq A.35 can be rewritten as:

$$\frac{\delta Q[iw]}{\delta w} = -\beta NiQ[iw]\frac{1}{Nn}\big\langle\hat{\rho}(\mathbf{r})\big\rangle = -i\beta\frac{Q[iw]}{n}\big\langle\hat{\rho}(\mathbf{r})\big\rangle \tag{A.36}$$

with $\langle\,\,\rangle$ denoting an average over the distribution defined by the single-chain partition function $Q[iw]$, eq A.34. In averaging $\hat{\rho}(\mathbf{r})$ of eq 2.2, all n chains involved in the summation for $\alpha{=}1$ to n yield the same contribution.

From eqs A.32, A.36 at the optimum:

$$\frac{\delta H}{\delta w} = -i\rho(\mathbf{r}) - \frac{1}{\beta}\exp(\beta\mu N)\tilde{N}Z_{\text{free}}\left(-i\beta\frac{Q[iw]}{\bar{n}}\big\langle\hat{\rho}(\mathbf{r})\big\rangle\right) = 0 \tag{A.37}$$

with $\bar{n}$ being the mean number of chains in the interfacial region. One obtains

$$\rho(\mathbf{r}) = \exp(\beta\mu N)\tilde{N}Z_{\text{free}}\frac{Q[iw]}{\bar{n}}\big\langle\hat{\rho}(\mathbf{r})\big\rangle \tag{A.38}$$

We also impose a maximum term approximation with respect to $\rho(\mathbf{r})$. From eq A.30,

$$\frac{\delta H}{\delta \rho(\mathbf{r})} = -iw(\mathbf{r}) + \frac{\delta F[\rho(\mathbf{r})]}{\delta \rho(\mathbf{r})} = 0 \qquad (A.39)$$

or

$$w(\mathbf{r}) = -i\frac{\delta F[\rho(\mathbf{r})]}{\delta \rho(\mathbf{r})} \qquad (A.40)$$

The self-consistent field turns out to be purely imaginary. With the maximum term approximation, eq A.30 gives:

$$\bar{H} = F[\rho(\mathbf{r})] - \int d^3r \left\{ \rho(\mathbf{r}) \frac{\delta F[\rho(\mathbf{r})]}{\delta \rho(\mathbf{r})} \right\} - \frac{1}{\beta} \exp(\beta\mu N)\tilde{N}Z_{\text{free}}Q[iw] \qquad (A.41)$$

By the saddle point approximation on eq A.29 we obtain eq 2.7 of the main text for the grand potential of our interfacial polymer, occupying volume V at temperature T and chain chemical potential μN.

B   Derivation of Grafted/Matrix Polymer System Equations

B.1   Grand Canonical Partition Function and Hamiltonian

We consider a polymer melt within an arbitrarily shaped three-dimensional region $\mathcal{R}$ of volume V at temperature T. The region $\mathcal{R}$ is not necessarily convex. It is partly bounded by one or multiple solid surfaces, which exert an external potential $u_s(\mathbf{r})$ per polymer segment at each position $\mathbf{r} \in \mathcal{R}$. The boundary of the domain $\mathcal{R}$ will be referred to as $\partial\mathcal{R}$. Part of $\partial\mathcal{R}$ may be defined by solid surfaces, while the rest of $\partial\mathcal{R}$ will be characterized by zero-flux Neumann boundary conditions.

The polymer consists of matrix chains of length N_m monomers/segments each. In addition, there are chains terminally grafted on the solid surfaces, the length of each grafted chain being N_g segments. Both matrix and grafted chains are assumed to be monodisperse, but matrix chains can have different chain length from grafted chains. In the context of the present work, matrix and grafted chains are of the same chemical composition, hence the potential energy field per segment, $u_s(\mathbf{r})$, is applicable to both.

We use the symbols n_m and n_g to denote the numbers of matrix and grafted chains, respectively. The number n_g will be fixed. The number n_m is free to fluctuate, subject to the condition that the matrix chains in the interfacial region are in equilibrium with a bulk polymer phase at temperature T, whose density, in segments per unit volume, is $\rho_{seg,bulk}$. Of course, $\rho_{seg,bulk}$ can be determined from the temperature T and the pressure P of the bulk polymer phase through an appropriate equation of state. From the same equation of state one can determine the chemical potential μ_m per chain segment in the bulk polymer.

In general, the mean segment density of polymer in the considered interfacial region, $\bar{\rho}_{seg} = \dfrac{n_m N_m + n_g N_g}{V}$, will be different from $\rho_{seg,bulk}$. The interfacial region and the bulk one will be at equilibrium; the chemical potential μ_m of matrix chain segments in $\mathcal{R}$ is the same as in a bulk phase of matrix chains.

The unperturbed mean square radii of gyration of matrix and grafted chains will be denoted as $\left\langle R_{G,g}{}^2 \right\rangle$ and $\left\langle R_{G,m}{}^2 \right\rangle$, respectively. The grafting points (starts of the grafted chains)

will be denoted by $\mathbf{r}_{g,i_g}$, i_g=1, 2, …, n_g. They all lie on solid surfaces which belong to $\partial\mathcal{R}$. In practice, the grafting point is located at a finite distance from the solid surface. Technically speaking, it is not possible to attach the end of the chain exactly on the surface, because this would result in a conflict between the grafted chains initial condition and the Dirichlet boundary conditions imposed on the solid boundaries.

The matrix chains in the interfacial region of volume V at temperature T and chemical potential $\mu_m N_m$ follow the probability distribution of the grand canonical ensemble. Treating all chains as Gaussian strings and describing the nonbonded interactions by an equation of state in conjunction with a gradient term, $f\left[\hat{\rho}(\mathbf{r}),\nabla\hat{\rho}(\mathbf{r})\right]$, we can write the grand partition function for the polymer contained in $\mathcal{R}$ as:

$$\Xi = \sum_{n_m=0}^{\infty} \frac{1}{n_m!} \exp\left[\beta\mu_m N_m n_m\right] \mathcal{A}_m^{n_m} \mathcal{A}_g^{n_g} \int \prod_{i_m=1}^{n_m} \mathcal{D}\mathbf{R}_{i_m}(\cdot)\mathcal{P}_m\left[\mathbf{R}_{i_m}(\cdot)\right]$$

$$\prod_{i_g=1}^{n_g} \mathcal{D}\mathbf{R}_{i_g}(\cdot)\mathcal{P}_g'\left[\mathbf{R}_{i_g}(\cdot)\right] \exp\left\{-\beta\int\left(f[\hat{\rho}(\mathbf{r}),\nabla\hat{\rho}(\mathbf{r})]+u_s(\mathbf{r})\hat{\rho}(\mathbf{r})\right)d\mathbf{r}\right\}$$

(B.1)

where $\beta = 1/(k_B T)$, $\int \mathcal{D}\mathbf{R}_{i_m}(\cdot)$ symbolizes a functional integral over all paths $\mathbf{R}_{i_m}(s)$, $0 \le s \le N_m$, of a matrix chain i_m ($1 \le i_m \le n_m$) and $\int \mathcal{D}\mathbf{R}_g(\cdot)$ symbolizes a functional integral over all paths $\mathbf{R}_{i_g}(s)$, $0 \le s \le N_g$, of a grafted chain i_g ($1 \le i_g \le n_g$). $\mathcal{A}_m, \mathcal{A}_g$ are normalizing factors per matrix and per grafted chain, respectively, appearing in the path integral formulation. They must be the same between the interfacial system and the bulk polymer and render the grand partition function, Ξ, dimensionless.

The functional $f\left[\hat{\rho}(\mathbf{r}),\nabla\hat{\rho}(\mathbf{r})\right]$ is the Helmholtz energy density (Helmholtz energy per unit volume) describing the nonbonded interactions between polymer segments, obtainable from an appropriate equation of state. Herein we identify f with an excess Helmholtz energy, i.e., the Helmholtz energy of a real polymer fluid consisting of a certain number of chains in a given volume minus the Helmholtz energy of an equal number of noninteracting (ideal gas) chains occupying the same volume. $U_s(\mathbf{r})$ is the total potential energy exerted by the solid on a polymer segment as a function of the position $\mathbf{r}$ of that segment.

Appendix B. Derivation of Grafted/Matrix Polymer System Equations

In the absence of a field, the probability density distribution (statistical weight) of a matrix chain conformation/path, $\mathbf{R}_{i_m}(s)$, and the corresponding one of a grafted chain, $\mathbf{R}_{i_g}(N)$, are given by eqs B.2 and B.3, respectively, in the context of the Gaussian chain model.

$$\mathscr{P}_m\left[\mathbf{R}_{i_m}(\cdot)\right] = \exp\left[-\frac{1}{4R_{G,m}^2}\int_0^{N_m}\left(\frac{d\mathbf{R}_{i_m}}{ds}\right)^2 ds\right] \tag{B.2}$$

$$\mathscr{P}'_g\left[\mathbf{R}_{i_g}(\cdot)\right] = \exp\left[-\frac{1}{4R_{G,g}^2}\int_0^{N_g}\left(\frac{d\mathbf{R}_{i_g}}{ds}\right)^2 ds\right]\delta\left[\mathbf{R}_{i_g}(0)-\mathbf{r}_{g,i_g}\right] = \mathscr{P}_g\left[\mathbf{R}_{i_g}(\cdot)\right]\delta\left[\mathbf{R}_{i_g}(0)-\mathbf{r}_{g,i_g}\right] \tag{B.3}$$

The reduced segment density operators $\hat{\varphi}_m(\mathbf{r})$, $\hat{\varphi}_g(\mathbf{r})$ are defined as shown in eqs B.4 and B.5 respectively.

$$\hat{\varphi}_m(\mathbf{r}) \equiv \frac{\hat{\rho}_m(\mathbf{r})}{\rho_{seg,bulk}} = \frac{\sum_{i_m=1}^{n_m}\int_0^{N_m}\delta\left(\mathbf{r}-\mathbf{R}_{i_m}(s)\right)ds}{\rho_{seg,bulk}} \tag{B.4}$$

$$\hat{\varphi}_g(\mathbf{r}) \equiv \frac{\hat{\rho}_g(\mathbf{r})}{\rho_{seg,bulk}} = \frac{\sum_{i_g=1}^{n_g}\int_0^{N_g}\delta\left(\mathbf{r}-\mathbf{R}_{i_g}(s)\right)ds}{\rho_{seg,bulk}} \tag{B.5}$$

and we set the total reduced segment density operator as $\hat{\varphi}(\mathbf{r}) = \hat{\varphi}_m(\mathbf{r}) + \hat{\varphi}_g(\mathbf{r})$. Next, we wish to re-express the Boltzmann factor on the right-hand side of eq B.1 in terms of a density field, $\rho(\mathbf{r})$, and a chemical potential field, $w(\mathbf{r})$. To begin with, this term can be written as presented in the following eq B.6.[269]

$$\exp\left\{-\beta\int\left(f[\hat{\rho}(\mathbf{r}),\nabla\hat{\rho}(\mathbf{r})]+u_s(\mathbf{r})\hat{\rho}(\mathbf{r})\right)d\mathbf{r}\right\} =$$
$$\int\mathscr{D}\rho(\mathbf{r})\,\delta[\rho(\mathbf{r})-\hat{\rho}(\mathbf{r})]\,\exp\left\{-\beta\int\left(f[\rho(\mathbf{r}),\nabla\rho(\mathbf{r})]+u_s(\mathbf{r})\rho(\mathbf{r})\right)d\mathbf{r}\right\} \tag{B.6}$$

Next, we write the Dirac delta functional as the inverse Fourier transform of eq B.7, which involves the two aforementioned fields.

$$\delta[\rho(\mathbf{r})-\hat{\rho}(\mathbf{r})] = C\int\mathscr{D}[\beta w(\mathbf{r})]\exp\left\{i\int d\mathbf{r}\beta w(\mathbf{r})[\rho(\mathbf{r})-\hat{\rho}(\mathbf{r})]\right\} \tag{B.7}$$

with C being a normalization constant.[91] Combining eqs B.6 and B.7, the following expression is obtained for the Boltzmann factor of the grand partition function of the system.

$$\exp\left\{-\beta\int\left(f[\hat{\rho}(\mathbf{r}),\nabla\hat{\rho}(\mathbf{r})]+u_s(\mathbf{r})\hat{\rho}(\mathbf{r})\right)d\mathbf{r}\right\}=$$

$$=C\int\mathcal{D}\rho(\mathbf{r})\int\mathcal{D}[\beta w(\mathbf{r})]\exp\left\{i\int d\mathbf{r}\beta w(\mathbf{r})[\rho(\mathbf{r})-\hat{\rho}(\mathbf{r})]\right\}\exp\left\{-\beta\int\left(f[\rho(\mathbf{r}),\nabla\rho(\mathbf{r})]+u_s(\mathbf{r})\rho(\mathbf{r})\right)d\mathbf{r}\right\}$$

(B.8)

Within the functional integral of the right-hand side of eq B.8, there is a term incorporating the density operator, $\hat{\rho}(\mathbf{r})$, which is the sum of $\hat{\rho}_m(\mathbf{r})$ and $\hat{\rho}_g(\mathbf{r})$. Introducing the definitions for these operators, eqs B.4 and B.5 respectively, that term can be written as in the following eq B.9.

$$\exp\left(-i\int d\mathbf{r}\beta w(\mathbf{r})\hat{\rho}(\mathbf{r})\right)=\exp\left[-i\int d\mathbf{r}\beta w(\mathbf{r})\left(\sum_{i_m=1}^{n_m}\int_0^{N_m}\delta\left(\mathbf{r}-\mathbf{R}_{i_m}(s)\right)ds+\sum_{i_g=1}^{n_g}\int_0^{N_g}\delta\left(\mathbf{r}-\mathbf{R}_{i_g}(s)\right)ds\right)\right]$$

$$=\exp\left[-\sum_{i_m=1}^{n_m}\int d\mathbf{r}\int_0^{N_m}ds\delta(\mathbf{r}-\mathbf{R}_{i_m}(s))i\beta w(\mathbf{r})\right]\cdot\exp\left[-\sum_{i_g=1}^{n_g}\int d\mathbf{r}\int_0^{N_g}ds\delta(\mathbf{r}-\mathbf{R}_{i_g}(s))i\beta w(\mathbf{r})\right]$$

$$=\prod_{i_m=1}^{n_m}\exp\left(-\int d\mathbf{r}\int_0^{N_m}ds\delta(\mathbf{r}-\mathbf{R}_{i_m}(s))i\beta w(\mathbf{r})\right)\cdot\prod_{i_g=1}^{n_g}\exp\left(-\int d\mathbf{r}\int_0^{N_g}ds\delta(\mathbf{r}-\mathbf{R}_{i_g}(s))i\beta w(\mathbf{r})\right)$$

$$=\prod_{i_m=1}^{n_m}\exp\left(-i\beta\int_0^{N_m}dsw(\mathbf{R}_{i_m}(s))\right)\cdot\prod_{i_g=1}^{n_g}\exp\left(-i\beta\int_0^{N_g}dsw(\mathbf{R}_{i_g}(s))\right)$$

(B.9)

Combining eqs B.1, B.8 and B.9 the following equation is obtained for the grand partition function.

$$\Xi=C\sum_{n_m=0}^{\infty}\frac{1}{n_m!}\exp[\beta\mu_m N_m n_m]\mathcal{A}_m^{n_m}\mathcal{A}_g^{n_g}\int\prod_{i_m=1}^{n_m}\mathcal{D}\mathbf{R}_{i_m}(\cdot)\mathcal{P}_m\left[\mathbf{R}_{i_m}(\cdot)\right]\prod_{i_g=1}^{n_g}\mathcal{D}\mathbf{R}_{i_g}(\cdot)\mathcal{P}_g'\left[\mathbf{R}_{i_g}(\cdot)\right]\frac{\partial^2\Omega}{\partial u^2}$$

$$\times\int\mathcal{D}\rho(\mathbf{r})\int\mathcal{D}[\beta w(\mathbf{r})]\exp\left\{i\int d\mathbf{r}\beta w(\mathbf{r})[\rho(\mathbf{r})-\hat{\rho}(\mathbf{r})]\right\}$$

$$\times\exp\left\{-\beta\int\left(f[\rho(\mathbf{r}),\nabla\rho(\mathbf{r})]+u_s(\mathbf{r})\rho(\mathbf{r})\right)d\mathbf{r}\right\}$$

$$=C\sum_{n_m=0}^{\infty}\frac{1}{n_m!}\exp[\beta\mu_m N_m n_m]\mathcal{A}_m^{n_m}\mathcal{A}_g^{n_g}$$

$$\times\int\mathcal{D}\rho(\mathbf{r})\int\mathcal{D}[\beta w(\mathbf{r})]\exp\left\{i\int d\mathbf{r}\beta w(\mathbf{r})\rho(\mathbf{r})\right\}\exp\left\{-\beta\int\left(f[\rho(\mathbf{r}),\nabla\rho(\mathbf{r})]+u_s(\mathbf{r})\rho(\mathbf{r})\right)d\mathbf{r}\right\}$$ (B.10)

$$\times\prod_{i_m=1}^{n_m}\int\mathcal{D}\mathbf{R}_{i_m}(\cdot)\mathcal{P}_m\left[\mathbf{R}_{i_m}(\cdot)\right]\prod_{i_m=1}^{n_m}\exp\left(-i\beta\int_0^{N_m}dsw(\mathbf{R}_{i_m}(s))\right)$$

$$\times\prod_{i_g=1}^{n_g}\int\mathcal{D}\mathbf{R}_{i_g}(\cdot)\mathcal{P}_g\left[\mathbf{R}_{i_g}(\cdot)\right]\delta\left[\mathbf{R}_{i_g}(0)-\mathbf{r}_{g,i_g}\right]\prod_{i_g=1}^{n_g}\exp\left(-i\beta\int_0^{N_g}dsw(\mathbf{R}_{i_g}(s))\right)$$

Appendix B. Derivation of Grafted/Matrix Polymer System Equations

The next step is to define the single chain partition functions (or functionals to be technically accurate) of a matrix and a grafted chain, $Q_{\mathrm{m}}[iw(\mathbf{r})]$ and $Q_{\mathrm{g}}[\mathbf{r}_{\mathrm{g},i_{\mathrm{g}}};iw(\mathbf{r})]$ respectively, in the field $iw(\mathbf{r})$ by the following eqs B.11 and B.12.

$$Q_{\mathrm{m}}[iw(\mathbf{r})] = \frac{\int \mathcal{D}\mathbf{R}_{i_{\mathrm{m}}}(\cdot)\mathcal{P}_{\mathrm{m}}\left[\mathbf{R}_{i_{\mathrm{m}}}(\cdot)\right]\exp\left[-i\beta\int_{0}^{N_{\mathrm{m}}}\mathrm{d}sw(\mathbf{R}_{i_{\mathrm{m}}}(s))\right]}{\int \mathcal{D}\mathbf{R}_{i_{\mathrm{m}}}(\cdot)\mathcal{P}_{\mathrm{m}}\left[\mathbf{R}_{i_{\mathrm{m}}}(\cdot)\right]} \tag{B.11}$$

$$Q_{\mathrm{g}}[\mathbf{r}_{\mathrm{g},i_{\mathrm{g}}};iw(\mathbf{r})] = \frac{\int \mathcal{D}\mathbf{R}_{i_{\mathrm{g}}}(\cdot)\mathcal{P}_{\mathrm{g}}\left[\mathbf{R}_{i_{\mathrm{g}}}(\cdot)\right]\delta\left[\mathbf{R}_{i_{\mathrm{g}}}(0)-\mathbf{r}_{\mathrm{g},i_{\mathrm{g}}}\right]\exp\left[-i\beta\int_{0}^{N_{\mathrm{g}}}\mathrm{d}sw(\mathbf{R}_{i_{\mathrm{g}}}(s))\right]}{\int \mathcal{D}\mathbf{R}_{i_{\mathrm{g}}}(\cdot)\mathcal{P}_{\mathrm{g}}\left[\mathbf{R}_{i_{\mathrm{g}}}(\cdot)\right]\delta\left[\mathbf{R}_{i_{\mathrm{g}}}(0)-\mathbf{r}_{\mathrm{g},i_{\mathrm{g}}}\right]} \tag{B.12}$$

where, $\int \mathcal{D}\mathbf{R}_{i_{\mathrm{m}}}(\cdot)\mathcal{P}_{\mathrm{m}}\left[\mathbf{R}_{i_{\mathrm{m}}}(\cdot)\right] = Z_{\mathrm{m,free}}V$ is the configurational integral of a field-free matrix chain and $\int \mathcal{D}\mathbf{R}_{i_{\mathrm{g}}}(\cdot)\mathcal{P}_{\mathrm{g}}\left[\mathbf{R}_{i_{\mathrm{g}}}(\cdot)\right]\delta\left[\mathbf{R}_{i_{\mathrm{g}}}(0)-\mathbf{r}_{\mathrm{g},i_{\mathrm{g}}}\right] = Z_{\mathrm{g,free}}$ is the configuration integral of a field-free grafted chain. $Q_{\mathrm{m}}[iw(\mathbf{r})]$ is the configurational integral or partition function of a single matrix chain of length N_{m}, whose segments are subject to the field $iw(\mathbf{r})$, relative to the corresponding partition function of a field-free chain (i.e., Gaussian string performing a random-walk) and is dimensionless by definition. In like manner, $Q_{\mathrm{g}}[\mathbf{r}_{\mathrm{g},i_{\mathrm{g}}};iw(\mathbf{r})]$ is the partition function of a grafted chain of length N_{g}, which starts at $\mathbf{r}_{\mathrm{g},i_{\mathrm{g}}}$ and whose segments are subject to the field $iw(\mathbf{r})$, relative to the partition function of a field-free chain of the same length starting at $\mathbf{r}_{\mathrm{g},i_{\mathrm{g}}}$. It is dimensionless as well.

Combining eqs B.10, B.11 and B.12 the grand partition function becomes:

$$\Xi = C\sum_{n_{\mathrm{m}}=0}^{\infty}\frac{1}{n_{\mathrm{m}}!}\exp\left[\beta\mu_{\mathrm{m}}N_{\mathrm{m}}n_{\mathrm{m}}\right]\mathcal{A}_{\mathrm{m}}^{n_{\mathrm{m}}}\mathcal{A}_{\mathrm{g}}^{n_{\mathrm{g}}} \tag{B.13}$$

$$\times\int \mathcal{D}\rho(\mathbf{r})\int \mathcal{D}[\beta w(\mathbf{r})]\exp\left\{i\int \mathrm{d}\mathbf{r}\beta w(\mathbf{r})\rho(\mathbf{r})\right\}\exp\left\{-\beta\int\left(f[\rho(\mathbf{r}),\nabla\rho(\mathbf{r})]+u_{\mathrm{s}}(\mathbf{r})\rho(\mathbf{r})\right)\mathrm{d}\mathbf{r}\right\}$$

$$\times\left(Z_{\mathrm{m,free}}V\right)^{n_{\mathrm{m}}}\left(Q_{\mathrm{m}}[iw(\mathbf{r})]\right)^{n_{\mathrm{m}}}Z_{\mathrm{g,free}}^{n_{\mathrm{g}}}\left(\prod_{i_{\mathrm{g}}=1}^{n_{\mathrm{g}}}Q_{\mathrm{g}}[\mathbf{r}_{\mathrm{g},i_{\mathrm{g}}};iw(\mathbf{r})]\right)$$

Or

$$\Xi = C \int \mathcal{D}\rho(\mathbf{r}) \int \mathcal{D}[\beta w(\mathbf{r})] \exp\left\{i \int d\mathbf{r} \beta w(\mathbf{r}) \rho(\mathbf{r})\right\} \exp\left\{-\beta \int \left(f[\rho(\mathbf{r}), \nabla \rho(\mathbf{r})] + u_s(\mathbf{r})\rho(\mathbf{r})\right) d\mathbf{r}\right\} \text{(B.14)}$$

$$\times \sum_{n_m=0}^{\infty} \frac{1}{n_m!} \exp[\beta \mu_m N_m n_m] \left(\mathcal{A}_m Z_{m,\text{free}} V\right)^{n_m} \left(Q_m[iw(\mathbf{r})]\right)^{n_m} \left(\mathcal{A}_g Z_{g,\text{free}}\right)^{n_g} \left(Q_g[iw(\mathbf{r})]\right)^{n_g}$$

$$= C \int \mathcal{D}\rho(\mathbf{r}) \int \mathcal{D}[\beta w(\mathbf{r})] \exp\left(\int d\mathbf{r} \beta \{iw(\mathbf{r})\rho(\mathbf{r}) - f[\rho(\mathbf{r}), \nabla \rho(\mathbf{r})] - u_s(\mathbf{r})\rho(\mathbf{r})\}\right)$$

$$\times \exp\left\{\exp[\beta \mu_m N_m] \mathcal{A}_m Z_{m,\text{free}} V Q_m[iw(\mathbf{r})]\right\} \prod_{i_g=1}^{n_g} \left(\mathcal{A}_g Z_{g,\text{free}} Q_g[\mathbf{r}_{g,i_g}; iw(\mathbf{r})]\right)$$

We set the grand partition function to be equal to:

$$\Xi = C \int \mathcal{D}[\rho(\mathbf{r})] \int \mathcal{D}[\beta w(\mathbf{r})] \exp\left(-\beta H[\rho(\mathbf{r}), \nabla \rho(\mathbf{r}), w(\mathbf{r})]\right) \tag{B.15}$$

where the Hamiltonian of the system, H, is a functional of the segment density, $\rho(r)$, of its spatial gradient, and of the chemical potential field, $w(r)$. Finally, using eqs B.14 and B.15, the general form of the Hamiltonian is given by eq B.16.

$$H[\rho(\mathbf{r}), \nabla \rho(\mathbf{r}), w(\mathbf{r})] = \int d\mathbf{r} \{-iw(\mathbf{r})\rho(\mathbf{r}) + f[\rho(\mathbf{r}), \nabla \rho(\mathbf{r})] + u_s(\mathbf{r})\rho(\mathbf{r})\}$$

$$- \frac{1}{\beta} \exp(\beta \mu_m N_m) \mathcal{A}_m Z_{m,\text{free}} V Q_m[iw(\mathbf{r})] - \frac{1}{\beta} \sum_{j=1}^{n_g} \ln\left(\mathcal{A}_g Z_{g,\text{free}} Q_g[\mathbf{r}_{g,i_g}; iw(\mathbf{r})]\right) \tag{B.16}$$

B.1.1 Grand Canonical Ppartition Function after Implementing the Saddle-Point Approximation

In the context of self-consistent field theory, we need to replace the functional integral of eq B.16 with its dominant term, i.e., the density and field configurations which have the highest probability and thus the maximum contribution to the Hamiltonian of the system. In order to determine those configurations, we need to perform a so-called saddle-point approximation, i.e., find the stationary point of the Hamiltonian functional with respect to $\rho(\mathbf{r})$ and $w(\mathbf{r})$. To this end, we first set the functional derivative of the Hamiltonian with respect to $w(\mathbf{r})$ equal to zero, as shown in eq B.17.

$$\frac{\delta H}{\delta w} = 0 \Leftrightarrow -i\rho(\mathbf{r}) - \frac{1}{\beta} \exp(\beta \mu_m) \mathcal{A}_m Z_{m,\text{free}} V \frac{\delta Q_m[iw(\mathbf{r})]}{\delta w} - \frac{1}{\beta} \sum_{i_g=1}^{n_g} \frac{\delta \ln Q_g[\mathbf{r}_{g,i_g}; iw(\mathbf{r})]}{\delta w} = 0 \tag{B.17}$$

Following eq B.11, we write:

Appendix B. Derivation of Grafted/Matrix Polymer System Equations

$$\frac{\delta Q_{\mathrm{m}}[iw(\mathbf{r})]}{\delta w} = \frac{\int \mathcal{D}\mathbf{R}_{i_{\mathrm{m}}}(\cdot)\mathcal{P}_{\mathrm{m}}\left[\mathbf{R}_{i_{\mathrm{m}}}(\cdot)\right]\left(-i\beta\int_0^{N_{\mathrm{m}}} ds\delta(\mathbf{r}-\mathbf{R}_{i_{\mathrm{m}}}(s))\right)\exp\left[-\int d\mathbf{r}\int_0^{N_{\mathrm{m}}} ds\delta(\mathbf{r}-\mathbf{R}_{i_{\mathrm{m}}}(s))i\beta w(\mathbf{r})\right]}{\int \mathcal{D}\mathbf{R}_{i_{\mathrm{m}}}(\cdot)\mathcal{P}_{\mathrm{m}}\left[\mathbf{R}_{i_{\mathrm{m}}}(\cdot)\right]}$$

$$= -\beta i Q_{\mathrm{m}}[iw(\mathbf{r})]\frac{\int \mathcal{D}\mathbf{R}_{i_{\mathrm{m}}}(\cdot)\mathcal{P}_{\mathrm{m}}\left[\mathbf{R}_{i_{\mathrm{m}}}(\cdot)\right]\left(\int_0^{N_{\mathrm{m}}} ds\delta(\mathbf{r}-\mathbf{R}_{i_{\mathrm{m}}}(s))\right)\exp\left[-\int d\mathbf{r}\int_0^{N_{\mathrm{m}}} ds\delta(\mathbf{r}-\mathbf{R}_{i_{\mathrm{m}}}(s))i\beta w(\mathbf{r})\right]}{\int \mathcal{D}\mathbf{R}_{i_{\mathrm{m}}}(\cdot)\mathcal{P}_{\mathrm{m}}\left[\mathbf{R}_{i_{\mathrm{m}}}(\cdot)\right]\exp\left[-\int d\mathbf{r}\int_0^{N_{\mathrm{m}}} ds\delta(\mathbf{r}-\mathbf{R}_{i_{\mathrm{m}}}(s))i\beta w(\mathbf{r})\right]}$$

$$= -\beta i Q_{\mathrm{m}}[iw(\mathbf{r})]\left\langle \int_0^{N_{\mathrm{m}}} ds\delta(\mathbf{r}-\mathbf{R}_{i_{\mathrm{m}}}(s))\right\rangle = -\frac{\beta i \rho_{\mathrm{seg,bulk}} Q_{\mathrm{m}}[iw(\mathbf{r})]}{\overline{n}_{\mathrm{m}}}\left\langle \frac{\sum_{i_{\mathrm{m}}=1}^{\overline{n}_{\mathrm{m}}}\int_0^{N_{\mathrm{m}}} ds\delta(\mathbf{r}-\mathbf{R}_{i_{\mathrm{m}}}(s))}{\rho_{\mathrm{seg,bulk}}}\right\rangle \qquad (B.18)$$

$$= -\frac{\beta i \rho_{\mathrm{seg,bulk}} Q_{\mathrm{m}}[iw(\mathbf{r})]}{\overline{n}_{\mathrm{m}}}\left\langle \hat{\varphi}_{\mathrm{m}}(\mathbf{r})\right\rangle = -\frac{\beta i \rho_{\mathrm{seg,bulk}} Q_{\mathrm{m}}[iw(\mathbf{r})]}{\overline{n}_{\mathrm{m}}}\varphi_{\mathrm{m}}(\mathbf{r})$$

Likewise, following equation B.12, we can write:

$$\frac{\delta \ln Q_{\mathrm{g}}[\mathbf{r}_{\mathrm{g},i_{\mathrm{g}}};iw(\mathbf{r})]}{\delta w} = \frac{1}{Q_{\mathrm{g}}[\mathbf{r}_{\mathrm{g},i_{\mathrm{g}}};iw(\mathbf{r})]}\frac{\delta Q_{\mathrm{g}}[\mathbf{r}_{\mathrm{g},i_{\mathrm{g}}};iw(\mathbf{r})]}{\delta w}$$

$$= \frac{1}{Q_{\mathrm{g}}[\mathbf{r}_{\mathrm{g},i_{\mathrm{g}}};iw(\mathbf{r})]}\frac{\int \mathcal{D}\mathbf{R}_{i_{\mathrm{g}}}(\cdot)\mathcal{P}'_{\mathrm{g}}\left[\mathbf{R}_{i_{\mathrm{g}}}(\cdot)\right]\left(-i\beta\int_0^{N_{\mathrm{g}}} ds\delta(\mathbf{r}-\mathbf{R}_{i_{\mathrm{g}}}(s))\right)\exp\left[-\int d\mathbf{r}\int_0^{N_{\mathrm{g}}} ds\delta(\mathbf{r}-\mathbf{R}_{i_{\mathrm{g}}}(s))i\beta w(\mathbf{r})\right]}{\int \mathcal{D}\mathbf{R}_{i_{\mathrm{g}}}(\cdot)\mathcal{P}'_{\mathrm{g}}\left[\mathbf{R}_{i_{\mathrm{g}}}(\cdot)\right]}$$

$$= -\beta i \frac{\int \mathcal{D}\mathbf{R}_{i_{\mathrm{g}}}(\cdot)\mathcal{P}'_{\mathrm{g}}\left[\mathbf{R}_{i_{\mathrm{g}}}(\cdot)\right]\left(\int_0^{N_{\mathrm{g}}} ds\delta(\mathbf{r}-\mathbf{R}_{i_{\mathrm{g}}}(s))\right)\exp\left[-\int d\mathbf{r}\int_0^{N_{\mathrm{g}}} ds\delta(\mathbf{r}-\mathbf{R}_{i_{\mathrm{g}}}(s))i\beta w(\mathbf{r})\right]}{\int \mathcal{D}\mathbf{R}_{i_{\mathrm{g}}}(\cdot)\mathcal{P}'_{\mathrm{g}}\left[\mathbf{R}_{i_{\mathrm{g}}}(\cdot)\right]\exp\left[-\int d\mathbf{r}\int_0^{N_{\mathrm{g}}} ds\delta(\mathbf{r}-\mathbf{R}_{i_{\mathrm{g}}}(s))i\beta w(\mathbf{r})\right]} \qquad (B.19)$$

$$= -\beta i \left\langle \int_0^{N_{\mathrm{g}}} dN\delta(\mathbf{r}-\mathbf{R}_{i_{\mathrm{g}}}(s))\right\rangle$$

and thus

$$\sum_{i_{\mathrm{g}}=1}^{n_{\mathrm{g}}}\frac{\delta \ln Q_{\mathrm{g}}[\mathbf{r}_{\mathrm{g},i_{\mathrm{g}}};iw(\mathbf{r})]}{\delta w} =$$

$$= -\beta i \rho_{\mathrm{seg,bulk}}\left\langle \frac{\sum_{i=1}^{n_{\mathrm{g}}}\int_0^{N_{\mathrm{g}}} ds\delta(\mathbf{r}-\mathbf{R}_{i_{\mathrm{g}}}(s))}{\rho_{\mathrm{seg,bulk}}}\right\rangle = -\beta i \rho_{\mathrm{seg,bulk}}\left\langle \hat{\varphi}_{\mathrm{g}}(\mathbf{r})\right\rangle = -\beta i \rho_{\mathrm{seg,bulk}}\varphi_{\mathrm{g}}(\mathbf{r}) \qquad (B.20)$$

Combining eqs B.17, B.18 and B.20, the following eq B.21 is obtained for the density field, $\rho(\mathbf{r})$.

$$\rho(\mathbf{r}) = \exp(\beta\mu_{\mathrm{m}})\mathcal{A}_{\mathrm{m}}Z_{\mathrm{m,free}}V\frac{Q_{\mathrm{m}}[iw(\mathbf{r})]}{\bar{n}_{\mathrm{m}}}\rho_{\mathrm{seg,bulk}}\varphi_{\mathrm{m}}(\mathbf{r}) + \rho_{\mathrm{seg,bulk}}\varphi_{\mathrm{g}}(\mathbf{r}) \tag{B.21}$$

The saddle point approximation requires that the functional derivative of the Hamiltonian with respect to the density field, $\rho(\mathbf{r})$, be also equal to zero:

$$\frac{\delta H}{\delta\rho(\mathbf{r})} = 0 \Leftrightarrow -iw(\mathbf{r}) + u_{\mathrm{s}}(\mathbf{r}) + \left[\frac{\partial f}{\partial\rho} - \nabla\cdot\frac{\partial f}{\partial\nabla\rho}\right]\bigg|_{\rho=\rho(\mathbf{r})} = 0$$

$$\Leftrightarrow w(\mathbf{r}) = -i\left(\left[\frac{\partial f}{\partial\rho} - \nabla\cdot\frac{\partial f}{\partial\nabla\rho}\right]\bigg|_{\rho=\rho(\mathbf{r})} + u_{\mathrm{s}}(\mathbf{r})\right) \tag{B.22}$$

After the saddle point approximation, the Hamiltonian of the system, from eq B.16, is given by eq B.23.

$$\bar{H} = \int d\mathbf{r}\left\{f\left[\rho(\mathbf{r}),\nabla\rho(\mathbf{r})\right] - \rho(\mathbf{r})\frac{\partial f}{\partial\rho}\bigg|_{\rho=\rho(\mathbf{r})} + \rho(\mathbf{r})\nabla\cdot\frac{\partial f}{\partial\nabla\rho}\bigg|_{\rho=\rho(\mathbf{r})}\right\}$$

$$-\frac{1}{\beta}\exp(\beta\mu_{\mathrm{m}})\mathcal{A}_{\mathrm{m}}Z_{\mathrm{m,free}}VQ_{\mathrm{m}}[iw(\mathbf{r})] - \frac{1}{\beta}\sum_{i_{\mathrm{g}}=1}^{n_{\mathrm{g}}}\ln\left(\mathcal{A}_{\mathrm{g}}Z_{\mathrm{g,free}}Q_{\mathrm{g}}[\mathbf{r}_{\mathrm{g},i_{\mathrm{g}}};iw(\mathbf{r})]\right) \tag{B.23}$$

B.1.2 Thermodynamic Properties

According to the saddle point approximation considerations which were developed in the previous section, the grand potential of our interfacial polymer system, occupying volume V at temperature T and chain chemical potential $\mu_{\mathrm{m}}N_{\mathrm{m}}$ is given by eq B.24.

$$\Omega(\mu_{\mathrm{m}},n_{\mathrm{g}},V,T) = -\frac{1}{\beta}\ln\Xi = -\frac{1}{\beta}\ln\left[\exp(-\beta\bar{H})\right] = \bar{H} \tag{B.24}$$

Any multiplicative factor arising in Ξ upon introduction of the saddle point approximation contributes an additive constant to Ω, which will cancel upon referring Ω to an equal amount of polymer in the bulk. Ω is an extensive—system size-dependent—thermodynamic property. It is convenient to express the system thermodynamics with reference to a bulk phase of matrix chains occupying volume V at temperature T and chemical potential $\mu_{\mathrm{m}}N_{\mathrm{m}}$, a set of n_{g} isolated end-pinned unperturbed chains of length N_{g} at temperature T, and an isolated bare nanoparticle, as described below.

Appendix B. Derivation of Grafted/Matrix Polymer System Equations

The grand potential of an amount of bulk polymer occupying volume V at temperature T and chemical potential $N_m \mu_m$ is:

$$\Omega_{\text{bulk}}(\mu_m, V, T) = -\frac{1}{\beta} \ln \Xi_{\text{bulk}} = \bar{H}_{\text{bulk}} \qquad (B.25)$$

with $\bar{H}_{\text{bulk}}$ being the effective Hamiltonian of eq B.22 applied to bulk polymer:

$$\bar{H}_{\text{bulk}} = \int d\mathbf{r} \left\{ f[\rho, 0] - \rho \frac{\partial f}{\partial \rho} \right\} \bigg|_{\rho = \rho_{\text{seg,bulk}}} - \frac{1}{\beta} \exp(\beta \mu_m) \mathcal{A}_m Z_{m,\text{free}} V Q_m[iw_{\text{bulk}}] \qquad (B.26)$$

Note that, for all forms of the local free energy density f considered here, $\dfrac{\partial f}{\partial \nabla \rho} = \mathbf{0}$ in the bulk polymer phase.

Application of eq B.21 for the density to the bulk polymer gives

$$\rho_{\text{seg,bulk}} = \exp(\beta \mu_m) \mathcal{A}_m Z_{m,\text{free}} V \frac{Q_m[iw_{\text{bulk}}]}{n_{m,\text{bulk}}} \rho_{\text{seg,bulk}} \Leftrightarrow \exp(\beta \mu_m) \mathcal{A}_m Z_{m,\text{free}} V Q_m[iw_{\text{bulk}}] = \frac{\rho_{\text{seg,bulk}} V}{N_m} \quad (B.27)$$

Combining eqs B.26 and B.27,

$$\bar{H}_{\text{bulk}} = \int d\mathbf{r} \left\{ f[\rho, 0] - \rho \frac{\partial f}{\partial \rho} \right\} \bigg|_{\rho = \rho_{\text{seg,bulk}}} - \frac{\rho_{\text{seg,bulk}} V}{\beta N_m} \qquad (B.28)$$

In the bulk melt, the self-consistent field from eq B.22 becomes

$$w_{\text{bulk}} = -i \frac{\partial f}{\partial \rho} \bigg|_{\rho = \rho_{\text{seg,bulk}}} \qquad (B.29)$$

and thus the matrix chain partition function from eq B.11 takes the form

$$Q_m[iw_{\text{bulk}}] = \exp \left(-\beta N_m \frac{\partial f}{\partial \rho} \bigg|_{\rho = \rho_{\text{seg,bulk}}} \right) \qquad (B.30)$$

On the other hand, for a set of isolated end-pinned unperturbed chains of length N_g at temperature T, which are identical in length and chemical composition to our grafted chains, the total Helmholtz energy in the context of our model is given by eq B.31.

$$A_g^{isol}(T,n_g) = -\frac{1}{\beta}\sum_{i_g=1}^{n_g}\ln\left(\mathcal{A}_g Z_{g,free}Q_g\left[\mathbf{r}_{g,i_g};iw_{bulk}\right]\right) \tag{B.31}$$

Subtracting eqs B.28 and B.31 from eq B.23:

$$\Delta\Omega = \Omega(\mu,V,T) - \Omega_{bulk}(\mu,V,T) - A_g^{isol}(T,n_g)$$

$$= \int d\mathbf{r}\left\{ f\left[\rho(\mathbf{r}),\nabla\rho(\mathbf{r})\right] - \rho(\mathbf{r})\frac{\partial f}{\partial\rho}\bigg|_{\rho=\rho(\mathbf{r})} + \rho(\mathbf{r})\nabla\cdot\frac{\partial f}{\partial\nabla\rho}\bigg|_{\rho=\rho(\mathbf{r})} \right\}$$

$$- \int d\mathbf{r}\left\{ f\left[\rho,\mathbf{0}\right] - \rho\frac{\partial f}{\partial\rho} \right\}\bigg|_{\rho=\rho_{seg,bulk}} \tag{B.32}$$

$$+ \frac{\rho_{seg,bulk}V}{\beta N_m}\left(1 - Q_m\left[w'(\mathbf{r}) - w'_{bulk}\right]\right)$$

$$- \frac{1}{\beta}\sum_{i_g=1}^{n_g}\ln Q_g\left[\mathbf{r}_{g,i_g};w'(\mathbf{r}) - w'_{bulk}\right]$$

In eq B.32 we have made the substitution

$$iw(\mathbf{r}) = w'(\mathbf{r}),\ \text{a real field.} \tag{B.33}$$

The second integral in eq B.32, referring to a homogeneous bulk phase of matrix chains, can be performed immediately, yielding a factor of V times the integrand.

By expressing eq B.22 in terms of the real field from eq B.33, $\partial f/\partial\rho = w'(\mathbf{r}) + \nabla\cdot\partial f/\partial\nabla\rho - u_s(\mathbf{r})$, and by substituting it to eq B.32, the latter can be expressed as follows:

$$\Delta\Omega = \int d\mathbf{r}\left\{ f\left[\rho(\mathbf{r}),\nabla\rho(\mathbf{r})\right] - f\left[\rho_{seg,bulk},\mathbf{0}\right]\right\}$$

$$- \int d\mathbf{r}\left\{\rho(\mathbf{r})w'(\mathbf{r}) - \rho_{seg,bulk}w'_{bulk}\right\}$$

$$+ \int d\mathbf{r}\left\{\rho(\mathbf{r})u_s(\mathbf{r})\right\} \tag{B.34}$$

$$+ \frac{\rho_{seg,bulk}V}{\beta N_m}\left(1 - Q_m\left[w'(\mathbf{r}) - w'_{bulk}\right]\right)$$

$$- \frac{1}{\beta}\sum_{i_g=1}^{n_g}\ln Q_g\left[\mathbf{r}_{g,i_g};w'(\mathbf{r}) - w'_{bulk}\right]$$

wherein the *first term* is the contribution of the cohesive interactions, the *second term* is the interaction energy between the density field and the chemical potential field, the third term describes the polymer-solid interactions, the *fourth term* describes the translational and

conformational entropy (relative to the bulk melt) of the matrix chains, and the *fifth term* is associated with the conformational entropy of the n_g grafted chains subject to the field w'.

B.1.3 Derivation of the Segment Balance Equations

To deal with the grafted and the matrix chains in the presence of the field w', we introduce the propagator $G(\mathbf{r}_{start}, \mathbf{r}, s)$ following Edwards[182]:

$$G(\mathbf{r}_{start},\mathbf{r},s) = \frac{\int_{\mathbf{R}(0)=\mathbf{r}_{start}}^{\mathbf{R}(s)=\mathbf{r}} \mathcal{D}\big[\mathbf{R}(\cdot)\big]\mathcal{P}\big[\mathbf{R}(\cdot)\big]\exp\left\{-\beta\int_{0}^{s}ds'w'\big(\mathbf{R}(s')\big)\right\}}{\int d\mathbf{r}\int_{\mathbf{R}(0)=\mathbf{r}_{start}}^{\mathbf{R}(s)=\mathbf{r}} \mathcal{D}\big[\mathbf{R}(\cdot)\big]\mathcal{P}\big[\mathbf{R}(\cdot)\big]} \qquad (B.35)$$

$G(\mathbf{r}_{start},\mathbf{r},s)$ has dimensions of inverse volume. It is proportional to the conditional probability that a chain, which has started at $\mathbf{r}_{start}$ and is subject to the field $w'(\mathbf{r})$ on its segments, finds itself at position $\mathbf{r}$ at contour length s, as depicted in Figure B.1. The denominator in eq B.35 is a partition function for a field-free chain, represented as a Gaussian string, which has started at $\mathbf{r}_{start}$ and may end anywhere in the system. The denominator is independent of $\mathbf{r}_{start}$ and $\mathbf{r}$; it depends only on s.
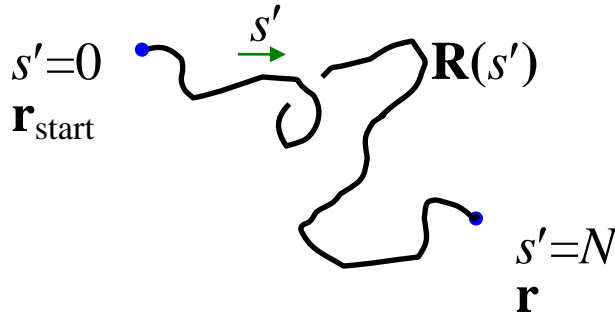
Figure B.1. Schematic representation of a Gaussian string starting at $s'=0$ and ending at $s'=N$.

We also define the restricted partition function of a matrix chain in the presence of the field $w'(\mathbf{r})$ by the following eq B.36.

$$q_m(\mathbf{r},s) = \int_V d\mathbf{r}_{start}G(\mathbf{r}_{start},\mathbf{r},s) \qquad (B.36)$$

This quantity is dimensionless and proportional to the probability that the segment at contour length N of a matrix chain subject to the field finds itself at position $\mathbf{r}$, regardless of where in the

system the particular matrix chain may have started. It is reduced by the corresponding probability of a field-free chain. Thus, it equals unity for a field-free chain. The partition function of a matrix chain, Q_m, is related to the corresponding restricted one by the equation:

$Q_m[w'(\mathbf{r})] = \frac{1}{V}\int_V d\mathbf{r}\; q_m(\mathbf{r},N_m)$. It is also dimensionless and normalized such that it would be

unity for a field-free chain in volume V.

The partition function, Q_g, of a chain which is grafted at $\mathbf{r}_g$, relative to a field-free chain of equal length, is given by eq B.37.

$$Q_g[\mathbf{r}_g; w'(\mathbf{r})] = \int_V d\mathbf{r}\; G(\mathbf{r}_g,\mathbf{r},N_g) \tag{B.37}$$

But, by definition, $G(\mathbf{r}_g,\mathbf{r},N_g) = G(\mathbf{r},\mathbf{r}_g,N_g)$, so:

$$Q_g[\mathbf{r}_g; w'(\mathbf{r})] = \int_V d\mathbf{r}\; G(\mathbf{r},\mathbf{r}_g,N_g) = q_m(\mathbf{r}_g,N_g) \tag{B.38}$$

Following eq B.35, the propagator of a grafted chain, whose grafted end lies at coordinates $\mathbf{r}_g$, can be written as:

$$
\begin{aligned}
G(\mathbf{r}_g,\mathbf{r},s) &= \frac{\int \mathcal{D}[\mathbf{R}'(\cdot)]\mathcal{P}[\mathbf{R}'(\cdot)]\delta(\mathbf{R}'(0)-\mathbf{r}_g)\delta(\mathbf{R}'(s)-\mathbf{r})\exp\left\{-\beta\int_0^s ds'w'(\mathbf{R}'(s'))\right\}}{\int \mathcal{D}[\mathbf{R}'(\cdot)]\mathcal{P}[\mathbf{R}'(\cdot)]\delta(\mathbf{R}'(0)-\mathbf{r}_g)} \\[2mm]
&= \frac{\int \mathcal{D}[\mathbf{R}'(\cdot)]\mathcal{P}[\mathbf{R}'(\cdot)]\delta(\mathbf{R}'(0)-\mathbf{r}_g)\delta(\mathbf{R}'(s)-\mathbf{r})\exp\left\{-\beta\int_0^s ds'w'(\mathbf{R}'(s'))\right\}}{\frac{1}{V}\int \mathcal{D}[\mathbf{R}'(\cdot)]\mathcal{P}[\mathbf{R}'(\cdot)]}
\end{aligned}
\tag{B.39}
$$

So far, we denote by $\mathbf{R}'(\cdot)$ the curve in three-dimensional space, which is followed by a Gaussian thread of length N. At this point, we introduce the symbol $\mathbf{R}''(\cdot)$, which represents the curve in three-dimensional space, which is followed by a Gaussian thread of length N_g-s. Using these definitions and combining eqs B.35 and B.36, the restricted partition function of a matrix chain can be written as follows.

$$q_m(\mathbf{r},N_g-s) = \frac{\int_V d\mathbf{r}_{start}\int \mathcal{D}[\mathbf{R}''(\cdot)]\mathcal{P}[\mathbf{R}''(\cdot)]\delta(\mathbf{R}''(0)-\mathbf{r}_{start})\delta(\mathbf{R}''(N_g-s)-\mathbf{r})\exp\left\{-\beta\int_0^{N_g-s} ds'w'(\mathbf{R}''(s'))\right\}}{\frac{1}{V}\int \mathcal{D}[\mathbf{R}''(\cdot)]\mathcal{P}[\mathbf{R}''(\cdot)]} \tag{B.40}$$

Next, we consider the product $G(\mathbf{r}_g, \mathbf{r}, s) \, q_m(\mathbf{r}, N_g - s)$. By eqs B.39 and B.40, the numerator of this product will be equal to the following expression.

$$numer = \int \mathcal{D}[\mathbf{R}'(\cdot)] \mathcal{P}[\mathbf{R}'(\cdot)] \delta(\mathbf{R}'(0) - \mathbf{r}_g) \delta(\mathbf{R}'(s) - \mathbf{r}) \exp\left\{-\beta \int_0^s ds' w'(\mathbf{R}'(s'))\right\}$$

$$\times \int_V d\mathbf{r}_{start} \int \mathcal{D}[\mathbf{R}''(\cdot)] \mathcal{P}[\mathbf{R}''(\cdot)] \delta(\mathbf{R}''(0) - \mathbf{r}_{start}) \delta(\mathbf{R}''(N_g - s) - \mathbf{r}) \exp\left\{-\beta \int_0^{N_g - s} ds' w'(\mathbf{R}''(s'))\right\} \quad \text{(B.41)}$$

Changing the integration variable from N' to $N_g - N'$ in the second line, eq B.41 is modified to:

$$numer = \int \mathcal{D}[\mathbf{R}'(\cdot)] \mathcal{P}[\mathbf{R}'(\cdot)] \delta(\mathbf{R}'(0) - \mathbf{r}_g) \delta(\mathbf{R}'(s) - \mathbf{r}) \exp\left\{-\beta \int_0^s ds' w'[\mathbf{R}'(s')]\right\}$$

$$\times \int_V d^3 r_{start} \int \mathcal{D}[\mathbf{R}''(\cdot)] \mathcal{P}[\mathbf{R}''(\cdot)] \delta(\mathbf{R}''(N_g) - \mathbf{r}_{start}) \delta(\mathbf{R}''(s) - \mathbf{r}) \exp\left\{-\beta \int_s^{N_g} ds' w'[\mathbf{R}''(s')]\right\} \quad \text{(B.42)}$$

$$= \frac{1}{V} \int \mathcal{D}[\mathbf{R}(\cdot)] \mathcal{P}[\mathbf{R}(\cdot)] \delta(\mathbf{R}(0) - \mathbf{r}_g) \delta(\mathbf{R}(s) - \mathbf{r}) \exp\left\{-\beta \int_0^{N_g} ds' w'[\mathbf{R}(s')]\right\}$$

where now the functional integration is performed over all paths $\mathbf{R}(\cdot)$ of an N_g segment-long (grafted) chain.

On the other hand, the denominator of the product $G(\mathbf{r}_g, \mathbf{r}, s) \, q_m(\mathbf{r}, N_g - s)$ becomes:

$$denom = \frac{1}{V^2} \int \mathcal{D}[\mathbf{R}'(\cdot)] \mathcal{P}[\mathbf{R}'(\cdot)] \int \mathcal{D}[\mathbf{R}''(\cdot)] \mathcal{P}[\mathbf{R}''(\cdot)] = \frac{1}{V^2} \int \mathcal{D}[\mathbf{R}(\cdot)] \mathcal{P}[\mathbf{R}(\cdot)] \quad \text{(B.43)}$$

Dividing eq B.42 with B.43, we obtain:

$$G(\mathbf{r}_g, \mathbf{r}, s) \, q_m(\mathbf{r}, N_g - s) =$$

$$\frac{\int \mathcal{D}[\mathbf{R}(\cdot)] \mathcal{P}[\mathbf{R}(\cdot)] \delta(\mathbf{R}(0) - \mathbf{r}_g) \delta(\mathbf{R}(s) - \mathbf{r}) \exp\left\{-\beta \int_0^{N_g} ds' w'[\mathbf{R}(s')]\right\}}{\frac{1}{V} \int \mathcal{D}[\mathbf{R}(\cdot)] \mathcal{P}[\mathbf{R}(\cdot)]} \quad \text{(B.44)}$$

Combining eqs B.37 and B.39, we can write the following B.45eq for the partition function of a grafted chain.

$$Q_g\left[\mathbf{r}_g;w'(\mathbf{r})\right] =$$

$$= \frac{\int_V d^3 r_{\text{end}} \int \mathcal{D}\left[\mathbf{R}(\cdot)\right]\mathcal{P}\left[\mathbf{R}(\cdot)\right]\delta\left(\mathbf{R}(0)-\mathbf{r}_g\right)\delta\left(\mathbf{R}(N_g)-\mathbf{r}_{\text{end}}\right)\exp\left\{-\beta\int_0^{N_g} dN' \, w'\left(\mathbf{R}(s')\right)\right\}}{\frac{1}{V}\int\mathcal{D}\left[\mathbf{R}(\cdot)\right]\mathcal{P}\left[\mathbf{R}(\cdot)\right]} \quad \text{(B.45)}$$

$$= \frac{\int \mathcal{D}\left[\mathbf{R}(\cdot)\right]\mathcal{P}\left[\mathbf{R}(\cdot)\right]\delta\left(\mathbf{R}(0)-\mathbf{r}_g\right)\exp\left\{-\beta\int_0^{N_g} ds' w'\left(\mathbf{R}(s')\right)\right\}}{\frac{1}{V}\int\mathcal{D}\left[\mathbf{R}(\cdot)\right]\mathcal{P}\left[\mathbf{R}(\cdot)\right]}$$

Dividing eq B.44 with B.45, we obtain the following expression:

$$\frac{1}{Q_g\left[\mathbf{r}_g;w'(\mathbf{r})\right]}\int_0^{N_g} ds \, G(\mathbf{r}_g,\mathbf{r},s)\, q_m(\mathbf{r},N_g-s)$$

$$= \frac{\int_0^{N_g} ds \int\mathcal{D}\left[\mathbf{R}(\cdot)\right]\mathcal{P}\left[\mathbf{R}(\cdot)\right]\delta\left(\mathbf{R}(0)-\mathbf{r}_g\right)\delta\left(\mathbf{R}(s)-\mathbf{r}\right)\exp\left\{-\beta\int_0^{N_g} ds'w'\left(\mathbf{R}(s')\right)\right\}}{\int\mathcal{D}\left[\mathbf{R}(\cdot)\right]\mathcal{P}\left[\mathbf{R}(\cdot)\right]\delta\left(\mathbf{R}(0)-\mathbf{r}_g\right)\exp\left\{-\beta\int_0^{N_g} ds'w'\left(\mathbf{R}(s')\right)\right\}}$$

$$= \frac{\int\mathcal{D}\left[\mathbf{R}(\cdot)\right]\mathcal{P}\left[\mathbf{R}(\cdot)\right]\delta\left(\mathbf{R}(0)-\mathbf{r}_g\right)\int_0^{N_g} dN'\delta\left(\mathbf{R}(N')-\mathbf{r}\right)\exp\left\{-\beta\int_0^{N_g} ds'w'\left(\mathbf{R}(s')\right)\right\}}{\int\mathcal{D}\left[\mathbf{R}(\cdot)\right]\mathcal{P}\left[\mathbf{R}(\cdot)\right]\delta\left(\mathbf{R}(0)-\mathbf{r}_g\right)\exp\left\{-\beta\int_0^{N_g} ds'w'\left(\mathbf{R}(s')\right)\right\}} \quad \text{(B.46)}$$

$$= \left\langle \int_0^{N_g} ds'\delta\left(\mathbf{R}(s')-\mathbf{r}\right)\right\rangle_{\substack{\mathbf{R}(0)=\mathbf{r}_g \\ \text{Field } w'}}$$

Using the definition eq B.5, we can write:

$$\frac{1}{Q_g\left[\mathbf{r}_g;w'(\mathbf{r})\right]}\int_0^{N_g} dN'G(\mathbf{r}_g,\mathbf{r},s')\, q_m(\mathbf{r},N_g-s') = \rho_{\text{seg,bulk}}\left\langle\hat{\varphi}_g(\mathbf{r})\right\rangle_{\substack{\mathbf{R}(0)=\mathbf{r}_g \\ \text{Field } w'}} = \rho_{\text{seg,bulk}}\varphi_g(\mathbf{r}) = \rho_g(\mathbf{r}) \quad \text{(B.47)}$$

where $\varphi_g(\mathbf{r})$ is the reduced density and $\rho_g(\mathbf{r})$ the segment density contributed by the considered grafted chain, at position $\mathbf{r}$.

Taking into account eq B.38, which relates the partition function of a grafted chain to the restricted partition function of a matrix chain, we rewrite eq B.47 for a specific grafted chain, i_g, as

Appendix B. Derivation of Grafted/Matrix Polymer System Equations

$$\varphi_{i_g}(\mathbf{r}) = \frac{1}{\rho_{seg,bulk} q_m\left(\mathbf{r}_{i_g}, N_g\right)} \int_0^{N_g} dN' G(\mathbf{r}_{i_g}, \mathbf{r}, s') \, q_m(\mathbf{r}, N_g - s') \tag{B.48}$$

The total reduced density due to all grafted chains will be:

$$
\begin{aligned}
\varphi_g(\mathbf{r}) = \sum_{i_g=1}^{n_g} \varphi_{i_g}(\mathbf{r}) &= \frac{1}{\rho_{seg,bulk}} \sum_{i_g=1}^{n_g} \frac{1}{q_m\left(\mathbf{r}_{i_g}, N_g\right)} \int_0^{N_g} dN' \, G(\mathbf{r}_{i_g}, \mathbf{r}, s') \, q_m(\mathbf{r}, N_g - s') = \\
&= \int_0^{N_g} ds' \left\{ \sum_{i_g=1}^{n_g} \frac{1}{\rho_{seg,bulk} q_m\left(\mathbf{r}_{i_g}, N_g\right)} G(\mathbf{r}_{i_g}, \mathbf{r}, s') \right\} q_m(\mathbf{r}, N_g - s')
\end{aligned}
\tag{B.49}
$$

Let us set

$$q_g(\mathbf{r}, s) = \sum_{i_g=1}^{n_g} \frac{N_g}{\rho_{seg,bulk} q_m\left(\mathbf{r}_{i_g}, N_g\right)} G(\mathbf{r}_{i_g}, \mathbf{r}, s) \tag{B.50}$$

With this definition,

$$\varphi_g(\mathbf{r}) = \frac{1}{N_g} \int_0^{N_g} ds \, q_g(\mathbf{r}, s) \, q_m(\mathbf{r}, N_g - s) \tag{B.51}$$

B.2   Hamaker Potential

In this work, the solid-polymer interactions are described via the Hamaker potential.[272] The essence of Hamaker theory is to treat the interacting bodies as collections of homogeneously distributed infinitesimal domains interacting via a nonbonded interaction potential (usually Lennard-Jones, 12-6). Then an integration along the volumes of the bodies takes place to account for interactions amongst all possible pairs of domains, resulting in the total potential energy. The Hamaker constant of the effective solid-polymer interaction can be estimated by the following geometric mean $A_{PS\text{-}SiO_2} = \sqrt{A_{PS} A_{SiO_2}}$. Vogiatzis and Theodorou[255] employed an effective solid-polymer interaction, $A_{PS\text{-}SiO_2}^{eff} = \sqrt{A_{PS} A_{SiO_2}} - A_{PS}$ instead of $A_{PS\text{-}SiO_2}$, in order to restore the proper effective cohesive interactions at the polymer/solid interface. In this study we opted to work with $A_{PS\text{-}SiO_2}$, since the energy of cohesion of the polymer is taken into account as

part of $f[\rho(\mathbf{r}), \nabla\rho(\mathbf{r})]$. Furthermore, the effective collision diameter can be calculated as $\sigma_{\text{eff}} = (\sigma_{\text{PS}} + \sigma_{\text{SiO}_2})/2$ with σ_{PS} and σ_{SiO_2} being the effective diameters of solid and polymeric segment interaction sites, respectively. In each of the following cases of interacting geometries a wall distance was used, so that the maximum value of the repulsive term felt by the polymer segments does not exceed 5 $k_{\text{B}}T$ (e.g., see Figure B.2).
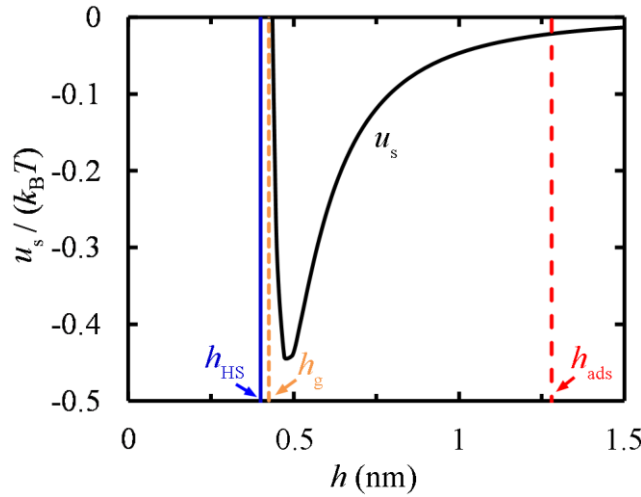
Figure B.2. Interaction energy $u_s(h)$ between a PS monomer unit and a planar SiO$_2$ substrate as calculated from the Hamaker potential at $T = 500$ K. The blue line, $h_{\text{HS}} = 0.4$ nm, intersects the u_s (h) curve at $u_s = 5$ $k_{\text{B}}T$ and depicts the distance of the hard-sphere wall from the surface employed in the calculations. The orange dashed line depicts the distance of the grafting points from the surface (h_{g}), and the red dashed line delimits the critical distance (h_{ads}), below which a matrix chain is considered adsorbed.

B.2.1 Sphere-Sphere

For the purpose of calculating the potential energy of dispersive interactions between the polystyrene, either matrix or grafted, and a nanoparticle immersed in it, we consider the atactic polystyrene monomers as small spheres with an effective radius $a_1 = \sqrt[3]{\dfrac{3}{4\pi\rho_{\text{seg}}}}$, interacting with the spherical silica nanoparticle of radius $a_2 = R_{\text{NP}}$. The solid-polymer interaction potential per monomer, u_{s}, can be split into an attractive[272] and a repulsive term.[137] The two terms, u_{A} and u_{R}

respectively, are functions of the center-to-center distance, r_{12}, between two interacting spherical bodies:

$$u_A = -\frac{A_{12}}{6}\left[\frac{2a_1a_2}{r_{12}{}^2-(a_1+a_2)^2}+\frac{2a_1a_2}{r_{12}{}^2-(a_1-a_2)^2}+\ln\left(\frac{r_{12}{}^2-(a_1+a_2)^2}{r_{12}{}^2-(a_1-a_2)^2}\right)\right] \tag{B.52a}$$

$$u_R = \frac{A_{12}}{37800}\frac{\sigma_{\text{eff}}^6}{r_{12}}\left[\begin{array}{c}\dfrac{r_{12}{}^2-7r_{12}(a_1+a_2)+6(a_1^2+7a_1a_2+a_2^2)}{(r_{12}-a_1-a_2)^7}\\[4mm]+\dfrac{r_{12}{}^2+7r_{12}(a_1+a_2)+6(a_1^2+7a_1a_2+a_2^2)}{(r_{12}+a_1+a_2)^7}\\[4mm]-\dfrac{r_{12}{}^2+7r_{12}(a_1-a_2)+6(a_1^2-7a_1a_2+a_2^2)}{(r_{12}+a_1-a_2)^7}\\[4mm]-\dfrac{r_{12}{}^2-7r_{12}(a_1-a_2)+6(a_1^2-7a_1a_2+a_2^2)}{(r_{12}-a_1+a_2)^7}\end{array}\right] \tag{B.52b}$$

where $A_{12} = A_{\text{PS-SiO}_2}$ is the Hamaker constant and σ_{eff} is the effective collision diameter.

B.2.2 Sphere-Flat Surface

The attractive and the repulsive components from the interaction of a sphere with a semi-infinite solid terminating at a flat surface can be obtained in the context of Hamaker theory as follows:

$$u_A = -\frac{A_{12}}{6}\left(\frac{1}{r'}+\frac{1}{2+r'}+\ln\left(\frac{r'}{2+r'}\right)\right) \tag{B.53a}$$

$$u_R = \frac{A_{12}}{7560}\frac{\sigma_{\text{eff}}^6}{a_1^6}\left(\frac{8+r'}{(2+r')^7}+\frac{6-r'}{r'^7}\right) \tag{B.53b}$$

with $r' = d_{12}/a_1$ and d_{12} being the distance between the surface of the sphere and the solid surface. We have $u_s = u_A + u_R$ for this case which is shown in Figure **B.2** as a function of $h = d_{12} + a_1$.

B.3   Predictions From a Simple Model with Homogeneous Density

It is instructive to compare the predictions of SCFT with the predictions of a simpler brush model such as that of incompressible Alexander brushes.[265,266] Let h_{edge} be the edge of a brush comprising n_g grafted chains of length N_g, emanating from a nanoparticle with radius, R_{NP}, such

as the one shown in Figure B.3(a). For simplicity, let us assume that the segment density is constant and equal to $\rho_{\text{seg,bulk}}$ across the region occupied by the brush of grafted chains, $\left[R_{\text{NP}}, R_{\text{NP}} + h_{\text{edge}} \right]$ which are terminated at h_{edge}; Figure B.3(c) presents the corresponding density profile for this model. Consequently, the volume occupied by the brush can be calculated as the number of the brush segments in this region divided by its segment density.

$$V = \frac{n_g N_g}{\rho_{\text{seg,bulk}}} = \frac{\sigma_g 4\pi R_{\text{NP}}^2 N_g}{\rho_{\text{seg,bulk}}} \tag{B.54}$$

(a)

(b)

(c)
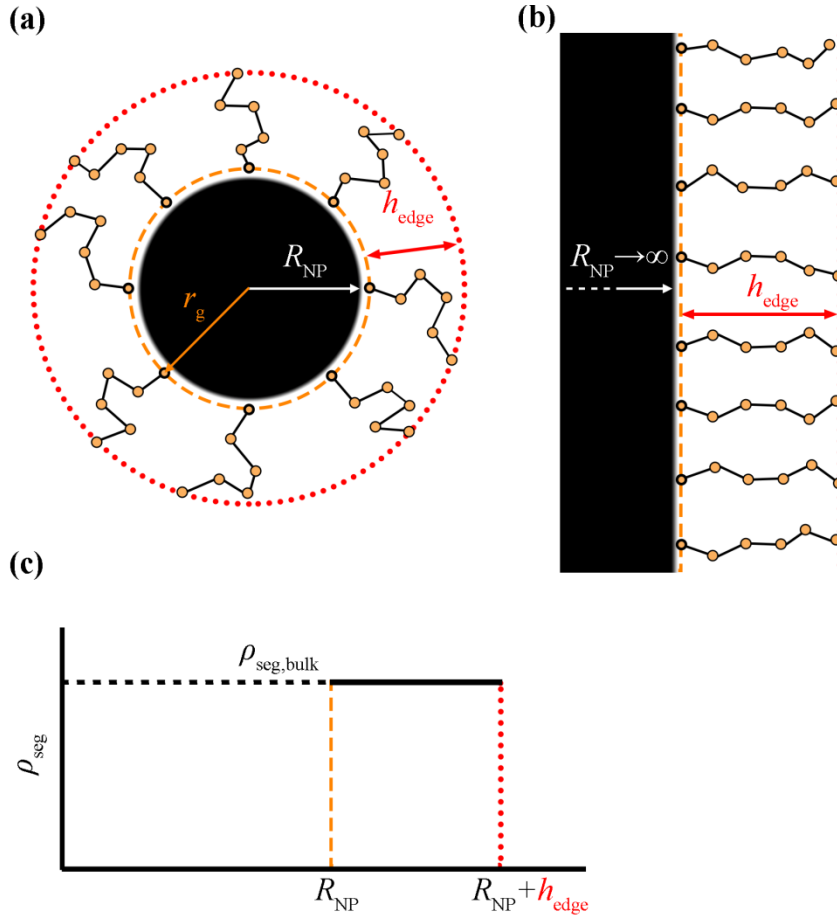
Figure B.3. (a) A nanoparticle with grafted chains that form a brush which ends at h_{edge}. **(b)** In the limit $R_{\text{NP}} \to \infty$, the surface of the nanoparticle becomes flat. **(c)** The segment density profile of a brush with constant segmental density, $\rho_{\text{seg,bulk}}$.

where $\sigma_g = N_g / \left(4\pi R_{\text{NP}}^2 \right)$ is the grafting density. Alternatively, the volume of a brush of constant density that terminates at h_{edge} can be calculated as follows:

Appendix B. Derivation of Grafted/Matrix Polymer System Equations

$$V = \frac{4}{3}\pi\left[\left(R_{\mathrm{NP}} + h_{\mathrm{edge}}\right)^3 - R_{\mathrm{NP}}^{\;3}\right]$$

(B.55)

By combining eqs B.54 and B.55, and solving for h_{edge}, we get for h_{edge}:

$$h_{\mathrm{edge}} = \left(\frac{3\sigma_{\mathrm{g}}N_{\mathrm{g}}}{\rho_{\mathrm{seg,bulk}}}R_{\mathrm{NP}}^{\;2} + R_{\mathrm{NP}}^{\;3}\right)^{\frac{1}{3}} - R_{\mathrm{NP}}$$

(B.56)

With h_{edge} known and given that the density profiles are uniform, $h_{\mathrm{g,99\%}}$, can be calculated as follows:

$$h_{\mathrm{g,99\%}} = 0.99 \cdot h_{\mathrm{edge}} + R_{\mathrm{NP}}$$

(B.57)

Similarly, $\left\langle h_{\mathrm{g}}^{\;2}\right\rangle^{1/2}$ can be obtained by eq B.58.

$$\left\langle h_{\mathrm{g}}^{\;2}\right\rangle^{1/2} = \left(\frac{\int_0^{h_{\mathrm{edge}}} h^2\rho(h)\mathrm{d}h}{\int_0^{h_{\mathrm{edge}}} \rho(h)\mathrm{d}h}\right)^{1/2} = \left(\frac{1}{h_{\mathrm{edge}}}\int_0^{h_{\mathrm{edge}}} h^2\mathrm{d}h\right)^{1/2} = \frac{1}{\sqrt{3}}h_{\mathrm{edge}}$$

$$= \frac{1}{\sqrt{3}}\left(\frac{3\sigma_{\mathrm{g}}N_{\mathrm{g}}}{\rho_{\mathrm{seg,bulk}}}R_{\mathrm{NP}}^{\;2} + R_{\mathrm{NP}}^{\;3}\right)^{\frac{1}{3}} - \frac{1}{\sqrt{3}}R_{\mathrm{NP}}$$

(B.58)

In the limit of very large nanoparticles (flat surfaces), $\left\langle h_{\mathrm{g}}^{\;2}\right\rangle^{1/2}$ becomes,

$$\lim_{R_{\mathrm{NP}}\to\infty}\left\langle h_{\mathrm{g}}^{\;2}\right\rangle^{1/2} = \frac{\sigma_{\mathrm{g}}N_{\mathrm{g}}}{\sqrt{3}\rho_{\mathrm{seg,bulk}}} = \frac{1}{\sqrt{3}}\lim_{R_{\mathrm{NP}}\to\infty}h_{\mathrm{edge}}$$

(B.59)

Thus, for this model $\left\langle h_{\mathrm{g}}^{\;2}\right\rangle^{1/2}$ appears to be proportional to σ_{g} and N_{g} in the limit of large nanoparticles/flat surfaces (i.e., see Figure B.3(b)). The thermodynamics of these brushes can be described by a total free energy which has as follows:

$$A_{\mathrm{total}} = A_{\mathrm{coh}} + A_{\mathrm{stretch}}$$

(B.60)

where A_{coh} is the contribution from the cohesive interactions described by the free energy density (i.e., $A_{\mathrm{coh}} \equiv \Omega_{\mathrm{coh}}$ from eq 9 in the main text), and A_{stretch} is the entropic contribution from the stretched grafted chains. Given that the grafted chains are terminated at the edge of the

brush, and assuming they can be described by Gaussian strings, the contribution of the brushes to the free energy due to stretching could be approximated as follows:

$$A_{\text{stretch}} = S_{\text{solid}} \sigma_{\text{g}} \frac{3 k_{\text{B}} T}{2 \langle R_{\text{end,g}}^{2} \rangle} h_{\text{edge}}^{2} \tag{B.61}$$

with $\langle R_{\text{end,g}}^{2} \rangle = N_{\text{g}} C_{\infty} l_{\text{c-c}}^{2}$ being the end-to-end distance of the grafted chain. Combining eqs B.61 and B.56, the stretching free energy per unit area as a function of R_{NP} is the following:

$$\frac{A_{\text{stretch}}}{S_{\text{solid}}} = \sigma_{\text{g}} \frac{3 k_{\text{B}} T}{2 \langle R_{\text{end,g}}^{2} \rangle} \left(\left[\frac{3 \sigma_{\text{g}} N_{\text{g}}}{\rho_{\text{seg,bulk}}} R_{\text{NP}}^{2} + R_{\text{NP}}^{3} \right]^{\frac{1}{3}} - R_{\text{NP}} \right)^{2} \tag{B.62}$$

C   Finite Element Shape Functions –Matrix Representation

C.1   Coordinate Transformations by Using 'Shape Functions'

The concept of using element shape functions for establishing curvilinear coordinates in the context of finite element analysis appears to have been first introduced by Taig.[329] In his first application, basic linear quadrilateral relations were used. Irons[330] generalized the idea for other elements. We search a relationship between a set of global Cartesian coordinates with a set of local coordinates. Once such coordinate relationships are known, shape functions can be specified in local coordinates and by suitable transformations the element properties established in the global coordinate system.

A convenient method of establishing the coordinate transformations is to use the 'standard' type of C_0 shape functions to represent the variation of the unknown function. Figure 5.1 depicts a general, four-node tetrahedral element to which we attach an element coordinate system that is, for now, assumed to be the same as the global system. We express the location of the four corner nodes with respect to the global Cartesian coordinates system (x, y, z) are $r_i = (x_i, y_i, z_i)$ with $i = 1, 2, 3, 4$

$$
\begin{aligned}
x &= N_1 x_1 + N_2 x_2 + N_3 x_3 + N_4 x_4 \\
y &= N_1 y_1 + \lambda_2 y_2 + N_3 y_3 + N_4 y_4 \\
z &= N_1 z_1 + N_2 z_2 + N_3 z_3 + N_4 z_4 \\
1 &= N_1 + N_2 + N_3 + N_4
\end{aligned}
\tag{C.1}
$$

in which N_i are standard shape functions given in terms of the local coordinates, then a relationship of the required form is immediately available.

$$
\begin{bmatrix} 1 \\ x \\ y \\ z \end{bmatrix} =
\begin{bmatrix}
1 & 1 & 1 & 1 \\
x_1 & x_2 & x_3 & x_4 \\
y_1 & y_2 & y_3 & y_4 \\
z_1 & z_2 & z_3 & z_4
\end{bmatrix}
\begin{bmatrix} N_1 \\ N_2 \\ N_3 \\ N_4 \end{bmatrix}
\tag{C.2}
$$

Here x_i y_i and z_i, refer to the coordinates of the 4 vertices of the tetrahedron. To solve for the polynomial coefficients, the matrix of coefficients in Equation C.2 must be inverted. Inversion of the matrix is algebraically tedious but straightforward, and we find

$$\begin{bmatrix} N_1 \\ N_2 \\ N_3 \\ N_4 \end{bmatrix} = \frac{1}{6V} \begin{bmatrix} 6v_1 & a_1 & b_1 & c_1 \\ 6v_2 & a_2 & b_2 & c_2 \\ 6v_3 & a_3 & b_3 & c_3 \\ 6v_4 & a_4 & b_4 & c_4 \end{bmatrix} \begin{bmatrix} 1 \\ x \\ y \\ z \end{bmatrix} \tag{C.3}$$

where the coefficients of this matrix can be calculated by forming the adjoints of the matrix eq C.2. The values of a_i, b_i and c_i, obtained by explicit inversion are

$$\begin{aligned}
a_1 &= y_2 z_{43} - y_3 z_{42} + y_4 z_{32} & b_1 &= -x_2 z_{43} + x_3 z_{42} - x_4 z_{32} & c_1 &= x_2 y_{43} - x_3 y_{42} + x_4 y_{32} \\
a_2 &= -y_1 z_{43} + y_3 z_{41} - y_4 z_{31} & b_2 &= x_1 z_{43} - x_3 z_{41} + x_4 z_{31} & c_2 &= -x_1 y_{43} + x_3 y_{41} - x_4 y_{31} \\
a_3 &= y_1 z_{43} - y_2 z_{42} + y_4 z_{21} & b_3 &= -x_1 z_{42} + x_2 z_{41} - x_4 z_{21} & c_3 &= x_1 y_{42} - x_2 y_{41} + x_4 y_{21} \\
a_4 &= -y_1 z_{43} + y_2 z_{31} + y_3 z_{21} & b_4 &= x_1 z_{32} - x_2 z_{31} + x_4 z_{21} & c_4 &= -x_1 y_{32} + x_2 y_{31} - x_4 y_{21}
\end{aligned} \tag{C.4}$$

in which the abbreviations $x_{ij} = x_i - x_j$, $y_{ij} = y_i - y_j$ and $z_{ij} = z_i - z_j$ are used. The volume V is given explicitly represents the volume of the tetrahedron by

$$V = \frac{1}{6} \begin{vmatrix} 1 & 1 & 1 & 1 \\ x_1 & x_2 & x_3 & x_4 \\ y_1 & y_2 & y_3 & y_4 \\ z_1 & z_2 & z_3 & z_4 \end{vmatrix} \tag{C.5}$$

Which results in

$$6V = x_{21}\left(y_{31}z_{41} - y_{41}z_{31}\right) + y_{21}\left(x_{41}z_{31} - x_{41}z_{31}\right) + z_{21}\left(x_{31}y_{41} - x_{41}y_{31}\right) \tag{C.6}$$

C.2   Construction of Shape Functions

Considerable simplification of the interpolation functions as well as the subsequently required integration is obtained via the use of volume coordinates. We can introduce the concept of volume coordinates using Figure 5.1 showing a four-node tetrahedral element divided into four volumes defined by the nodes and an arbitrary interior point $P(x_P, y_P, z_P)$. As indicated by the dotted lines, point P and the four nodes define four other tetrahedra having volumes

$$V_1 = V_{P234}, \quad V_2 = V_{P134}, \quad V_3 = V_{P124}, \quad V_4 = V_{P123} \tag{C.7}$$

The volume or "tetrahedral" coordinates L_1, L_2, L_3, L_4 are defined as

$$L_a = V_a / V, \quad a = 1, 2, 3, 4 \tag{C.8}$$

where V is the total volume of the element given by eq C.5. V_1 is given by replacing the coordinates of the P, x_P, y_P, z_P with x, y, z in eq C.5

$$V_1 = \frac{1}{6} \begin{vmatrix} 1 & 1 & 1 & 1 \\ x_P & x_2 & x_3 & x_4 \\ y_P & y_2 & y_3 & y_4 \\ z_P & z_2 & z_3 & z_4 \end{vmatrix} \tag{C.9}$$

by same procedure we can calculate V_2, V_3, V_4 respectively. The value of L_1 is one at corner 1, zero at the other 3 corners (i.e. on the opposite face) and varies linearly as one traverses the distance from the corner to the face. As the volume coordinates vary linearly with the Cartesian ones from unity at one node to zero at the opposite face, then shape functions for first order tetrahedral (linear) elements are simply

$$N_a = L_a, \quad a = 1, 2, 3, 4 \tag{C.10}$$

For constructing the second order quadratic shape functions we have 10 monomial terms. We can determine shape functions by placing nodes at the four vertices and at the midpoints of the six edges. The quadratic shape function N_1 associated with vertex node 1 of a tetrahedron (Figure 4.4b) is required to vanish at all nodes but node 1. The plane $L_1 = 0$ passes through face A234 and, hence, Nodes 2, 3, 4, 6, 9, 10. Likewise, the plane $L_1 = 1/2$ passes through Nodes 5, 7 and 8. Thus, N_1 must have the form

$$N_1 = \sigma L_1 (L_1 - 1/2) \tag{C.11}$$

Since $N_a = 1$ at Node 1 $L_a = 0$, we find $\sigma = 2$ and thus

$$N_1 = 2L_1 (L_1 - 1) \tag{C.12}$$

Similarly, the shape function N_5 associated with edge Node 5 is required to vanish on the planes $L_a = 0$ (Nodes 2, 3, 4, 6, 9, 10) and $L_a = 0$ (Nodes 1, 3, 4, 7, 8; 10) and have unit value at Node 5 ($L_1 = L_2 = 1/2$). Thus, it must be

$$N_5 = 4L_2 L_1 \tag{C.13}$$

According to the above discussion, the shape functions become

- For vertex nodes

$$N_1 = L_1(2L_1 - 1), \ N_2 = L_2(2L_2 - 1), \ N_3 = L_3(2L_3 - 1), \ N_4 = L_4(2L_4 - 1) \qquad \text{(C.14)}$$

- For mid-edge nodes

$$N_5 = 4L_2L_1, \ N_6 = 4L_3L_1, \ N_7 = 4L_4L_1,$$
$$N_8 = 4L_2L_3, \ N_9 = 4L_3L_4, \ N_{10} = 4L_4L_2 \qquad \text{(C.15)}$$

C.3   Unity Tetrahedron

Figure A.3 shows the transformation of a curved tetrahedron in global coordinates to a unity tetrahedron in an isoparametric system. We can consider a set of local coordinates, (ξ, η, ζ) corresponding set of global coordinates (x, y, z). Although it is feasible to obtain a relation between the global coordinates and local coordinates, this is of no interest in what follows. We are primarily concerned with their derivatives relations and their shape functions. If we assume the shape functions N_i in terms of ξ, η, ζ , then. by the chain rule of partial differentiation, we can write, for instance, the ξ derivative as

$$\frac{\partial N_i}{\partial \xi} = \frac{\partial N_i}{\partial x}\frac{\partial x}{\partial \xi} + \frac{\partial N_i}{\partial y}\frac{\partial y}{\partial \xi} + \frac{\partial N_i}{\partial z}\frac{\partial z}{\partial \xi} \qquad \text{(C.16)}$$
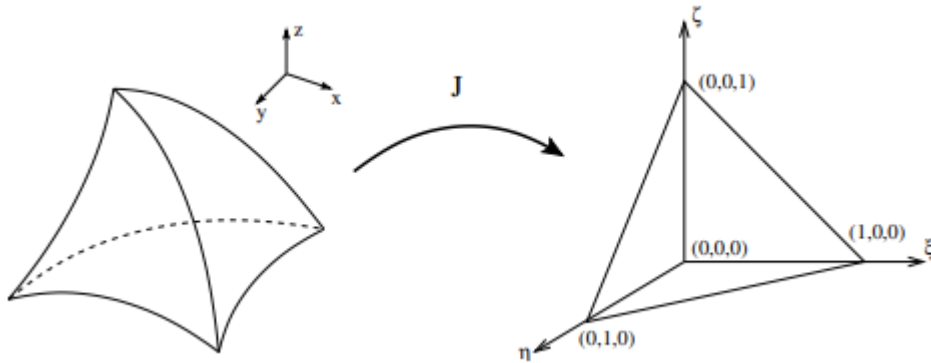

Figure C.1. Mapping of curved element into a standard element in ξ, η and ζ

Performing the same differentiation with respect to the other two coordinates and writing in matrix form we have

$$
\begin{bmatrix} \dfrac{\partial N_i}{\partial \eta} \\[2mm] \dfrac{\partial N_i}{\partial \xi} \\[2mm] \dfrac{\partial N_i}{\partial \zeta} \end{bmatrix} = \begin{bmatrix} \dfrac{\partial x}{\partial \xi} & \dfrac{\partial y}{\partial \xi} & \dfrac{\partial z}{\partial \xi} \\[2mm] \dfrac{\partial x}{\partial \eta} & \dfrac{\partial y}{\partial \eta} & \dfrac{\partial z}{\partial \eta} \\[2mm] \dfrac{\partial x}{\partial \zeta} & \dfrac{\partial y}{\partial \zeta} & \dfrac{\partial z}{\partial \zeta} \end{bmatrix} \begin{bmatrix} \dfrac{\partial N_i}{\partial x} \\[2mm] \dfrac{\partial N_i}{\partial z} \\[2mm] \dfrac{\partial N_i}{\partial z} \end{bmatrix} = \mathbf{J} \begin{bmatrix} \dfrac{\partial N_i}{\partial x} \\[2mm] \dfrac{\partial N_i}{\partial z} \\[2mm] \dfrac{\partial N_i}{\partial z} \end{bmatrix} \tag{C.17}
$$

In the above, the left-hand side can be evaluated as the functions N_i are specified in local| coordinates. Further, as x, y, z are explicitly given by the relation defining the curvilinear coordinates, the matrix $\mathbf{J}$ can be found explicitly in terms of the local coordinates. This matrix is known as the Jacobian matrix.

To transform the variables and the region with respect to which the integration is made, a standard process will be used which involves the determinant of $\mathbf{J}$. Thus, for instance, a volume element becomes

$$
dxdydz = \det \mathbf{J} d\xi d\eta d\zeta \tag{C.18}
$$

C.4   Relation Between (ξ, η, ζ) and (L_1, L_2, L_3, L_4) Coordinates

The general relationship C.1 for coordinate mapping and indeed all the following theorems are equally valid for any set of local coordinates and could relate the local L_1, L_2, L_3, L_4 coordinates used for tetrahedra in section C.2, to the global Cartesian ones. Indeed most of the discussion of the previous chapter is valid if we simply rename the local coordinates suitably. However, two important differences arise.

The first concerns the fact that the local coordinates are not independent, and in fact are by one more than those used in the Cartesian system. The matrix $\mathbf{J}$ would apparently therefore become rectangular and would not possess an inverse. The second is simply the difference of integration limits which have to correspond to a tetrahedral 'parent'.

The simplest, though perhaps not the most elegant, way out of the first difficulty is to consider the last variable as a dependent one. Thus, for example, we can introduce formally, in the case of the tetrahedra.

$$\begin{aligned} \xi &= L_1 \\ \eta &= L_2 \\ \zeta &= L_3 \\ 1 - \xi - \zeta - \eta &= L_4 \end{aligned} \tag{C.19}$$

As the functions N_i are given in fact in terms of L_1, L_2, L_3, L_4, we must observe that where derivatives $\dfrac{\partial N_i}{\partial \xi_k}$ can be elaborated using

$$\frac{\partial N_i}{\partial \xi_k} = \frac{\partial N_i}{\partial L_1}\frac{\partial L_1}{\partial \xi_k} + \frac{\partial N_i}{\partial L_1}\frac{\partial L_1}{\partial \xi_k} + \frac{\partial N_i}{\partial L_1}\frac{\partial L_1}{\partial \xi_k} + \frac{\partial N_i}{\partial L_4}\frac{\partial L_4}{\partial \xi_k} \tag{C.20}$$

On using Eq C.19 this becomes simply

$$\begin{aligned} \frac{\partial N_i}{\partial \xi} &= \frac{\partial N_i}{\partial L_1}\frac{\partial L_1}{\partial \xi} - \frac{\partial N_i}{\partial L_4}\frac{\partial L_4}{\partial \xi} \\[2mm] \frac{\partial N_i}{\partial \eta} &= \frac{\partial N_i}{\partial L_2}\frac{\partial L_2}{\partial \eta} - \frac{\partial N_i}{\partial L_4}\frac{\partial L_4}{\partial \eta} \\[2mm] \frac{\partial N_i}{\partial \zeta} &= \frac{\partial N_i}{\partial L_3}\frac{\partial L_3}{\partial \zeta} - \frac{\partial N_i}{\partial L_4}\frac{\partial L_4}{\partial \zeta} \end{aligned} \tag{C.21}$$

Derivatives $\dfrac{\partial r_i}{\partial \xi_k}$ which can be encountered in the Jacobian matrix can be found by starting the equation given for global coordinates $r_p = \begin{bmatrix} x^p & y^p & z^p \end{bmatrix}$ of any arbitrary point p which can be expressed as

$$\mathbf{r}_p = \sum_{i=1}^{Nnod} N_i{}^p \mathbf{r}_i \tag{C.22}$$

By using the eq C.22

$$\mathbf{J} = \begin{vmatrix} \dfrac{\partial x}{\partial \xi} & \dfrac{\partial y}{\partial \xi} & \dfrac{\partial z}{\partial \xi} \\[3mm] \dfrac{\partial x}{\partial \eta} & \dfrac{\partial y}{\partial \eta} & \dfrac{\partial z}{\partial \eta} \\[3mm] \dfrac{\partial x}{\partial \zeta} & \dfrac{\partial y}{\partial \zeta} & \dfrac{\partial z}{\partial \zeta} \end{vmatrix} = \begin{bmatrix} \displaystyle\sum_{i=1}^{Nnod} \dfrac{\partial N_i}{\partial \xi} x_i & \displaystyle\sum_{i=1}^{Nnod} \dfrac{\partial N_i}{\partial \xi} y_i & \displaystyle\sum_{i=1}^{Nnod} \dfrac{\partial N_i}{\partial \xi} z_i \\[4mm] \displaystyle\sum_{i=1}^{Nnod} \dfrac{\partial N_i}{\partial \eta} x_i & \displaystyle\sum_{i=1}^{Nnod} \dfrac{\partial N_i}{\partial \eta} y_i & \displaystyle\sum_{i=1}^{Nnod} \dfrac{\partial N_i}{\partial \eta} z_i \\[4mm] \displaystyle\sum_{i=1}^{Nnod} \dfrac{\partial N_i}{\partial \zeta} x_i & \displaystyle\sum_{i=1}^{Nnod} \dfrac{\partial N_i}{\partial \zeta} y_i & \displaystyle\sum_{i=1}^{Nnod} \dfrac{\partial N_i}{\partial \zeta} z_i \end{bmatrix} \tag{C.23}$$

Apart from the Jacobian, the derivatives $\dfrac{\partial N_i}{\partial \mathbf{r}}$ appearing in the integration points are needed to construct the FEM matrices. These derivatives can be expressed in terms of coordinates (ξ, η, ζ) as:

$$\frac{\partial N_i}{\partial r_j} = \frac{\partial N_i}{\partial \eta}\frac{\partial \eta}{\partial r_j} + \frac{\partial N_i}{\partial \xi}\frac{\partial \xi}{\partial r_j} + \frac{\partial N_i}{\partial \zeta}\frac{\partial \zeta}{\partial r_j} \quad \text{with } j=1,2,3 \tag{C.24}$$

To find the global derivatives we can use eq C.17 invert **J** and write

$$\begin{bmatrix} \dfrac{\partial N_i}{\partial x} \\[2mm] \dfrac{\partial N_i}{\partial z} \\[2mm] \dfrac{\partial N_i}{\partial z} \end{bmatrix} = \mathbf{J}^{-1} \begin{bmatrix} \dfrac{\partial N_i}{\partial \eta} \\[2mm] \dfrac{\partial N_i}{\partial \xi} \\[2mm] \dfrac{\partial N_i}{\partial \zeta} \end{bmatrix} \tag{C.25}$$

The $\mathbf{J^{-1}}$ can be calculated from eq C.23 by inverting the jacobian matrix.

C.5 Matrix Representation

By using the shape functions as weight functions (Galerkin method), eq 5.42 becomes:

$$\left[\begin{aligned} &\sum_{e=1}^{N_{el}} \int_{\Omega_e} \sum_{I=1}^{N_{nod,e}} N_I(\xi^e) \sum_{J=1}^{N_{nod,e}} N_J(\xi^e)\dot{q}^J(s)\mathrm{d}\Omega + \sum_{e=1}^{N_{el}} \int_{\Omega_e} \left(\sum_{I=1}^{N_{nod,e}} N_I(\xi^e) \right)\left(\sum_{J=1}^{N_{nod,e}} N_J(\xi^e)\omega^J q^J(s) \right)\mathrm{d}\Omega \\ &+\sum_{e=1}^{N_{el}} \int_{\Omega_e} \sum_{i} \left(\sum_{I=1}^{N_{nod,e}} \frac{\partial N_I(\xi^e)^I}{\partial r_i} \right)\left(\sum_{J=1}^{N_{nod,e}} \frac{\partial N_J(\xi^e)}{\partial r_i} q^J(s) \right)\mathrm{d}\Omega \\ &-\sum_{e=1}^{N_{el}} \int_{\Gamma_e} \sum_{i} \left(\sum_{I=1}^{N_{nod,e}} N_I(\xi^e) \right)\left(\sum_{J=1}^{N_{nod,e}} \frac{\partial N_J(\xi^e)}{\partial r_i} q^J(s) \right)\mathrm{d}\Omega \end{aligned} \right] = 0 \tag{C.26}$$

where ω^J is the value of the external function at the nodal point J. In order for the above integral to be well defined, the fourth term of the above equation referred to surface integrals between adjacent elements must vanish. This occurs under the condition that shape functions are continuous and the first derivatives may be discontinuous in Ω.

We can express the integral form of the eq C.26 in terms of local shape functions by using the eq 5.52, 5.53, and 5.54. By these definitions the first term in eq C.26 becomes

$$\sum_{e=1}^{N_{el}} \int_{\Omega_e} \left(\sum_{I=1}^{N_{nod,e}} N_I\left(\xi^e\right) \right)\left(\sum_{J=1}^{N_{nod,e}} N_J\left(\xi^e\right)\dot{q}^J(s) \right) d\Omega = \sum_{e=1}^{N_{el}} \sum_{I=1}^{N_{nod,e}} \sum_{J=1}^{N_{nod,e}} \dot{q}^J(s)\int_{\Omega_e} N_I\left(\xi^e\right)N_J\left(\xi^e\right)d\Omega$$

$$= \sum_{e=1}^{N_{el}} \sum_{I=1}^{N_{nod,e}} \sum_{J=1}^{N_{nod,e}} \dot{q}^J(s)\int_e N_I\left(\xi^e\right)N_J\left(\xi^e\right)\left|\mathbf{J}^e\right|d\xi \qquad (C.27)$$

$$= \sum_{e=1}^{N_{el}} \sum_{I=1}^{N_{nod,e}} \sum_{J=1}^{N_{nod,e}} M_{IJ}^e \dot{q}^J(s)$$

The second term becomes

$$\sum_{e=1}^{N_{el}} \int_{\Omega_e} \left(\sum_{I=1}^{N_{nod,e}} N_I\left(\xi^e\right) \right)\left(\sum_{J=1}^{N_{nod,e}} N_J\left(\xi^e\right)\omega^J q^J(s) \right) d\Omega = \sum_{e=1}^{N_{el}} \sum_{I=1}^{N_{nod,e}} \sum_{J=1}^{N_{nod,e}} \omega^J q^J(s)\int_{\Omega_e} N_I\left(\xi^e\right)N_J\left(\xi^e\right)d\Omega$$

$$= \sum_{e=1}^{N_{el}} \sum_{I=1}^{N_{nod,e}} \sum_{J=1}^{N_{nod,e}} \omega^J q^J(s)\int_e N_I\left(\xi^e\right)N_J\left(\xi^e\right)\left|\mathbf{J}^e\right|d\xi \quad (C.28)$$

$$= \sum_{e=1}^{N_{el}} \sum_{I=1}^{N_{nod,e}} \sum_{J=1}^{N_{nod,e}} W_{IJ}^e q^J(s)$$

The third term by using eq 5.54 becomes

$$\sum_{e=1}^{N_{el}} \int_{\Omega_e} \sum_i \left(\sum_{I=1}^{N_{nod,e}} \frac{\partial N_I\left(\xi^e\right)^I}{\partial r_i} \right)\left(\sum_{J=1}^{N_{nod,e}} \frac{\partial N_J\left(\xi^e\right)}{\partial r_i} q^J(s) \right) d\Omega =$$

$$= \sum_{e=1}^{N_{el}} \sum_{I=1}^{N_{nod,e}} \sum_{J=1}^{N_{nod,e}} q^J(s)\int_{\Omega_e} \left(\sum_i \frac{\partial N_I\left(\xi^e\right)}{\partial r_i} \frac{\partial N_J\left(\xi^e\right)}{\partial r_i} \right) d\Omega$$

$$= \sum_{e=1}^{N_{el}} \sum_{I=1}^{N_{nod,e}} \sum_{J=1}^{N_{nod,e}} q^J(s)\int_{\Omega_e} \left(\sum_i \frac{\partial N_I\left(\xi^e\right)}{\partial r_i} \frac{\partial N_J\left(\xi^e\right)}{\partial r_i} \right)\left|\mathbf{J}^e\right|d\xi \qquad (C.29)$$

$$= \sum_{e=1}^{N_{el}} \sum_{I=1}^{N_{nod,e}} \sum_{J=1}^{N_{nod,e}} \left(\sum_i \sum_j \sum_l \int_e \frac{\partial N_I\left(\xi^e\right)}{\partial \xi_j^e} k \frac{\partial N_J\left(\xi^e\right)}{\partial \xi_l^e}\left(J^{e,-1}\right)_{ji}\left(J^{e,-1}\right)_{li} \right)\left|\mathbf{J}^e\right|d\xi q^J(s)$$

$$= \sum_{e=1}^{N_{el}} \sum_{I=1}^{N_{nod,e}} \sum_{J=1}^{N_{nod,e}} K_{IJ}^e q^J(s)$$

In eq C.29, the indices i, j, l run over the values 1, 2, 3, corresponding to the three coordinate directions.

References

(1)   Bower, D. I. *An Introduction to Polymer Physics*; Cambridge University Press, 2002; Vol. 53.

(2)   Gedde, U. W. *Polymer Physics*; Springer Netherlands: Dordrecht, 1999.

(3)   Kawakatsu, T. *Statistical Physics of Polymers*; Advanced Texts in Physics; Springer Berlin Heidelberg: Berlin, Heidelberg, 2004.

(4)   Flory, P. J. *In Principles of Polymer Chemistry*; 1953.

(5)   de Gennes, P. G. Conformations of Polymers Attached to an Interface. *Macromolecules* **1980**, *13*, 1069–1075.

(6)   Namazi, H. Polymers in Our Daily Life. *BioImpacts* **2017**, *7*, 73–74.

(7)   Carraher, C. E. *Carraher's Polymer Chemistry*; CRC Press, Taylor & Francis Group, 2018.

(8)   Rubinstein, M.; Colby, R. H. *Polymer Physics*; Oxford University Press, 2003.

(9)   Staudinger, H. Über Polymerisation. *Berichte der Dtsch. Chem. Gesellschaft (A B Ser.* **1920**, *53*, 1073–1085.

(10)   Kuhn, W.; Kuhn, H. Rigidity of Chain Molecules and Its Determination from Viscosity and Flow Birefringence in Dilute Solutions. *J. Colloid Sci.* **1948**, *3*, 11–32.

(11)   Huggins, M. L. Solutions of Long Chain Compounds. *J. Chem. Phys.* **1941**, *9*, 440–440.

(12)   Flory, P. J. Thermodynamics of High Polymer Solutions. *J. Chem. Phys.* **1941**, *9*, 660–660.

(13)   Stockmayer, W. H. Theory of Molecular Size Distribution and Gel Formation in Branched Polymers: II. General Cross Linking. *J. Chem. Phys.* **1944**, *12*, 125–131.

(14) Flory, P. J. Molecular Size Distribution in Three Dimensional Polymers. II. Trifunctional Branching Units. *J. Am. Chem. Soc.* **1941**, *63*, 3091–3096.

(15) James, H. M.; Guth, E. Theory of the Elastic Properties of Rubber. *J. Chem. Phys.* **1943**, *11*, 455–481.

(16) Rouse, P. E. A Theory of the Linear Viscoelastic Properties of Dilute Solutions of Coiling Polymers. *J. Chem. Phys.* **1953**, *21*, 1272–1280.

(17) Zimm, B. H. Dynamics of Polymer Molecules in Dilute Solution: Viscoelasticity, Flow Birefringence and Dielectric Loss. *J. Chem. Phys.* **1956**, *24*, 269–278.

(18) Edwards, S. F. The Statistical Mechanics of Polymers with Excluded Volume. *Proc. Phys. Soc.* **1965**, *85*, 613–624.

(19) des Cloizeaux, J. The Lagrangian Theory of Polymer Solutions at Intermediate Concentrations. *J. Phys.* **1975**, *36*, 281–291.

(20) Gennes, P. G. de. Entangled Polymers. *Phys. Today* **1983**, *36*, 33–39.

(21) Doi, M.; Edwards, S. F. Dynamics of Concentrated Polymer Systems. Part 2.-Molecular Motion under Flow. *J. Chem. Soc., Faraday Trans. 2* **1978**, *74*, 1802–1817.

(22) Sgouros, A. P.; Megariotis, G.; Theodorou, D. N. Slip-Spring Model for the Linear and Nonlinear Viscoelastic Properties of Molten Polyethylene Derived from Atomistic Simulations. *Macromolecules* **2017**, *50*, 4524–4541.

(23) Harmandaris, V. A.; Mavrantzas, V. G.; Theodorou, D. N.; Kröger, M.; Ramírez, J.; Öttinger, H. C.; Vlassopoulos, D. Crossover from the Rouse to the Entangled Polymer Melt Regime: Signals from Long, Detailed Atomistic Molecular Dynamics Simulations, Supported by Rheological Experiments. *Macromolecules* **2003**, *36*, 1376–1387.

(24) Daoulas, K. C.; Theodorou, D. N.; Harmandaris, V. A.; Karayiannis, N. C.; Mavrantzas, V. G. Self-Consistent-Field Study of Compressible Semiflexible Melts Adsorbed on a Solid Substrate and Comparison with Atomistic Simulations. *Macromolecules* **2005**, *38*, 7134–7149.

(25) Kritikos, G. Transition of the Bounded Polymer Layer to a Rigid Amorphous Phase: A Computational and DSC Study. *Polym. (United Kingdom)* **2014**, *55*, 4658–4670.

(26) Lakkas, A. T.; Sgouros, A. P.; Theodorou, D. N. Self-Consistent Field Theory Coupled

with Square Gradient Theory of Free Surfaces of Molten Polymers and Compared to Atomistic Simulations and Experiment. *Macromolecules* **2019**, *52*, 5337–5356.

(27) Tzoumanekas, C.; Theodorou, D. N. Topological Analysis of Linear Polymer Melts. *Macromolecules* **2006**, *39*, 4592–4604.

(28) Wick, C. D.; Theodorou, D. N. Connectivity-Altering Monte Carlo Simulations of the End Group Effects on Volumetric Properties for Poly(Ethylene Oxide). *Macromolecules* **2004**, *37*, 7026–7033.

(29) Mavrantzas, V. G.; Boone, T. D.; Zervopoulou, E.; Theodorou, D. N. End-Bridging Monte Carlo: A Fast Algorithm for Atomistic Simulation of Condensed Phases of Long Polymer Chains. *Macromolecules* **1999**, *32*, 5072–5096.

(30) Anogiannakis, S. D.; Tzoumanekas, C.; Theodorou, D. N. Microscopic Description of Entanglements in Polyethylene Networks and Melts: Strong, Weak, Pairwise, and Collective Attributes. *Macromolecules* **2012**, *45*, 9475–9492.

(31) Theodorou, D. N.; Vogiatzis, G. G.; Kritikos, G. Self-Consistent-Field Study of Adsorption and Desorption Kinetics of Polyethylene Melts on Graphite and Comparison with Atomistic Simulations. *Macromolecules* **2014**, *47*, 6964–6981.

(32) Fredrickson, G. H. The Equilibrium Theory of Inhomogeneous Polymers. *Equilib. Theory Inhomogeneous Polym.* **2013**, 1–456.

(33) Auhl, R.; Everaers, R.; Grest, G. S.; Kremer, K.; Plimpton, S. J. Equilibration of Long Chain Polymer Melts in Computer Simulations. *J. Chem. Phys.* **2003**, *119*, 12718–12728.

(34) Whitmore, M. D.; Vavasour, J. D. Self-Consistent Field Theory of Block Copolymers and Block Copolymer Blends. *Acta Polym.* **1995**, *46*, 341–360.

(35) Müller, M. Miscibility Behavior and Single Chain Properties in Polymer Blends: A Bond Fluctuation Model Study. *Macromol. Theory Simulations* **1999**, *8*, 343–374.

(36) Feng, H.; Lu, X.; Wang, W.; Kang, N. G.; Mays, J. W. Block Copolymers: Synthesis, Self-Assembly, and Applications. *Polymers (Basel).* **2017**, *9*.

(37) Hur, S.-M.; Frischknecht, A. L.; Huber, D. L.; Fredrickson, G. H. Self-Consistent Field Simulations of Self- and Directed-Assembly in a Mixed Polymer Brush. *Soft Matter* **2011**, *7*, 8776.

(38) Yang, T.; Berber, S.; Liu, J. F.; Miller, G. P.; Tománek, D. Self-Assembly of Long Chain Alkanes and Their Derivatives on Graphite. *J. Chem. Phys.* **2008**, *128*.

(39) Tang, S.; Lo, T. Y.; Horton, J. M.; Bao, C.; Tang, P.; Qiu, F.; Ho, R. M.; Zhao, B.; Zhu, L. Direct Visualization of Three-Dimensional Morphology in Hierarchically Self-Assembled Mixed Poly(Tert -Butyl Acrylate)/Polystyrene Brush-Grafted Silica Nanoparticles. *Macromolecules* **2013**, *46*, 6575–6584.

(40) Striolo, A. On the Solution Self-Assembly of Nanocolloidal Brushes: Insights from Simulations. *Nanotechnology* **2008**, *19*.

(41) Vogiatzis, G. G.; Voyiatzis, E.; Theodorou, D. N. Monte Carlo Simulations of a Coarse Grained Model for an Athermal All-Polystyrene Nanocomposite System. *Eur. Polym. J.* **2011**, *47*, 699–712.

(42) Green, P. F. The Structure of Chain End-Grafted Nanoparticle/Homopolymer Nanocomposites. *Soft Matter* **2011**, *7*, 7914–7926.

(43) Roan, J. R.; Kawakatsu, T. Self-Consistent-Field Theory for Interacting Polymeric Assemblies. II. Steric Stabilization of Colloidal Particles. *J. Chem. Phys.* **2002**, *116*, 7295–7310.

(44) Lenart, W. R.; Hore, M. J. A. Structure–Property Relationships of Polymer-Grafted Nanospheres for Designing Advanced Nanocomposites. *Nano-Structures and Nano-Objects* **2018**, *16*, 428–440.

(45) Mathioudakis, I. G.; Vogiatzis, G. G.; Tzoumanekas, C.; Theodorou, D. N. Molecular Modeling and Simulation of Polymer Nanocomposites at Multiple Length Scales. *IEEE Trans. Nanotechnol.* **2016**, *15*, 416–422.

(46) Hooper, J. B.; Schweizer, K. S. Contact Aggregation, Bridging, and Steric Stabilization in Dense Polymer-Particle Mixtures. *Macromolecules* **2005**, *38*, 8858–8869.

(47) Xu, C.; Ohno, K.; Ladmiral, V.; Milkie, D. E.; Kikkawa, J. M.; Composto, R. J. Simultaneous Block Copolymer and Magnetic Nanoparticle Assembly in Nanocomposite Films. *Macromolecules* **2009**, *42*, 1219–1228.

(48) Tu, Y.; Zhou, L.; Jin, Y. Z.; Gao, C.; Ye, Z. Z.; Yang, Y. F.; Wang, Q. L. Transparent and Flexible Thin Films of ZnO-Polystyrene Nanocomposite for UV-Shielding Applications.

J. Mater. Chem. **2010**, *20*, 1594–1599.

(49)   Chan, E. R.; Striolo, A.; McCabe, C.; Cummings, P. T.; Glotzer, S. C. Coarse-Grained Force Field for Simulating Polymer-Tethered Silsesquioxane Self-Assembly in Solution. *J. Chem. Phys.* **2007**, *127*.

(50)   Pedersen, J. S. Structure Factors Effects in Small-Angle Scattering from Block Copolymer Micelles and Star Polymers. *J. Chem. Phys.* **2001**, *114*, 2839–2846.

(51)   Kim, S.; Hyun, K.; Struth, B.; Ahn, K. H.; Clasen, C. Structural Development of Nanoparticle Dispersion during Drying in Polymer Nanocomposite Films. *Macromolecules* **2016**, *49*, 9068–9079.

(52)   Adamson, A. W.; Gast, A. P. *Physical Chemistry of Surfaces Sixth Edition*; John Wiley and Sons: New York, 1990.

(53)   Evans, S. D.; Henderson, J. R. *Physics of Polymer Surfaces and Interfaces*; 1993; Vol. 34.

(54)   Theodorou, D. N. Variable-Density Model of Polymer Melt Surfaces: Structure and Surface Tension. *Macromolecules* **1989**, *22*, 4578–4589.

(55)   Babick, F. *Suspensions of Colloidal Particles and Aggregates*; 2016; Vol. 20.

(56)   Daoulas, K. C.; Harmandaris, V. A.; Mavrantzas, V. G. Detailed Atomistic Simulation of a Polymer Melt/Solid Interface : Structure, Density, and Conformation of a Thin Film of Polyethylene Melt Adsorbed on Graphite. *Macromolecules* **2005**, *38*, 5780–5795.

(57)   Vogiatzis, G. G.; Theodorou, D. N. Structure of Polymer Layers Grafted to Nanoparticles in Silica–Polystyrene Nanocomposites. *Macromolecules* **2013**, *46*, 4670–4683.

(58)   Mansfield, K. F.; Theodorou, D. N. Atomistic Simulation of a Glassy Polymer/Graphite Interface. *Macromolecules* **1991**, *24*, 4295–4309.

(59)   Mathioudakis, I. G.; Vogiatzis, G. G.; Tzoumanekas, C.; Theodorou, D. N. Multiscale Simulations of PS-SiO2 Nanocomposites: From Melt to Glassy State. *Soft Matter* **2016**, *12*, 7585–7605.

(60)   Galata, A. A.; Anogiannakis, S. D.; Theodorou, D. N. Thermodynamic Analysis of Lennard-Jones Binary Mixtures Using Kirkwood-Buff Theory. *Fluid Phase Equilib.* **2018**, *470*, 25–37.

(61)   Spyriouni, T.; Tzoumanekas, C.; Theodorou, D.; Müller-Plathe, F.; Milano, G. Coarse-Grained and Reverse-Mapped United-Atom Simulations of Long-Chain Atactic Polystyrene Melts: Structure, Thermodynamic Properties, Chain Conformation, and Entanglements. *Macromolecules* **2007**, *40*, 3876–3885.

(62)   Masubuchi, Y.; Takimoto, J. I.; Koyama, K.; Ianniruberto, G.; Marrucci, G.; Greco, F. Brownian Simulations of a Network of Reptating Primitive Chains. *J. Chem. Phys.* **2001**, *115*, 4387–4394.

(63)   van Gunsteren, W. F.; Berendsen, H. J. C. Algorithms for Brownian Dynamics. *Mol. Phys.* **1982**, *45*, 637–647.

(64)   Nair, D. M.; Schieber, J. D. Linear Viscoelastic Predictions of a Consistently Unconstrained Brownian Slip-Link Model. *Macromolecules* **2006**, *39*, 3386–3397.

(65)   Landau, L. D.; Lifshitz, L. M. Debye's Interpolation Formula. *Stat. Phys.* **1980**, 544.

(66)   Ginzburg, V. L.; Landau, L. D. On the Theory of Superconductivity. *Zh. Eksp. Teor. Fiz.* **1950**, *20*, 1064–1082.

(67)   Cahn, J. W.; Hilliard, J. E. Free Energy of a Nonuniform System. I. Interfacial Free Energy. *J. Chem. Phys.* **1958**, *28*, 258–267.

(68)   Theodorou, D. N. Variable-Density Model of Polymer Melt/Solid Interfaces: Structure, Adhesion Tension, and Surface Forces. *Macromolecules* **1989**, *22*, 4589–4597.

(69)   Wu, J. *Variational Methods in Molecular Modeling*; Wu, J., Ed.; Molecular Modeling and Simulation; Springer Singapore: Singapore, 2017.

(70)   Muller M; Schmid F. Incorporating Fluctuations and Dynamics in Self-Consistent Field Theories for Polymer Blends. *Adv. Polym. Sci.* **2005**, *185*, 1–58.

(71)   Fredrickson, G. H. CHAPTER 1 - Theoretical Methods for Polymer Surfaces and Interfaces. In *Physics of Polymer Surfaces and Interfaces*; Sanchez, I. C., Ed.; Butterworth-Heinemann: Boston, 1992; pp 1–28.

(72)   Vogiatzis, G. G.; Theodorou, D. N. *Multiscale Molecular Simulations of Polymer-Matrix Nanocomposites: Or What Molecular Simulations Have Taught Us About the Fascinating Nanoworld*; Springer Netherlands, 2018; Vol. 25.

(73)   Vaia, R. A.; Wagner, H. D. Framework for Nanocomposites. *Mater. Today* **2004**, *7*, 32–

37.

(74)   Jiang, X.; Zhao, B.; Zhong, G.; Jin, N.; Horton, J. M.; Zhu, L.; Hafner, R. S.; Lodge, T. P. Microphase Separation of High Grafting Density Asymmetric Mixed Homopolymer Brushes on Silica Particles. *Macromolecules* **2010**, *43*, 8209–8217.

(75)   Giovino, M.; Pribyl, J.; Benicewicz, B.; Kumar, S.; Schadler, L. Linear Rheology of Polymer Nanocomposites with Polymer-Grafted Nanoparticles. *Polymer (Guildf).* **2017**, *131*, 104–110.

(76)   Chevigny, C.; Dalmas, F.; Di Cola, E.; Gigmes, D.; Bertin, D.; Boué, F.; Jestin, J. Polymer-Grafted-Nanoparticles Nanocomposites: Dispersion, Grafted Chain Conformation, and Rheological Behavior. *Macromolecules* **2011**, *44*, 122–133.

(77)   Abbas, Z. M.; Tawfilas, M.; Khani, M. M.; Golian, K.; Marsh, Z. M.; Jhalaria, M.; Simonutti, R.; Stefik, M.; Kumar, S. K.; Benicewicz, B. C. Reinforcement of Polychloroprene by Grafted Silica Nanoparticles. *Polymer (Guildf).* **2019**, *171*, 96–105.

(78)   Moll, J. F.; Akcora, P.; Rungta, A.; Gong, S.; Colby, R. H.; Benicewicz, B. C.; Kumar, S. K. Mechanical Reinforcement in Polymer Melts Filled with Polymer Grafted Nanoparticles. *Macromolecules* **2011**, *44*, 7473–7477.

(79)   Savin, D. A.; Pyun, J.; Patterson, G. D.; Kowalewski, T.; Matyjaszewski, K. Synthesis and Characterization of Silica-Graft-Polystyrene Hybrid Nanoparticles: Effect of Constraint on the Glass-Transition Temperature of Spherical Polymer Brushes. *J. Polym. Sci. Part B Polym. Phys.* **2002**, *40*, 2667–2676.

(80)   Giovino, M.; Buenning, E.; Jimenez, A.; Kumar, S. K.; Schadler, L. Polymer Grafted Nanoparticle Viscosity Modifiers. *Macromol. Chem. Phys.* **2019**, *220*, 1–7.

(81)   Zhao, D.; Ge, S.; Senses, E.; Akcora, P.; Jestin, J.; Kumar, S. K. Role of Filler Shape and Connectivity on the Viscoelastic Behavior in Polymer Nanocomposites. *Macromolecules* **2015**, *48*, 5433–5438.

(82)   Askar, S.; Li, L.; Torkelson, J. M. Polystyrene-Grafted Silica Nanoparticles: Investigating the Molecular Weight Dependence of Glass Transition and Fragility Behavior. *Macromolecules* **2017**, *50*, 1589–1598.

(83)   Akcora, P.; Liu, H.; Kumar, S. K.; Moll, J.; Li, Y.; Benicewicz, B. C.; Schadler, L. S.;

Acehan, D.; Panagiotopoulos, A. Z.; Pryamitsyn, V.; Ganesan, V.; Ilavsky, J.; Thiyagarajan, P.; Colby, R. H.; Douglas, J. F. Anisotropic Self-Assembly of Spherical Polymer-Grafted Nanoparticles. *Nat. Mater.* **2009**, *8*, 354–359.

(84)   Goodyear, C. Goodyear's Verfahren Zur Fabrication von Gegenständen Aus Kautschuk Und Gutta-Percha. *Polytech. J.* **1856**, *139*, 376–390.

(85)   Walter, P.; Mäder, D.; Reichert, P.; Mülhaupt, R. Novel Polypropylene Materials. *J. Macromol. Sci. - Pure Appl. Chem.* **1999**, *36 A*, 1613–1639.

(86)   Kojima, Y.; Usuki, A.; Kawasumi, M.; Okada, A.; Kurauchi, T.; Kamigaito, O. Synthesis of Nylon 6–Clay Hybrid by Montmorillonite Intercalated with ε-Caprolactam. *J. Polym. Sci. Part A Polym. Chem.* **1993**, *31*, 983–986.

(87)   Ajayan. *Nanocomposite Science and Technology*; Ajayan, P. M., Schadler, L. S., Braun, P. V., Eds.; Wiley, 2003.

(88)   Bhattacharya, S. N.; Kamal, M. R.; Gupta, R. K. *Polymeric Nanocomposites: Theory and Practice*; Carl Hanser Publishers, 2008.

(89)   Edwards, S. F. The Statistical Mechanics of Polymers with Excluded Volume. *Proc. Phys. Soc.* **1965**, *85*, 613.

(90)   Helfand, E. Theory of Inhomogeneous Polymers: Fundamentals of the Gaussian Random-Walk Model. *J. Chem. Phys.* **1975**, *62*, 999.

(91)   Hong, K. M.; Noolandi, J. Conformational Entropy Effects in a Compressible Lattice Fluid Theory of Polymers. *Macromolecules* **1981**, *14*, 1229–1234.

(92)   Shull, K. R. Mean-Field Theory of Block Copolymers: Bulk Melts, Surfaces, and Thin Films. *Macromolecules* **1992**, *25*, 2122–2133.

(93)   Vavasour, J. D.; Whitmore, M. D. Self-Consistent Mean Field Theory of the Microphases of Diblock Copolymers. *Macromolecules* **1992**, *25*, 5477–5486.

(94)   Geisinger, T.; Müller, M.; Binder, K. Symmetric Diblock Copolymers in Thin Films. I. Phase Stability in Self-Consistent Field Calculations and Monte Carlo Simulations. *J. Chem. Phys.* **1999**, *111*, 5241–5250.

(95)   Shi, A.-C.; Noolandi, J.; Desai, R. C. Theory of Anisotropic Fluctuations in Ordered Block Copolymer Phases. *Macromolecules* **1996**, *29*, 6487–6504.

(96) Drolet, F.; Fredrickson, G. H. Combinatorial Screening of Complex Block Copolymer Assembly with Self-Consistent Field Theory. *Phys. Rev. Lett.* **1999**, *83*, 4317–4320.

(97) Delaney, K. T.; Fredrickson, G. H. Recent Developments in Fully Fluctuating Field-Theoretic Simulations of Polymer Melts and Solutions. *J. Phys. Chem. B* **2016**, *120*, 7615–7634.

(98) Schmid, F. Self-Consistent-Field Theories for Complex Fluids. *J. Phys. Condens. Matter* **1998**, *10*, 8105–8138.

(99) Matsen, M. W. Self-Consistent Field Theory and Its Applications. In *Soft Matter Vol. 1*; Wiley-VCH Verlag GmbH & Co. KGaA: Weinheim, Germany, 2006; Vol. 1, pp 87–178.

(100) Yang, Y.; Qiu, F.; Zhang, H.; Yang, Y. Cylindrical Phase of Diblock Copolymers Confined in Thin Films. A Real-Space Self-Consistent Field Theory Study. *Polymer (Guildf).* **2006**, *47*, 2205–2216.

(101) Han, W.; Tang, P.; Li, X.; Qiu, F.; Zhang, H.; Yang, Y. Self-Assembly of Star ABC Triblock Copolymer Thin Films: Self-Consistent Field Theory. *J. Phys. Chem. B* **2008**, *112*, 13738–13748.

(102) Tang, Q.; Gao, X.; Peng, T.; Yang, S.; Li, Q. Modelling of Disjoining Pressure for Lennard-Jones Free Thin Films. *Mod. Phys. Lett. B* **2016**, *30*, 1650169.

(103) Lyulin, A. V.; Balabaev, N. K.; Baljon, A. R. C.; Mendoza, G.; Frank, C. W.; Yoon, D. Y. Interfacial and Topological Effects on the Glass Transition in Free-Standing Polystyrene Films. *J. Chem. Phys.* **2017**, *146*.

(104) Sgouros, A. P.; Vogiatzis, G. G.; Kritikos, G.; Boziki, A.; Nikolakopoulou, A.; Liveris, D.; Theodorou, D. N. Molecular Simulations of Free and Graphite Capped Polyethylene Films: Estimation of the Interfacial Free Energies. *Macromolecules* **2017**, *50*, 8827–8844.

(105) Mansfield, K. F.; Theodorou, D. N. Interfacial Structure and Dynamics of Macromolecular Liquids: A Monte Carlo Simulation Approach. *Macromolecules* **1989**, *22*, 3143–3152.

(106) Mecke, M.; Winkelmann, J.; Fischer, J. Molecular Dynamics Simulation of the Liquid-Vapor Interface: The Lennard-Jones Fluid. *J. Chem. Phys.* **1997**, *107*, 9264–9270.

(107) Doruker, P.; Mattice, W. L. Simulation of Polyethylene Thin Films on a High

Coordination Lattice. *Macromolecules* **1998**, *31*, 1418–1426.

(108) Trokhymchuk, A.; Alejandre, J. Computer Simulations of Liquid/Vapor Interface in Lennard-Jones Fluids: Some Questions and Answers. *J. Chem. Phys.* **1999**, *111*, 8510–8523.

(109) Weng, J.-G.; Park, S.; Lukes, J. R.; Tien, C.-L. Molecular Dynamics Investigation of Thickness Effect on Liquid Films. *J. Chem. Phys.* **2000**, *113*, 5917–5923.

(110) Bhatt, D.; Newman, J.; Radke, C. J. Molecular Simulation of Disjoining-Pressure Isotherms for Free Liquid, Lennard-Jones Thin Films. *J. Phys. Chem. B* **2002**, *106*, 6529–6537.

(111) Matsen, M. W. Thin Films of Block Copolymer. *J. Chem. Phys.* **2002**, *106*, 7781–7791.

(112) Carey, V. P.; Wemhoff, A. P. Disjoining Pressure Effects in Ultra-Thin Liquid Films in Micropassages—Comparison of Thermodynamic Theory With Predictions of Molecular Dynamics Simulations. *J. Heat Transfer* **2006**, *128*, 1276.

(113) Lyulin, A. V.; Balabaev, N. K.; Baljon, A. R. C. C.; Mendoza, G.; Frank, C. W.; Yoon, D. Y. Interfacial and Topological Effects on the Glass Transition in Free-Standing Polystyrene Films. *J. Chem. Phys.* **2017**, *146*, 203314.

(114) Duque, D.; Pàmies, J. C.; Vega, L. F. Interfacial Properties of Lennard-Jones Chains by Direct Simulation and Density Gradient Theory. *J. Chem. Phys.* **2004**, *121*, 11395–11401.

(115) Miqueu, C.; Mendiboure, B.; Graciaa, A.; Lachaise, J. Modeling of the Surface Tension of Multicomponent Mixtures with the Gradient Theory of Fluid Interfaces. *Ind. Eng. Chem. Res.* **2005**, *44*, 3321–3329.

(116) Lin, H.; Duan, Y.-Y.; Min, Q. Gradient Theory Modeling of Surface Tension for Pure Fluids and Binary Mixtures. *Fluid Phase Equilib.* **2007**, *254*, 75–90.

(117) Schmidt, K. A. G.; Folas, G. K.; Kvamme, B. Calculation of the Interfacial Tension of the Methane-Water System with the Linear Gradient Theory. *Fluid Phase Equilib.* **2007**, *261*, 230–237.

(118) Breure, B.; Peters, C. J. Modeling of the Surface Tension of Pure Components and Mixtures Using the Density Gradient Theory Combined with a Theoretically Derived Influence Parameter Correlation. *Fluid Phase Equilib.* **2012**, *334*, 189–196.

(119) Magnanelli, E.; Wilhelmsen, Ø.; Bedeaux, D.; Kjelstrup, S. Extending the Nonequilibrium Square-Gradient Model with Temperature-Dependent Influence Parameters. *Phys. Rev. E - Stat. Nonlinear, Soft Matter Phys.* **2014**, *90*, 1–10.

(120) Wilhelmsen, Ø.; Trinh, T. T.; Kjelstrup, S.; Bedeaux, D. Influence of Curvature on the Transfer Coefficients for Evaporation and Condensation of Lennard-Jones Fluid from Square-Gradient Theory and Nonequilibrium Molecular Dynamics. *J. Phys. Chem. C* **2015**, *119*, 8160–8173.

(121) Poser, C. I.; Sanchez, I. C. Surface Tension Theory of Pure Liquids and Polymer Melts. *J. Colloid Interface Sci.* **1979**, *69*, 539–548.

(122) Poser, C. I.; Sanchez, I. C. Interfacial Tension Theory of Low and High Molecular Weight Liquid Mixtures. *Macromolecules* **1981**, *14*, 361–370.

(123) Helfand, E.; Sapse, A. M. Theory of Unsymmetric Polymer-Polymer Interfaces. *J. Chem. Phys.* **1975**, *62*, 1327–1331.

(124) Tang, H.; Freed, K. F. Free Energy Functional Expansion for Inhomogeneous Polymer Blends. *J. Chem. Phys.* **1991**, *94*, 1572–1583.

(125) Yang, A. J. M.; Fleming, P. D.; Gibbs, J. H. Molecular Theory of Surface Tension. *J. Chem. Phys.* **1976**, *64*, 3732–3747.

(126) Zuo, Y.-X.; Stenby, E. H. A Linear Gradient Theory Model for Calculating Interfacial Tensions of Mixtures. *J. Colloid Interface Sci.* **1996**, *182*, 126–132.

(127) Cornelisse, P. M. W.; Peters, C. J.; De Swaan Arons, J. On the Fundamentals of the Gradient Theory of van Der Waals. *J. Chem. Phys.* **1997**, *106*, 9820–9834.

(128) Kahl, H.; Enders, S. Calculation of Surface Properties of Pure Fluids Using Density Gradient Theory and SAFT-EOS. *Fluid Phase Equilib.* **2000**, *172*, 27–42.

(129) Enders, S.; Quitzsch, K. Calculation of Interfacial Properties of Demixed Fluids Using Density Gradient Theory. *Langmuir* **2002**, *14*, 4606–4614.

(130) Miqueu, C.; Mendiboure, B.; Graciaa, A.; Lachaise, J. Modelling of the Surface Tension of Pure Components with the Gradient Theory of Fluid Interfaces: A Simple and Accurate Expression for the Influence Parameters. *Fluid Phase Equilib.* **2003**, *207*, 225–246.

(131) Wu, D. T.; Fredrickson, G. H.; Carton, J.-P.; Ajdari, A.; Leibler, L. Distribution of Chain

Ends at the Surface of a Polymer Melt: Compensation Effects and Surface Tension. *J. Polym. Sci. Part B Polym. Phys.* **1995**, *33*, 2373–2389.

(132) Schmid, F. A Self-consistent-field Approach to Surfaces of Compressible Polymer Blends. *J. Chem. Phys.* **1996**, *104*, 9191–9201.

(133) Müller, M.; MacDowell, L. G. Interface and Surface Properties of Short Polymers in Solution: Monte Carlo Simulations and Self-Consistent Field Theory. *Macromolecules* **2000**, *33*, 3902–3923.

(134) Kumar, S. K.; Ganesan, V.; Riggleman, R. A. Perspective: Outstanding Theoretical Questions in Polymer-Nanoparticle Hybrids. *J. Chem. Phys.* **2017**, *147*.

(135) Matsen, M. W.; Gardiner, J. M. Autophobic Dewetting of Homopolymer on a Brush and Entropic Attraction between Opposing Brushes in a Homopolymer Matrix. *J. Chem. Phys.* **2001**, *115*, 2794–2804.

(136) Sunday, D.; Ilavsky, J.; Green, D. L. A Phase Diagram for Polymer-Grafted Nanoparticles in Homopolymer Matrices. *Macromolecules* **2012**, *45*, 4007–4011.

(137) Everaers, R.; Ejtehadi, M. R. Interaction Potentials for Soft and Hard Ellipsoids. *Phys. Rev. E - Stat. Physics, Plasmas, Fluids, Relat. Interdiscip. Top.* **2003**, *67*, 8.

(138) Ndoro, T. V. M.; Voyiatzis, E.; Ghanbari, A.; Theodorou, D. N.; Böhm, M. C.; Müller-Plathe, F. Interface of Grafted and Ungrafted Silica Nanoparticles with a Polystyrene Matrix: Atomistic Molecular Dynamics Simulations. *Macromolecules* **2011**, *44*, 2316–2327.

(139) Meng, D.; Kumar, S. K.; D. Lane, J. M.; Grest, G. S. Effective Interactions between Grafted Nanoparticles in a Polymer Matrix. *Soft Matter* **2012**, *8*, 5002–5010.

(140) Kalb, J.; Dukes, D.; Kumar, S. K.; Hoy, R. S.; Grest, G. S. End Grafted Polymernanoparticles in a Polymeric Matrix: Effect of Coverage and Curvature. *Soft Matter* **2011**, *7*, 1418–1425.

(141) Ibergay, C.; Malfreyt, P.; Tildesley, D. J. Electrostatic Interactions in Dissipative Particle Dynamics: Toward a Mesoscale Modeling of the Polyelectrolyte Brushes. *J. Chem. Theory Comput.* **2009**, *5*, 3245–3259.

(142) Lo Verso, F.; Egorov, S. A.; Milchev, A.; Binder, K. Spherical Polymer Brushes under

Good Solvent Conditions: Molecular Dynamics Results Compared to Density Functional Theory. *J. Chem. Phys.* **2010**, *133*, 184901.

(143) Vogiatzis, G. G.; Theodorou, D. N. Structure of Polymer Layers Grafted to Nanoparticles in Silica–Polystyrene Nanocomposites. *Macromolecules* **2013**, *46*, 4670–4683.

(144) Chantawansri, T. L.; Hur, S. M.; Garca-Cervera, C. J.; Ceniceros, H. D.; Fredrickson, G. H. Spectral Collocation Methods for Polymer Brushes. *J. Chem. Phys.* **2011**, *134*.

(145) Tong, C. Numerical Self-Consistent Field Theory Study of the Response of Strong Polyelectrolyte Brushes to External Electric Fields. *J. Chem. Phys.* **2015**, *143*, 054903.

(146) Müller, M. Phase Diagram of a Mixed Polymer Brush. *Phys. Rev. E - Stat. Nonlinear, Soft Matter Phys.* **2002**, *65*, 1–4.

(147) Zhulina, E. B.; Borisov, O. V.; Pryamitsyn, V. A.; Birshtein, T. M. Coil-Globule Type Transitions in Polymers. 1. Collapse of Layers of Grafted Polymer Chains. *Macromolecules* **1991**, *24*, 140–149.

(148) Irvine, D. J.; Mayes, A. M.; Griffith-Cima, L. Self-Consistent Field Analysis of Grafted Star Polymers. *Macromolecules* **1996**, *29*, 6037–6043.

(149) Deng, S.; Zhang, L.; Zhou, X.; Fan, C.; Lin, Q.; Lin, J. Exploring Microstructures and Interphase Properties of Surface- Grafted Diblock Copolymers in a Homopolymer Melt by Self-Consistent Field Theory Simulations. *J. Macromol. Sci. Part B Phys.* **2015**, *54*, 348–364.

(150) Hu, J.; Zhang, H.; Yang, Y. Morphology and Interactions of Polymer Brush-Coated Spheres. *J. Polym. Sci.* **2006**, *44*, 2811–2820.

(151) Harton, S. E.; Kumar, S. K. Mean-Field Theoretical Analysis of Brush-Coated Nanoparticle Dispersion in Polymer Matrices. *J. Polym. Sci. Part B Polym. Phys.* **2008**, *46*, 351–358.

(152) Pépin, M. P.; Whitmore, M. D. Monte Carlo and Numerical Self-Consistent Field Study of Systems with End-Grafted and Free Polymers in Good Solvent. *J. Chem. Phys.* **2001**, *114*, 8181–8195.

(153) Roan, J. R.; Kawakatsu, T. Self-Consistent-Field Theory for Interacting Polymeric Assemblies. I. Formulation, Implementation, and Benchmark Tests. *J. Chem. Phys.* **2002**,

116, 7283–7294.

(154) Amestoy, P. R.; Duff, I. S.; Koster, J.; L'Excellent, J.-Y. A Fully Asynchronous Multifrontal Solver Using Distributed Dynamic Scheduling. *SIAM J. Matrix Anal. Appl.* **2001**, *23*, 15–41.

(155) Wei, H.; Xu, M.; Si, W.; Jiang, K. A Finite Element Method of the Self-Consistent Field Theory on General Curved Surfaces. *J. Comput. Phys.* **2019**, *387*, 230–244.

(156) Ackerman, D. M.; Delaney, K.; Fredrickson, G. H.; Ganapathysubramanian, B. A Finite Element Approach to Self-Consistent Field Theory Calculations of Multiblock Polymers. *J. Comput. Phys.* **2017**, *331*, 280–296.

(157) Baeurle, S. A.; Fredrickson, G. H.; Gusev, A. A. Prediction of Elastic Properties of a Poly(Styrene-Butadiene-Styrene) Copolymer Using a Mixed Finite Element Approach. *Macromolecules* **2004**, *37*, 5784–5791.

(158) Ohno, K.; Esfarjani, K.; Kawazoe, Y. *Computational Materials Science: From Ab Initio to Monte Carlo Methods*; Springer Series in Solid-State Sciences; Springer Berlin Heidelberg, 1999.

(159) Cramer, C. J. *Essentials of Computational Chemistry : Theories and Models*, 2nd ed.; Chichester, West Sussex, England, 2004.

(160) Parr, R. G.; Craig, D. P.; Ross, I. G. Molecular Orbital Calculations of the Lower Excited Electronic Levels of Benzene, Configuration Interaction Included. *J. Chem. Phys.* **1950**, *18*, 1561–1563.

(161) Levine, I. N. *Quantum Chemistry*, 4th ed.; Prentice-Hall: Englewood Cliffs, N.J, 1991.

(162) Friesner, R. A. Ab Initio Quantum Chemistry: Methodology and Applications. *Proc. Natl. Acad. Sci. U. S. A.* **2005**, *102*, 6648–6653.

(163) Harmandaris, V. A.; Mavrantzas, V. G. Segmental Dynamics in Polyethylene Melts through Atomistic Molecular Dynamics Simulations. In *Recent Research Topics and Developments in Chemical Physics: From Quantum Scale to Macroscale*; Terzis, A. F., Paspalakis, E., Eds.; Research Signpost, 2008; Vol. 661, pp 179–196.

(164) Allen, M. P.; Tildeslay, D. J. *Computer Simulation of Liquids*; Clarendon Press: New York, 1989.

(165) Frenkel, D.; Smit, B. *Understanding Molecular Simulation. From Algorithms to Applications*; Academic Press: San Diego, 2002.

(166) Sadus, R. J. *Molecular Simulation of Fluids: Theory, Algorithms and Object-Orientation*; Elsevier Science Inc.: USA, 1999.

(167) Rapaport, D. C. *The Art of Molecular Dynamics Simulation*, 2nd ed.; Cambridge University Press: USA, 2004.

(168) Chandler, D. *Introduction to Modern Statistical Mechanics*; Oxford University Press, 1987.

(169) June, R. L.; Bell, A. T.; Theodorou, D. N. Transition-State Studies of Xenon and Sulfur Hexafluoride Diffusion in Silicalite. *J. Phys. Chem.* **1991**, *95*, 8866–8878.

(170) Szleifer, I.; Carignano, M. a. *Tethered Polymer Layers*; 1996; Vol. 94.

(171) Baschnagel, J.; Meyer, H.; Varnik, F.; Metzger, S.; Aichele, M.; Müller, M.; Binder, K. Computer Simulations of Polymers Close to Solid Interfaces: Some Selected Topics. *Interface Sci.* **2003**, *11*, 159–173.

(172) Vogiatzis, G. G.; Megariotis, G.; Theodorou, D. N. Equation of State-Based Slip-Spring Model for Entangled Polymer Dynamics. *Macromolecules* **2017**, *50*, 3004–3029.

(173) Binder, K. *Monte Carlo and Molecular Dynamics Simulations in Polymer Science*; Oxford University Press, 1995.

(174) Murat, M.; Grest, G. S.; Kremer, K. Statics and Dynamics of Symmetric Diblock Copolymers: A Molecular Dynamics Study. *Macromolecules* **1999**, *32*, 595–609.

(175) Müller, M.; Binder, K. Wetting and Capillary Condensation in Symmetric Polymer Blends: A Comparison between Monte Carlo Simulations and Self-Consistent Field Calculations. *Macromolecules* **1998**, *31*, 8323–8346.

(176) Parisi, G. *Statistical Field Theory*; Basic Books, 1988.

(177) Sides, S. W.; Fredrickson, G. H. Parallel Algorithm for Numerical Self-Consistent Field Theory Simulations of Block Copolymer Structure. *Polymer (Guildf).* **2003**, *44*, 5859–5866.

(178) de Gennes, P. G. *Scaling Concepts in Polymer Physics*; Cornell University Press, 1979.

(179) Bates, F. S.; Fredrickson, G. H. Block Copolymers—Designer Soft Materials. *Phys. Today* **1999**, *52*, 32–38.

(180) Rubinstein, M.; Colby, R. H. M_Rubinstein,_Ralph_H_Colby,_Polymer.Pdf. 2003.

(181) Flory, P. J.; Volkenstein, M. Statistical Mechanics of Chain Molecules. *Biopolymers* **1969**, *8*, 699–700.

(182) Doi, M., Edwards, S. F. *The Theory of Polymer Dynamics*; Clarendon Press, 1986.

(183) Kleinert, H. *Path Integrals in Quantum Mechanics, Statistics, Polymer Physics, and Financial Markets*; WORLD SCIENTIFIC, 2009.

(184) Riley, K. F.; Hobson, M. P.; Bence, S. J. *Mathematical Methods for Physics and Engineering: A Comprehensive Guide*; Cambridge University Press, 2006.

(185) Van Kampen, N. G. *Stochastic Processes in Physics and Chemistry*; North-Holland Personal Library; Elsevier Science, 2011.

(186) Feynman, R. P.; Hibbs, A. R.; Styer, D. F. *Quantum Mechanics and Path Integrals*; Dover Books on Physics; Dover Publications, 2010.

(187) Doi, M.; Edwards, S. F. *The Theory of Polymer Dynamics*; Clarendon Press, 1988.

(188) Freed, K. F. Functional Integrals and Polymer Statistics. *Adv. Chem. Phys.* **1972**, *22*, 1–128.

(189) Gibbs, J. W. *Elementary Principles in Statistical Mechanics: Developed with Especial Reference to the Rational Foundations of Thermodynamics*; Elementary Principles in Statistical Mechanics: Developed with Especial Reference to the Rational Foundation of Thermodynamics; C. Scribner's sons, 1902.

(190) Gennes, P.-G. De. Some Conformation Problems for Long Macromolecules. *Reports Prog. Phys.* **1969**, *32*, 304.

(191) De Gennes, P. G. Scaling Concepts in Polymer Physics. Cornell University Press. *Ithaca N.Y.,* **1979**.

(192) Sanchez, I. C.; Lacombe, R. H. An Elementary Molecular Theory of Classical Fluids. Pure Fluids. *J. Phys. Chem.* **1976**, *80*, 2352–2362.

(193) Theodorou, D. N. Polymers at Surfaces and Interfaces. In *Computer Simulations of*

Surfaces and Interfaces; Springer Netherlands: Dordrecht, 2003; pp 329–419.

(194) Sgouros, A. P.; Lakkas, A. T.; Megariotis, G.; Theodorou, D. N. Mesoscopic Simulations of Free Surfaces of Molten Polyethylene: Brownian Dynamics/Kinetic Monte Carlo Coupled with Square Gradient Theory and Compared to Atomistic Calculations and Experiment. *Macromolecules* **2018**, *51*, 9798–9815.

(195) Jang, J. H.; Ozisik, R.; Mattice, W. L. A Monte Carlo Simulation on the Effects of Chain End Modification on Freely Standing Thin Films of Amorphous Polyethylene Melts. *Macromolecules* **2000**, *33*, 7663–7671.

(196) Hwang, C. C.; Hsieh, J. Y.; Chang, K. H.; Liao, J. J. A Study of Rupture Process of Thin Liquid Films by a Molecular Dynamics Simulation. *Phys. A Stat. Mech. its Appl.* **1998**, *256*, 333–341.

(197) Helfand, E.; Tagami, Y. Theory of the Interface between Immiscible Polymers. II. *J. Chem. Phys.* **1972**, *56*, 3592–3601.

(198) Hong, K. M.; Noolandi, J. Theory of Inhomogeneous Multicomponent Polymer Systems. *Macromolecules* **1981**, *14*, 727–736.

(199) Matsen, M. W. The Standard Gaussian Model for Block Copolymer Melts. *J. Phys. Condens. Matter* **2002**, *14*, 21–47.

(200) Thompson, R. B.; MacDonald, J. R.; Chen, P. Origin of Change in Molecular-Weight Dependence for Polymer Surface Tension. *Phys. Rev. E - Stat. Nonlinear, Soft Matter Phys.* **2008**, *78*, 3–6.

(201) Daoulas, K. C.; Müller, M. Exploring Thermodynamic Stability of the Stalk Fusion-Intermediate with Three-Dimensional Self-Consistent Field Theory Calculations. *Soft Matter* **2013**, *9*, 4097–4102.

(202) Hong, K. M.; Noolandi, J. Theory of Phase Equilibria in Systems Containing Block Copolymers. *Macromolecules* **1983**, *16*, 1083–1093.

(203) Ohta, T.; Kawasaki, K. Equilibrium Morphology of Block Copolymer Melts. *Macromolecules* **1986**, *19*, 2621–2632.

(204) Bongiorno, V.; Davis, H. T. Modified Van Der Waals Theory of Fluid Interfaces. *Phys. Rev. A* **1975**, *12*, 2213–2224.

(205) Bongiorno, V.; Scriven, L. E.; Davis, H. T. Molecular Theory of Fluid Interfaces. *J. Colloid Interface Sci.* **1976**, *57*, 462–475.

(206) Carey, B. S. The Gradient Theory of Fluid Interfaces, Minnesota Univ., Minneapolis, 1979.

(207) Baidakov, V. G.; Protsenko, S. P.; Chernykh, G. G.; Boltachev, G. S. Statistical Substantiation of the van Der Waals Theory of Inhomogeneous Fluids. *Phys. Rev. E - Stat. Physics, Plasmas, Fluids, Relat. Interdiscip. Top.* **2002**, *65*, 16.

(208) Carey, B. S.; Scriven, L. E.; Davis, H. T. Semiempirical Theory of Surface Tensions of Pure Normal Alkanes and Alcohols. *AIChE J.* **1978**, *24*, 1076–1080.

(209) Carey, B. S.; Scriven, L. E.; Davis, H. T. Semiempirical Theory of Surface Tension of Binary Systems. *AIChE J.* **1980**, *26*, 705–711.

(210) Mejía, A.; Segura, H.; Vega, L. F.; Wisniak, J. Simultaneous Prediction of Interfacial Tension and Phase Equilibria in Binary Mixtures: An Approach Based on Cubic Equations of State with Improved Mixing Rules. *Fluid Phase Equilib.* **2005**, *227*, 225–238.

(211) Zuo, Y. Calculation of Interfacial Tensions with Gradient Theory. *Fluid Phase Equilib.* **1997**, *132*, 139–158.

(212) Matsen, M. W. Melts of Semiflexible Diblock Copolymer. *J. Chem. Phys.* **1996**, *104*, 7758–7764.

(213) Matsen, M. W.; Griffiths, G. H. Melt Brushes of Diblock Copolymer. *Eur. Phys. J. E* **2009**, *29*, 219–227.

(214) Fredrickson, G. H.; Ganesan, V.; Drolet, F. Field-Theoretic Computer Simulation Methods for Polymers and Complex Fluids. *Macromolecules* **2002**, *35*, 16–39.

(215) Morse, D. C.; Fredrickson, G. H. Semiflexible Polymers near Interfaces. *Phys. Rev. Lett.* **1994**, *73*, 3235–3238.

(216) Wu, J. Square-Gradient Model for Inhomogeneous Systems: From Simple Fluids to Microemulsions, Polymer Blends and Electronic Structure; 2017; pp 31–64.

(217) Lin, H.; Duan, Y. Y.; Min, Q. Gradient Theory Modeling of Surface Tension for Pure Fluids and Binary Mixtures. *Fluid Phase Equilib.* **2007**, *254*, 75–90.

(218) Garrido, J. M.; Mejía, A.; Piñeiro, M. M.; Blas, F. J.; Müller, E. A. Interfacial Tensions of Industrial Fluids from a Molecular-Based Square Gradient Theory. *AIChE J.* **2016**, *62*, 1781–1794.

(219) Sauer, B. B.; Dee, G. T. Studies of Polymer, Copolymer, and Associating Liquids by Melt Surface Tension Methods and Cahn-Hilliard Density-Gradient Theory. *J. Colloid Interface Sci.* **1994**, *162*, 25–35.

(220) Panayiotou, C. Interfacial Tension and Interfacial Profiles: An Equation-of-State Approach. *J. Colloid Interface Sci.* **2003**, *267*, 418–428.

(221) Wilhelmsen, Ø.; Bedeaux, D.; Kjelstrup, S.; Reguera, D. Thermodynamic Stability of Nanosized Multicomponent Bubbles/Droplets: The Square Gradient Theory and the Capillary Approach. *J. Chem. Phys.* **2014**, *140*, 024704.

(222) Humphrey, W.; Dalke, A.; Schulten, K. VMD: Visual Molecular Dynamics. *J. Mol. Graph.* **1996**, *14*, 33–38.

(223) Thomas, L. H. *Elliptic Problems in Linear Differential Equations over a Network*; 1949.

(224) Sanchez, I. C.; Lacombe, R. H. Statistical Thermodynamics of Polymer Solutions. *Macromolecules* **1978**, *11*, 1145–1156.

(225) Chen, J. Thermal and Mechanical Cracking in TIPS-Pentacene Thin Films. *J. Polym. Sci. Part B Polym. Phys.* **2007**, *45*, 1390–1398.

(226) Tzounis, P. N.; Anogiannakis, S. D.; Theodorou, D. N. General Methodology for Estimating the Stiffness of Polymer Chains from Their Chemical Constitution: A Single Unperturbed Chain Monte Carlo Algorithm. *Macromolecules* **2017**, *50*, 4575–4587.

(227) Hiorns, R. Polymer Handbook. *Polym. Int.* **2000**, *49*, 807–807.

(228) Fetters, L. J.; Lohse, D. J.; Richter, D.; Witten, T. A.; Zirkel, A. Connection between Polymer Molecular Weight, Density, Chain Dimensions, and Melt Viscoelastic Properties. *Macromolecules* **1994**, *27*, 4639–4647.

(229) Plimpton, S. Fast Parallel Algorithms for Short-Range Molecular Dynamics. *J. Comp. Phys.* **1995**, *117*, 1–19.

(230) Martin, M. G.; Siepmann, J. I. Transferable Potentials for Phase Equilibria. 1. United-Atom Description of n -Alkanes. *J. Phys. Chem. B* **1998**, *102*, 2569–2577.

(231) Nath, S. K.; Escobedo, F. A.; de Pablo, J. J. On the Simulation of Vapor–Liquid Equilibria for Alkanes. *J. Chem. Phys.* **1998**, *108*, 9905.

(232) Chevalier, S.; Chaudhury, M. K. Further Reflections on the Geometric Mean Combining Rule for Interfacial Tension. *Langmuir* **2015**, *31*, 11296–11304.

(233) Semenov, A. N.; Bonet-Avalos, J.; Johner, A.; Joanny, J. F. Adsorption of Polymer Solutions onto a Flat Surface. *Macromolecules* **1996**, *29*, 2179–2196.

(234) Scheutjens, J. M. H. M.; Fleer, G. J. Statistical Theory of the Adsorption of Interacting Chain Molecules. 2. Train, Loop, and Tail Size Distribution. *J. Phys. Chem.* **1980**, *84*, 178–190.

(235) Theodorou, D. N. Microscopic Structure and Thermodynamic Properties of Bulk Copolymers and Surface-Active Polymers at Interfaces. 1. Theory. *Macromolecules* **1988**, *21*, 1411–1421.

(236) Semenov, A. N. Contribution to the Theory of Microphase Layering in Block-Copolymer Melts. *Sov. Phys. JETP* **1985**, *61*, 733–742.

(237) Lakkas, A. T.; Sgouros, A. P.; Revelas, C. J.; Theodorou, D. N. Structure and Thermodynamics of Grafted Silica/Polystyrene Dilute Nanocomposites Investigated through Self-Consistent Field Theory. *Soft Matter* **2021**.

(238) Trombly, D. M.; Ganesan, V. Curvature Effects upon Interactions of Polymer-Grafted Nanoparticles in Chemically Identical Polymer Matrices. *J. Chem. Phys.* **2010**, *133*.

(239) Askar, S.; Li, L.; Torkelson, J. M. Polystyrene-Grafted Silica Nanoparticles: Investigating the Molecular Weight Dependence of Glass Transition and Fragility Behavior. *Macromolecules* **2017**, *50*, 1589–1598.

(240) Jiang, X.; Zhao, B.; Zhong, G.; Jin, N.; Horton, J. M.; Zhu, L.; Hafner, R. S.; Lodge, T. P. Microphase Separation of High Grafting Density Asymmetric Mixed Homopolymer Brushes on Silica Particles. *Macromolecules* **2010**, *43*, 8209–8217.

(241) Savin, D. A.; Pyun, J.; Patterson, G. D.; Kowalewski, T.; Matyjaszewski, K. Synthesis and Characterization of Silica-Graft-Polystyrene Hybrid Nanoparticles: Effect of Constraint on the Glass-Transition Temperature of Spherical Polymer Brushes. *J. Polym. Sci. Part B Polym. Phys.* **2002**, *40*, 2667–2676.

(242) Kim, S.; Hyun, K.; Struth, B.; Ahn, K. H.; Clasen, C. Structural Development of Nanoparticle Dispersion during Drying in Polymer Nanocomposite Films. *Macromolecules* **2016**, *49*, 9068–9079.

(243) Jiao, Y.; Hsiao, M.-S.; Vaia, R. A.; Tibbits, A.; Drummy, L. F.; Gillman, A.; Buskohl, P. Deformation Behavior of Polystyrene-Grafted Nanoparticle Assemblies with Low Grafting Density. *Macromolecules* **2018**, *51*, 7257–7265.

(244) Wei, Y.; Xu, Y.; Faraone, A.; Hore, M. J. A. Local Structure and Relaxation Dynamics in the Brush of Polymer-Grafted Silica Nanoparticles. *ACS Macro Lett.* **2018**, *7*, 699–704.

(245) Jhalaria, M.; Buenning, E.; Huang, Y.; Tyagi, M.; Zorn, R.; Zamponi, M.; García-Sakai, V.; Jestin, J.; Benicewicz, B. C.; Kumar, S. K. Accelerated Local Dynamics in Matrix-Free Polymer Grafted Nanoparticles. *Phys. Rev. Lett.* **2019**, *123*, 158003.

(246) Kalb, J.; Dukes, D.; Kumar, S. K.; Hoy, R. S.; Grest, G. S. End Grafted Polymer Nanoparticles in a Polymeric Matrix: Effect of Coverage and Curvature. *Soft Matter* **2011**, *7*, 1418–1425.

(247) Ethier, J. G.; Hall, L. M. Modeling Individual and Pairs of Adsorbed Polymer-Grafted Nanoparticles: Structure and Entanglements. *Soft Matter* **2018**, *14*, 643–652.

(248) Smith, G. D.; Bedrov, D. Dispersing Nanoparticles in a Polymer Matrix: Are Long, Dense Polymer Tethers Really Necessary? *Langmuir* **2009**, *25*, 11239–11243.

(249) Martin, T. B.; Dodd, P. M.; Jayaraman, A. Polydispersity for Tuning the Potential of Mean Force between Polymer Grafted Nanoparticles in a Polymer Matrix. *Phys. Rev. Lett.* **2013**, *110*, 018301.

(250) Jayaraman, A.; Nair, N. Integrating PRISM Theory and Monte Carlo Simulation to Study Polymer-Functionalised Particles and Polymer Nanocomposites. *Mol. Simul.* **2012**, *38*, 751–761.

(251) Barnett, J. W.; Kumar, S. K. Modeling Gas Transport in Polymer-Grafted Nanoparticle Membranes. *Soft Matter* **2019**, *15*, 424–432.

(252) Chakrabarti, A.; Nelson, P.; Toral, R. Structure of Polymer Chains End-Grafted on an Interacting Surface. *Physical Review A*. 1992, pp 4930–4934.

(253) Lafitte, T.; Kumar, S. K.; Panagiotopoulos, A. Z. Self-Assembly of Polymer-Grafted

Nanoparticles in Thin Films. *Soft Matter* **2014**, *10*, 786–794.

(254) Bilchak, C. R.; Buenning, E.; Asai, M.; Zhang, K.; Durning, C. J.; Kumar, S. K.; Huang, Y.; Benicewicz, B. C.; Gidley, D. W.; Cheng, S.; Sokolov, A. P.; Minelli, M.; Doghieri, F. Polymer-Grafted Nanoparticle Membranes with Controllable Free Volume. *Macromolecules* **2017**, *50*, 7111–7120.

(255) Vogiatzis, G. G.; Theodorou, D. N. Structure of Polymer Layers Grafted to Nanoparticles in Silica-Polystyrene Nanocomposites. *Macromolecules* **2013**, *46*, 4670–4683.

(256) Harton, S. E.; Kumar, S. K. Mean-Field Theoretical Analysis of Brush-Coated Nanoparticle Dispersion in Polymer Matrices. *J. Polym. Sci.* **2008**, *46*, 351–358.

(257) Müller, M. Phase Diagram of a Mixed Polymer Brush. *Phys. Rev. E - Stat. Physics, Plasmas, Fluids, Relat. Interdiscip. Top.* **2002**, *65*, 1–4.

(258) Fredrickson, G. H.; Ganesan, V.; Drolet, F. Field-Theoretical Computer Simulation Methods for Polymer and Complex Fluids. *Macromolecules* **2002**, *35*, 16–39.

(259) Fredrickson, G. H. *The Equilibrium Theory of Inhomogeneous Polymers*; International Series of Monographs on Physics, Oxford University Press: Oxford, UK, 2006.

(260) Mayer, M. The Microscopic Structure of Polymer Grafted Nanoparticles, Ph.D. Thesis, Westfälischen Wilhelms-Universitäat Müunster: Müunster, 2012.

(261) Munaò, G.; Pizzirusso, A.; Kalogirou, A.; De Nicola, A.; Kawakatsu, T.; Müller-Plathe, F.; Milano, G. Molecular Structure and Multi-Body Potential of Mean Force in Silica-Polystyrene Nanocomposites. *Nanoscale* **2018**, *10*, 21656–21670.

(262) Munaò, G.; Correa, A.; Pizzirusso, A.; Milano, G. On the Calculation of the Potential of Mean Force between Atomistic Nanoparticles. *Eur. Phys. J. E* **2018**, *41*.

(263) Theodorou, D. N. Structure and Thermodynamics of Bulk Homopolymer/Solid Interfaces: A Site Lattice Model Approach. *Macromolecules* **1988**, *21*, 1400–1410.

(264) Daoud, M.; Cotton, J. P. Star Shaped Polymers: A Model for the Conformation and Its Concentration Dependence. *J. Phys. Paris* **1982**, *43*, 531–538.

(265) Alexander, S. Adsorption of Chain Molecules with a Polar Head - A Scaling Description. *Le J. Phys.* **1977**, *38*, 983–987.

(266) de Gennes, P. G. Conformations of Polymers Attached to an Interface. *Macromolecules* **1980**, *13*, 1069–1075.

(267) Midya, J.; Rubinstein, M.; Kumar, S. K.; Nikoubashman, A. Structure of Polymer-Grafted Nanoparticle Melts. *ACS Nano* **2020**, *14*, 15505–15516.

(268) Bilchak, C. R.; Jhalaria, M.; Huang, Y.; Abbas, Z.; Midya, J.; Benedetti, F. M.; Parisi, D.; Egger, W.; Dickmann, M.; Minelli, M.; Doghieri, F.; Nikoubashman, A.; Durning, C. J.; Vlassopoulos, D.; Jestin, J.; Smith, Z. P.; Benicewicz, B. C.; Rubinstein, M.; Leibler, L.; Kumar, S. K. Tuning Selectivities in Gas Separation Membranes Based on Polymer-Grafted Nanoparticles. *ACS Nano* **2020**, *14*, 17174–17183.

(269) Schmidt, F. Self-Consistent-Field Theories for Complex Fluids. *J. Phys Condens. Matter* **1998**, *10*, 8105–8138.

(270) Sanchez, I. C.; Lacombe, R. H. Statistical Thermodynamics of Polymer Solutions. *Macromolecules* **1978**, *11*, 1145–1156.

(271) Rowlinson, J. S. Translation of J. D. van Der Waals' "The Thermodynamik Theory of Capillarity under the Hypothesis of a Continuous Variation of Density." *J. Stat. Phys.* **1979**, *20*, 197–200.

(272) Hamaker, H. C. The London—van Der Waals Attraction between Spherical Particles. *Physica* **1937**, *4*, 1058–1072.

(273) Kim, J. U.; Matsen, M. W. Finite-Stretching Corrections to the Milner-Witten-Cates Theory for Polymer Brushes. *Eur. Phys. J. E* **2007**, *23*, 135–144.

(274) Matsen, M. W.; Griffiths, G. H. Melt Brushes of Diblock Copolymer. *Eur. Phys. J. E* **2009**, *29*, 219–227.

(275) Revelas, C. J.; Sgouros, A. P.; Lakkas, A. T.; Theodorou, D. N. A Three-Dimensional Finite Element Methodology for Addressing Heterogeneous Polymer Systems with Simulations Based on Self-Consistent Field Theory; 2021; p 130002.

(276) Sanders, J. Veusz-3.2.1. 2020.

(277) Mathioudakis, I. G.; Vogiatzis, G. G.; Tzoumanekas, C.; Theodorou, D. N. Multiscale Simulations of PS–SiO $_2$ Nanocomposites: From Melt to Glassy State. *Soft Matter* **2016**, *12*, 7585–7605.

(278) Träskelin, P.; Kuhl, T. L.; Faller, R. Molecular Dynamics Simulations of Polystyrene Brushes in Dry Conditions and in Toluene Solution. *Phys. Chem. Chem. Phys.* **2009**, *11*, 11324–11332.

(279) Gharib-Zahedi, M. R.; Tafazzoli, M.; Böhm, M. C.; Alaghemandi, M. Interfacial Thermal Transport and Structural Preferences in Carbon Nanotube-Polyamide-6,6 Nanocomposites: How Important Are Chemical Functionalization Effects? *Phys. Chem. Chem. Phys.* **2015**, *17*, 14502–14512.

(280) de Gennes, P. G. Polymers at an Interface; a Simplified View. *Adv. Colloid Interface Sci.* **1987**, *27*, 189–209.

(281) Mortezaei, M.; Famili, M. H. N.; Kokabi, M. The Role of Interfacial Interactions on the Glass-Transition and Viscoelastic Properties of Silica/Polystyrene Nanocomposite. *Compos. Sci. Technol.* **2011**, *71*, 1039–1045.

(282) Theodorou, D. N. Lattice Models for Bulk Polymers at Interfaces. *Macromolecules* **1988**, *21*, 1391–1400.

(283) Milner, S. T.; Witten, T. A.; Cates, M. E. Theory of the Grafted Polymer Brush. *Macromolecules* **1988**, *21*, 2610–2619.

(284) Wijmans, C. M.; Zhulina, E. B. Polymer Brushes at Curved Surfaces. *Macromolecules* **1993**, *26*, 7214–7224.

(285) Candau, F.; Rempp, P.; Benoit, H. A New Theoretical Approach to the Problem of Solution Behavior of Branched Polymers. *Macromolecules* **1972**.

(286) Schmid, F.; Müller, M.; Mueller, M. Quantitative Comparison of Self-Consistent Field Theories for Polymers near Interfaces with Monte Carlo Simulations. *Macromolecules* **1995**, *28*, 8639–8645.

(287) Zienkiewicz, O. C.; Taylor, R. L. *The Finite Element Method: The Basis*; Butterworth-Heinemann, 2000.

(288) Bathe, K. K. J. Finite Element Procedures. *Engineering*. Prentice Hall 1996, p 1073.

(289) Huttom, D. V. *Fundamentals of Finite Element Analysis*; McGraw Hill, 2004.

(290) Jiang, K.; Huang, Y.; Zhang, P. Spectral Method for Exploring Patterns of Diblock Copolymers. *J. Comput. Phys.* **2010**, *229*, 7796–7805.

(291) Xu, W.; Jiang, K.; Zhang, P.; Shi, A. C. A Strategy to Explore Stable and Metastable Ordered Phases of Block Copolymers. *J. Phys. Chem. B* **2013**, *117*, 5296–5305.

(292) Jiang, K.; Wang, C.; Huang, Y.; Zhang, P. Discovery of New Metastable Patterns in Diblock Copolymers. *Commun. Comput. Phys.* **2013**, *14*, 443–460.

(293) Chantawansri, T. L.; Bosse, A. W.; Hexemer, A.; Ceniceros, H. D.; García-Cervera, C. J.; Kramer, E. J.; Fredrickson, G. H. Self-Consistent Field Theory Simulations of Block Copolymer Assembly on a Sphere. *Phys. Rev. E - Stat. Nonlinear, Soft Matter Phys.* **2007**, *75*, 1–17.

(294) Ceniceros, H. D.; Fredrickson, G. H. Numerical Solution of Polymer Self-Consistent Field Theory. *Multiscale Model. Simul.* **2004**, *2*, 452–474.

(295) Matthews, F. L.; Davies, G. A. O.; Hitchings, D.; Soutis, C. Fundamentals of Finite Element Analysis. In *Finite Element Modelling of Composite Materials and Structures*; Elsevier, 2000; pp 41–68.

(296) Smith, I. M., Griffiths, D. V., Margetts, L. *Programming the Finite Element Method*, Fifth.; Wiley, 2014.

(297) Boyd, J. P. *Chebyshev and Fourier Spectral Methods*; 2000.

(298) Hutton, D. V. *Fundamentals of Finite Element Analysis*; McGraw-Hill series in mechanical engineering; McGraw-Hill: Boston, 2004.

(299) Courant, R. Variational Methods for the Solution of Problems of Equilibrium and Vibrations. *Bull. Am. Math. Soc.* **1943**, *49*, 1–23.

(300) Clough, R. W. Original Formulation of the Finite Element Method. *Finite Elem. Anal. Des.* **1990**, *7*, 89–101.

(301) Idol, W. K.; Anderson, J. L. Effects of Adsorbed Polyelectrolytes on Convective Flow and Diffusion in Porous Membranes. *J. Memb. Sci.* **1986**, *28*, 269–286.

(302) Witten, T. a.; Pincus, P. a. Colloid Stabilization by Long Grafted Polymers. *Macromolecules* **1986**, *19*, 2509–2513.

(303) Sidorenko, A.; Minko, S.; Schenk-Meuser, K.; Duschner, H.; Stamm, M. Switching of Polymer Brushes. *Langmuir* **1999**, *15*, 8349–8355.

(304) Kim, J. U.; Matsen, M. W. Finite-Stretching Corrections to the Milner-Witten-Cates Theory for Polymer Brushes. *Eur. Phys. J. E* **2007**, *23*, 135–144.

(305) Reiter, G.; Auroy, P.; Auvray, L. Instabilities of Thin Polymer Films on Layers of Chemically Identical Grafted Molecules. *Macromolecules* **1996**, *29*, 2150–2157.

(306) Advincula, R. C. W. B.; Caster, K. C.; Rühe, J. *Polymer Brushes*; Advincula, R. C., Brittain, W. J., Caster, K. C., Rühe, J., Eds.; Wiley, 2004.

(307) Ferreira, P. G.; Ajdari, A.; Leibler, L. Scaling Law for Entropic Effects at Interfaces between Grafted Layers and Polymer Melts. *Macromolecules* **1998**, *31*, 3994–4003.

(308) Aubouy, M.; Raphaë, E.; Fredrickson, G. H.; Pincus, P.; Zhulina, E. B.; Birshtein, T. M.; Borisov, O. V.; Corbierre, M. K.; Cameron, N. S.; Sutton, M.; Laaziri, K.; Lennox, R. B.; Akcora, P.; Liu, H.; Kumar, S. K.; Moll, J.; Li, Y.; Benicewicz, B. C.; Schadler, L. S.; Acehan, D.; Panagiotopoulos, A. Z.; Pryamitsyn, V.; Ganesan, V.; Ilavsky, J.; Thiyagarajan, P.; Colby, R. H.; Douglas, J. F.; Sunday, D.; Ilavsky, J.; Green, D. L.; Hasegawa, R.; Aoki, Y.; Doi, M. A Phase Diagram for Polymer-Grafted Nanoparticles in Homopolymer Matrices. *Macromolecules* **1995**, *28*, 6063–6072.

(309) Milner, S. T.; Witten, T. A.; Cates, M. E. A Parabolic Density Profile for Grafted Polymers. *Europhys. Lett.* **1988**, *5*, 413–418.

(310) Zhulina, E. B.; Birshtein, T. M.; Borisov, O. V. Theory of Ionizable Polymer Brushes. *Macromolecules* **1995**, *28*, 1491–1499.

(311) Solin, P.; Segeth, K.; Dolezel, I. *Higher-Order Finite Element Methods*; 2003.

(312) Reddy, J. N.; Reddy, J. N. *An Introduction to Nonlinear Finite Element Analysis: With Applications to Heat Transfer, Fluid Mechanics, and Solid Mechanics*; Oxford University Press, 2015.

(313) Multiphysics, C. Introduction to COMSOL Multiphysics®. *COMSOL Multiphysics, Burlington, MA, accessed Feb* **1998**, *9*, 2018.

(314) MATLAB. *Version 7.10.0 (R2010a)*; The MathWorks Inc.: Natick, Massachusetts, 2010.

(315) Dee, G. T.; Ougizawa, T.; Walsh, D. J. The Pressure-Volume-Temperature Properties of Polyethylene, Poly(Dimethyl Siloxane), Poly(Ethylene Glycol) and Poly(Propylene Glycol) as a Function of Molecular Weight. *Polymer (Guildf).* **1992**, *33*, 3462–3469.

(316) Karayiannis, N. C.; Giannousaki, A. E.; Mavrantzas, V. G.; Theodorou, D. N. Atomistic Monte Carlo Simulation of Strictly Monodisperse Long Polyethylene Melts through a Generalized Chain Bridging Algorithm. *J. Chem. Phys.* **2002**, *117*, 5465–5479.

(317) Ghanbari, A.; Ndoro, T. V. M.; Leroy, F.; Rahimi, M.; Böhm, M. C.; Müller-Plathe, F. Interphase Structure in Silica-Polystyrene Nanocomposites: A Coarse-Grained Molecular Dynamics Study. *Macromolecules* **2012**, *45*, 572–584.

(318) Kritikos, G.; Terzis, A. F. Theoretical Study of Polymer Brushes by a New Numerical Mean Field Theory. *Polymer (Guildf).* **2007**, *48*, 638–651.

(319) Pandey, Y. N.; Doxastakis, M. Detailed Atomistic Monte Carlo Simulations of a Polymer Melt on a Solid Surface and around a Nanoparticle. *J. Chem. Phys.* **2012**, *136*.

(320) Pastorino, C.; Binder, K.; Müller, M. Coarse-Grained Description of a Brush− Melt Interface in Equilibrium and under Flow. *Macromolecules* **2008**, 401–410.

(321) Sgouros, A. P.; Revelas, C. J.; Lakkas, A. T.; Theodorou, D. N. Potential of Mean Force between Bare or Grafted Silica/Polystyrene Surfaces from Self-Consistent Field Theory. *Polymers (Basel).* **2021**, *13*, 1197.

(322) OriginLab Corporation. Origin(Pro). OriginLab: Northampton, MA, USA.

(323) Revelas, C. J.; Sgouros, A. P.; Lakkas, A. T.; Theodorou, D. N. RuSseL: A Self-Consistent Field Theory Code for Inhomogeneous Polymer Interphases. *Computation* **2021**, *9*, 57.

(324) Roe, R.-J. Surface Tension of Polymer Liquids. *J. Phys. Chem.* **1968**, *72*, 2013–2017.

(325) Kritikos, G.; Sgouros, A.; Vogiatzis, G. G.; Theodorou, D. N. Molecular Dynamics Study of Polyethylene under Extreme Confinement. *J. Phys. Conf. Ser.* **2016**, *738*, 012012.

(326) Boyd, G. E.; Livingstone, H. K. Adsorption and the Energy Changes at Crystalline Solid Surfaces. *J. Am. Chem. Soc.* **1942**, *64*, 2382–2388.

(327) Grest, G. S. Grafted Polymer Brushes in Polymeric Matrices. *J. Chem. Phys.* **1996**, *105*, 5532–5541.

(328) Maas, J. H.; Fleer, G. J.; Leermakers, F. A. M.; Cohen Stuart, M. A. Wetting of a Polymer Brush by a Chemically Identical Polymer Melt: Phase Diagram and Film Stability. *Langmuir* **2002**, *18*, 8871–8880.

(329) Brenner, S. C.; Scott, L. R. *The Mathematical Theory of Finite Element Methods*; Texts in Applied Mathematics; Springer New York: New York, NY, 2008; Vol. 15.

(330) Irons, B.; Ahmad, S. *Techniques of Finite Elements / Bruce Irons and Sohrab Ahmad*; E. Horwood ; Halsted Press Chichester [Eng.] : New York, 1980.

APPOSTOLOS THOMAS LAKKAS

Mobile Phone Number: +30 6976994444
E-mail Adress: alakkas@mail.ntua.gr

Personal Data

Date of Birth	14 February 1981
Place of Birth	Ioannina, Greece
Marital Status	Married
Languages	Greek, English, Spanish

Academic Education

2016 – today	PhD candidate, National Technical University of Athens, School of Chemical Engineering. Ph.D. thesis title: *Self-Consistent Field Theory for Inhomogeneous Homopolymers and Grafted Polymers* (Supervisor: Professor Doros N. Theodorou). Thesis to be defended in November 2021.
2013 – 2015	MSc from National Technical University of Athens- University of Piraeus, Interdepartmental Graduate Program in Techno-Economic Systems (8.71/10). Thesis title: *"Typology of greek businesses (cluster - statistical analysis)"* (Supervisor: Tsakanikas, A.)
2008 – 2012	Diploma from the National Technical University of Athens, School of Chemical Engineering. (9.32/10). Thesis title: *"Production of ethyl ester fatty acid and evaluation of their properties"* (Supervisor: Karonis, D.)
1998 – 2002	BSc from the Hellenic Army Academy. (8.99/10).

Technical Skills

Programming Languages	Fortran, C++, Python, Matlab
Simulation Packages	Comsol Multiphysics, FEAP

Co-supervision

2018 – 2019	Dipl. Thesis student: Konstantinos Zinelis *"Self-consistent field theory to predict the surface properties of polymer melts"*.
2017 – 2018	MSc Thesis student: George Kissas *"A computational study of Self-Consistent Field Theory for polymer interfaces"*.

Papers Published in International Journals

1. Sgouros, A. P.; Lakkas, A. T.; Megariotis, G.; Theodorou, D. N. Mesoscopic Simulations of Free Surfaces of Molten Polyethylene: Brownian Dynamics/Kinetic Monte Carlo Coupled with Square Gradient Theory and Compared to Atomistic Calculations and Experiment. *Macromolecules* **2018**, *51*, 9798–9815.

2. Lakkas, A. T.; Sgouros, A. P.; Theodorou, D. N. Self-Consistent Field Theory Coupled with Square Gradient Theory of Free Surfaces of Molten Polymers and Compared to Atomistic Simulations and Experiment. *Macromolecules* **2019**, *52*, 5337–5356.

3. Lakkas, A. T.; Sgouros, A. P.; Revelas, C. J.; Theodorou, D. N. Structure and Thermodynamics of Grafted Silica/Polystyrene Dilute Nanocomposites Investigated through Self-Consistent Field Theory. *Soft Matter* **2021**.

4. Sgouros, A. P.; Revelas, C. J.; Lakkas, A. T.; Theodorou, D. N. Potential of Mean Force between Bare or Grafted Silica/Polystyrene Surfaces from Self-Consistent Field Theory. *Polymers (Basel).* **2021**, *13*, 1197.

5. Revelas, C. J.; Sgouros, A. P.; Lakkas, A. T.; Theodorou, D. N. RuSseL: A Self-Consistent Field Theory Code for Inhomogeneous Polymer Interphases. *Computation* **2021**, *9*, 57.

Conference Papers

1. Revelas, C. J.; Sgouros, A. P.; Lakkas, A. T.; Theodorou, D. N. A Three-Dimensional Finite Element Methodology for Addressing Heterogeneous Polymer Systems with Simulations Based on Self-Consistent Field Theory. *AIP Conference Proceedings* **2021**, *2343*, 130002.

Oral/Poster Presentations on International Conference

1. Lakkas, T. A.; Sgouros, A. P.; Megariotis, G.; Theodorou, D. N. "Self-Consistent Field Model of Inhomogeneous Polymer Systems Solution by the FEM". Oral presentation, *FEMS EUROMAT 2017*, Thessaloniki, 17-22 September (2017).

2. Sgouros, A. P.; Megariotis, G.; Lakkas, T. A.; Theodorou, D. N. Multiscale Modeling of polymer/solid interfaces. Oral presentation, *FEMS EUROMAT 2017*, Thessaloniki, 17-22 September (2017).

3. Sgouros, A. P.; Lakkas, T. A.; Megariotis, G.; Vogiatzis, G. G.; Theodorou, D. N. "Multiscale Modelling of Interfacial Polymer Systems", Oral presentation, 11th *Hellenic Polymer Society International Conference*, Heraklion Crete, Greece, Nov. 3-5 (2016).

Oral/Poster Presentations on National Conferences

1. Lakkas, T. A.; Kissas, G.; Sgouros, A. P.; Liveris, D.; Megariotis, G.; Theodorou, D. N. Self-Consistent Field Theory in the Study of Polymer Interfaces. Oral presentation, 11th *Panhellenic Scientific Conference of Chemical Engineering* (11PSXM), Thessaloniki, Greece, 25-27 May (2017).